

## Durham E-Theses

---

*From a potential absorber material ( $\text{Cu}_2\text{ZnSnS}_4$ )  
toward a low-cost advanced thin film solar cell device*

ALLUHAYBI, ASAAD,MUTYIALLAH,D

### How to cite:

---

ALLUHAYBI, ASAAD,MUTYIALLAH,D (2024) *From a potential absorber material ( $\text{Cu}_2\text{ZnSnS}_4$ ) toward a low-cost advanced thin film solar cell device*, Durham theses, Durham University. Available at Durham E-Theses Online: <http://etheses.dur.ac.uk/15505/>

### Use policy

---

The full-text may be used and/or reproduced, and given to third parties in any format or medium, without prior permission or charge, for personal research or study, educational, or not-for-profit purposes provided that:

- a full bibliographic reference is made to the original source
- a [link](#) is made to the metadata record in Durham E-Theses
- the full-text is not changed in any way

The full-text must not be sold in any format or medium without the formal permission of the copyright holders.

Please consult the [full Durham E-Theses policy](#) for further details.

**From a potential absorber  
material ( $\text{Cu}_2\text{ZnSnS}_4$ ) toward a  
low-cost advanced thin film  
solar cell device**

Asaad Alluhaybi



A thesis submitted in [February 2024] to the  
Physics Department of the University of Durham  
in candidature for the degree of  
Doctor of Philosophy

© [2024 Asaad Alluhaybi]

All rights reserved.

The copyright of this thesis rests with the author. No quotation from it should be published without the author's prior written consent and information derived from it should be acknowledged.

None of the work presented in this thesis has been submitted by the author for any previous degree and it is not being submitted for any other degree.

All the work presented in this thesis was carried out by the author with the following exceptions:

- The deposition of glass/Mo layers in chapter 8 were done by Dr. Kalel Alsaeed.
- The deposition of ZnO/ITO layers in chapter 8 were done by Dr. Julius de Rojas.
- The cross-section images by SEM and the EDS mapping of CZTS devices in chapter 8 were done by Mr. Leon Bowen.

# Abstract

The focus of this thesis is to use low-cost fabrication and deposition methods to synthesize  $\text{Cu}_2\text{ZnSnS}_4$  (CZTS) nanocrystal inks as thin films to study the impacts of several variables to determine the most desirable conditions to improve the efficiency of CZTS solar cell devices. These variables are the hot injection synthesis reaction temperatures and times, tin contents of the composition synthesis, the spin coating speed and acceleration index for the deposition of the inks and the post deposition annealing temperatures and times. From the results of these conditions, CZTS PV devices were built and tested. The films were characterized using X-ray diffraction (XRD), Scanning Electron Microscope (SEM), Energy-dispersive X-ray spectroscopy (EDS), Raman spectroscopy and Ultraviolet-visible spectroscopy (UV-vis). Devices were tested by measuring  $I$ - $V$  characteristics under illumination.

The low-cost, non-vacuum hot injection technique was used for synthesising the CZTS nanoparticle thin films with spin coating for deposition on a soda lime glass substrate. For the reaction temperatures, the optical data confirms that the energy bandgap decreased with raised reaction temperatures from  $1.55 \pm 0.02$  to  $1.34 \pm 0.02$  eV for the range of temperatures 225-300 °C. The samples fabricated at 300 °C showed absence of secondary phases in Raman spectra. In the reaction times, 15-60 minutes was examined for 225 °C, 250 °C and 275 °C. It was found that the energy bandgap increased with the increase of reaction times for the three reaction temperatures tested from  $1.40 \pm 0.02$  to  $1.54 \pm 0.02$  eV for 225 °C,  $1.41 \pm 0.01$  to  $1.56 \pm 0.03$  eV for 250 °C and  $1.35 \pm 0.03$  to  $1.46 \pm 0.01$  eV for 275 °C. The sample produced at 250 °C for 30 minutes demonstrates well matching peaks and locations with the theoretically expected values for the  $a$ ,  $c$  lattice constants,  $d$ -spacing and Raman shifts. For the tin contents, the optical properties showed a trend where the bandgap increases from  $1.34 \pm 0.04$  to  $1.71 \pm 0.01$  eV as the tin contents increases from 0.60-0.90 mmol. Two secondary phases of  $\text{Cu}_4\text{SnS}_4$  and  $\text{CuS}$  were detected by Raman at locations of 317 and 472  $\text{cm}^{-1}$  in the sample of 0.70 mmol Sn. Different spin coating speeds from 1300-9700 rpm were studied where the XRD data revealed that the size of scattering domain decreases with the increase of the spin coating speed from  $17 \pm 2$  to  $7 \pm 3$  nm. However, the optical properties of CZTS seem to be less affected by the spin coating speed as a slight change were demonstrated in the bandgap fluctuating between  $1.40 \pm 0.03$  to  $1.52 \pm 0.03$  eV. Different spin coating acceleration rates from 80-2400  $\text{rpm s}^{-2}$  were investigated. The bandgaps obtained were in the range of the theoretical expected values of

between 1.40-1.60 eV. There was a possible secondary phase of SnS present at peak location of  $288\text{ cm}^{-1}$  in the sample of  $2400\text{ rpm s}^{-2}$  observed by Raman. It is found that acceleration index has a more significant effect on thin film properties than spin coating speed. Increasing acceleration index produced films with a smaller scattering domain, more Zn, less S, and a larger energy bandgap.

A range of different annealing temperatures  $560\text{ }^{\circ}\text{C}$ ,  $585\text{ }^{\circ}\text{C}$ ,  $610\text{ }^{\circ}\text{C}$ ,  $635\text{ }^{\circ}\text{C}$  with  $\text{N}_2\text{:H}_2\text{S}$  80:20, and  $585\text{ }^{\circ}\text{C}$  with  $\text{N}_2$  only atmosphere were investigated. From the optical properties, the films demonstrate improvement in uniformity and crystallinity of CZTS with annealing especially the sample of  $585\text{ }^{\circ}\text{C}$  with  $\text{N}_2$  and  $\text{H}_2\text{S}$  environment for 60 minutes as the gaps and cracks visible in microscopy images almost disappeared in comparison with the sample before annealing and formed a continuous thin film in the sample. This annealing temperature was chosen to further the investigation, but on the annealing times 30, 60 and 120 minutes. The 60 minutes sample showed a better performance in respect of energy bandgap, uniformity and crystallinity. This sample has an energy bandgap of  $1.50 \pm 0.01\text{ eV}$  which is near the optimum value to achieve the highest PV device efficiency. In addition, it showed less gaps and cracks in comparison to the sample examined before annealing and 30 minutes. Moreover, no secondary phases were present by Raman measurement in the sample of 60 minutes.

Batches of solar cell devices with structure of Mo/CZTS/CdS/ZnO/ITO/Au grid were built with different CZTS ink conditions for the reason of studying the  $I$ - $V$  device performance and efficiency and the composition and structure of the device layers. Of particular relevance are CZTS nanoparticle reaction temperatures and reaction times. The cross-section images of the devices were done by SEM which showed a formation of  $\text{MoS}_2$  thin layer on top of the Mo back contact. A thick CZTS layer was deposited on top of Mo with thickness between 1630 to 4680 nm in all devices. The illuminated-dark  $I$ - $V$  curve of these devices showed PV conversion. Among the devices tested,  $2.6 \pm 0.05\%$  was the highest efficiency performance reported. However, this is a low efficiency value which indicates that the fabrication of devices has not been fully successful. An EDS mapping image was presented for the highest efficiency performance. This mapping showed a good agreement with SEM images of the formation of a thin layer of  $\text{MoS}_2$  on top of Mo. The distribution of all measured elements throughout the device is confirmed by EDS mapping. A higher concentration of S in  $\text{MoS}_2$  compared with CZTS was confirmed by S element map. Cu, Zn, and Sn were distributed approximately evenly and uniformly among the CZTS nanocrystals. It was not possible to correlate overall device efficiency with CZTS fabrication conditions

---

because of the low efficiency due to large recombination losses, meaning that to determine the impact of different absorber layers on device efficiency is not possible at this stage.



# Contents

<b>Abstract.....</b>	<b>iii</b>
<b>Contents.....</b>	<b>vii</b>
<b>Acknowledgements .....</b>	<b>xiii</b>
<b>Publications .....</b>	<b>xv</b>
<b>1. Introduction .....</b>	<b>1</b>
1.1. An overview on energy and motivations.....	2
1.2. Solar energy.....	3
1.3. Short history of solar cells .....	4
1.4. Three generations of PV.....	6
1.4.1. Best research-cell efficiency chart.....	8
1.5. International shift to solar energy .....	10
1.6. References.....	14
<b>2. Fundamentals of solar cells .....</b>	<b>19</b>
2.1. The PV effect .....	19
2.2. The solar spectrum and optical absorption .....	19
2.3. Semiconductors.....	21
2.4. The bond model.....	23
2.5. The energy band model .....	24
2.6. Doping of semiconductors.....	25
2.7. The practical solar cell.....	26
2.8. Light absorption.....	26
2.9. Direct and indirect bandgap semiconductors.....	27
2.10. Junctions in semiconductor devices.....	29
2.11. P-N junction formation .....	30



---

2.12. Energy band alignment .....	32
2.13. Ideal diode equation and current-voltage curve .....	32
2.14. Short circuit current ( $I_{sc}$ ) .....	34
2.15. Open circuit voltage ( $V_{oc}$ ) .....	34
2.16. Fill factor (FF) .....	34
2.17. Efficiency ( $\eta$ ) .....	34
2.18. Power losses in solar cells .....	35
2.18.1. Shockley-Queisser limit .....	35
2.18.2. Recombination losses .....	39
2.18.3. Extrinsic losses, optical losses .....	40
2.18.4. Electrical losses .....	40
2.18.5. Shading .....	41
2.19. Solar cell device structure .....	41
2.20. References .....	43
<b>3. <math>\text{Cu}_2\text{ZnSnS}_4</math> material .....</b>	<b>49</b>
3.1. Why use CZTS? .....	49
3.2. What is CZTS? .....	51
3.3. Crystal structure of CZTS .....	52
3.4. Optical properties .....	54
3.5. Secondary phases .....	55
3.6. Point defects .....	58
3.7. CZTS bandgap variation and band tailing .....	59
3.8. Device structure .....	62
3.9. Vacuum and non-vacuum deposition methods .....	63
3.10. Hot injection solution method .....	63
3.11. Ink deposition method .....	65
3.12. References .....	66

---

<b>4. Experimental methodology and characterisation techniques .....</b>	<b>77</b>
4.1. Experimental methodology .....	77
4.1.1. CZTS nanocrystal preparation .....	77
4.1.2. Ink deposition .....	79
4.1.3. Annealing treatment .....	79
4.2. Characterisation techniques .....	80
4.2.1. X-ray diffraction spectroscopy (XRD) .....	80
4.2.2. Focused ion beam microscopy (FIB) .....	82
4.2.3. Energy dispersive spectroscopy (EDS) .....	83
4.2.4. Raman spectroscopy .....	84
4.2.5. Ultraviolet-visible (UV-vis) spectroscopy .....	86
4.3. References .....	87
<b>5. Investigations of CZTS nanocrystal ink synthesis temperatures, times and tin content .....</b>	<b>91</b>
5.1. Introduction .....	91
5.2. Reaction temperatures .....	92
5.3. Experimental methodology .....	92
5.3.1. The fabrication of CZTS nanoparticles .....	92
5.3.2. Ink deposition .....	93
5.4. Results and discussion .....	93
5.4.1. Crystal structure - XRD .....	93
5.4.2. Raman spectroscopy .....	96
5.4.3. Morphology .....	98
5.4.4. Chemical composition .....	99
5.4.5. Optical properties .....	102
5.5. Reaction times .....	106
5.6. Experimental methodology .....	106
5.6.1. The fabrication of CZTS nanoparticles .....	106
5.6.2. Ink deposition .....	106
5.7. Results and discussion .....	107
5.7.1. Reaction temperature of 225 °C .....	107

---

5.7.2. Crystal structure – XRD.....	107
5.7.3. Raman spectroscopy .....	108
5.7.4. Morphology.....	109
5.7.5. Chemical composition.....	110
5.7.6. Optical properties.....	111
5.7.7. Reaction temperature of 250 °C.....	113
5.7.8. Crystal structure – XRD.....	113
5.7.9. Raman spectroscopy .....	115
5.7.10. Morphology.....	116
5.7.11. Chemical composition.....	116
5.7.12. Optical properties.....	117
5.7.13. Reaction temperature of 275 °C.....	119
5.7.14. Crystal structure – XRD.....	119
5.7.15. Raman spectroscopy .....	121
5.7.16. Morphology.....	122
5.7.17. Chemical composition.....	122
5.7.18. Optical properties.....	123
5.7.19. Impact of reaction temperature and time on CZTS properties .....	126
5.8. Tin content .....	128
5.9. Experimental methodology .....	128
5.9.1. The fabrication of CZTS nanoparticles .....	128
5.9.2. Ink deposition.....	129
5.10. Results and discussion.....	129
5.10.1. Crystal structure – XRD.....	129
5.10.2. Raman spectroscopy .....	131
5.10.3. Morphology.....	133
5.10.4. Chemical composition.....	134
5.10.5. Optical properties.....	135
5.11. References.....	138
<b>6. Investigations of spin coating deposition conditions .....</b>	<b>143</b>
6.1. Introduction.....	143
6.2. Spin coating speeds.....	143

---

6.3.	Experimental methodology .....	144
6.3.1.	The fabrication of CZTS nanoparticles .....	144
6.3.2.	Ink deposition .....	144
6.4.	Results and discussion.....	144
6.4.1.	Crystal structure - XRD.....	144
6.4.2.	Raman spectroscopy .....	146
6.4.3.	Morphology.....	148
6.4.4.	Chemical composition .....	149
6.4.5.	Optical properties.....	150
6.5.	Spin coating acceleration index.....	152
6.6.	Experimental methodology .....	153
6.6.1.	The fabrication of CZTS nanoparticles .....	153
6.6.2.	Ink deposition .....	153
6.7.	Results and discussion.....	154
6.7.1.	Crystal structure - XRD.....	154
6.7.2.	Raman spectroscopy .....	156
6.7.3.	Morphology.....	157
6.7.4.	Chemical composition .....	158
6.7.5.	Optical properties.....	158
6.8.	References.....	162
<b>7.</b>	<b>Investigation of annealing temperatures and times .....</b>	<b>163</b>
7.1.	Introduction.....	163
7.2.	Annealing temperatures .....	163
7.3.	Experimental methodology .....	164
7.3.1.	The fabrication of CZTS nanoparticles .....	164
7.3.2.	Ink deposition .....	164
7.3.3.	Annealing treatment.....	164
7.4.	Results and discussion.....	165
7.4.1.	Crystal structure - XRD.....	165
7.4.2.	Raman spectroscopy .....	166
7.4.3.	Morphology.....	168

---

7.4.4. Chemical composition .....	169
7.4.5. Optical properties.....	169
7.5. Annealing times.....	172
7.6. Experimental methodology .....	172
7.6.1. The fabrication of CZTS nanoparticles .....	172
7.6.2. Ink deposition.....	173
7.6.3. Annealing treatment.....	173
7.7. Results and discussion.....	173
7.7.1. Crystal structure - XRD.....	173
7.7.2. Raman spectroscopy .....	174
7.7.3. Morphology.....	175
7.7.4. Chemical composition .....	176
7.7.5. Optical properties.....	176
7.8. References.....	180
<b>8. Impact of the reaction conditions of CZTS nanocrystal ink on solar cell device performance.....</b>	<b>182</b>
8.1. Introduction.....	182
8.2. Device structure.....	182
8.2.1. The fabrication of CZTS nanoparticles .....	183
8.2.2. Ink deposition.....	184
8.2.3. Annealing treatment.....	184
8.3. Results and discussion.....	184
8.3.1. Morphology.....	184
8.3.2. $I$ - $V$ curve measurements .....	186
8.3.3. EDS mapping .....	188
8.4. References.....	192
<b>9. Conclusions.....</b>	<b>193</b>
9.1. Conclusions .....	193
9.2. Recommendations for future studies.....	196

# Acknowledgements

I would like to acknowledge that this PhD study would not be done without the great help, continuous support, excellent comments, encouragement both in my research and personal life in Durham and guidance of my kind and friendly supervisors Prof. Douglas Halliday and Prof. Marek Szablewski. I would like to thank them for giving me the opportunity to undertake the research under their supervision. To both, I will be always grateful and thankful with my highest sincere gratitude.

I also want to express my special thanks to who have helped me during my PhD study by any means of training, discussion, comments and encouragements including:

Dr Yasir Altowairqi for his kindness, great ideas, discussion and training in the lab, Mr Leon Bowen for FIB, SEM and EDS training, help and support, Mr David Pattinson for technical work especially with annealing treatment, Mr Duncan McCallum for lab support, Dr Aidan Hindmarch for sputtering training, Dr. Kalel Alsaeed and Dr. Julius de Rojas for their help on deposition of the Mo, ZnO and ITO layers for the CZTS devices.

I would like also to thank Mr Gary Oswald for XRD training and help, Prof. Andrew Beeby for Raman measurement help in the chemistry department.

I would like also to thank all administration team in the physics department in Durham University for providing me the excellent environment and facilities to finish out my project.

I was fully sponsored by the government of Saudi Arabia and Jeddah University, so I also would like to thank them for the great support.

I also thank members and colleagues of the physics department.

My many thanks expression would be to my great mother, my father soul who died during my study, my brothers and sisters for their support. A special thanks to my wife, son and daughter who made my journey easy and enjoyable for their love and great supports.



# Publications

Work included in this thesis has been published in the following:

1. A. Alluhaybi, D. Halliday, M. Szablewski, A Study of the Role of the Annealing Temperatures and Times on  $\text{Cu}_2\text{ZnSnS}_4$  Nanocrystal Thin Films Properties, EU PVSEC-22. Proceedings. Milan, Italy. (2022) 346-350. <https://doi.org/10.4229/WCPEC-82022-2AV.2.27>.
2. A. Alluhaybi, D. Halliday, M. Szablewski, L. Bowen, The Influence of the Reaction Times on the Properties of  $\text{Cu}_2\text{ZnSnS}_4$  Nanocrystal Thin Films, ICNTREE-23. Proceedings. AlJouf, Saudi Arabia. (2023). (Accepted).
3. A. Alluhaybi, D.P. Halliday, M. Szablewski, L. Bowen, The Impact of Hot Injection Reaction Temperature on the Properties of  $\text{Cu}_2\text{ZnSnS}_4$  Nanocrystal Thin Films for PV Devices, IEEE Journal of Photovoltaics. 14 (2023) 240-245. <https://doi.org/10.1109/JPHOTOV.2023.3338859>.
4. A. Alluhaybi, D. Halliday, M. Szablewski, The Impact of Different Spin Coating Speed on the Properties of  $\text{Cu}_2\text{ZnSnS}_4$  Nanocrystal Thin Films, E-MRS-23 Proceedings. Strasbourg, France. (2023) (Accepted).
5. A. Alluhaybi, D. Halliday, M. Szablewski, The Impact of Different Spin Coating Acceleration Index on the Properties of  $\text{Cu}_2\text{ZnSnS}_4$  Nanocrystal Thin Films, EU PVSEC-23. Proceedings. Lisbon, Portugal. (2023) 001-004. <https://doi.org/10.4229/EUPVSEC2023/2CV.2.2>.
6. A. Alluhaybi, D. P. Halliday, M. Szablewski, The Impact of Different Tin Contents on the Properties of  $\text{Cu}_2\text{ZnSnS}_4$  Nanocrystal Thin Films, Solar Energy Materials and Solar Cells. (2024) (In preparation).





**From a potential absorber  
material ( $\text{Cu}_2\text{ZnSnS}_4$ ) toward a  
low-cost advanced thin film  
solar cell device**

---

# Chapter 1:

## Introduction

The increase of the world's population will lead to an increase in global energy demand. Yet, to meet these demands, the major energy supply of primary energy is still the conventional source of fossil fuels. This source needs to be replaced or significantly reduced via having another energy source to fulfil the demands since it is harming the environment via CO<sub>2</sub> emission which is one of the main causes of climate change. Renewable sources of energy are the key to addressing this issue to result in a carbon neutral energy system. Solar energy is one of the most significant sources of renewable clean energy. However, harnessing this energy to usable products has several obstacles currently, preventing it from completely replacing fossil fuels or even being fully competitive. The high cost of the solar technology, the scarcity of some semiconductor materials which are at the heart of a solar cell device, toxicity and the high cost of materials for some technologies are examples of these obstacles which motivate researchers in the field of solar energy to investigate and look for promising materials for low-cost and efficient solar cell devices.

Cu<sub>2</sub>ZnSnS<sub>4</sub> (CZTS) is one of the most promising candidates to be used as an absorber layer in thin film solar cell devices due to its excellent properties. Being considered as an earth abundant material, composed of non-toxic elements, it has a near optimum direct bandgap energy of  $\sim 1.5$  eV, high absorption coefficient greater than  $10^4$  cm<sup>-1</sup> at the energy bandgap and lower processing cost are among the promising properties.

Recently, politicians, researchers and several green environmental organisations have been attempting to attract more global attention toward the issue of global warming. A lot of studies show a link between human activities, mainly the increase of fossil fuel consumption, and the global warming issue. Global warming is the change of the earth's surface temperature mostly increasing due to a larger concentration of greenhouse gases in the atmosphere, causing weather instability which might eventually lead to melting ice at the earth's poles and the rapid increment of sea levels [1, 2]. In addressing this serious issue, the so-called Paris Agreement was adopted from the Paris climate conference (COP21) in

2015 [3]. It is an international treaty on climate change to bring countries together for the settled goal of limiting global warming to well below 1.5 °C degrees, compared to pre-industrial levels by mid-century [4].

This chapter is an introduction that explains in more details the energy issue, the possible alternative energy sources (renewable solar energy). A short history of solar cells is presented, including the three generations of photovoltaic (PV) device technology.

## 1.1. An overview on energy and motivations

The current world's population in 2023 is more than 8 billion and continuously growing according to the United Nations [5]. This growth leads to an increase of the industrial sector globally, resulting in a rapid rise of the energy demand to satisfy human society's needs for their energy daily life usage [6-8]. The consumption of power for the whole world was around 16 TW ( $16 \times 10^{12}$  Watt) in 2019 and it is estimated to rise to 30 TW in 2050 [9]. In 2020, the global energy demand decreased sharply by 4.5% due to the COVID-19 pandemic lockdown but rebounded by 5.8% in 2021 [10].

The energy production field still depends heavily on conventional sources of energy known as fossil fuels (coal, petroleum, and natural gas) in which carbon is the main element, and which accounts for 82% of the world's energy consumption in 2021 [10, 11]. The energy production process from fossil fuels requires burning carbon, leading to the emission of greenhouse gasses such as CO<sub>2</sub>, CH<sub>4</sub> and NO which are associated with issues related to the environment widely known as climate change [12-14].

Due to several challenges such as environmental issues like climate change, oil depletion meaning limited source of energy, the escape from dependence on fossil fuels, the ambitious Shell Sky scenario of achieving net zero CO<sub>2</sub> emissions or carbon neutrality by around 2070, political issues such as the Arab crisis in 1973, and the war between Russia and Ukraine in 2022, researchers are continually motivated to put more effort in addressing and responding to these challenges by suggesting alternative sources of energy for humanity [15-20]. Renewable sources of energy are the alternative source which is simply defined as the energy that can be obtained from the natural environment and can be continuously replenished. The principal renewable energies are solar, wind, hydropower, wave, geothermal and biomass. Among these renewable energies, solar energy is the most promising source as it is the primary source of sunlight for the earth. However, capturing and harnessing its energy for

conversion to another form of energy is not yet a fully matured technology to the point of being competitive with the well-developed technology of energy from fossil fuel (oil) as a source of energy. The radiant (solar) energy carried by light and several other forms of energy including mechanical (kinetic and potential), chemical, thermal, nuclear, gravitational, and wind energy can be converted to electricity as shown in figure 1.1.

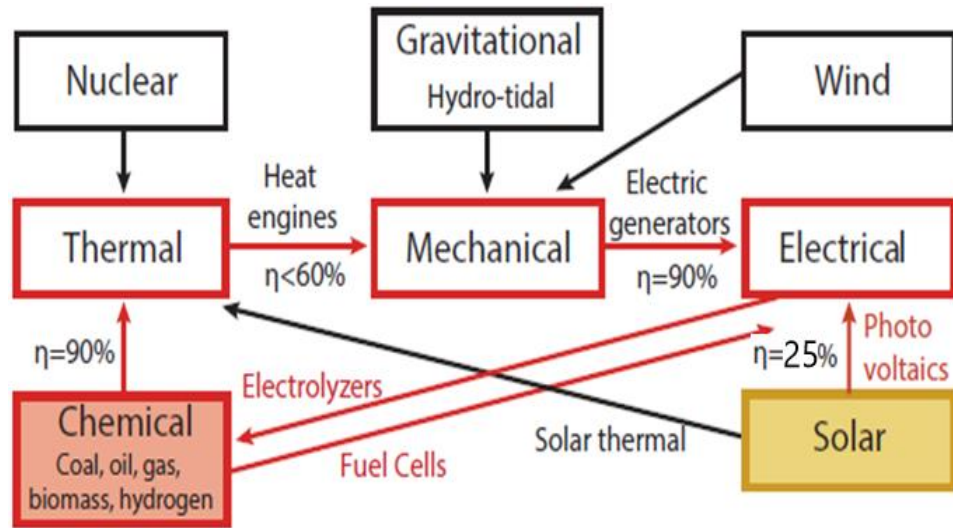


Figure 1.1 Different forms of energy including their efficiency ( $\eta$ ) with the way that they can be converted to electricity (from [21,22]).

In figure 1.1, for the solar energy to be converted to electrical form of energy, the photovoltaic technology abbreviated as PV is the key. It is a technology uses the photovoltaic effect to directly convert the light to electricity by a device named solar cell which will be explained in more details in section 1.3.

## 1.2. Solar energy

Solar energy is a form of radiation energy that can be obtained from the sun as electromagnetic radiation (light or heat). The visible incident sunlight on the earth is only a small fraction of the whole energy spectrum emitted by the sun as figure 1.2 shows. Sunlight is a form of electromagnetic radiation including the visible light which is a portion of this electromagnetic spectrum, which is described in chapter 2, section 2.2. The light indeed travels through space in packages of energy called photons. The energy of photons depends on the frequency or colour (wavelength) of the light [23]. These photons are travelling at the

speed of light as they have zero rest mass [24]. The photons incident on the earth's atmosphere will be either reflected, absorbed or transmitted through. To conclude this section, showing the importance of solar energy to be the key as a suitable alternative source of energy for the world today, it is enough to know that one hour of solar radiant incident on the earth is enough to meet the total global energy consumption for a year [25].

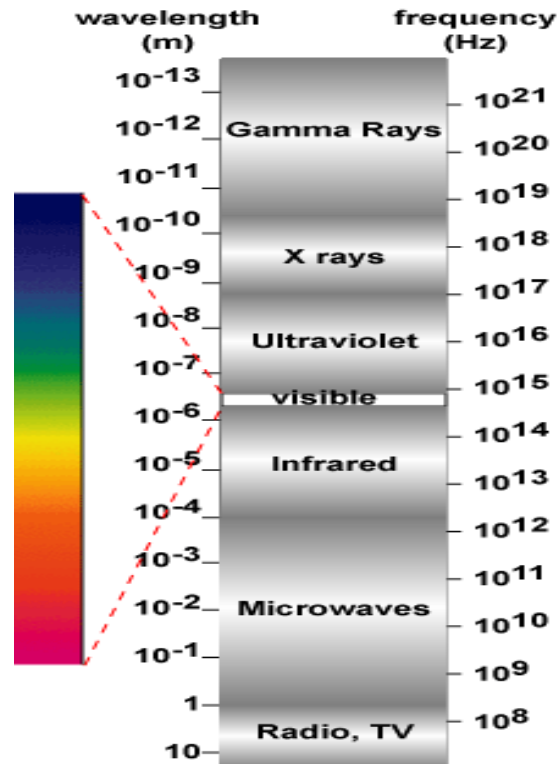


Figure 1.2 Electromagnetic spectrum (from [26]).

### 1.3. Short history of solar cells

A solar cell is a semiconductor device that converts the direct sunlight energy (photons) to the form of electrical energy through the photovoltaic effect. The concept has been known for almost a century, with several attempts of improving the first silicon solar cell which was only 6% efficient made in 1954 [27]. Silicon is the major material used to make solar cells because of its abundance in nature and cheap cost. In 1958, silicon solar cells were considered to be suitable to use in generating energy in space and remote areas [28]. For instance, the

cells can be very useful for powering communications equipment or weather monitoring stations as well as optimal for supplying power for the satellites and vehicles being improved for the space industry [29]. Indeed, solar cells and PV technology are considered to be the fastest growing renewable energy technology globally. The photovoltaic technology has been used for a wide range of applications which include providing power for consumer products such as electronic calculators, garden lights and for supplying energy for developing countries [30].

An individual solar cell generates only a very low voltage (related to the semiconductor fundamental energy gap) depending on the type of materials used in the cell which is generally around 0.6 V for silicon [31]. Therefore, several of these individual cells can be connected to each other in series creating a solar module to increase the output voltage to around 12 or 24 V or to the desired output voltage. These solar modules can be connected together to form a solar panel with higher voltage to meet the desired voltage needed by the energy system. The solar modules are covered by glass to protect the solar cells from the ambient and commonly installed on rooftops of houses that run their energy by PV. The solar panel can be grouped and wired to form larger solar array, meaning higher output power. Figure 1.3 shows a diagram of the building blocks for a PV system.

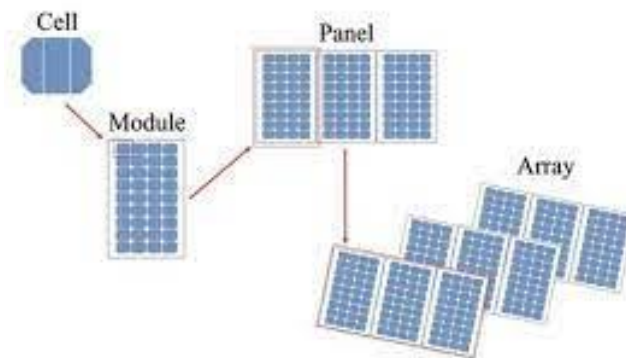


Figure 1.3 Building blocks for PV system (cell, module, panel and array) (from [32]).

A practical solar cell is indeed packaged into modules which contain either a number of crystalline silicon cells that are connected in series or a layer of thin film material that is internally connected in series [33]. Since the solar cell is a direct current (DC) device, an inverter is required to alter the DC signal into alternating current (AC) for the purpose of feeding the distribution system as electrical energy is normally distributed in AC mode. A storage device like a battery is sometimes required, especially in a stand-alone system for

---

storing the solar energy to use it after sunset especially in rural or remote areas or in developing countries where the electrical infrastructure is not good enough.

## 1.4. Three generations of PV

PV technology has developed in three generations. First generation basically comprised of the manufacturing of the original solar cell concept such as Si and single-junction gallium arsenide (GaAs). They are the most commonly used in the current stage. In fact, silicon wafer-based PV technology which is first generation accounts for around 90% of the total solar panel production in 2021 [34]. These silicon-based solar cells are yet still an excellent option for solar cell technology with continuous cost reduction due to the abundance of silicon materials in the earth's crust and the stability of the silicon based solar cells under outdoor conditions. Thus, silicon solar cells dominate our rooftops and are sold commercially to customers in our markets. The first generation or silicon wafer based solar cells demonstrate a performance up to roughly 26.7% efficiency for mono-crystalline, multi-crystalline silicon wafer-based technology can perform around 24.4% efficiency [34, 35]. The first generation of PV has a serious drawback in that silicon is an indirect bandgap semiconductor, meaning the absorption coefficient is relatively weak, leading to a requirement of certain thickness of the materials, between 100-500  $\mu\text{m}$ , to absorb sufficient sunlight. This leads to using more material which, combined with high-temperature fabrication process, results in increased manufacturing cost. To achieve lower cost manufacturing and improved manufacturability at larger scales, less material consumption and easy cheap fabrication process are needed which can be achieved by the so-called thin films, the second generation of PV.

The second generation thin film is mainly based on amorphous silicon (a-Si) and polycrystalline silicon in a lower cost material compared to the first generation. The typical performance of these second-generation cells is around 8% to 26% efficiency [35]. Since this cell avoids utilization of silicon wafers and comprises a lower material consumption, around 1  $\mu\text{m}$  thick by direct transition bandgap semiconductor materials, it has been possible to reduce the costs of these types of solar cells which is considered a great improvement of the cells. Common examples of thin film semiconductor materials for solar cells devices are cadmium telluride (CdTe), copper indium gallium selenide (CIGS) and copper zinc tin sulphide (CZTS). Among these common thin films materials, CZTS is a promising candidate



for a thin film solar cell device absorber layer since it possesses a near optimum direct bandgap energy of around 1.5 eV and high absorption coefficient more than  $10^4 \text{ cm}^{-1}$  [36-40]. CZTS is similar to the well-studied materials CIGS chalcopyrite structure, but with the replacement of the toxic and scarce elements In/Ga with non-toxic and abundant element Zn/Sn [41-44]. Since CZTS is the focus of this thesis, more details of CZTS will be covered in chapter 3.

Third generation solar cell is a concept for enhancing the performance of the cells. There are many approaches or technologies involved in third generation PV such as tandem multijunction cells and hot carrier cells which figure 1.4 shows several of these approaches.

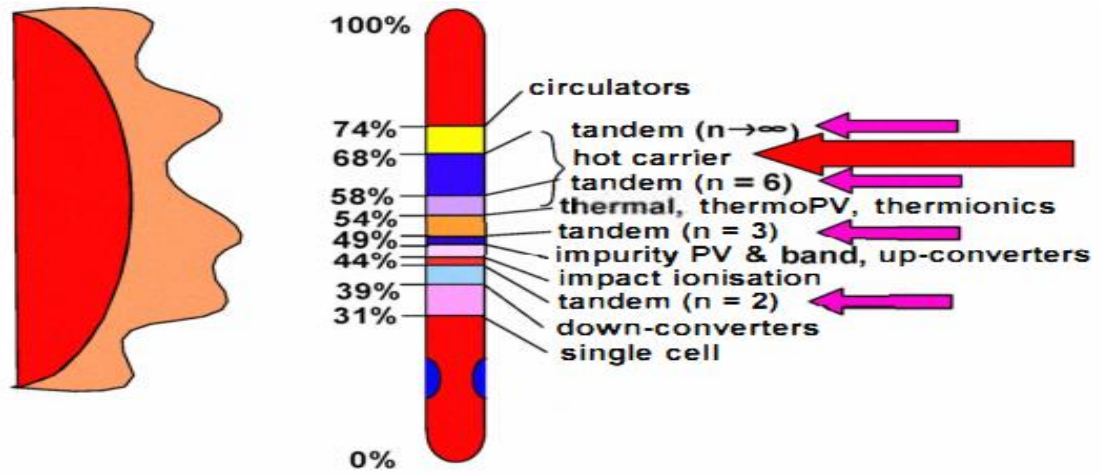


Figure 1.4 A range of technologies of 3rd generation solar cells showing approaches to increase device efficiency (from [45]).

Multijunction cells contain several p-n junctions (or sub cells) where each p-n junction has a different bandgap absorber material, meaning that these different p-n junctions can absorb different wavelengths of the solar spectrum [46]. This configuration can increase the conversion efficiency in comparison to that of a single p-n junction. However, the manufacturing cost will be increased and the complexity in growth are drawbacks of this cell design. Hot carrier cells are cells that attempt to capture carriers before thermalization which is a promising route to higher efficiencies [47].

These cell technologies are focusing on overcoming the Shockley-Queisser limit for single-bandgap devices [48, 49]. This limits the device of the single absorber layer cell efficiencies to around 32% or a little more, depending on concentration ratio [48, 49] to the Shockley-Queisser efficiency limit. More details about this limit will be presented in chapter 2.

---

#### 1.4.1. Best research-cell efficiency chart

The USA National Renewable Energy Laboratory (NREL) regularly publishes an updated chart of various solar cell technologies over time showing their efficiency improvement. Figure 1.5 demonstrates the best research-cell efficiencies globally for numerous solar cell technologies. In this figure, cell efficiency is provided within families of semiconductors: multijunction cells, single-junction gallium arsenide cells, crystalline silicon cells, thin film technologies and emerging PV. The figure presents thin film technology as a fast-growing sector of photovoltaic technologies. For instance, CZTS and CZTSSe are showing continuous performance increasing since 2010 from 9.7% to 13% in 2023.

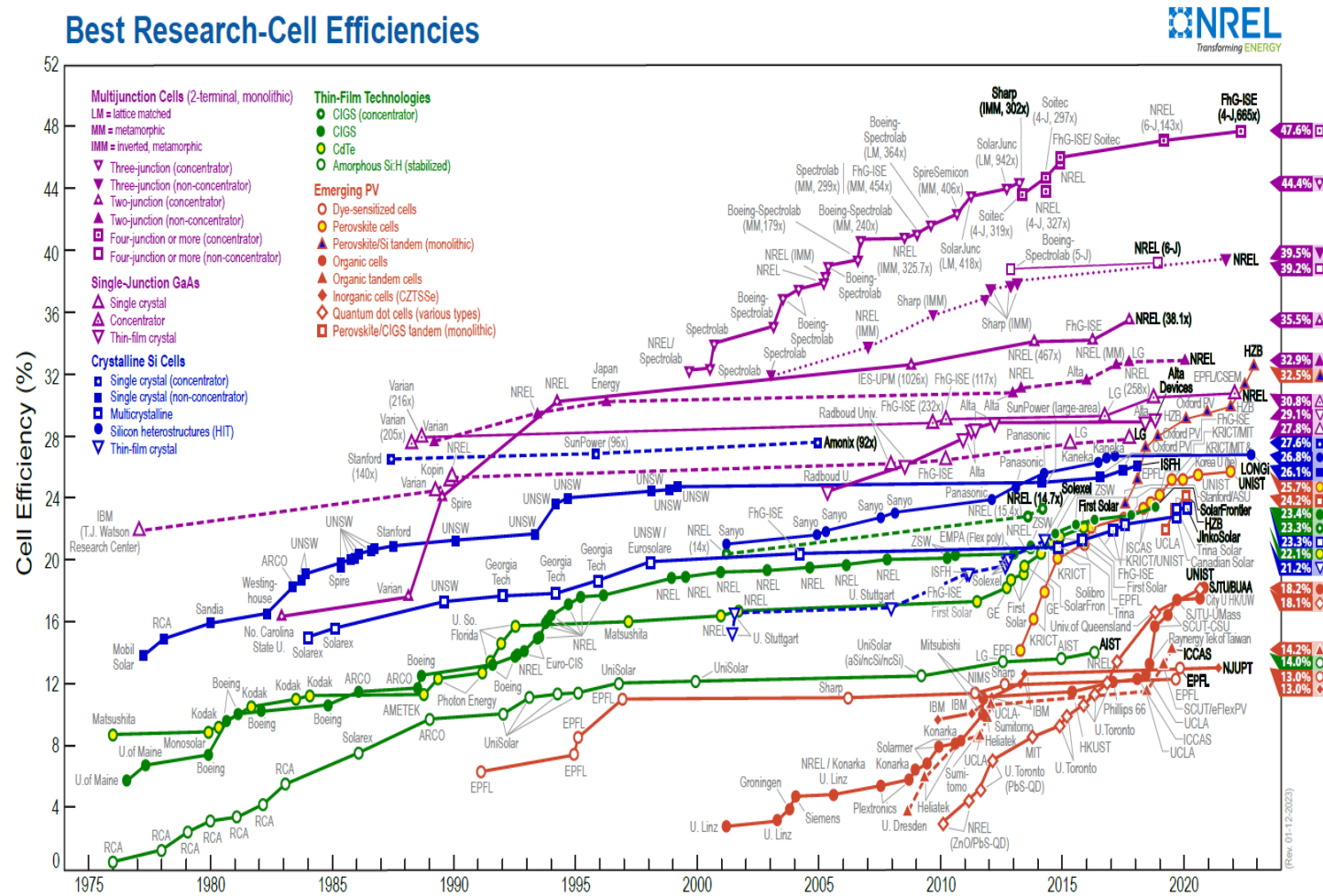


Figure 1.5 Efficiency of various solar cell technologies (from [50]).

---

## 1.5. International shift to solar energy

In responding to the Paris Agreement in 2015, most of the countries around the world agreed to act upon reducing CO<sub>2</sub> emissions. All countries actions such as shifting toward solar cells as power source or the financial support to less developed countries are counted to be valuable to reach the zero CO<sub>2</sub> emissions goal. The international economic cooperative group of countries known as The Group of Twenty (G20) accounts for more than 70% of the global CO<sub>2</sub> emissions as figure 1.6 shows [51]. Therefore, the most effective and critical response should come from them.

One example of a country action and response among the G20 is Saudi Arabia. Being one of the biggest oil producers in the world, shifting to PV is already happening there. The climatic benefits and distinct geographical area position that Saudi has, makes utilizing solar energy sources economically attractive. Saudi has supported the diversification of the domestic energy mix which is part of its Vision 2030 goals. Therefore, building solar plants such as The Sakaka Solar Power Plant in 2020 was accounted as an action of contribution toward reducing the CO<sub>2</sub> emissions [52]. This reduction from the Sakaka solar plant is 606 ktons per year. This solar plant consists of 1.2 million solar panels arranged over a land area of 6 km<sup>2</sup> [52]. The Saudi technical team made great effort to ensure the highest possible quality of electrical power generation by carefully choosing the site. This solar plant set a new world record for low cost in the solar PV sector [52]. This cost is accounted to be SAR0.08775 per kWh which is equivalent to around \$0.023 per kWh on Feb 2023 currency conversion [52]. In addition, for the contribution to the reduction of CO<sub>2</sub> emissions, similar projects were built. The production capacity of these projects is shown in table 1.1 below. It should be noted that more renewable projects were built such as Dumat Al-Jandal wind farm with 400 MW production capacity. In fact, it has a world record for the cheapest cost of electricity produced by wind [53].

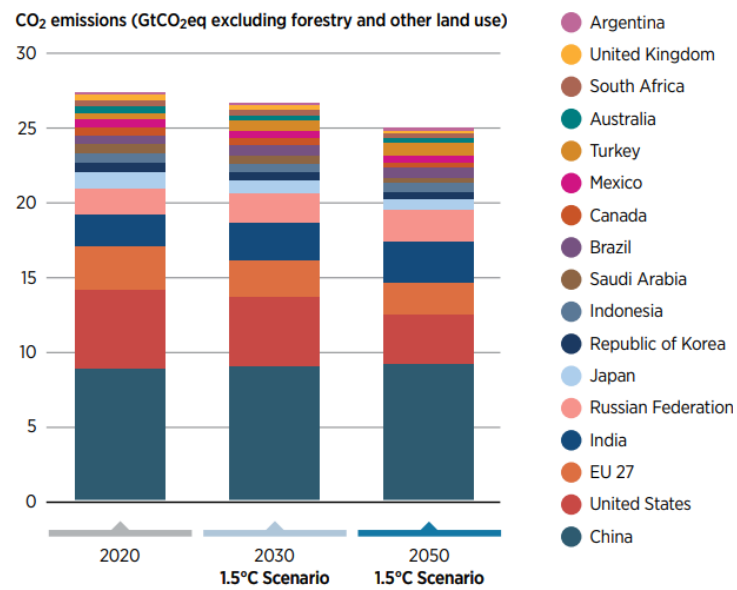


Figure 1.6 CO<sub>2</sub> emissions by the G20 countries. GtCO<sub>2</sub>eq means one billion tonnes of carbon dioxide equivalent (from [51]).

Project (PV power plant)	Production capacity (MW)
Sakaka	300
Shuaibah	600
Rabigh	300
Jeddah	300
Qurayyat	200
Medina	50
Rafha	20
Sudair	1500

**Table 1.1:** Several solar power plant projects in Saudi Arabia and their production capacity [53].





Figure 1.7 Pictures of several solar power plant in Saudi Arabia [53]. From the top left: Sakaka, Shuaibah, Rabigh, Jeddah, Qurayyat, Medina, Rafha and Sudair.

---

On top of these actions to the contribution to the reduction of CO<sub>2</sub> emissions, two important initiatives have been launched in Saudi. These two initiatives are the Saudi Green Initiative (SGI) and the Middle East Initiative (MEI) started in 2021 [54]. MEI is a regional effort led by Saudi Arabia to mitigate the impact of climate change on the region. Their primary goal is to contribute to the reduction of global CO<sub>2</sub> emissions by 10%. To achieve this goal, 50 billion trees will be planted across the middle east region (10 billion in Saudi and 40 billion in the region) which account for 5% of the global target for planting trees. This will enhance reducing the global CO<sub>2</sub> emissions by 2.5%. In addition, 60% of CO<sub>2</sub> emissions caused by oil will be reduced.

## 1.6. References

1. T. Anderson, E. Hawkins, P. Jones, CO<sub>2</sub>, The Greenhouse Effect and Global Warming: From the Pioneering Work of Arrhenius and Callendar to Today's Earth System Models, *Endeavour*. 40 (2016) 178-187. <https://doi.org/10.1016/j.endeavour.2016.07.002>.
2. H. Nugroho, G. Refantero, N. Septiani, M. Iqbal, S. Marno, H. Abdullah, E. Prima, B. Yuliarto, A Progress Review on The Modification of CZTS (e)-Based Thin Film Solar Cells. *J. Industrial. Eng. Chem.* 105 (2022) 83-110. <https://doi.org/10.1016/j.jiec.2021.09.010>.
3. European Commission, Climate Action, Paris Agreement, (2023). [Online]. Available: <https://www.commission.europa.eu>.
4. United Nation Climate Change, The Paris Agreement (2023). [Online]. Available: <https://www.unfccc.int>.
5. World Meter, (2023). [Online]. Available: <https://www.worldmeters.info/world-population/>.
6. P. Zhao, Z. Lu, J. Fang, S.R. Paramati, K. Jiang, Determinants of Renewable and Non-renewable Energy Demand in China, *Struct. Chang. Econ. Dyn.* 54 (2020) 202–209. <https://doi.org/10.1016/j.strueco.2020.05.002>.
7. M.A. Islam, H.S. Che, M. Hasanuzzaman, N.A. Rahim, Chapter 5 – Energy Demand Forecasting: in *Energy for Sustainable Development*, Academic. Press. (2020) 105–123. <https://doi.org/10.1016/B978-0-12-814645-3.00005-5>.
8. M. Shahbaz, G. Gozgor, S. Hammoudeh, Human Capital and Export Diversification as New Determinants of Energy Demand in the United States, *Energy Econ.* 78 (2019) 335–349. <https://doi.org/10.1016/j.eneco.2018.11.016>.
9. K. Pal, P. Singh, A. Bhaduri, K. Thapa, Current Challenges and Future Prospects for a Highly Efficient (> 20%) Kesterite CZTS Solar Cell: A Review. *Sol. Energy. Mater. Sol. Cells.* 196 (2019) 138-156. <https://doi.org/10.1016/j.solmat.2019.03.001>.
10. BP Statistical Review of World Energy, (2022) 71st edition. [Online]. Available: <https://www.bp.com/content/dam/bp/business-sites/en/global/corporate/pdfs/energy-economics/statistical-review/bp-stats-review-2022-full-report.pdf>.
11. H. Khatib, IEA World Energy Outlook 2011—A Comment, *Energy. policy.* 48 (2012) 737-743. <https://doi.org/10.1016/j.enpol.2012.06.007>.
12. P. D. Antunez, D. M. Bishop, Y. Luo, R. Haight, Efficient Kesterite Solar Cells with High Open Circuit Voltage for Applications in Powering Distributed Devices, *Nat. Energy.* 2 (2017) 884–890. <https://doi.org/10.1038/s41560-017-0028-5>.



- 
13. Y. Cao, X. Zhu, H. Chen, X. Zhang, J. Zhou, Z. Hu, J. Pang, Towards High Efficiency Inverted  $\text{Sb}_2\text{Se}_3$  Thin Film Solar Cells, *Sol. Energy Mater. Sol. Cells.* 200 (2019) 109945. <https://doi.org/10.1016/j.solmat.2019.109945>.
  14. C. Yan, J. Huang, K. Sun, S. Johnston, Y. Zhang, H. Sun, A. Pu, M. He, F. Liu, K. Eder, L. Yang, J. M. Cairney, N. J. Ekins-Daukes, Z. Hameiri, J. A. Stride, S. Chen, M. A. Green, X. Hao,  $\text{Cu}_2\text{ZnSnS}_4$  Solar Cells with Over 10% Power Conversion Efficiency Enabled by Heterojunction Heat Treatment, *Nat. Energy.* 3 (2018) 764–772. <https://doi.org/10.1038/s41560-018-0206-0>.
  15. M. A. Green, *Power to the People: Sunlight to Electricity Using Solar Cells*, UNSW. Press. (2000).
  16. World Energy Outlook, International Energy Agency, (2022). [Online]. Available: <http://www.iea.org/>.
  17. EEnergy Informer, The International Energy Newsletter, 33 (2023). ISSN: 1084-0419. [Online]. Available: <http://www.eenergyinformer.com/>.
  18. S. Khalate, R. Kate, R. Deokate, A Review on Energy Economics and The Recent Research and Development in Energy and The  $\text{Cu}_2\text{ZnSnS}_4$  (CZTS) Solar Cells: A Focus Towards Efficiency, *Sol. Energy* 169 (2018) 616–633. <https://doi.org/10.1016/j.solener.2018.05.036>.
  19. Y. Yin, J. Pang, J. Wang, X. Lu, Q. Hao, E. Saei Ghareh Naz, X. Zhou, L. Ma, O. Schmidt, Graphene-Activated Optoplasmonic Nanomembrane Cavities for Photodegradation Detection, *ACS. Appl. Mater. Interfaces* 11, (2019) 15891–15897. <https://doi.org/10.1021/acsami.9b00733>.
  20. Royal Dutch Shell, *Shell Scenarios: Sky - Meeting the Goals of the Paris Agreement*, Royal Dutch Shell Strategic Report. (2018).
  21. K. Jager, O. Isabella, A. H. Smets, R. A. Van Swaaij, M. Zeman, *Solar Energy Fundamentals: Technology and Systems*, UIT. Cambridge. (2016).
  22. D. Infield, L. Freris, *Renewable Energy in Power Systems*, John Wiley & Sons. (2020).
  23. J. Nelson, *The Physics of Solar Cells*, World Scientific Publishing Company. (2003).
  24. J. Balfour, J. R. Michael, Shaw, Sharlene, *Introduction to Photovoltaic*, Lawrence J. Goodrich Publishers. (2013).
  25. O. Morton, Solar Energy: A New Day Dawning? Silicon Valley Sunrise, *Nature.* 443, (2006).
  26. C. B. Honsberg, S. G. Bowden, *Photovoltaics Education Website*, (2023). [Online]. Available: [www.pveducation.org](http://www.pveducation.org).

- 
27. R. Miles, K. Hynes, I. Forbes, Photovoltaic Solar Cells: An Overview of State-of-the-art Cell Development and Environmental Issues, *Prog. Cryst. Growth Charact. Mater.* 51 (2005) 1-42. <https://doi.org/10.1016/j.pcrysgrow.2005.10.002>.
  28. M. Green, *Solar Cells: Operating Principles, Technology, and System Applications*, Englewood Cliffs. (1982).
  29. L. Fraas, L. Partain, *Solar Cells and Their Applications*, Hoboken. NJ: Wiley. (2010).
  30. G. Singh, Solar Power Generation by PV (Photovoltaic) Technology: A Review, *Energy.* 53 (2013) 1-3. <https://doi.org/10.1016/j.energy.2013.02.057>.
  31. I. Karki, Effect of Temperature on The  $I-V$  Characteristics of a Polycrystalline Solar Cell. *J. Nepal. Phys. Soc.* 3 (2015) 35-40. <https://doi.org/10.3126/jnphysoc.v3i1.14440>.
  32. A. Roderick, Understanding the Composition of a Solar Cell, *EE. Power.* (2021). [Online]. Available: <https://eepower.com/>.
  33. A. Goetzberger, C. Hebling, H. Schock, Photovoltaic Materials, History, Status and Outlook, *Mater. Sci. Eng: R: Reports.* 40 (2003) 1-46. [https://doi.org/10.1016/S0927796X\(02\)00092-X](https://doi.org/10.1016/S0927796X(02)00092-X).
  34. Fraunhofer Institute for Solar Energy Systems ISE, *Photovoltaics Report*, (2022). [Online]. Available: <https://www.ise.fraunhofer.de>.
  35. M. Green, E. Dunlop, J. Hohl-Ebinger, M. Yoshita, N. Kopidakis, K. Bothe, D. Hinken, M. Rauer, X. Hao, Solar Cell Efficiency Tables (Version 60), *Prog. Photovolt. Res. Appl.* 30 (2022) 687-701. <https://doi.org/10.1002/pip.3595>.
  36. A.D. Adewoyin, M.A. Olopade, M. Chendo, Prediction and Optimization of The Performance Characteristics of CZTS Thin Film Solar Cell Using Bandgap Grading, *Opt. Quant. Electron.* 49 (2017) 336. <https://doi.org/10.1007/s11082-017-1176-3>.
  37. K. Gunavathy, V. Parthibaraj, C. Rangasami, K. Tamilarasan, Prospects of Alternate Buffer Layers for CZTS Based Thin Films Solar Cells from Numerical Analysis—A Review, *South Asian J. Eng. Technol.* 2 (2016) 88-96. ISSN No: 2454-9614.
  38. D. Cozza, C.M. Ruiz, D. Duche, J.J. Simon, L. Escoubas, Modeling the Back Contact of  $\text{Cu}_2\text{ZnSnSe}_4$  Solar Cells, *IEEE J. Photovolt.* 6 (2016) 1292-1297. <https://doi.org/10.1109/JPHOTOV.2016.2576678>.
  39. Y. Zhang, Z. Jia, Z. Zhao, Secondary Phases in  $\text{Cu}_2\text{ZnSnS}_4$  Thin Film Solar Cell: The Role of Interfaces, *Phys. B Condens. Matter.* 626 (2022) 413539. <https://doi.org/10.1016/j.physb.2021.413539>.

- 
40. S. Mazumder, K. Senthilkumar K, Device Study and Optimisation of CZTS/ZnS Based Solar Cell with CuI Hole Transport Layer for Different Conduction Band Offset, *Sol. Energy*. 237 (2022) 414-431. <https://doi.org/10.1016/j.solener.2022.03.036>.
41. S. Das, K. Mandal, R. Bhattacharya, Earth-Abundant  $\text{Cu}_2\text{ZnSn}(\text{S},\text{Se})_4$  (CZTSSe) Solar Cells. In: M. Paranthaman, M. Wong-Ng, R. Bhattacharya, (eds) *Semiconductor Materials for Solar Photovoltaic Cells*, Springer Series in Materials Science. Springer. Cham. 218 (2016) 25-74. [https://doi.org/10.1007/978-3-319-20331-7\\_2](https://doi.org/10.1007/978-3-319-20331-7_2).
42. O. Simya, A. Mahaboobbatcha, K. Balachander, A Comparative Study on The Performance of Kesterite Based Thin Film Solar Cells Using SCAPS Simulation Program, *Superlattices. Microstructures*. 82 (2015) 248-261. <https://doi.org/10.1016/j.spmi.2015.02.020>.
43. M. Yeh, P. Lei, S. Lin, C. Yang, Copper-Zinc-Tin-Sulfur Thin Film Using Spin Coating Technology, *Mater*. 9 (2016) 526. <https://doi.org/10.3390/ma9070526>.
44. M. Moustafa, B. Mourched, S. Salem, S. Yasin, Performance Enhancement of CZTS-Based Solar Cells with Tungsten Disulfide as A New Buffer Layer. *Solid. State. Communications*. 359 (2023) 115007. <https://doi.org/10.1016/j.ssc.2022.115007>.
45. M. Green, G. Conibeer, D. König, S. Shrestha, S. Huang, P. Aliberti, L. Treiber, R. Patterson, B. Veettil, A. Hsieh, Y. Feng, Hot Carrier Solar Cells: Challenges and Recent Progress, 35th IEEE Photovolt. Specialists Conf. (2010) 57-60. <https://doi.org/10.1109/PVSC.2010.5614200>.
46. U. Bhagya-Rajasekaraiah, A. Saini, S. Krishnan, R. Vatedka, Studying the Effect of Space Radiation Induced Defects in Multijunction solar Cell Using APSYS Simulation Software and Comparison with The Experimental Data, *Nuclear. Instruments. Methods Phys. Res. Section B: Beam. Interactions. Mater. Atoms*. 535 (2023) 74-87. <https://doi.org/10.1016/j.nimb.2022.12.006>.
47. D. König, K. Casalenuovo, Y. Takeda, G. Conibeer, J. Guillemoles, R. Patterson, L. Huang, M. Green, Hot Carrier Solar Cells: Principles, Materials and Design. *Physica E: Low-dimensional. Systems. Nanostructures*. 42 (2010) 2862-2866. <https://doi.org/10.1016/j.physe.2009.12.032>.
48. G. Conibeer, Third-Generation Photovoltaics, *Mater. today*. 10 (2007) 42-50. [https://doi.org/10.1016/S1369-7021\(07\)70278-X](https://doi.org/10.1016/S1369-7021(07)70278-X).
49. G. Conibeer, M. Green, R. Corkish, Y. Cho, E. Cho, C. Jiang, T. Fangsuwannarak, E. Pink, Y. Huang, T. Puzzer, T. Trupke, Silicon Nanostructures for Third Generation

- 
- Photovoltaic Solar Cells. Thin. Solid. Films. 511-512 (2006) 654-662.  
<https://doi.org/10.1016/j.tsf.2005.12.119>.
50. National Renewable Energy Laboratory, Best Research-Cell Efficiencies. United States of America: National Renewable Energy Laboratory. (2023). [Online]. Available: <https://www.nrel.gov>.
51. World Energy Transitions Outlook 2022: 1.5°C Pathway, International Renewable Energy Agency IRENA. Abu Dhabi. 2022. [Online]. Available: [www.irena.org/publications](http://www.irena.org/publications). ISBN: 978-92-9260-429-5.
52. The Progress and Achievements of Saudi Arabia: Vision 2030 Projects: Sakaka Solar Power [Online]. Available: <https://www.vision2030.gov.sa/v2030/v2030-projects/sakaka-solar-power-plant/>.
53. Energy Projects, Ministry of Energy, Saudi Arabia. 2023. [Online]. Available: <https://www.moenergy.gov.sa/en/Projects/Pages/default.aspx>.
54. Saudi and Middle East Initiatives, Saudi Arabia. 2023. [Online]. Available: <https://www.greeninitiatives.gov.sa>.

---

# Chapter 2:

## Fundamentals of solar cells

Solar cells as mentioned in chapter 1, are semiconductor devices that convert the direct sunlight energy (photons) to electrical energy through the PV effect. To understand the physics of PV, the essential definitions such as the PV effect, solar spectrum, the interaction of light with matter, the concept of semiconductor, the absorption of light, the formation of p-n junctions and some of the parameters of solar cells are presented in this chapter.

### 2.1. The PV effect

In 1839, a young French experimental physicist named Edmond Becquerel experimented with an electrolytic cell made up of two metal electrodes which was placed in an electrically conducting solution [1-3]. This experiment resulted in the discovery of the PV effect. The result showed that when exposing certain materials to sunlight, a weak electrical current can be generated. This phenomenon results in the creation of a voltage, or a corresponding electric current from a material when exposed to electromagnetic radiation [4]. In fact, the PV effect is the basic process in which a solar cell converts sunlight into electricity. This effect later was first studied in solids like selenium in the 1870s by Heinrich Hertz [5-7]. Soon afterward, selenium photovoltaic (PV) cells achieved 1% to 2% efficiency [8].

### 2.2. The solar spectrum and optical absorption

A black body is simply a case of an ideal absorber of all radiation incident on its surface, and emitter of radiation based on its temperature such as the sun. Light is emitted as electromagnetic radiation by the sun over a range of wavelengths known as the solar spectrum which is emitted as a black body at 5760 K. The earth's atmosphere which photons travel through to earth can affect

this solar spectrum. This can be measured via a concept called the air mass (AM). The air mass can be defined as the path length of light through the atmosphere to the earth's surface [9]. If the sky is clear, the maximum sunlight intensity can hit the earth's surface when the sun is directly overhead which means that the sunlight has the shortest path length through the atmosphere. This path length can be expressed as

$$AM = \frac{1}{\cos \theta_z} . \quad (2.1)$$

Where  $\theta_z$  is the angle between the sun and the point directly overhead [10]. The air mass global spectrum which includes both direct and diffuse radiation is referred to as AM1.5G and corresponds to a power density of  $930 \text{ Wm}^{-2}$  of light incident at  $48.20^\circ$  of angle from overhead. Similarly, the AM1.5D is the direct air mass (includes direct radiation only) which corresponds to  $900 \text{ Wm}^{-2}$  of light incident at  $48.20^\circ$  of angle. AM1.5 has become the standard for photovoltaic work. Figure 2.1 shows the solar spectrum for AM0 and AM1.5.

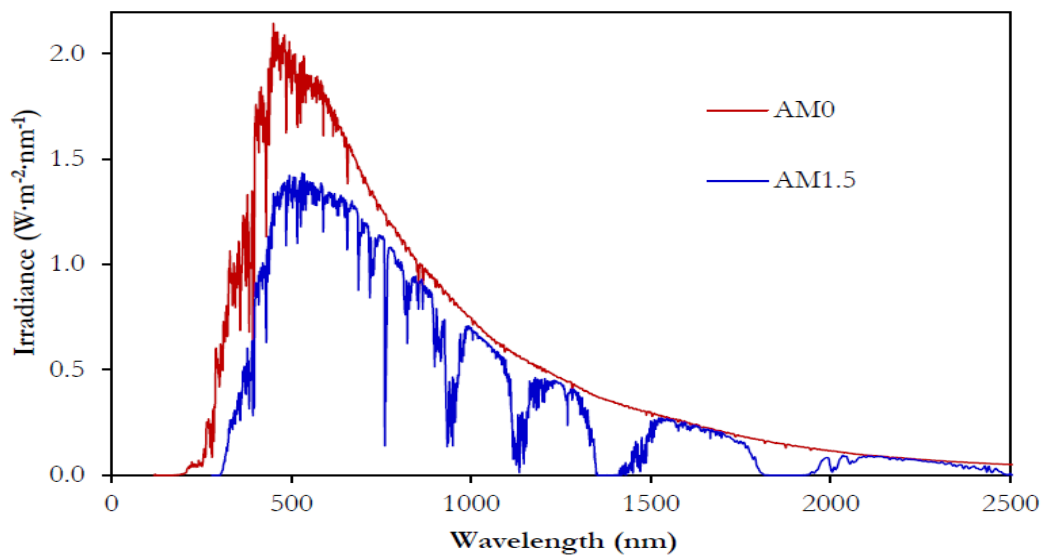


Figure 2.1 The solar spectrum for AM0 (outside earth's atmosphere) and AM1.5 at the surface of the earth (from [11]).

Sunlight passing through the earth's atmosphere is reduced by a percentage of around 30% when it reaches the earth's surface. This reduction is due to several effects as follows: Rayleigh scattering by molecules in the atmosphere, scattering by aerosols or dust particles and absorption by atmospheric gases such as oxygen, water vapour, ozone and nitrogen [12, 13]. The effect of

absorption by gases in the atmosphere can be seen as absorption bands in figure 2.1 corresponding to molecular vibrational modes.

The light can interact with matter in four forms related to refractive index change as: reflection or scattering, transmission and absorption [14]. The form of reflection is the change in light direction at a fixed angle during the interaction with materials. Scattering similarly is the change in light direction but at different angles. Transmission is the passage of light through the material without loss of energy. Absorption is the transfer of light radiation to energy within a material, normally through excitation of electrons across energy bands. In solar cells, absorption upon these forms is favourable, the other forms (transmission and reflection) are considered to be loss mechanisms of energy as photons which are not absorbed in the cell will not generate carriers (electrons and holes) leading to no power generated [15]. For the absorption to occur in the solar cells, the incident photons should have energy greater than the energy bandgap of the solar cells materials. Photons with energy less than the bandgap will not be absorbed and transmitted through the solar cell materials.

## 2.3. Semiconductors

Semiconductor materials are the basic materials used for construction of solar cells which eventually can produce electricity. Electricity is the movement of the charged carriers such as electrons and holes in the form of an electrical current [16]. Therefore, from an electrical point of view, all materials can be divided into three classifications, according to their capability of carrying charged carriers as electrical current. These classifications are conductors, semiconductors and insulator materials [17]. To understand the electrical properties of these materials and their electrical conductivity, it is recommended to know the basic concept of the energy levels in an atom and the electronic distribution in these levels.

Each electron in the atoms can be located in an energy level which means that the electrons are usually distributed in different energy levels in the atoms due to the Pauli Exclusion Principle. The electrons which are close to the nucleus of the atom will be tightly connected to the nucleus and have stronger connection with the nucleus than the more distant electrons. Electrons in the most distant orbital from the nucleus are called valence electrons as they have the weakest connection with the nucleus being in the outer orbitals and are distributed in valence band (VB) [18]. The VB is defined as the band of energy levels occupied by the valence electrons [19]. Electrons in the VB form covalent bonds which give the semiconductor its crystal structure. When the valence

electrons obtain a certain amount of energy, they can transfer to excited energy levels, called the conduction band (CB) which usually has a significantly lower concentration of electrons. The CB and the VB are separated by a gap called the energy bandgap ( $E_g$ ) to show the differences in energy between the two bands leading to determination of the type of the material. For example, if the energy gap is less than 0.5 eV, then the material will be a conductor. To be a semiconductor material, the energy gap should be between 0.5 to 3.5 eV. Insulator materials will have energy gaps greater than 3.5 eV [20]. The bandgap arises because of the interaction between electron wave function and the periodic potential of crystal atoms. Figure 2.2 shows the VB, CB and the  $E_g$  of a typical direct bandgap semiconductor.

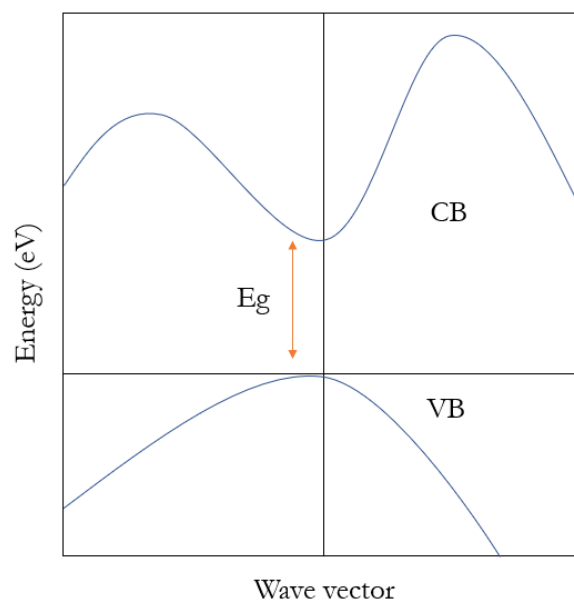


Figure 2.2 Simplified energy bandgap structure of a typical direct bandgap semiconductor showing the main features. During optical excitation by a photon, the excited electron jumps from the VB to CB across the energy bandgap leaving a hole in the VB, as shown by the red arrow.

Electrons in the CB are free to move throughout the materials [21]. However, electrons in VB do not move or respond to electric fields as the band is completely filled. In the insulator, the  $E_g$  is very much bigger than in the semiconductors and conductors meaning that the electrons in the VB need a higher energy to enable them to transfer to the CB. Semiconductors have different electronic configuration from that of insulators and metals. The energy gap is between that of insulators and conductors which means the electrons in the valence band need a smaller amount of energy to transfer to the conduction band [22]. This can be achieved by thermal excitation or absorption of photons. In metals, the outer energy band is only partially filled allowing electrons



to move easily into other energy states, thus electrical conductivity can occur at normal temperatures. In the case of conductors, electrons are distributed between the CB and the VB according to the Fermi-Dirac distribution.

Semiconductor materials have resistivity values between a conductor and an insulator [23]. In other words, the semiconductor can act as a material that is an insulator at low temperatures, but as a conductor when energy is available. Table 2.1 gives examples of several elements used to produce semiconductors. Table 2.2 shows material families used to produce semiconductors.

Group I	Group II	Group III	Group IV	Group V	Group VI
Cu	Zn	B	C	N	S
Ag	Cd	Al	Si	P	Se
-	-	Ga	Ge	As	Te
-	-	In	Sn	Sb	O

**Table 2.1:** Common elements used to produce semiconductors with their groups assigned in the Periodic Table [24].

Semiconductor family	Examples of semiconductors
Elemental semiconductors	Si, Ge
III-V semiconductors	AlN, AlP, AlAs, AlSb GaN, GaP, GaAs, GaSb InN, InP, InAs, InSb
II-VI semiconductors	ZnS, ZnSe, ZnTe, ZnO CdS, CdSe, CdTe, CdO
Ternary compound semiconductors	CuInSe <sub>2</sub> (CIS), Cd <sub>x</sub> Mn <sub>(1-x)</sub> Te, Cd <sub>x</sub> Hg <sub>(1-x)</sub> Te, Al <sub>x</sub> Ga <sub>(1-x)</sub> As
Quaternary compound semiconductors	CuInGaSe <sub>2</sub> (CIGS), AgInGaSSe, Cu <sub>2</sub> ZnSnS <sub>4</sub> (CZTS)

**Table 2.2:** Several families of semiconductor materials that are of possible use in PV devices [24].

## 2.4. The bond model

The bond model is a model that describes semiconductor behaviour [25, 26]. To illustrate the model, silicon semiconductor (as silicon is very common semiconductor material) will be used as

an example. Silicon semiconductor has an atomic number of 14 and its electron configuration will be as follow:  $1s^2 2s^2 2p^6 3s^2 3p^2$ . The number of electrons is distributed in different energy levels as in the first level (shell) is 2, in the second level is 8 and in the third level is 4 electrons. The four electrons in the third level which is the outer shell will be called valence electrons or valence shell containing 2 electrons in the s atomic orbital and 2 in the p orbital. As Si atoms interact with each other, the atomic orbitals 3s and 3p mix hybridizing to minimize the energy of the system into  $4sp^3$  molecular orbitals which leads to the resulting tetrahedral crystal structure. The 4 valence electrons which populate these molecular orbitals represent the covalent bonds that hold the lattice together. For instance, in silicon crystalline form, each silicon atom is bound to four other silicon neighbour atoms by the covalent bond in a tetrahedral arrangement (tetrahedral crystal structure) as figure 2.3 shows below. Each covalent bond consists of two electrons which are shared between the two bound atoms. Now, at low temperature, the chemical covalent bonds will be stable and the silicon semiconductor behaves as an insulator material. However, at high temperatures electrons are excited to the CB enabling the electrons to move freely in the silicon crystal lattice meanwhile the empty electron state leaves behind a hole, a positive charged carrier, meaning that a vacancy position is waiting for other electrons from neighbouring atoms to be filled. This movement of charged carriers results in the conduction of the materials [27].

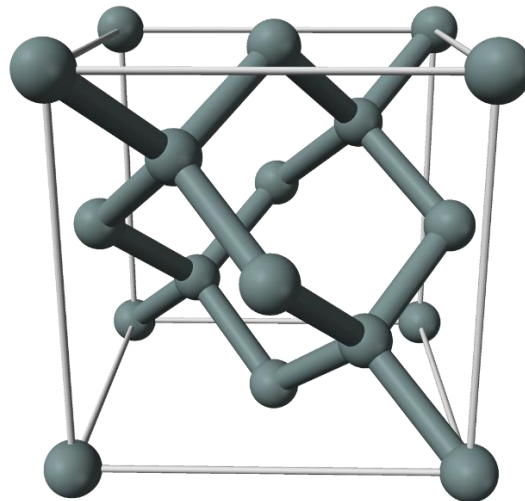


Figure 2.3 The tetrahedral crystal structure of silicon.

## 2.5. The energy band model

The energy band model is also a model that describes semiconductor behaviour using the quantum mechanical model of solids, but in terms of the energy levels between valence band and conduction

band [28,29]. The electrons in the valence band need a certain amount of energy to be excited up to the conduction band. This amount of energy depends on the forbidden gap  $E_g$  which is the minimum energy required to excite an electron from VB to CB, thus the energy gained by the electrons should be greater than the bandgap to enable the electrons to jump. When an electron is transferred to the conduction band, a hole vacancy will be created in the valence band. This process will enable electrical conduction, the process of the movement of charge carriers [30].

The energy gap can be calculated as:

$$E_g = E_c - E_v. \quad (2.2)$$

Where,  $E_c$  is the energy level at the bottom of the conduction band and  $E_v$  is the energy level at the top of the valence band.

## 2.6. Doping of semiconductors

One of the very advantageous properties of the semiconductor is the ability to change the number of electrons and holes in the crystal lattice of materials to modify the electrical and optical properties of the semiconductor [31]. This process is known as doping which is defined as the introduction of the impurities into an intrinsic semiconductor. Intrinsic semiconductors or undoped semiconductors simply mean a pure semiconductor that have the property of the number of excited electrons are equal to the number of holes ( $n_i = p_i$ ) [32]. Atoms with an extra valence electron, compared to the atom being replaced, will donate the extra electron to the semiconductor CB producing n-type material. A donor dopant such as group V phosphorus is commonly used to produce n-type silicon. Atoms with missing electron will accept an electron from the semiconductor VB and will be called p-type material, acceptor dopant such as group III boron is commonly used to produce p-type silicon [33, 34]. The concentrations of donor and acceptor atoms can be extracted from the law of mass action which can be expressed as:

$$n_o p_o = n_i^2. \quad (2.3)$$

Where,  $n_o$  and  $p_o$  are the electron and hole concentrations,  $n_i$  is the intrinsic carrier concentration. For n-type, the concentration of carriers is given as follows:

$$n_o = N_D, p_o = \frac{n_i^2}{N_D}. \quad (2.4)$$

and for p-type, the concentration of carriers is given as follows:

$$p_o = N_A, n_o = \frac{n_i^2}{N_A}, \quad (2.5)$$

where  $N_A$  and  $N_D$  are the doping densities of acceptors and donors respectively.

## 2.7. The practical solar cell

The basic operation for solar cell devices to function will usually include charged carrier generation by light absorption, charge separation by a p-n junction and charge collection in an external load [35]. If any of these operations is not occurring, the solar cell device will show poor output efficiency or even no PV activity at all. In practical devices, the power losses of the solar cell devices should be considered as the devices will suffer usually from several factors affecting the device performance. A detailed section about power losses in solar cell devices will be given in 2.16.

## 2.8. Light absorption

When photons (light) strike the semiconductor material or solar cell device, photons with energy less than the bandgap energy ( $E_{ph} < E_g$ ) will be transmitted through the semiconductor device. These photons will be considered as lost energy. However, photons with energy greater than the bandgap energy ( $E_{ph} > E_g$ ) will be absorbed in the semiconductor device. The absorbed photons will interact with the electrons in the VB and excite them. An electron in the VB will be excited to jump up to the CB leaving behind a positive charged carrier called a hole in the VB. This process is called electron-hole pair generation where each photon with energy greater than the energy of the bandgap will create one electron-hole pair (photoelectric effect) [36]. Now, the electrons in the CB can move freely as there are a large number of unoccupied states of energy. This movement can lead to current flow. The charged carriers whether they are electrons or holes need to be separated by an electric field which can be provided by a p-n junction in the semiconductor solar cell device in order to avoid recombination. More details will be provided later in section 2.11

about p-n junctions. Recombination simply is the reverse process of the electron-hole pair generation [37].

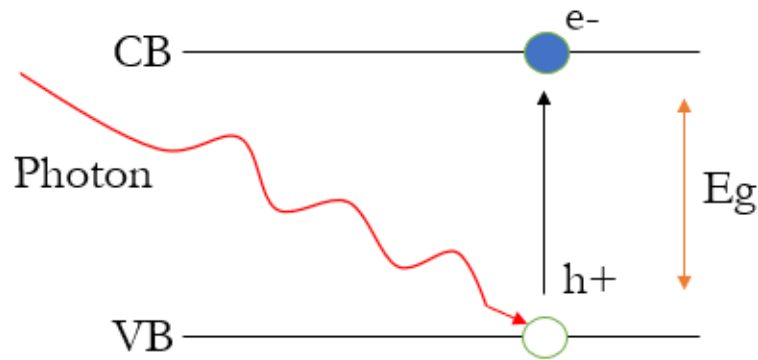


Figure 2.4 The absorption of light in the semiconductor solar cell device.

The creation of electron-hole pairs ( $E_{ph} > E_g$ ) can be given as:

$$E_{ph} = h\nu = \frac{hc}{\lambda}, \quad (2.6)$$

where,  $E_{ph}$  = photon energy,  $h$  = Planck's constant,  $\nu$  = frequency,  $c$  = speed of light and  $\lambda$  = wavelength.

The absorption coefficient,  $\alpha$ , can be expressed by:

$$\alpha = A\sqrt{(h\nu - E_g)}. \quad (2.7)$$

Where  $A$  is a constant determined by the electronic band structure,  $h$  is the Planck constant,  $\nu$  is the frequency of the light, and  $E_g$  is the bandgap of the material. This relationship is due to the bulk 3D energy density of states [38].

## 2.9. Direct and indirect bandgap semiconductors

Semiconductor materials can be divided into two different kinds regarding the bandgap of the materials, direct and indirect bandgap. In the direct bandgap semiconductor, the top (maximum) energy of the valence band occurs at the same value of the crystal momentum ( $k$ -vector) in the Brillouin zone as the bottom (minimum) energy of the conduction band at  $k = 0$  or the  $\Gamma$  point [39]. Absorption does not need any assistance from lattice vibration called a phonon and the

electron is excited directly from the maximum energy of the valence band to the minimum energy of the conduction band without any change in its  $k$ -vector (crystal momentum), because the photon momentum is very small. GaAs and CZTS are examples of direct bandgap semiconductors [40]. However, in the indirect bandgap semiconductor, the maximum energy of the valence band does not occur at the same value of the crystal momentum to the minimum energy in the conduction band. The photon absorption process requires assistance from a phonon and the electron has to undergo a significant change in its momentum to be excited from the valence band to the conduction band leading to a slower process rate and also smaller absorption coefficient than in the direct bandgap semiconductor. Silicon is an example of the indirect bandgap semiconductor [41]. The energy and momentum are conserved for both direct and indirect bandgap semiconductor [42]. Figures 2.5 and 2.6 illustrate both direct and indirect bandgap semiconductors.

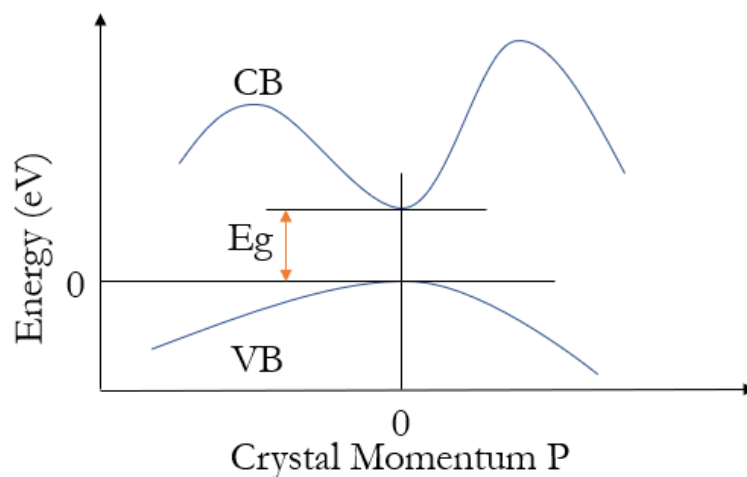


Figure 2.5 Direct bandgap semiconductor where the electron is excited directly from the VB to CB without any change in crystal momentum.

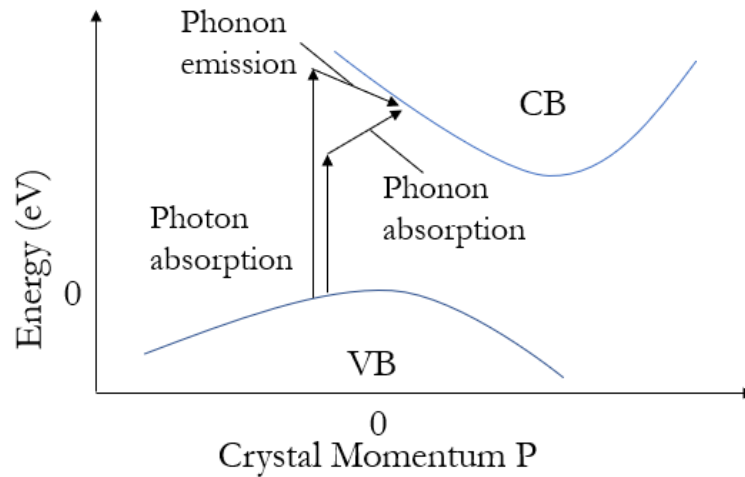


Figure 2.6 Indirect bandgap semiconductor, where the electron needs assistance of a photon and a phonon to be excited from the VB to CB.

## 2.10. Junctions in semiconductor devices

The term junction in semiconductor devices usually means the boundary or interface between two types of semiconductor materials inside a single crystal of the semiconductor [43]. When semiconductors come into contact with another semiconductor material, an internal electric field at the junction or the interface can be created [44]. Two basic types of junctions can be used in the solar cell devices for the purpose of separating the charged carriers: Schottky junction and p-n junction [45].

The Schottky junction can be formed, if a metal and a semiconductor are joined together [46]. The resulting junction can be of two possible types of contact depending on the work function (the minimum amount of energy that is required to remove an electron to the vacuum from its surface) [47]. One type of contact might be a rectifier, if the work function for the metal is larger than the work function of the semiconductor [48]. This rectifier is also known as the Schottky barrier contact and can only allow charged carriers to pass in one direction between the metal and the semiconductor, similar to a diode [49]. The other type of contact might be an Ohmic junction, if the work function for the metal is smaller than the semiconductor [50]. The Ohmic junction can allow current to pass in both directions between the metal and semiconductor [51].

The p-n junction can be formed, if two layers of semiconductor come to contact, a p-type doped layer and n-type doped layer with different majority carrier types [52]. Two different possible results can be formed, a homojunction and a heterojunction. If the two semiconductor layers of the p-n junction are of the same materials, the junction will be a p-n homojunction, and if they are

different materials and they have different bandgaps, then the junction will be a p-n heterojunction [53-55].

## 2.11. P-N junction formation

In 1962, the p-n junction's band structure model was studied by R. L. Anderson [56]. The p-n junction can be formed, when the two semiconductors (p-type and n-type) are in contact with each other which result in a rearrangement of the p-n junction's band structure [57]. As the two semiconductors combine together, with their different charged carrier's concentrations, a diffusion of these charged carriers (electrons and holes) across the junction will occur. The process of this diffusion will be a movement from the high carrier's concentration areas to the low carrier's concentration areas. The electrons or the negative charged carriers in the n-type semiconductor will flow to the p-type and leave positive charged ions (exposed positive ion cores) behind in the n-type near the junction. Similarly, the holes in the p-type will flow to the n-type, leaving negative charged (exposed negative ion cores) behind in the p-type [58]. A recombination process can occur at this moment where free electrons and holes coexist. Recombination leads to the formation of a fixed space-charge creating a built in electric field. An equilibrium is established between diffusion and drift. At this stage, the two semiconductors' band structures will realign which means that the Fermi level is close to CB in the n-type and close to VB in the p-type. The charged carriers' movement and the exposed charged ions will result in the creation of an electric field at the junction between the positive ion cores in the n-type material and the negative ion cores in the p-type, leading to the formation of a region called the depletion region. In this region, the electric field can quickly sweep the charged carriers out. A built-in potential  $V_{bi}$  is formed at the junction due to the electric field [59, 60]. This electric field can cause a drift of carriers through a drift current in the opposite direction of the diffusion. The depletion region is also known as the space charge region. Figure 2.7 shows the steps of p-n junction formation.

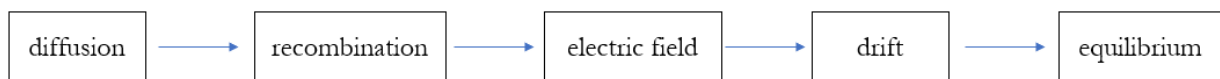


Figure 2.7. P-N junction formation steps.

If a bias voltage is applied across the p-n junction, the width of the depletion region will be changed. In the forward bias, the depletion region width will decrease, the positive terminal of an external power source connects to the p-side of the p-n junction and the negative terminal



connects to the n-side of the p-n junction [61]. In the reverse bias, the depletion region width will increase, the positive terminal of an external power source connects to the n-side of the p-n junction and the negative terminal connects to the p-side of the p-n junction [62]. Figure 2.8 illustrates the p-n junction and its band energy for the three cases mentioned above.

The built-in potential ( $V_{bi}$ ) can be calculated as:

$$V_{bi} = \frac{k_B T}{q} \ln \left( \frac{N_A N_D}{n_i^2} \right). \quad (2.8)$$

The edges of the depletion region in p or n type:

$$X_p = \left[ \left( \frac{2\epsilon V_{bi}}{q} \right) \left( \frac{N_D}{N_A} \right) \left( \frac{1}{N_A + N_D} \right) \right]^{\frac{1}{2}} \quad (2.9)$$

$$X_n = \left[ \left( \frac{2\epsilon V_{bi}}{q} \right) \left( \frac{N_A}{N_D} \right) \left( \frac{1}{N_A + N_D} \right) \right]^{\frac{1}{2}}, \quad (2.10)$$

where  $\epsilon$  is the maximum electric field produced by the space charge within the p-n junction.

The total width of the depletion region ( $W$ ) can be then calculated as:

$$W = X_p + X_n. \quad (2.11)$$

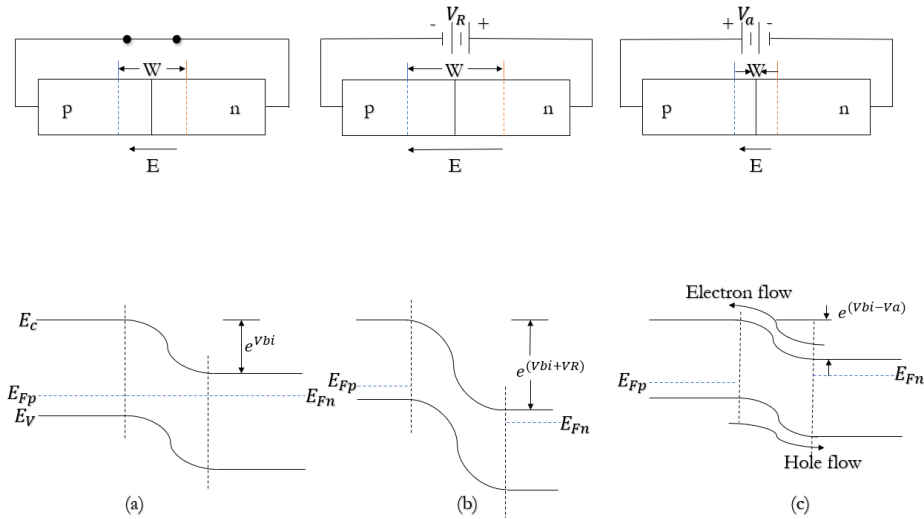


Figure 2.8 p-n junction and its band energy diagram for (a) at equilibrium (b) reverse bias (c) forward bias (from [23, 41]).

## 2.12. Energy band alignment

At the interfaces of a p-n semiconductor heterojunction, alignment of conduction and valence energy bands results in a band offset [63]. This band offset can be simply explained as a mismatch or discontinuity between the relative energy positions of the band edges in the interfaces of the p-type and n-type semiconductors. This can play a significant role in the ability of the charge carriers to cross the junction, either assisting or preventing them in charge separation [64].

For heterojunction semiconductor solar cells, a spike-like conduction band offset forms when the conduction band edge of the p-type material is lower than that of the n-type material, leading to an energy barrier for the electrons to move from the p-type material to the n-type [65]. However, when the conduction band edge of the p-type material is higher than that of the n-type material, a cliff-like conduction band offset is formed, leading to an enhancement for the electrons to move from the p-type material to the n-type.

## 2.13. Ideal diode equation and current-voltage curve

The solar cell device acts similar to a p-n diode which means that the device has the current-voltage ( $I$ - $V$ ) characteristic of a diode [66]. The  $I$ - $V$  curve represents a relationship between the current flowing through an electrical device and the voltage applied across it. This relationship is one of the most common methods to determine the function of an electrical device in a circuit. To measure the  $I$ - $V$  curve, a series of voltages are applied to the measured device where at each voltage, the current flowing through it is measured by an ammeter. A voltmeter is used to measure the applied voltages.

The ideal diode equation, also known as the Shockley diode equation, can describe the  $I$ - $V$  curve of a diode and is given as:

$$I = I_0 \left[ \exp \left( \frac{qV}{n k_B T} \right) - 1 \right]. \quad (2.12)$$

Where,  $I$  is the diode current,  $I_0$  is the saturation current,  $q$  is the charge of electron,  $V$  is the voltage across the diode,  $n$  is the diode ideality factor,  $k_B$  is Boltzmann constant,  $T$  is the absolute temperature of the p-n junction.

Under illumination, the  $I$ - $V$  curve of the p-n junction is shifted down in the current axis and the equation can be rewritten as:

$$I = I_0 \left[ \exp \left( \frac{qV}{nk_B T} \right) - 1 \right] - I_L. \quad (2.13)$$

Where,  $I_L$  is the light generated photocurrent.

It should be noted that for the ease of studying how much current is being generated in the solar cell, current density  $J$  should be used as the generated current is normalized by the area of the active device layer. The current density defines as the volumetric flow of charge per unit area through a conductor which usually use the units of  $\text{mAcm}^{-2}$ .

Some important parameters of solar cells can be determined from the equation 2.13 and from the  $I$ - $V$  curve. These parameters are short circuit current  $I_{SC}$ , open circuit voltage  $V_{OC}$ , fill factor FF and efficiency  $\eta$  [67].

The current-voltage relationship under dark and illuminated conditions can be illustrated in figure 2.9 below.

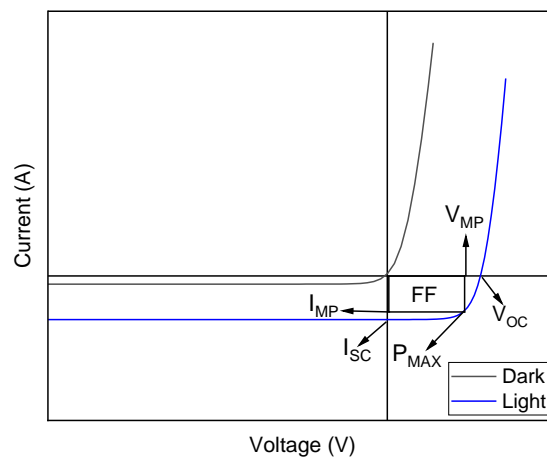


Figure 2.9 The current-voltage curve under dark and illuminated conditions. Where,  $I_{MP}$  is the maximum power current,  $V_{MP}$  is the maximum power voltage.

The maximum power point ( $P_{max}$ ) can be defined as:

$$P_{\max} = V_{MP} \times I_{MP}. \quad (2.14)$$

## 2.14. Short circuit current ( $I_{sc}$ )

The short circuit current ( $I_{sc}$ ) is the maximum current from a solar cell when there is no voltage (zero) across the device. If there are no parasitic resistance losses, then under illumination at zero bias we have  $I = I_{sc} = I_L$  as shown in figure 2.9.

## 2.15. Open circuit voltage ( $V_{oc}$ )

The open circuit voltage ( $V_{oc}$ ) is the maximum voltage from a solar cell when there is no current (zero) through the device. The open circuit voltage can be determined as:

$$V_{oc} = \frac{n k_B T}{q} \ln \left( \frac{I_L}{I_o} + 1 \right). \quad (2.15)$$

## 2.16. Fill factor (FF)

The fill factor (FF) is the ratio of the maximum power from the solar cell to the product of the short circuit current and the open circuit voltage and can be expressed as:

$$FF = \frac{P_{\max}}{I_{sc} \times V_{oc}}. \quad (2.16)$$

Also, can be written as:

$$FF = \frac{V_{MP} \times I_{MP}}{I_{sc} \times V_{oc}}. \quad (2.17)$$

## 2.17. Efficiency ( $\eta$ )

The Efficiency parameter is usually used to show the performance of the solar cell devices. It is defined as the ratio of the output energy of the solar cell to the input energy of the sunlight. Then, the efficiency can be calculated as:

$$\eta = \frac{I_{SC} \times V_{oc} \times FF}{P_{in}}. \quad (2.18)$$

Another formula can be written as:

$$\eta = \frac{P_{out}}{P_{in}}, \quad (2.19)$$

where  $P_{out}$  is the output energy of the solar cell and  $P_{in}$  is the incident sunlight to the solar cell.

## 2.18. Power losses in solar cells

The power loss process of solar cell devices in a single bandgap under one sun concentration can be categorised into two categories: intrinsic and extrinsic losses [68]. The intrinsic losses can be explained with the fundamental thermodynamic limit on the efficiency of solar cells and the theoretical accepted limit usually known as Shockley-Queisser limit (see section 2.18.1). The extrinsic losses are related to the recombination process, optical, electrical and shading losses. It should be noted that some of the intrinsic losses such as the thermodynamic losses are unfortunately unavoidable. On the other hand, the extrinsic losses are avoidable, if the solar cell device engineers optimise devices very carefully.

### 2.18.1. Shockley-Queisser limit

In 1961, W. Shockley and H. Queisser applied the principles of the detailed balance limit of efficiency, used usually in thermodynamics, for an ideal solar cell case to find out the efficiency limit for a single p-n junction based solar cell [69]. In this limit, several assumptions were made including: the concentration of light is one sun (no concentrated optics are used), the radiative recombination of hole-electron pairs was the only recombination mechanism considered as in an ideal semiconductor, and the sun and the cell act as a black body where their temperatures are  $T_s = 6000$  K and  $T_c = 300$  K, respectively.

A solar cell device can be considered as a heat or Carnot engine which can do electric work during a process where the heat can flow from the sun as a hot reservoir at 6000 K to a much colder reservoir; the earth's atmosphere at 300 K. During the conversion of the thermal energy to the electrical work, some energy will be lost. This lost energy can reduce the 100% incident light by 5%. Another loss of energy by around 9% occurs due to the inequality of absorption and emission

angles from the solar cell devices as the cell absorbs the light in one direction into the device surface and emits in all directions, resulting in an entropy generation process. This loss is usually referred to Boltzmann loss. One more percentage loss of energy is coming from the spontaneous recombination in pure semiconductor materials. Another 55% out of the 85% remaining of the incident light from the sun is lost from the non-absorption of photons by the semiconductor. The photons with less energy than the bandgap energy will not be able to excite electrons from the VB to CB, meaning the energy is lost as no absorption occur. This loss can be accounted for around 25%. Another loss may occur in a cell, if the photon's energy is much greater than the bandgap energy, a pair of electron-holes can be created and quickly the excess energy is lost through thermalisation to the band edge by emitting phonons as heat. This loss can be accounted for around 30%. These losses can limit the solar cell device to around 32% for a single solar cell under standard AM1.5G conditions.

Beside the S-Q limit, figure 2.10 attempts to illustrate the loss mechanism in single p-n junction based solar cell.

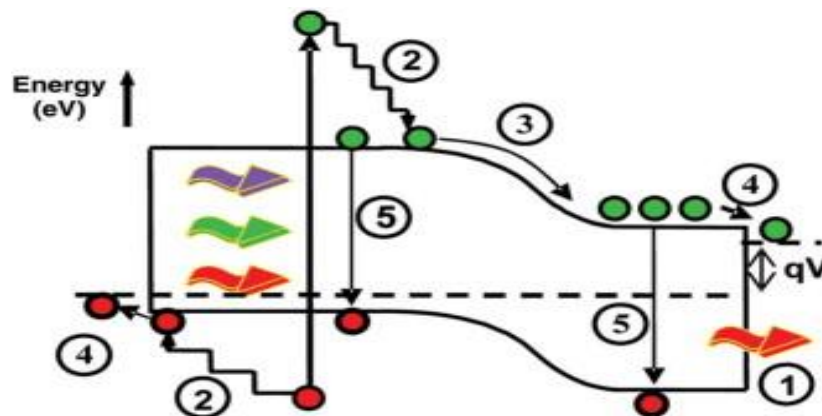


Figure 2.10 The loss mechanism of single solar cell device as (1) inability of absorption of below bandgap photons, (2) thermalization loss, (3) and (4) junction and contact voltage losses and (5) recombination loss (from [70]).

The S-Q limit efficiency varies with the bandgap of materials as shown in figure 2.11. Materials with bandgaps around 1.1-1.5 eV can achieve near S-Q limit for efficiency.

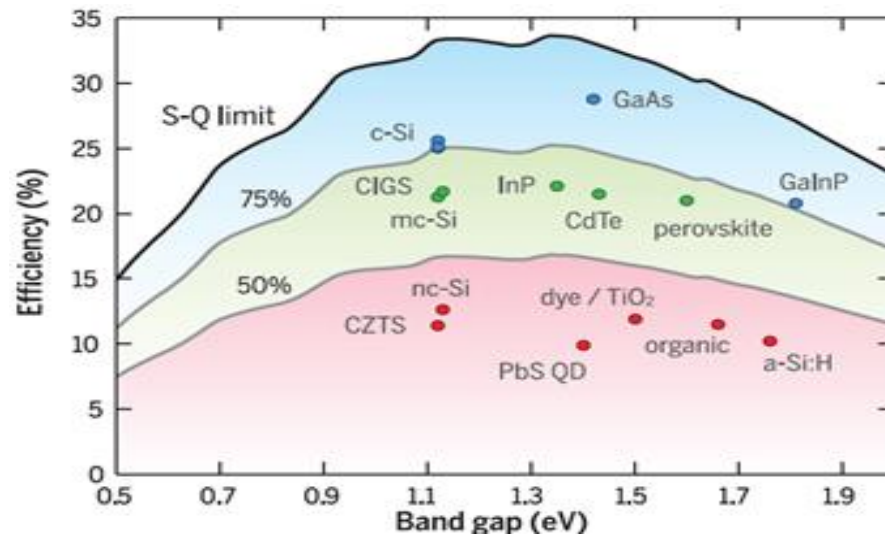


Figure 2.11 The theoretical S-Q efficiency limit as function of bandgap for several materials (from [71]). The red colour corresponds to materials of solar cells achieving less than 50% of their S-Q limit, green 50 to 75% and blue more than 75%.

Several other important attempts were done to understand the power loss mechanisms in solar cells which table 2.3 shows below.

Paper title	Year	References
Maximum Efficiency of Solar Energy Conversion by Quantum Processes.	1955	[72]
Photovoltaic Effect Derived from the Carnot Cycle.	1960	[73]
Upper Limit of Efficiency for Photovoltaic Solar Cells.	1977	[74]
Thermodynamics of the Conversion of Diluted Radiation.	1979	[75]
Limiting Efficiencies of Ideal Single and Multiple Energy Gap Terrestrial Solar Cells.	1980	[76]
Upper Limit for the Conversion of Solar Energy.	1980	[77]
Detailed balance limit of the efficiency of tandem solar cells.	1980	[78]
Thermodynamic Energy Conversion Efficiencies.	1980	[79]
On the Thermodynamic Limit of Photovoltaic Energy Conversion.	1981	[80]
Entropy Fluxes, Endoreversibility, and Solar Energy conversion.	1993	[81]
Absolute Limiting Efficiencies for Photovoltaic Energy Conversion.	1994	[82]
On Some Thermodynamic Aspects of Photovoltaic Solar Energy Conversion.	1995	[83]
Limiting Efficiencies for Photovoltaic Energy Conversion in Multigap Systems.	1996	[84]
Entropy Production in Photovoltaic Conversion.	1997	[85]
The Carnot Factor in Solar-Cell Theory.	1998	[86]
Third Generation Photovoltaics: Ultra-high Conversion Efficiency at Low Cost.	2001	[87]
Thermodynamics and Reciprocity of Solar Energy Conversion.	2002	[88]
Thermodynamic Limitations to Solar Energy Conversion.	2002	[89]
Thermodynamics of Losses in Photovoltaic Conversion.	2007	[90]
Solar Cell as Heat Engine: Energy-Entropy Analysis of Photovoltaic Conversion.	2008	[91]
Fundamental Losses in Solar Cells.	2011	[68]
Fundamentals of PV Efficiency Interpreted by a Two-Level Model.	2013	[92]

**Table 2.3:** Important research papers on mechanisms which limit efficiencies in solar cells.



### 2.18.2. Recombination losses

Recombination in a semiconductor occurs when the energetic generated electron-hole pairs combine together before they are collected. The uncollected useful energy is lost in this case as the charged carriers return to their ground state which negatively influence the efficiency of the solar cell. Recombination is possible via three main mechanisms: Shockley-Read-Hall recombination (SRH), radiative recombination and Auger recombination. Figure 2.12 illustrates these recombination types.

SRH recombination can also be called non-radiative recombination or through trap recombination or defect recombination since it describes the recombination of electrons with holes through different energy levels in the energy gap [93]. These levels are located in the bandgap where phonons are released from the excess energy of the carriers. This type of recombination is dominant in practical solar cell devices due to the difficulty of growing highly pure semiconductors. Impurities, defects or vacancies are expected to be incorporated into the crystal structure during the practical semiconductor material growth, leading to defects within the bandgap. These defects can also be referred to as traps which can capture a delocalized free carrier.

The radiative recombination, band-to-band recombination, is a result of the direct recombination of electrons in the CB with holes in VB through the emission of photons at the bandgap energy  $E_g$ . It is the reverse process of the electron-hole pair generation [94].

Auger recombination is non-radiative recombination which involves three carriers. An electron recombines with a hole, giving the energy to a third free carrier, rather than emitting the energy as a photon. This third free carrier, an electron in the CB then relaxes back down to the conduction band edge very quickly in less than a picosecond by emitting multiple phonons in the process known as thermalization [95].

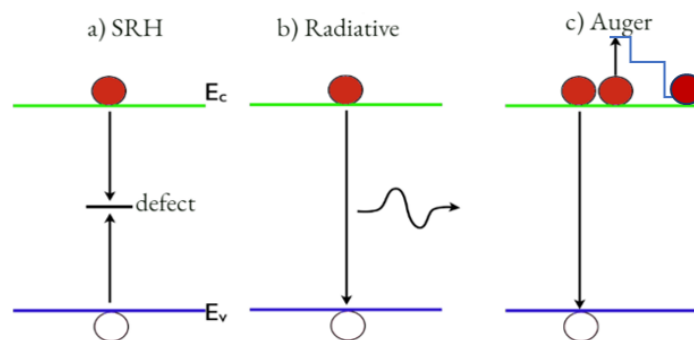


Figure 2.12 The three main recombination mechanisms in a solar cell.  $E_c$  is the energy level at the bottom of the CB and  $E_v$  is the energy level at the top of the VB.

### 2.18.3. Extrinsic losses, optical losses

Optical losses can reduce solar cell device efficiency in three main locations in practical solar cell devices. Incident light coming to the device can be blocked by the front contact coverage. In other locations, on the surface of the device, the light can be reflected and considered as a loss of useful energy. The third possible way of optical loss is the reflection of light from the back contact in the device. Figure 2.13 illustrates these optical losses.

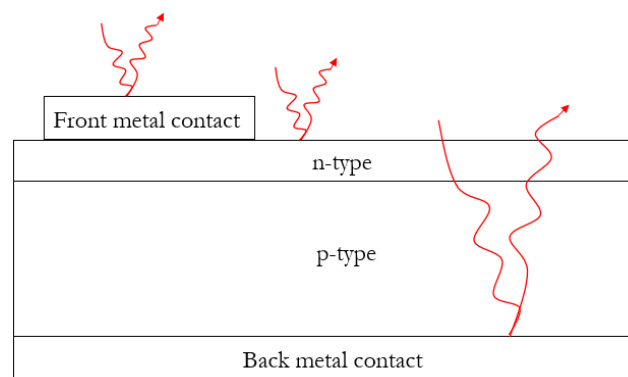


Figure 2.13 Optical losses in a solar cell device.

To reduce these optical losses, several techniques can be applied to the device. Minimising the front contact coverage in the top cell surface is a good technique. However, this can result in increased series resistance which negatively influences the solar cell by reducing the FF. Another way is the common technique of using antireflection coatings which can be located at the top surface of a device, leading to cancellation of the reflection of light from the top surface of the device. Texturing the surface of a device is also another way to reduce reflection, since roughening of the surface can increase the opportunities of reflected light to bounce back onto the surface. Light trapping in the back contact is also useful in reducing the optical losses as the possibility of light absorption can be increased.

### 2.18.4. Electrical losses

Electrical losses or parasitic resistance are unfortunately always present in practical solar cell devices which reduces the output of the device; hence they can not be ignored. The major impact electrically here is to reduce the FF. The parasitic resistance can be divided into two resistances:

series resistance  $R_S$  and shunt resistance  $R_{SH}$ . The causes of the series resistance  $R_S$  are mainly from the current movement through the bulk materials of a semiconductor and the resistance of the contact between the semiconductor materials and front or back metal contact. A negative impact on the FF of the solar cells can be a result from the increasing of  $R_S$ . In addition, excessively high value of  $R_S$  might reduce the short circuit current  $I_{SC}$ . The shunt resistance  $R_{SH}$  typically is a result of the manufacturing defects and indicates increased recombination losses. A decrease in the open circuit voltage  $V_{oc}$  might occur in the case of having low  $R_{SH}$  in the device.

### 2.18.5. Shading

The issue of shading is serious since even if a single solar cell is affected by shading in a module it can have a negative impact on the whole efficiency of the system. To illustrate this, since several individual cells are connected to each other in series creating a solar module, as mentioned in chapter 1 in section 1.3, the drop in current by shading of a tree or building or any reasons can reduce the whole current in the system lowering the system performance.

## 2.19. Solar cell device structure

In the matter of the structure or architecture of a solar cell device, two configurations can be designed: substrate and superstrate. The substrate configuration can be designed as front metal contact/transparent conducting oxide/window layer/buffer n-type/absorber p-type/back metal contact/glass. In this configuration, the light strikes the solar cell device from the top surface side, having an advantage of extending the possibility of recrystallizing the p-type absorber layer and then activating the junction by independently controlling the interface of the n-type buffer and the p-type absorber layers [96]. An appropriate choice of back metal layer is crucial in this configuration as this layer has the main role in having a low resistance Ohmic contact formation with the p-type absorber layer.

The superstrate configuration is a reverse configuration of the substrate configuration design which can be designed as glass/transparent conducting oxide as back contact/window layer/buffer n-type/absorber p-type/front metal contact. Unlike the substrate configuration, the light in this configuration strikes the solar cell device from the glass substrate side which has a transparent conducting oxide layer, indium titanium oxide (ITO) can be used and is deposited or

coated onto the glass substrate to help the light pass through the cell, reaching the absorber layer.

Figure 2.14 below illustrates the two configurations of solar cell device.

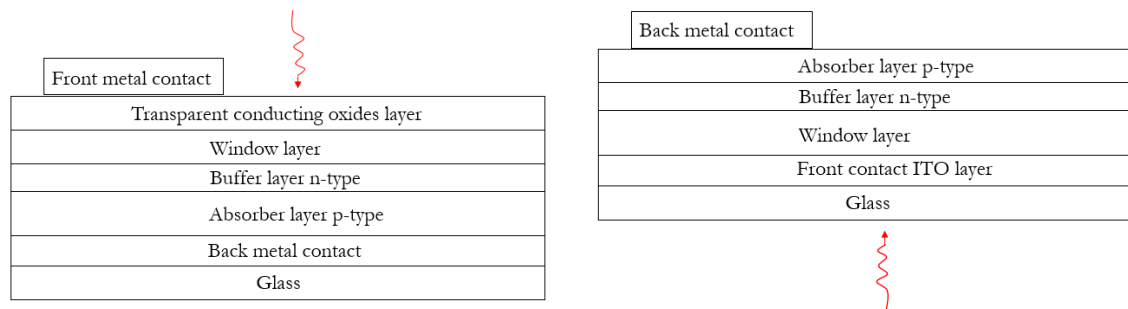


Figure 2.14 The substrate (left) and superstrate (right) configuration of solar cell devices.

---

## 2.20. References

1. W. Palz, *Power for The World: The Emergence of Electricity from The Sun*, Pan. Stanford. Publishing. (2010).
2. P. Hersch, K. Zweibel, *Basic Photovoltaic Principles and Methods*, National. Technical. Information. Service. (1982).
3. S. Wenham, M. Green, M. Watt, R. Corkish, A. Sproul, *Applied Photovoltaics*, Routledge. (2013).
4. G. Boyle, *Renewable Energy: Power for A Sustainable Future*, Oxford. University. Press. (1996).
5. W. Smith, Effect of Light on Selenium During the Passage of An Electric Current, *Nature*. 7 (1873) 303. <https://doi.org/10.1038/007303e0>.
6. E. Weston, *Art of Utilizing Solar Radiant Energy*, US. Patent. (1888).
7. W. Adams, R. Day, IX. The Action of Light on Selenium, *Philosophical. Transactions. of the Royal Society of London*. 167 (1877). <https://doi.org/10.1098/rstl.1877.0009>.
8. G. Cook, L. Billman, R. Adcock, *Photovoltaic Fundamentals*, Solar Energy Research Institute. (1991).
9. P. Würfel, *Physics of Solar Cells from Principles to New Concepts*, Wiley-VCH. (2005).
10. GP. Smestad, *Optoelectronics of Solar Cells*, SPIE press. (2002).
11. C. Bosson, *Understanding Cu<sub>2</sub>ZnSnS<sub>4</sub> as A Photovoltaic Absorber for The Future of Solar Electricity*, PhD Thesis. Durham University. (2018).
12. M. Green, *Solar Cells: Operating Principles, Technology, and System Applications*, Englewood Cliffs. (1982).
13. Hu. Chenming, M. Richard, *Solar Cells: From Basics to Advanced Systems*, NanoHUB. (2012). <https://nanohub.org/resources/13141>.
14. J. Flammer, M. Mozaffarieh, H. Bebie, The Interaction Between Light and Matter. In: *Basic Sciences in Ophthalmology*. Springer, Berlin, Heidelberg. (2013) 21-39. [https://doi.org/10.1007/978-3-642-32261-7\\_2](https://doi.org/10.1007/978-3-642-32261-7_2).
15. JL. Gray, *The Physics of the Solar Cell*. *Handbook of Photovoltaic Science and Engineering*, John Wiley & Sons Ltd. (2003) 82-128.
16. B. Baigrie, *Electricity and Magnetism: A History Perspective*, Greenwood Press Publishing Group. (2007).
17. C. Kittel, *Introduction to Solid State Physics*, 8th edn, John Willey and Sons. (2004).
18. W. G. Watkins, *Macromolecules: Synthesis, Materials and Technology*, Volume 2: By HG Elias. pp 1342. Plenum, New York. (1984). ISBN 0-306-41085-0.

- 
19. R. J. Komp, *Practical Photovoltaics: Electricity from Solar Cells*, Ann Arbor: AATEC. Publications. (1995).
  20. J. Nelson, *The Physics of Solar Cells*, World Scientific Publishing Company. (2003).
  21. M. Marone, *The Art of Teaching Physics with Ancient Chinese Science and Technology*, Synthesis Lectures on Engineering, Science, and Technology, Springer. (2020).
  22. J. P. Colinge, C. A. Colinge, *Physics of Semiconductor Devices*, Springer Science and Business Media. (2006).
  23. P. Y. Yu, M. Cardona, *Fundamentals of Semiconductors: Physics and Materials Properties*. Springer. (2010).
  24. I. M. Dharmadasa, *Advances in Thin Film Solar Cells*, Pan Stanford Publishing. (2012).
  25. J. Balfour, J. R. Michael, Shaw, Sharlene, *Introduction to Photovoltaic*, Lawrence J. Goodrich Publishers. (2013).
  26. P. Valizadeh, *Field Effect Transistors, A Comprehensive Overview: From Basic Concepts to Novel Technologies*, Wiley. (2016).
  27. R. C. Neville, *Solar Energy Conversion: The Solar Cell*, Elsevier. (1995).
  28. I. Glover, S. R. Pennock, P. R. Shepherd, *Microwave Devices, Circuits and Subsystems for Communications Engineering*, John Wiley & Sons. (2005).
  29. A. Durrant, *Quantum Physics of Matter*, CRC Press. (2000).
  30. B. K. Sharma, *Industrial Chemistry*, Krishna Prakashan Media. (1991).
  31. E. F. Schubert, *Doping in III-V Semiconductors*, (1993).
  32. A. K. Sharma, *Semiconductor Electronics*, New Age International P Ltd. Publisher. (1996).
  33. N. W. Ashcroft, N. D. Mermin, *Solid State Physics*, Harcourt. Inc. (1976).
  34. B. I. Shklovskii, A. L. Efros, *Electronic Properties of Doped Semiconductors*, Springer Science & Business Media. (2013).
  35. S. Fonash, *Solar Cell Device Physics*, Elsevier. (2012).
  36. C. S. Solanki, *Solar Photovoltaics: Fundamentals, Technologies and Applications*, Phi learning pvt. Ltd. (2015).
  37. S. D. Stranks, V. M. Burlakov, T. Leijtens, J. M. Ball, A. Goriely, H. J. Snaith, *Recombination Kinetics in Organic-Inorganic Perovskites: Excitons, Free Charge, and Subgap States*, *Phys. Rev. Applied.* 2 (2014) 034007. <https://doi.org/10.1103/PhysRevApplied.2.034007>.
  38. F. Urbach, *The Long-Wavelength Edge of Photographic Sensitivity and of The Electronic Absorption of Solids*, *Phys. Rev.* 92 (1953) 1324. <https://doi.org/10.1103/PhysRev.92.1324>.
  39. C. Hamaguchi, *Basic Semiconductor Physics*, 3<sup>rd</sup> edition, Springer Cham. (2017). <https://doi.org/10.1007/978-3-319-66860-4>.

- 
40. S. M. Sze, Y. Li, K. Ng, *Physics of Semiconductor Devices*, 4<sup>th</sup> edition, John Wiley & Sons. Inc. (2021).
  41. K. Seeger, *Semiconductor Physics*, Springer-Verlag Wien GmbH. (1973).
  42. G. Parker. *Introductory Semiconductor Device Physics*, CRC Press. (2004).
  43. M. Kaltschmitt, W. Streicher, A. Wiese, *Renewable Energy: Technology, Economics and Environment*, Springer. (2007.)
  44. A. A. Ojo, W. M. Cranton, I. M. Dharmadasa, *Next Generation Multilayer Graded Bandgap Solar Cells*, Springer Cham. (2019). <https://doi.org/10.1007/978-3-319-96667-0>.
  45. J. D. Patterson, B. C. Bailey, *Solid-State Physics: Introduction to the Theory*, Springer Science & Business Media. (2007).
  46. U. K. Mishra, J. Singh, *Semiconductor Device Physics and Design*, Springer Dordrecht. (2008). <https://doi.org/10.1007/978-1-4020-6481-4>.
  47. J. S. Yuan, J. J. Liou, *Microdevices Physics and Fabrication Technologies: Semiconductor Device Physics and Simulation*, Plenum Press. New York. (1998).
  48. M. Balkanski, R. F. Wallis, *Semiconductor Physics and Applications*, Oxford University Press. (2000).
  49. B. L. Sharma, *Metal-semiconductor Schottky Barrier Junctions and their Applications*, Springer Science & Business Media. (2013).
  50. D. J. Klotzkin, *Introduction to Semiconductor Lasers for Optical Communications: An Applied Approach*, Springer Cham. (2020). <https://doi.org/10.1007/978-3-030-24501-6>.
  51. A. Rockett, *The Materials Science of Semiconductors*, Springer. (2008).
  52. J. I. Pankove, *Optical Processes in Semiconductors*, Dover Publications. Inc. New York. (1972).
  53. N. Dasgupta, A. Dasgupta, *Semiconductor Devices: Modelling and Technology*, Phi Learning Pvt. Ltd. (2004).
  54. B. L. Sharma, R. K. Purohit, *Semiconductor Hetrojunctions*, Elsevier. (2015).
  55. S. S. Perlman, D. L. Feucht, P-N Hetrojunctions, *Solid-State Electron.* 7 (1964) 911-923. [https://doi.org/10.1016/0038-1101\(64\)90070-X](https://doi.org/10.1016/0038-1101(64)90070-X).
  56. R. L. Anderson, Experiments on Ge-GaAs Hetrojunctions, *Solid-State Electron.* 5 (1962) 345-351. [https://doi.org/10.1016/0038-1101\(62\)90115-6](https://doi.org/10.1016/0038-1101(62)90115-6).
  57. B. G. Yacobi, *Microdevices Physics and Fabrication Technologies: Semiconductor Materials: An Introduction to Basic Principles*, Kluwer Academic/Plenum Publishers. New York. (2003).
  58. B. Kumar, S. B. Jain, *Electronic Devices and Circuits*, PHI Learning Private Limited. (2014).
  59. B. Grob, *Basic Electronics*, Gregg Division McGraw-Hill Book Company. New York. (1977).

- 
60. S. T. Karris, *Electronic Devices and Amplifier Circuits with MATLAB® Applications*, Orchard Publications. (2005).
  61. G. W. Neudeck, *The PN Junction Diode*, Addison Wesley Publishing Company. (1983).
  62. De. Debashis, *Basic Electronics*, Dorling Kindersley (India) Pvt. Ltd. (2010).
  63. E. T. Yu, J. O. McCaldin, T. C. McGill, Band Offsets in Semiconductor Heterojunctions, *Solid State Phys.* 46 (1992) 1-146. [https://doi.org/10.1016/S0081-1947\(08\)60397-5](https://doi.org/10.1016/S0081-1947(08)60397-5).
  64. A. Klein, Energy Band Alignment at Interfaces of Semiconductor Oxides: A Review of Experimental Determination Using Photoelectron Spectroscopy and Comparison with Theoretical Predictions by the Electron Affinity Rule, Charge Neutrality Levels, and the Common Anion Rule, *Thin. Solid. Films.* 520 (2012) 3721-3728. <https://doi.org/10.1016/j.tsf.2011.10.055>.
  65. W. Hu, J. Yang, Two-Dimensional Van Der Waals Heterojunctions for Functional Materials and Devices, *J. Mater. Chem. C.* 5 (2017) 12289-12297. <https://doi.org/10.1039/C7TC04697A>.
  66. F. C. Krebs, *Polymeric Solar Cells: Materials, Design, Manufacture*, DEStech Publications, Inc. (2010).
  67. E. A. Gibson, *Solar Energy Capture Materials*, Royal Society of Chemistry. (2019).
  68. L. C. Hirst, N. J. Ekins-Daukes, Fundamental Losses in Solar Cells, *Prog. Photovolt: Res. Appl.* 19 (2011) 286-293. <https://doi.org/10.1002/pip.1024>.
  69. W. Shockley, H. Queisser, Detailed Balance Limit of efficiency of p-n Junction Solar Cells, *J. Appl. Phys.* 32 (1961) 510-519. <https://doi.org/10.1063/1.1736034>.
  70. M. A. Green, *Third Generation Photovoltaics: Advanced Solar Energy Conversion*, Springer. (2003).
  71. A. Polman, M. Knight, E. C. Garnett, B. Ehrler, W. C. Sinke, Photovoltaic Materials: Present Efficiencies and Future Challenges, *Sci.* 352 (2016) 6283. <https://doi.org/10.1126/science.aad4424>.
  72. D. Trivich, P. A. Flinn, F. Daniels, J. A. Duffie, *Maximum Efficiency of Solar Energy Conversion by Quantum Processes*, Solar Energy Research, Thames and Hudson. London. (1955) 143.
  73. A. Ross, Photovoltaic Effect Derived from the Carnot Cycle, *J. Appl. Phys.* 31 (1960) 1640-1641. <https://doi.org/10.1063/1.1735906>.
  74. C. D. Mathers, Upper Limit of Efficiency for Photovoltaic Solar Cells, *J. Appl. Phys.* 48 (1977) 3181-3182. <https://doi.org/10.1063/1.324059>.
  75. P. T. Landsberg, G. Tonge, Thermodynamics of the Conversion of Diluted Radiation, *J. Phys. A: Math. Gen.* 12 (1979) 551. <https://doi.org/10.1088/0305-4470/12/4/015>.



- 
76. C. H. Henry, Limiting Efficiencies of Ideal Single and Multiple Energy Gap Terrestrial Solar Cells, *J. Appl. Phys.* 51 (1980) 4494-4500. <https://doi.org/10.1063/1.328272>.
  77. W. Ruppel, P. Wurfel, Upper Limit for the Conversion of Solar Energy, *IEEE. Transactions on Electron. Devices.* 27 (1980) 877-882. <https://doi.org/10.1109/T-ED.1980.19950>.
  78. A. De. Vos, Detailed Balance Limit of the Efficiency of Tandem Solar Cells, *J. Phys. D: Appl. Phys.* 13 (1980) 839. <https://doi.org/10.1088/0022-3727/13/5/018>.
  79. P. T. Landsberg, G. Tonge, Thermodynamic Energy Conversion Efficiencies, *J. Appl. Phys.* 51 (1980) 1-20. <https://doi.org/10.1063/1.328187>.
  80. A. De. Vos, H. Pauwels, On the Thermodynamic Limit of Photovoltaic Energy Conversion, *Appl. Phys.* 25 (1981) 119-125. <https://doi.org/10.1007/BF00901283>.
  81. A. De. Vos, P. T. Landsberg, P. Baruch, J. E. Parrott, Entropy Fluxes, Endoreversibility, and Solar Energy Conversion, *J. Appl. Phys.* 74 (1993) 3631-3637. <https://doi.org/10.1063/1.354503>.
  82. G. L. Araújo, A. Martí, Absolute Limiting Efficiencies for Photovoltaic Energy Conversion, *Sol. Energy Mater. Sol. cells.* 33 (1994) 213-240. [https://doi.org/10.1016/0927-0248\(94\)90209-7](https://doi.org/10.1016/0927-0248(94)90209-7).
  83. P. Baruch, A. De. Vos, P. T. Landsberg, J. E. Parrott, On Some Thermodynamic Aspects of Photovoltaic Solar Energy Conversion, *Sol. Energy Mater. Sol. Cells.* 36 (1995) 201-222. [https://doi.org/10.1016/0927-0248\(95\)80004-2](https://doi.org/10.1016/0927-0248(95)80004-2).
  84. A. Martí, G. L. Araújo, Limiting Efficiencies for Photovoltaic Energy Conversion in Multigap Systems, *Sol. Energy. Mater. Sol. Cells.* 43 (1996) 203-222. [https://doi.org/10.1016/0927-0248\(96\)00015-3](https://doi.org/10.1016/0927-0248(96)00015-3).
  85. A. Luque A. Martí, Entropy Production in Photovoltaic Conversion, *Phys. Rev.* 55 (1997) 6994. <https://doi.org/10.1103/PhysRevB.55.6994>.
  86. P. T. Landsberg, T. Markvart, The Carnot Factor in Solar-Cell Theory, *Solid-State Electron.* 42 (1998) 657-659. [https://doi.org/10.1016/S0038-1101\(97\)00253-0](https://doi.org/10.1016/S0038-1101(97)00253-0).
  87. M. A. Green, Third Generation Photovoltaics: Ultra-high Conversion Efficiency at Low Cost, *Prog. Photovolt: Res. Appl.* 9 (2001) 123-135. <https://doi.org/10.1002/pip.360>.
  88. T. Markvart, P. T. Landsberg, Thermodynamics and Reciprocity of Solar Energy Conversion, *Physica. E: Low-dimensional Systems and Nanostructures.* 14 (2002) 71-77. [https://doi.org/10.1016/S1386-9477\(02\)00352-1](https://doi.org/10.1016/S1386-9477(02)00352-1).
  89. P. Würfel, Thermodynamic Limitations to Solar Energy Conversion, *Physica E: Low-dimensional Systems and Nanostructures.* 14 (2002) 18-26. [https://doi.org/10.1016/S1386-9477\(02\)00355-7](https://doi.org/10.1016/S1386-9477(02)00355-7).
  90. T. Markvart, Thermodynamics of Losses in Photovoltaic Conversion, *Appl. Phys. Lett.* 91 (2007) 064102. <https://doi.org/10.1063/1.2766857>.

- 
91. T. Markvart, Solar Cell as Heat Engine: Energy-Entropy Analysis of Photovoltaic Conversion, *Physica. Status. Solidi. A.* 205 (2008) 2752-2756. <https://doi.org/10.1002/pssa.200880460>.
  92. M. A. Alam, M. R. Khan, Fundamentals of PV Efficiency Interpreted by a Two-Level Model, *Am. J. Phys.* 81 (2013) 655-662. <https://doi.org/10.1119/1.4812594>.
  93. W. Shockley, W. T. Read, Statistics of the Recombinations of Holes and electrons, *Phys. Rev.* 87 (1952) 835. <https://doi.org/10.1103/PhysRev.87.835>.
  94. A. Reinders, P. Verlinden, W. Sark, A. Freundlich, *Photovoltaic Solar Energy: From Fundamentals to Applications*, John Wiley & Sons, Ltd. (2017).
  95. G. Benz, R. Conradt, Auger Recombination in GaAs and GaSb, *Phys. Rev.* 16 (1977) 843. <https://doi.org/10.1103/PhysRevB.16.843>.
  96. A. Romeo, D. L. Batzner, H. Zogg, A. N. Tiwari, A Comparison of the Vacuum Evaporated CdTe for Substrate and Superstrate Solar Cells, *InProc. 16th European Photovolt. Solar Energy Conf. and Exhibition (Glasgow)*. (2000) 843-846.

---

# Chapter 3:

## Cu<sub>2</sub>ZnSnS<sub>4</sub> material

### 3.1. Why use CZTS?

To achieve the ideal solar cell device in a commercial sense, several requirements for the materials being used in the device should be considered. These material's requirements are:

- Availability of earth abundant materials
- Non-toxic materials
- Direct bandgap structure
- A bandgap between 1.1 to 1.7 eV
- High absorption coefficient
- Suitable for large scale production
- Long-term stability.

All the chemical elements in CZTS are abundant in the earth's crust which may enhance solving the serious issue of the availability at production scale for several elements used currently in absorber materials for solar cell devices [1]. For example, In, Ga and Te in CIGS, GaAs and CdTe solar cells are simply scarce metals in the earth's crust which mean that the production of these solar cells will be limited or not amenable for large-scale production. Element toxicity is also a consideration. Table 3.1 below shows the global abundance of several elements used in current solar cells as parts per million (ppm).

Element	Abundance in earth's crust (ppm)
Cu	50.00
Zn	75.00
Sn	2.200
S	260.0
In	0.049
Ga	18.00
As	1.500
Cd	0.110
Te	0.005
Si	277.1

**Table 3.1:** The abundance of several elements in the earth's crust that are used in CZTS, CIGS, GaAs, CdTe and Si based solar cell devices technologies [2, 3].

Indeed, the availability of Zn and Sn is much higher than the rare metal In by 514 times [4]. Moreover, Zn and Sn have more global production by 20 and 340 times respectively in comparison to the expensive metal In [4]. It should be noted that Si is the second most abundant element in the earth's crust. However, one of the significant drawbacks of Si based solar cells is the expensive manufacturing cost which was explained in chapter 1 (section 1.4). Zn, Cu, Ga, In and Cd elements are 24<sup>th</sup>, 26<sup>th</sup>, 35<sup>th</sup>, 63<sup>rd</sup> and 65<sup>th</sup> most abundant elements in the earth's crust, respectively.

CZTS elements are environmentally friendly or non-toxic in comparison to Cd in the solar cell of CdTe device [5]. However, the fabrication process of the complete CZTS solar cell device might include toxic stages such as the annealing of CZTS thin film inks by using  $\text{H}_2\text{S}$  (sulphurisation stage) especially in the solution fabrication method, and the use of the toxic Cd-containing layer (CdS) as the buffer layer (n-type layer) for the CZTS device [6]. The CdS buffer layer is typically less than 0.1  $\mu\text{m}$  thick, using a small amount of material.

CZTS is an excellent absorber material as it has a near optimum direct bandgap energy of  $\sim 1.5$  eV for PV applications and high absorption coefficient within the visible region more than  $10^4 \text{ cm}^{-1}$  at the energy bandgap [7, 8]. In addition, CZTS thin film is a low-cost absorber material for solar cell device production in comparison to CIGS solar cells since Cu and Zn elements are 100 times cheaper than Ga and In metals. CZTS is also less costly in production than Si based device technologies [9, 10].

The long-term stability of solar cells is an issue for many PV technologies such as perovskite and organic based solar cell technologies. Even though these technologies exhibit high record of device efficiencies, a significant drop in their output performance might occur within minutes or several

hours or days due to long-term stability issue. For example, the power conversion efficiency of perovskite solar cells can be more than 25%, but the cells decompose in a short-time upon exposure to UV-A, moisture and thermal radiation which means that these cells still suffer from long-term stability issues [11, 12]. Hence, this issue plays a major role of being an obstacle for the devices to be used widely commercially from the industrial point of view [13, 14].

These beneficial CZTS properties give an indication that CZTS material can fulfil the above-mentioned material requirements. Hence CZTS has a great potential to be an ideal alternative candidate absorber layer suitable and promising for an advanced solar cell device [15, 16].

### 3.2. What is CZTS?

CZTS is abbreviated from and represented by the chemical formula  $\text{Cu}_2\text{ZnSnS}_4$ . It is considered to be one of the chalcogenide materials, meaning that a chalcogen from Group 16 in the periodic table (O, S, Se, Te,) is included as its anion. Other chalcogenide materials are the binary materials II-VI such as ZnS and the ternary materials I-III-VI<sub>2</sub> such as  $\text{CuInS}_2$ . CZTS as quaternary material I<sub>2</sub>-II-IV-VI<sub>4</sub> compound semiconductor is evolved from the ternary materials structure I-III-VI<sub>2</sub> ( $\text{CuInS}_2$ ) by the replacement of In of Group III by Zn of Group II and Sn of Group IV [17, 18]. Figure 3.1 below demonstrates the evolution of CZTS. The CZTS structure is similar to CIGS chalcopyrite structure with replacing the In/Ga atoms with Zn and Sn [19-21].

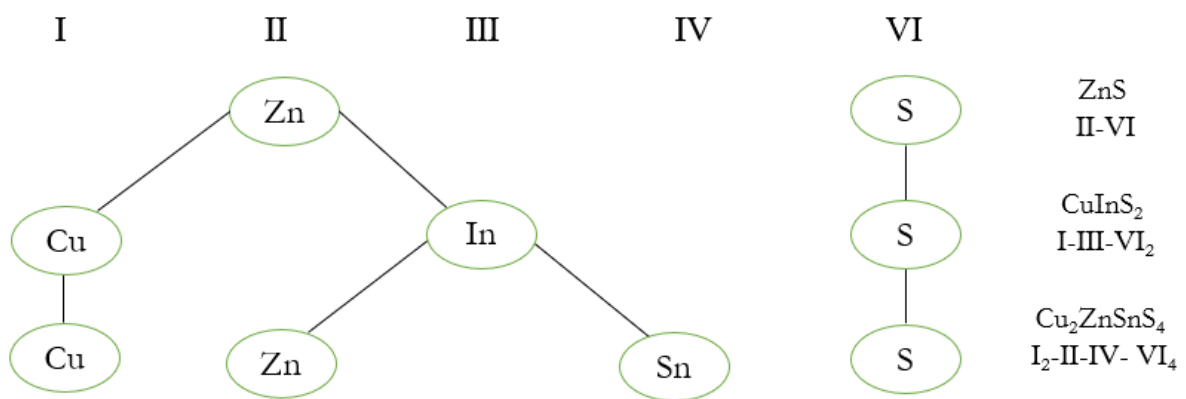


Figure 3.1 The evolution of the quaternary CZTS in relation with binary and ternary materials.

CZTS is found naturally on earth as a mineral kesterite ( $\text{Cu}_2\text{Zn}_{1-x}\text{Fe}_x\text{SnS}_4$ ) [22, 23]. In 1967, Nitsche et al., created pure CZTS by chemical vapour deposition [24]. However, the photovoltaic effect of this CZTS material was first recognised in 1988 via Nakazawa and Ito at Shinshu University in

Japan by using atom-beam sputtering [25]. In 1996, Katagiri et al., succeeded to record the CZTS solar cell efficiency at 0.66% [26, 27]. Since then, the performance of CZTS solar cells has continuously improved. It reached 2.63% in 2001 by Katagiri et al., followed by further improvement to 6.77% in 2008 [8, 15]. In 2013, with the introducing of Se (doping) to CZTS to produce CZTSSe, the efficiency reached 12.6% [28]. Currently, in 2023, CZTSSe has an efficiency of 14.1% and CZTS has 11.4% [29, 30]. CZTS can be doped or compounded with other elements such as Se, Ge, Cd, Fe, Ag and Li known as CZTSSe, CZTGS, CZCTS, CZITS, CSZTS and CLZTS respectively. This variation of elements can be found in detail in Adachi's book [31].

The major issues that limit CZTS PV device performance are having a low open circuit voltage and the presence of secondary phases. Therefore, in order to improve the performance of CZTS, a deep understanding of these areas should be attempted including interface optimisation, defect characterisation and phase stability [32].

### 3.3. Crystal structure of CZTS

Crystals can be defined as ordered structures where the atoms (ions) are arranged in a periodic lattice which is repeated throughout the entire material (solid) in three dimensions. Certain symmetry properties can be shown by this periodic arrangement. They are rotational symmetry, mirror symmetry, inversion symmetry, screw rotational symmetry and glide mirror symmetry [17]. A crystal structure is made up of a lattice and a basis where the lattice is a group of organised spaced points that is occupied by a basis. A basis can be an atom or a molecule that is repeated at every lattice point (along the principal axes). The smallest set of particles in the material which constitutes this repeating pattern (along the principal axes) is called the unit cell of the structure where the edges of this unit cell are the same as the principal axes and their length are called the lattice constants ( $a$ ,  $b$ ,  $c$ ) [33].

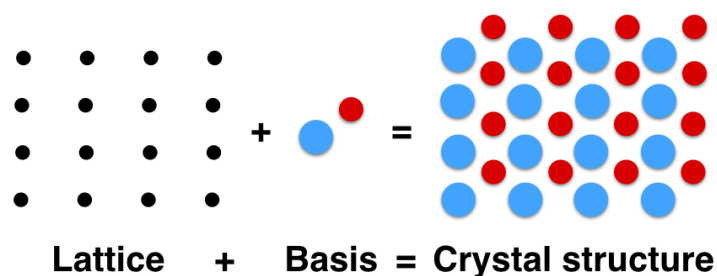


Figure 3.2 A simple diagram illustrates how the crystal structure is made [34].

CZTS crystallises in a tetrahedral coordinated structure where each sulphur anion is bonded to four cations as well as each cation is bonded to four sulphur anions [35]. CZTS is considered to be a tetragonal structure that can exist in four different fundamental crystal structures [36]. The first one is the kesterite structure (KS) with the space group  $\bar{I}4$  (number 82) where  $I$  represents the body centred Bravais lattice and  $\bar{4}$  is a rotation-inversion axis which has an angle of rotation of  $360^\circ/4$  [37]. The second structure is the stannite structure (ST) with the space group  $\bar{I}4_2m$  (number 121) where 2 represents the rotation axis with an angle of rotation  $360^\circ/2$  and  $m$  is a mirror symmetry plane [38]. The third structure is the primitive mixed Cu-Au structure (PMCA) with the space group  $P\bar{4}_2m$  (number 111) where  $P$  represents the primitive Bravais lattice [39]. Figure 3.3 shows different possible CZTS structures. Another possible CZTS structure is called wurtzite structure (a hexagonal structure) at high reaction temperature [40]. Moreover to the possible CZTS structure existence, disordered kesterite structure can exist. The KS structure should be more stable thermodynamically compared to the ST structure, thus CZTS will usually appear in KS structure [41-43]. The two structures KS and ST are similar, but they have different arrangement of Cu and Zn atoms, while Sn is located at same structural site in both KS and ST structures [44, 45]. For practical photovoltaics, kesterite is most favourable because of the optimum value of the bandgap energy [46, 47]. The tetragonal crystal structure of CZTS has a lattice constant of  $a = 5.4 \text{ \AA}$  and  $c = 10.9 \text{ \AA}$ , thus the ratio of  $c/a$  is almost equal to two [48].

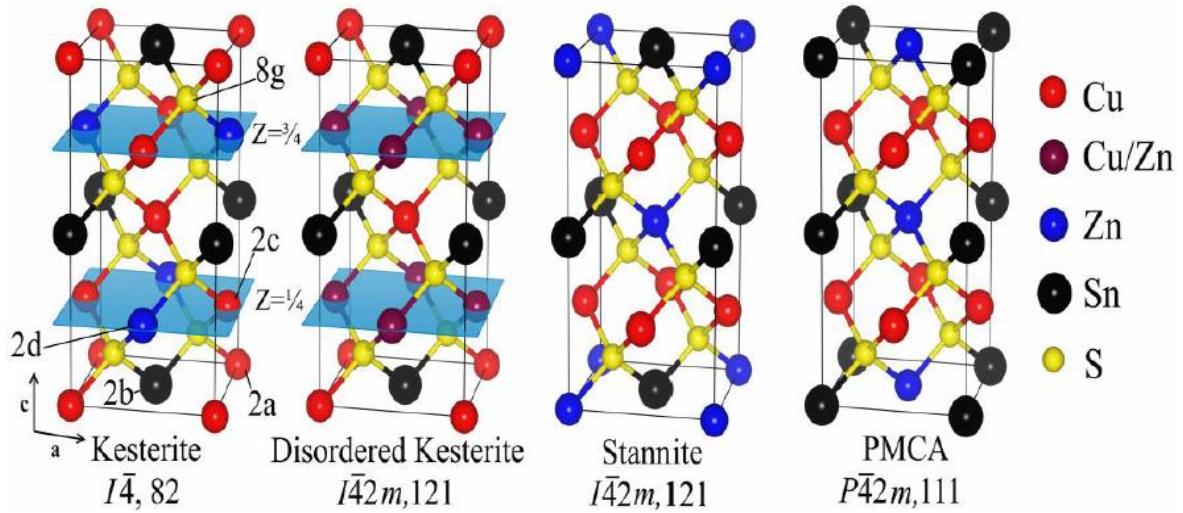


Figure 3.3 Different CZTS possible structures (from [40]). The labelled sites in Kesterite structure  $2a$ ,  $2b$ ,  $2c$ ,  $2d$  and  $8g$  represent Wyckoff points where the atomic position can be  $(0, 0, 0)$  for Cu as  $2a$ ,  $(0, 0, \frac{1}{2})$  for Sn as  $2b$ ,  $(0, \frac{1}{2}, \frac{1}{4})$  for Cu as  $2c$ ,  $(0, \frac{1}{2}, \frac{3}{4})$  for Zn as  $2d$  and  $(x, y, z)$  for S as  $8g$ .

### 3.4. Optical properties

CZTS has a near optimum direct bandgap energy ranging between 1.40 to 1.6 eV. This CZTS bandgap energy varies with different composition, thus the bandgap energy is considered to be tuneable. For instance, reducing Sn/Cu ratio will lead to decreasing the bandgap energy [49]. This bandgap is also dependent on temperature where it will decrease with increasing of temperature as a result of the increasing of phonon population leading to more carrier-phonon interaction [50]. Figure 3.4 shows the energy band diagram of CZTS which is preferable for solar cell devices. In addition, it has high absorption coefficient  $> 10^4 \text{ cm}^{-1}$  at the bandgap, thus using a very thin layer (about 1  $\mu\text{m}$ ) of film in a CZTS solar cell device can absorb more than 99% of the incident photons [51, 52]. Such a direct bandgap and high absorption coefficient will enhance decreasing the thickness of the absorber material required to absorb the incident light resulting in reducing material costs and panel weight. The absorption coefficient,  $\alpha$  can be extracted from the experimental measurement of reflectance  $R$  and transmittance  $T$  as follows:

$$\alpha(\lambda) = \frac{1}{x} \ln \left( \frac{1-R(\lambda)}{T(\lambda)} \right). \quad (3.1)$$

Where  $x$  is the thickness of the film. Then the energy gap can be determined by the Tauc plot where a straight line can be drawn to extrapolate the plot of absorption squared  $(\alpha h\nu)^2$  in the y axis versus the energy gap ( $E_g$ ) in the x axis using the following equation:

$$(\alpha h\nu) = A \sqrt{(h\nu - E_g)}. \quad (3.2)$$

Where  $A$  is a constant determined by the electronic band structure,  $h$  is the Planck constant,  $\nu$  is the frequency of the light, and  $E_g$  is the bandgap of the material [53, 54], proportional to  $(\alpha h\nu)^{\frac{1}{2}}$  for a direct bandgap semiconductor. This is a consequence of the  $E^{\frac{1}{2}}$  energy dependence of the 3D energy density of states function.



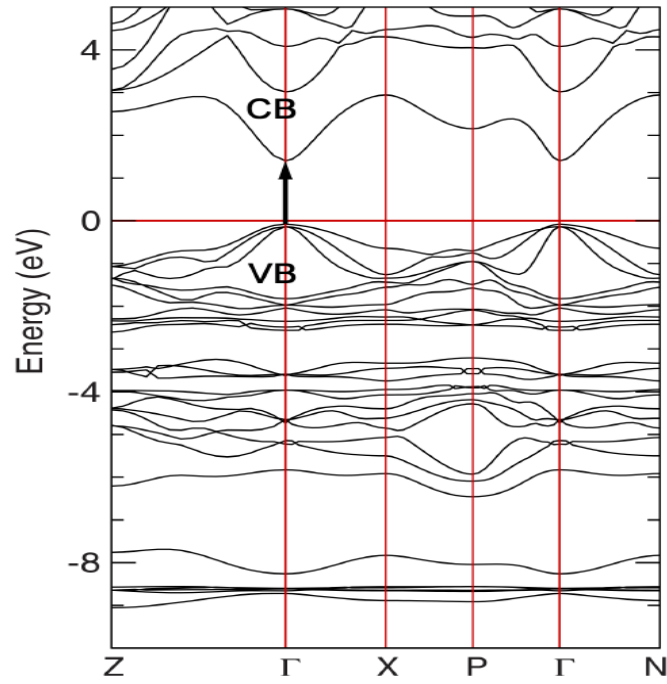


Figure 3.4 Band structure of the direct bandgap of the KS structure of CZTS semiconductor (from [46]). The direct energy bandgap is shown by the arrow.

### 3.5. Secondary phases

The growth mechanism of a single-phase or pure CZTS seems to be difficult to achieve as it occurs only in a very narrow region of the ternary phase diagram presented below in figure 3.5 [55-60]. Therefore, experimentally, secondary phases are expected to be present in the formation of CZTS.

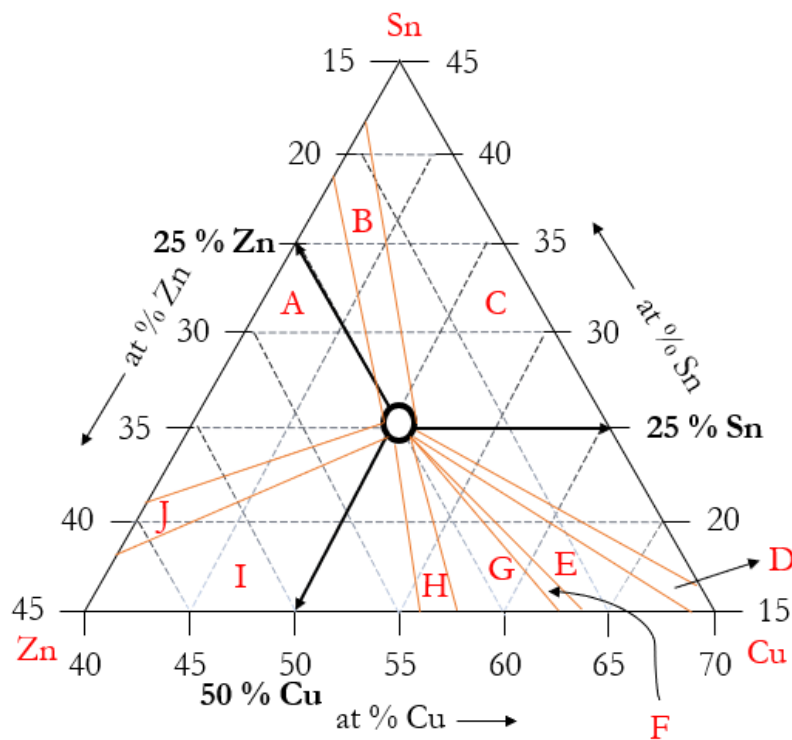


Figure 3.5 CZTS ternary phase diagram including several possible secondary phases. A)  $\text{ZnS} + \text{Cu}_2\text{ZnSn}_3\text{S}_8$ , B)  $\text{ZnS}$ , C)  $\text{ZnS} + \text{Cu}_2\text{S}$ , D)  $\text{Cu}_2\text{S}$ , E)  $\text{Cu}_2\text{S} + \text{Cu}_4\text{SnS}_4$ , F)  $\text{Cu}_4\text{SnS}_4$ , G)  $\text{Cu}_4\text{SnS}_4 + \text{Cu}_2\text{SnS}_3$ , H)  $\text{Cu}_2\text{SnS}_3$ , I)  $\text{Cu}_2\text{ZnSn}_3\text{S}_8 + \text{Cu}_2\text{SnS}_3$  and J)  $\text{Cu}_2\text{ZnSn}_3\text{S}_8$ . The central circled area is the pure CZTS. This diagram assumes that the amount of sulphur is always presented in the correct amount in CZTS (adapted from [57]).

Secondary phases are considered to be a significant issue for CZTS for two main reasons. The first one is that they might reduce the conductivity of the CZTS solar cells, meaning efficiency reduction of the cells because secondary phases may act as recombination centres [61, 62]. The second reason is that the secondary phases play a main role in decreasing the open circuit voltage in the CZTS solar cells especially those with bandgaps lower than the bandgap of CZTS. The most expected secondary phases to be present in CZTS are listed in the table 3.2 below with their bandgap.

Secondary phase	Bandgap (eV)	References
CuS	1.0	[63]
$\text{Cu}_2\text{S}$	1.2	[64]
ZnS	3.8	[65]
SnS	1.3	[66]
$\text{SnS}_2$	2.2	[67]
$\text{Sn}_2\text{S}_3$	2.1	[68]
$\text{Cu}_2\text{SnS}_3$	1.4	[69]
$\text{Cu}_3\text{SnS}_4$	1.2	[70]
$\text{Cu}_4\text{SnS}_4$	1.2	[71]
$\text{Cu}_2\text{ZnSn}_3\text{S}_8$	?	[57]

**Table 3.2:** The expected secondary phases in CZTS and their bandgaps.

CuS might create a shunting pathway within the CZTS solar cells since it acts as a metallic conductor leading to a decrease of the cell's efficiency.

$\text{Cu}_2\text{S}$  has a high electrical conductivity which might short-circuit the CZTS cells by the effect of recombination [72].

SnS exhibits p-type conductivity, and it might be found on the surface of CZTS [66].

ZnS,  $\text{SnS}_2$  and  $\text{Sn}_2\text{S}_3$  have larger bandgaps than that of CZTS which means they can act as a resistive barrier to carriers created preventing the charge collection from CZTS [73]. In addition, ZnS can decrease the open circuit voltage due to the increment of the series resistance of the CZTS cells [74].

$\text{Cu}_2\text{SnS}_3$ ,  $\text{Cu}_3\text{SnS}_4$  and  $\text{Cu}_4\text{SnS}_4$  have a smaller bandgap than that of CZTS and may act as recombination centres [75].

$\text{Cu}_2\text{ZnSn}_3\text{S}_8$  needs more research since there are not many details about it in the literature and it is rarely observed [60].

Some secondary phases can be removed by post-fabrication etching. To remove unwanted  $\text{Cu}_x\text{S}$  impurities, KCN aqueous solution should be used [76]. For ZnS removing, an aqueous HCl solution is efficient to be used [77]. To eliminate SnS, etching by  $\text{Na}_2\text{S}$  can be used [78].

### 3.6. Point defects

There are around thirteen possible intrinsic point defects in KS structure that might form during the crystal growth of the CZTS thin film. These are four vacancy defects ( $V_{Cu}$ ,  $V_{Zn}$ ,  $V_{Sn}$ , and  $V_S$ ), six antisite defects ( $Cu_{Zn}$ ,  $Zn_{Cu}$ ,  $Cu_{Sn}$ ,  $Sn_{Cu}$ ,  $Zn_{Sn}$ , and  $Sn_{Zn}$ ) and three interstitial defects ( $Cu_i$ ,  $Zn_i$ , and  $Sn_i$ ) [79]. These point defects can be located as shallow or deep levels in the bandgap. Shallow level defects can play role in influencing the majority and minority carrier concentrations, thus the electrical conductivity. Deep level defects might act as recombination centres for photogenerated electron-hole pairs. The  $V_{Cu}$  defects can play a significant role in achieving high efficiency of solar cells [40]. Figure 3.6 shows the energy levels of point defects within the bandgap of CZTS. It is also possible for charge compensating defect complexes to form arising from the Coulomb interaction between positively and negatively charged defect such as  $(Cu_{Zn}^- + Zn_{Cu}^+)$ .

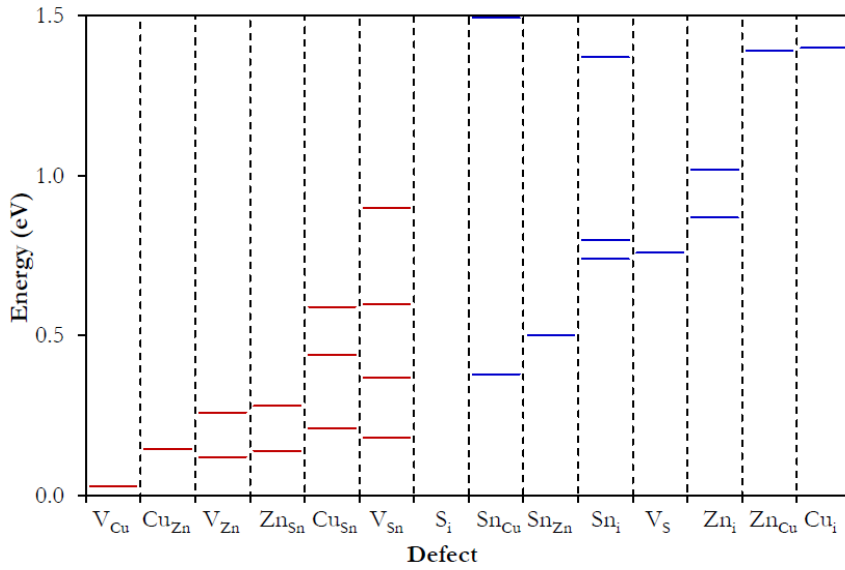


Figure 3.6 The defect energy levels of point defects in CZTS bandgap (from [80]).

CZTS acts as a p-type absorber layer (self-doping and intrinsic p-type conductivity) due to the existence of these point defects especially  $Cu_{Zn}$  antisite defects [81]. As CZTS is p-type, more free holes than free electrons will be occurring in the semiconductor material under equilibrium conditions [82]. The ratios of atomic percentages of the cations in CZTS are usually used to show the composition whether they are stoichiometric or non-stoichiometric. These ratios are as follows:

$$\frac{\text{Cu}}{\text{Zn}+\text{Sn}}, \quad (3.3)$$

$$\frac{\text{Zn}}{\text{Sn}}. \quad (3.4)$$

If both ratios are equal to one, then the composition is stoichiometric. If the ratio (3.3) is less than one and the ratio of (3.4) is more than one, then the composition is called Cu-poor and Zn-rich [83]. This non-stoichiometric Cu-poor and Zn-rich CZTS composition is found to be preferable for solar cell device performance, but it will increase the probability of defects and secondary phase formation where these are not desired [84].

### 3.7. CZTS bandgap variation and band tailing

Because CZTS is a quaternary semiconductor, with a significant number of possible point defects, and defect complexes, there are many different parameters which affect the fundamental energy bandgap. The energy bandgap of CZTS determined from theoretical calculations is  $E_g = 1.5$  eV, in agreement with experimental data in the range of 1.4-1.6 eV for kesterite CZTS [85]. The proximity of the bandgap to the solar optimum is one of the reasons CZTS is being developed for thin film solar cells.

The bandgap of CZTS varies with composition providing an opportunity for control and possible tuning [47]. The bandgap energy decreases significantly, by up to 140 meV, with decreasing Sn/Cu ratio from Sn/Cu = 1.15 to 1.1, possibly related to changes in defect density. It is also observed that changing Zn concentration has minimal impact on the bandgap [49]. Malerba et al [49] conclude that the most likely explanation is a defect induced reduction of the energy bandgap with a reduced Sn content probably introducing a number of acceptor defects including:  $V_{\text{Sn}}$ , and  $\text{Cu}_{\text{Sn}}$  and  $\text{Zn}_{\text{Sn}}$  antisites. This suggests that control of Sn concentration would be a primary means of controlling the CZTS bandgap. However, it should be noted that other possible explanations for the link between bandgap and composition could offer alternative models. These are: 1) a possible transition between the two polymorphs kesterite and stannite, or 2) the formation of solid solutions between CZTS and secondary phases. Both are discounted by Malerba et al, as neither of these explanations fits their data [49].

CZTS is prone to significant levels of cation disorder, principally through Cu-Zn exchange. Increased cation ordering can increase the bandgap by up to 110 meV in CZTS<sub>Se</sub> [86]. First-

principles electronic structure calculations show that the bandgap of kesterite CZTS is reduced by Cu+Zn disorder by around 40 meV [36]. From this it is known that two processes, increased Cu/Zn cation ordering, and increased Sn/Cu ratio can lead to an increase in the CZTS energy bandgap. The latter can be obtained from EDS data. None of the techniques used in this work can quantify Zn/Cu disorder. However, this can be measured from high resolution resonant X-ray diffraction [87, 88].

The presence of secondary phases which have energy bandgaps different from CZTS can alter the average bandgap value of the material and adversely impact solar device performance. The presence of secondary phases also distorts the bandgap value obtained by the methods used in this work. Bandgap values of common secondary phases are included in table 3.2 above.

Figure 3.4 above shows the energy band structure for CZTS calculated by density functional theory [61]. The direct energy bandgap can be seen at the  $\Gamma$  point of the Brillouin Zone. The dispersion of the lowest conduction band and the highest valence band in CZTS is relatively flat so that direct gaps at points away from  $\Gamma$  in reciprocal space are similar to states at the  $\Gamma$  point [85]. Further details on the general electronic structure are found in Persson [85] and Paier et al. [61].

In CZTS, the presence of intrinsic point defects, and defect complexes, can lead to potential fluctuations in the energy band structure [89, 90]. The associated band tailing, of energy states into the CZTS bandgap, may lead to a decrease in the CZTS energy bandgap [91]. However, the origin and impact of band tailing in CZTS is under active discussion in the literature. Some state that electrostatic potential fluctuations rather than bandgap fluctuations are responsible for tail states [92, 93], whereas others state that bandgap fluctuations originating from nanoscale variations in chemical composition are responsible [94]. Despite this uncertainty, the relationship between band tails and cation disorder, along with related defects, is seen as a key issue in CZTS devices [94, 95]. Disorder in CZTS is related at the nanoscale level with variations in composition [96].

When determining the energy bandgap of CZTS using optical absorption, it is important to also consider band tailing which is observed as weak optical absorption into the energy bandgap. This is illustrated in figure 3.7 [31].

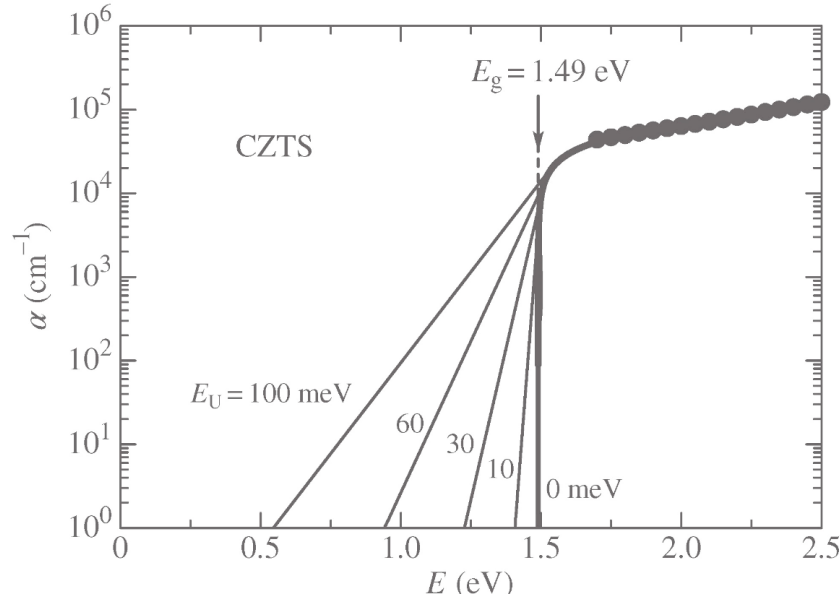


Figure 3.7 Semilogarithmic plot of optical absorption of CZTS at the bandgap. Data represented by data points. Theoretical calculations represented by solid lines showing the impact of changing the energy of the empirical Urbach parameter (from [31]).

The observation of the Urbach Tail in optical absorption is described by the phenomenological relationship  $\alpha$ :

$$\alpha(E, T) = \alpha_0 \exp\left(\frac{E - E_g(T)}{E_U(T)}\right), \quad (3.5)$$

where  $E_g(T)$  is the bandgap energy and the Urbach parameter  $E_U(T)$  determines the width of the absorption tail known as Urbach's rule [97]. Higher values of the Urbach parameter give absorption spread over a larger energy range into the energy bandgap. The absorption tail in CZTS is generally attributed to disorder in CZTS, typically from Cu-Zn exchange, and other impurities, point defects and complexes. As seen in figure 3.7 the steepness of the absorption edge depends on the width of the absorption tail described by the Urbach parameter  $E_U$ . Tail states arising from disorder and impurities can form energy bands when present at sufficiently high concentrations. Tail states can also be formed by perturbation of the valence and conduction band edges via Coulomb interactions and the deformation potential [98].

### 3.8. Device structure

CZTS solar cell design is very similar to the standard CIGS design. The design consists of several layers, starting from the substrate which is usually soda lime glass (SLG) as it is a low-cost material and can be stable at high temperature. The second layer is the back contact which is usually made of molybdenum (Mo) with a thickness of between 600 to 800 nm that is deposited on the substrate via the sputtering technique. Then the absorber layer (CZTS) as the p-type with thickness of about 1000 nm will be deposited on (Mo) via any of several vacuum or non-vacuum deposition methods (in this work, spin coating will be used). The fourth layer is the buffer layer, where the n-type CdS with a thickness of between 50 to 70 nm is deposited via chemical bath deposition (CBD) to form the p-n junction. The fifth layer is the undoped (intrinsic) ZnO layer as window layer with a thickness of between 80 to 100 nm which will be deposited by sputtering technique. On top of the previous layer comes the transparent conductive layer ITO with a thickness of 300 nm which is deposited by sputtering technique as well. Finally, the front contact layer Au grid of 300 nm thick is deposited to achieve electric contact. An anti-reflective coating might be used to increase the overall photovoltaic efficiency of a device. This arrangement of layers is shown in figure 3.7 below.

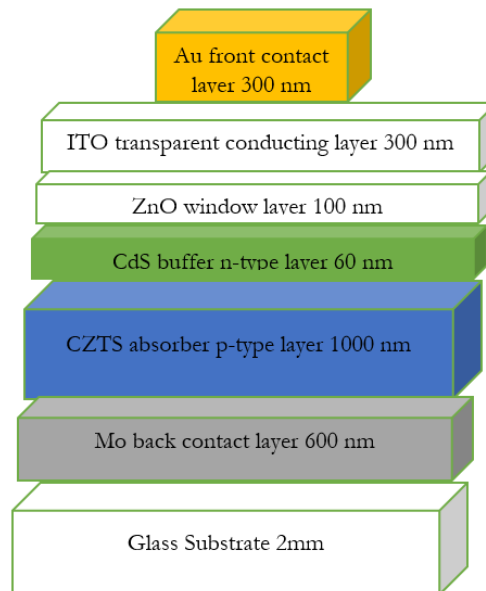


Figure 3.7 The design of a CZTS solar cell.



## 3.9. Vacuum and non-vacuum deposition methods

The methods for the fabrication of CZTS thin films can be classified into two categories: vacuum and non-vacuum based techniques [99]. Vacuum fabrication techniques normally can produce higher-quality samples as they have the advantage of controlling the chemical composition easily as well as the phase profile in the thin films. However, these techniques are considered to be more expensive than the non-vacuum techniques as well as they suffer from slow throughput. These techniques include: sputtering, evaporation, and pulsed laser deposition (PLD) [100, 101]. Non-vacuum fabrication techniques can be used to reduce the production cost [90]. One of the possible issues in these techniques is non-uniformity. These techniques include: spray pyrolysis, spin coating, screen printing and electrodeposition [102-105]. The deposition method that is used in this project is spin coating of hot injection method synthesised nanoparticle solutions.

## 3.10. Hot injection solution method

In this project, the hot injection solution synthesis method is used to prepare the CZTS nanocrystal inks. This hot injection method involves injecting a cold solution of precursors into a hot surfactant solution, resulting in the immediate nucleation and growth of nanocrystals [106, 107]. A cold solution of precursors consisting of sulphur dissolved in oleylamine (OLA) is injected into a highly concentrated and hot surfactant solution containing copper, zinc and tin dissolved in OLA in order to form CZTS nanocrystals. After the reaction, the nanocrystal solution is washed several times using standard precipitation and suspension techniques [108, 109].

Guo et al. [110] were the first to report the hot-injection synthesis of CZTS nanocrystals in demonstrating their use in nanocrystal inks for the deposition of solar cell absorber layers. When fabricating CZTS nanoparticles using the hot injection method, it is generally expected that a distribution of nanoparticle sizes will be produced rather than a single size. It is also expected that particles will have a range of compositions and some variation in crystallinity. These different properties are interrelated. It is known that there is a relationship between particle size and composition [111], with smaller particles, around 5 nm in size, found to be Cu- and Sn-rich, and larger particles, greater than 10 nm in size, found to be Zn-rich. This is probably due to variations in formation, nucleation and growth of nanoparticles in solution. When considering CZTS devices,

it is accepted that monodisperse particles are more desirable, however, previous studies have shown that variations in size or composition may have some beneficial effects for devices [111]. In the hot injection method, long-chain organic ligands provide stabilization of the reaction where Cu, Zn and Sn cations react with S anions in solution. For CZTS, the solvent used is OLA [112], as described in section 4.1.1.

Annealing of deposited films leads to decomposition of organic ligands resulting in large concentrations of carbon in the CZTS films [113]. However, annealing under controlled conditions enhances nanocrystalline films resulting in densely packed, large-grained bulk material generally improving overall PV device performance [113]. During the annealing process, grain growth is observed with the formation of micron-sized grains and a continuous polycrystalline CZTS film. It has been reported that annealed films exhibit a bimodal size distribution having a fine-grained bottom layer and larger grains of CZTS sitting on top of the film [114-116]. Chernomordik et al. observed that the uniform nanoparticles at the bottom undergo normal grain growth forming an underlying floor layer, and that faster growing larger grains on the film surface are formed and are generally called abnormal grains [114, 116]. They also found that an increase of sulphur pressure during annealing enhances grain growth rates. The sulphur vapour may enable the removal of carbon by reaction into volatile compounds. Grain size is effected by the presence of carbon as lower carbon concentrations are measured in films annealed at higher sulphur pressure.

As-synthesised nanoparticles are coated with a layer of capping ligands left over from the hot injection reaction. These capping ligands are recognized as detrimental to charge transport and lower device efficiency [117]. Carbon impacts grain boundaries and limits grain growth [114]. However, complete removal of ligands is generally not attempted as this can produce surface defects acting as traps for charge carriers [117]. It is known that carbon content decreases during annealing [114] due to evaporation, thermal decomposition, or a reaction with the sulphur vapour as discussed by Chernomordik et al. [114].

Using thermogravimetric analysis and mass spectrometry, Engberg et al. [115] confirmed the thermal decomposition of residual solvents during annealing, showing that oleylamine capping ligands disaggregated into smaller fragments above 270 °C. Williams et al. [116] concluded that carbon plays a more complex role in the formation of the final absorber layer than generally accepted and additionally that it may even have some benefits by enhancing rapid grain growth. Less carbon appears to be better for uniform grain growth, whereas large grains are achieved in a short time with modest carbon content, which may be useful in the fabrication process.

---

Finally, it should be noted that, in the case of CZTS, quantum confinement effects only occur for nanocrystals with diameters smaller than 3 nm [118]. Particles smaller than this will always exhibit some distinct quantum size effect properties compared to bulk material. Quantum properties are not considered in this work as particle sizes generally do not fall into this range.

### 3.11. Ink deposition method

Drops of CZTS nanocrystal ink solution are applied to the centre of a SLG substrate and deposited by the spin coating deposition method in order to create the thin film. The spin coating machine produces a centrifugal force to ensure that the ink is spread evenly and uniformly over the substrate. The solvent is usually volatile and simultaneously evaporates, resulting in the thin film of nanoparticles. This thin film can then undergo sulphurisation annealing in a suitable atmosphere to improve the crystallinity.

Two general methods for the spin coating technique can be used. The first is when the ink is deposited onto the substrate while spinning, and the process is called dynamic dispense spin coating technique. The second is when the ink is deposited onto the substrate before spinning, and the process is called static dispense spin coating technique. It should be noted that the centrifugal motion of the spin coater will spread the solution across the substrate in both cases. However, the dynamic dispense technique is preferred as it uses less ink in general for deposition in comparison with the static dispense technique [119]. Moreover, it is a more controlled process than the static dispense technique [119]. For these reasons, the dynamic dispense spin coating technique is used in this work.

## 3.12. References

1. R. Christopher. Endangered Elements, Critical Raw Materials and Conflict Minerals, *Sci. Prog.* 102 (2019) 304-350. <https://doi.org/10.1177/0036850419884873>.
2. L. Wei-Sheng, H. Chien-Sheng, C. Shih-Yuan, L. Ming-Yuan, K. Hsing-Chun, Investigation of  $\text{Cu}_2\text{ZnSnS}_4$  Thin Film with Preannealing Process and ZnS Buffer Layer Prepared by Magnetron Sputtering Deposition, *J. All. Com.* 884 (2021) 161015. <https://doi.org/10.1016/j.jallcom.2021.161015>.
3. B. Abdellah. Effect of CZTS Parameters on Photovoltaic Solar Cell from Numerical Simulation, *J. Energy. Power. Eng.* 13 (2019) 32-36. <https://doi.org/10.17265/1934-8975/2019.01.003>.
4. National Minerals Information Center, Commodity Statistics and Information, (2023). [Online]. Available: <http://minerals.usgs.gov/minerals/pubs/commodity/>.
5. J. Henry, K. Mohanraj, G. Sivakumar, Electrical and Optical Properties of CZTS Thin Films Prepared by SILAR Method, *J. Asian. Ceram. Soc.* 4 (2015) 81-84. <https://doi.org/10.1016/j.jascr.2015.12.003>.
6. G. Q. Yang, S. Z. Wang, R. H. Zhou, S. Z. Sun, Endemic Selenium Intoxication of Humans in China, *J. American. Clinical. Nutrition.* 37 (1983) 872-881. <https://doi.org/10.1093/ajcn/37.5.872>.
7. X. Cui, K. Sun, J. Huang, J. S. Yun, C. Lee, C. Yan, H. Sun, Y. Zhang, C. Xue, K. Eder, L. Yang, J. M. Cairney, J. Seidel, N. J. Ekins-Daukes, M. Green, B. Hoex, X. Hao, Cd-Free  $\text{Cu}_2\text{ZnSnS}_4$  Solar Cell with an Efficiency Greater Than 10% Enabled by  $\text{Al}_2\text{O}_3$  Passivation Layers, *Energy. Environ. Sci.* 12 (2019) 2751-2764. <https://doi.org/10.1039/C9EE01726G>.
8. H. Katagiri, K. Saitoh, T. Washio, H. Shinohara, T. Kurumadani, S. Miyajima, Development of Thin Film Solar Cell Based on  $\text{Cu}_2\text{ZnSnS}_4$  Thin Films, *Sol. Energy. Mater. Sol. Cells.* 65 (2001) 141-148. [https://doi.org/10.1016/S0927-0248\(00\)00088-X](https://doi.org/10.1016/S0927-0248(00)00088-X).
9. Y. Gu, X. Yin, J. Han, Y. Zhou, M. Tai, Q. Zhang, J. Li, X. Hao, H. Lin, All Solution-Processed  $\text{Cu}_2\text{ZnSnS}_4$  Solar Cell by Using High-Boiling-Point Solvent Treated Ball-Milling Process with Efficiency Exceeding 6%, *Chem. Select.* 4 (2019) 982-989. <https://doi.org/10.1002/slct.201804028>.
10. A. S. Nazligul, M. Wang, K. L. Choy, Recent Development in Earth-abundant Kesterite Materials and Their Applications, *Sustainability.* 12 (2020) 5138-5157. <https://doi.org/10.3390/su12125138>.

- 
11. D. Kim, J. Lee, R. Jeong, J. Boo, A High-Efficiency and Stable Perovskite Solar Cell Fabricated in Ambient Air Using a Polyaniline Passivation Layer, *Sci. Rep.* 12 (2022) 697. <https://doi.org/10.1038/s41598-021-04547-3>.
  12. D. Gao, B. Li, Z. Li, X. Wu, S. Zhang, D. Zhao, X. Jiang, C. Zhang, Y. Wang, Z. Li, N. li, S. Xiao, W. C. Choy, A. jen, S. Yang, Z. Zhu, highly Efficient flexible Perovskite Solar Cells Through Pentylammonium Acetate Modification with Certified Efficiency of 23.35%, *Adv. Mater.* 35 (2023) 2206387. <https://doi.org/10.1002/adma.202206387>.
  13. M. Saliba, T. Matsui, J. Y. Seo, K. Domanski, J. Correa-Baena, M. K. Nazeeruddin, S. M. Zakeeruddin, W. Tress, A. Abate, A. Hagfeldt. Cesium-Containing Triple Cation Perovskite Solar Cells: Improved Stability, Reproducibility and High Efficiency, *Energy. Environ. Sci.* 9 (2016) 1989-1997. <https://doi.org/10.1039/C5EE03874J>.
  14. U. Krishnan, M. Kaur, M. Kumar, A. Kumar, Factors Affecting the Stability of Perovskite Solar Cells: A Comprehensive Review, *J. Photonics. Energy.* 9 (2019) 02101. <https://doi.org/10.1117/1.JPE.9.021001>.
  15. H. Katagiri, K. Jimbo, W. S. Maw, K. Oishi, M. Yamazaki, H. Araki, A. Takeuchi, Development of CZTS-Based Thin Film Solar Cells, *Thin. Solid. Films.* 517 (2009) 2455-2460. <https://doi.org/10.1016/j.tsf.2008.11.002>.
  16. S. E. Habas, H. Platt, M. Van Hest, D. Ginley, Low-Cost Inorganic Solar Cells: From Ink to Printed device, *Chem. Rev.* 110 (2010) 6571-6594. <https://doi.org/10.1021/cr100191d>.
  17. K. Ito, Copper Zinc Tin Sulfide-Based Thin Film Solar Cells, John Wiley & Sons. Ltd. (2015).
  18. A. Walsh, S. Chen, S. Wei, X. Gong, Kesterite Thin film Solar Cells: Advances in Materials Modelling of Cu<sub>2</sub>ZnSnS<sub>4</sub>, *Adv. Energy. Mater.* 2 (2012) 400–409. <https://doi.org/10.1002/aenm.201100630>.
  19. S. Hashmi, *Comprehensive Materials Processing*, Elsevier. (2014).
  20. J. J. Scragg, Copper Zinc Tin Sulfide Thin Films for Photovoltaics Synthesis and Characterisation by Electrochemical Methods, Springer. (2002).
  21. R. Chen, First-principles Study on Electronic and Optical Properties of Copper-based Chalcogenide Photovoltaic Materials, KTH Royal Institute of Technology. (2017).
  22. B. K. Durant, B. A. Parkinson, Photovoltaic Response of Natural Kesterite Crystals, *Sol. Energy. Mater. Sol. Cells.* 144 (2016) 586-591. <https://doi.org/10.1016/j.solmat.2015.09.055>.
  23. S. A. Kissin, A Reinvestigation of the Stannite (Cu<sub>2</sub>FeSnS<sub>4</sub>) – Kesterite (Cu<sub>2</sub>ZnSnS<sub>4</sub>) Pseudobinary System, *Can. Mineral.* 27 (1989) 689-697.

- 
24. R. Nitsche, D. F. Sargent, P. Wild, Crystal Growth of Quaternary 122464 Chalcogenides by Iodine Vapour Transport, *J. Cryst. Growth.* 1 (1967) 52-53. [https://doi.org/10.1016/0022-0248\(67\)90009-7](https://doi.org/10.1016/0022-0248(67)90009-7).
  25. K. Ito, T. Nakazawa, Electrical and Optical Properties of Stannite-type Quaternary Semiconductor Thin films, *Jpn. J. Appl. Phys.* 27 (1988) 2094-2097. <https://doi.org/10.1143/JJAP.27.2094>.
  26. H. Katagiri, M. Nishimura, T. Onozawa, S. Maruyama, M. Fujita, T. Segal, T. Watanabe, Rare-metal Free Thin Film Solar Cell, in *Proceedings of the Power Conversion Conference.* 2 (1997) 1003–1006. <https://doi.org/10.1109/PCCON.1997.638392>.
  27. H. Katagiri, N. Sasaguchi, S. Hando, S. Hoshino, J. Ohashi, T. Yokota, Preparation and Evaluation of Cu<sub>2</sub>ZnSnS<sub>4</sub> Thin Films by Sulfurization of E-B Evaporated Precursors, *Sol. Energy. Mater. Sol. Cells.* 49 (1997) 407-414. [https://doi.org/10.1016/S0927-0248\(97\)00119-0](https://doi.org/10.1016/S0927-0248(97)00119-0).
  28. M. Green, K. Emery, Y. Hishikawa, W. Warta, E. Dunlop, D. Barkhouse, O. Gunawan, T. Gokment, T. Todorov, D. Mitzi, Solar Cell Efficiency Table (Version 40), *Ieee. Trans. Fuzzy. Syst.* 20 (2012) 1114-1129. <https://doi.org/10.1002/pip>.
  29. J. Zhou, X. Xu, H. Wu, J. Wang, L. Lou, K. Yin, Y. Gong, J. Shi, Y. Luo, D. Li, H. Xin, Q. Meng, Control of the Phase Evolution of Kesterite by Tuning of the Selenium Partial Pressure for Solar Cells with 13.8% Certified Efficiency, *Nat. Energy.* 8 (2023) 526-535. <https://doi.org/10.1038/s41560-023-01251-6>.
  30. M. Green, E. D. Dunlop, M. Yoshita, N. Kopidakis, K. Bothe, G. Siefer, X. Hao, Solar Cell Efficiency Table (Version 62), *Prog. Photovolt. Res. Appl.* 31 (2023) 651-663. <https://doi.org/10.1002/pip.3726>.
  31. S. Adachi, *Earth-abundant Materials for Solar Cells: Cu<sub>2</sub>-II-IV-VI<sub>4</sub> Semiconductor*, Wiley. (2015).
  32. A. Polizzotti, I. L. Repins, R. Noufi, S. Wei, D. B. Mitzi, The State and Future Prospects of Kesterite Photovoltaics, *Energy. Environ. Sci.* 6 (2013) 3171-3182. <https://doi.org/10.1039/C3EE41781F>.
  33. J. T. Windowlin, A. Alavudeen, N. Venkateshwaran, *A Textbook of Engineering Materials and Metallurgy*, Laxmi Publications (P) Ltd. (2006).
  34. J. Fast, *Investigation of Bismuth Iodine as Light Absorbing Materials for Solar Cell Applications: From Synthesis to XPS Characterisation*, Uppsala University. (2017).
  35. R. Haight, T. Gershon, O. Gunawan, P. Antunez, D. Bishop, Y. S. Lee, T. Gokmen, K. Sardashti, E. Chagarov, A. Kummel, *Industrial Perspectives on Earth Abundant, Multinary Thin*

---

Film Photovoltaics, *Semicond. Sci. Technol.* 32 (2017) 033004. <https://doi.org/10.1088/1361-6641/aa5c18>.

36. S. Chen, X. G. Gong, A. Walsh, S. Wei, Crystal and Electronic Band Structure of Cu<sub>2</sub>ZnSnX<sub>4</sub> (X = S and Se) Photovoltaic Absorbers: First-principles Insights, *Appl. Phys. Lett.* 94 (2009) 041903. <https://doi.org/10.1063/1.3074499>.

37. D. B. Mitzi, O. Gunawan, T. K. Todorov, K. Wang, S. Guha, The Path Towards a High-performance Solution-processed Kesterite Solar Cell, *Sol. Energy. Mater. Sol. Cells.* 95, (2011) 1421-1436. <https://doi.org/10.1016/j.solmat.2010.11.028>.

38. D. Brandon, W. D. Kaplan, *Microstructural Characterization of Materials: 2nd Edition*, Wiley. (2008).

39. A. Khare, B. Himmetoglu, M. Johnson, D. J. Norris, M. Cococcioni, E. S. Aydil, Calculation of the Lattice Dynamics and Raman Spectra of Copper Zinc Tin Chalcogenides and Comparison to Experiments, *J. Appl. Phys.* 111 (2012) 083707. <https://doi.org/10.1063/1.4704191>.

40. Y. Altowairqi, Copper Zinc Tin Sulphide (Cu<sub>2</sub>ZnSnS<sub>4</sub>) Nanoparticle Ink Solar Cells, PhD Thesis. Durham. Uni. (2019).

41. S. Schorr, Structural Aspects of Adamantine Like Multinary Chalcogenides, *Thin. Solid. Films.* 515 (2007) 5985-5991. <https://doi.org/10.1016/j.tsf.2006.12.100>.

42. T. Maeda, S. Nakamura, T. Wada, Electronic Structure and Phase Stability of In-free Photovoltaic Semiconductors, Cu<sub>2</sub>ZnSnSe<sub>4</sub> and Cu<sub>2</sub>ZnSnS<sub>4</sub> by First-principles Calculation, *MRS Online Proceedings Library (OPL)*, 1165 (2011) 403. <https://doi.org/10.1557/PROC-1165-M04-03>.

43. G. Altamura, Development of CZTSSe Thin Films Based Solar Cells, PhD Thesis. Uni. Joseph-Fourier-Grenoble I. (2014).

44. H. Wang, Progress in Thin Film Solar Cells Based on Cu<sub>2</sub>ZnSnS<sub>4</sub>, *Int. J. Photoenergy.* 2011 (2011) 801292. <https://doi.org/10.1155/2011/801292>.

45. Kesterite, Cu<sub>2</sub>(Zn,Fe)SnS<sub>4</sub>, and Stannite, Cu<sub>2</sub>(Fe,Zn)SnS<sub>4</sub>, Structurally Similar but Distinct Minerals, *Can. Mineral.* 16 (1978) 131-137.

46. K. Stroh, Cu<sub>2</sub>ZnSnS<sub>4</sub> Nanocrystal Ink Absorber Layers for Thin Film Solar Cells, MSc Thesis. Durham. Uni. (2019).

47. H. Zhou, W. Hsu, H. Duan, B. Bob, W. Yang, T. Song, C. Hsu, Y. Yang, CZTS Nanocrystals: A Promising Approach for Next Generation Thin Film Photovoltaics, *Energy. Environ. Sci.* 6 (2013) 2822-2838. <https://doi.org/10.1039/C3EE41627E>.

48. C. Persson, Electronic and Optical Properties of Cu<sub>2</sub>ZnSnS<sub>4</sub> and Cu<sub>2</sub>ZnSnSe<sub>4</sub>, *J. Appl. Phys.* 107 (2010) 053710. <https://doi.org/10.1063/1.3318468>.

- 
49. C. Malerba, F. Biccari, C. Ricardo, M. Valentini, R. Chierchia, M. Muller, A. Santoni, E. Esposito, P. Mangiapane, P. Scardi, A. Mittiga, CZTS Stoichiometry Effects on the Bandgap Energy, *J. Alloys. Comp.* 582 (2014) 528-534. <https://doi.org/10.1016/j.jallcom.2013.07.199>.
50. P. K. Sarswat, M. L. Free, A Study of Energy Bandgap Versus Temperature for Cu<sub>2</sub>ZnSnS<sub>4</sub> Thin Films, *Phys. B: Condensed Matter.* 407 (2012) 108-111. <https://doi.org/10.1016/j.physb.2011.09.134>.
51. K. Jimbo, R. Kimura, T. Kamimura, S. Yamada, W. S. Maw, H. Araki, K. Oishi, H. Katagiri, Cu<sub>2</sub>ZnSnS<sub>4</sub>-type Thin Film Solar Cells Using Abundant Materials, *Thin. Solid. Films.* 515 (2007) 5997-5999. <https://doi.org/10.1016/j.tsf.2006.12.103>.
52. M. I. Hossain, Prospects of CZTS Solar Cells from the Perspective of Material Properties, Fabrication Methods and Current Research Challenges, *Chalcogenide. Lett.* 9 (2012) 231-242.
53. J. Tauc, Optical Properties and Electronic Structure of Amorphous Ge and Si, *Mater. Res. Bull.* 3 (1968) 37-46. [https://doi.org/10.1016/0025-5408\(68\)90023-8](https://doi.org/10.1016/0025-5408(68)90023-8).
54. A. Gupta, S. Farhad, M. S. Habib, M. R. Hossain, K. Hossain, N. Das, M. Quamruzzaman, M. A. Matin, N. Amin, Characterizations of Extrinsicly Doped CZTS Thin Films for Solar Cell Absorbers Fabricated by Sol-gel Spin Coating Method, *Appl. Surface. Sci. Adv.* 13 (2023) 100352. <https://doi.org/10.1016/j.apsadv.2022.100352>.
55. X. Song, X. Ji, M. Li, W. Lin, X. Luo, H. Zhang, A Review on Development Prospect of CZTS Based Thin Film Solar Cells, *Int. J. Photoenergy.* 2014 (2014) 613173. <https://doi.org/10.1155/2014/613173>.
56. G. H. Moh, Tin-containing Mineral System, Part II: Phase Relations and Mineral Assemblages in the Cu-Fe-Zn-Sn-S System, *Chem. Erde.* 34 (1975) 1-61.
57. I. D. Olekseyuk, I. V. Dudchak, L. V. Piskach, Phase Equilibria in the Cu<sub>2</sub>S-ZnS-SnS<sub>2</sub> System, *J. Alloys. Comp.* 368 (2004) 135-143. <https://doi.org/10.1016/j.jallcom.2003.08.084>.
58. J. Just, D. Lutzenkirchen-Hecht, R. Frahm, S. Schorr, T. Unold, Determination of Secondary Phases in Kesterite Cu<sub>2</sub>ZnSnS<sub>4</sub> Thin Films by X-ray Absorption Near Edge Structure Analysis, *Appl. Phys. Lett.* 99 (2011) 262105. <https://doi.org/10.1063/1.3671994>.
59. K. Muska, M. Kauk, M. Altosaar, M. Pilvet, M. Grossberg, O. Volobujeva, Synthesis of Cu<sub>2</sub>ZnSnS<sub>4</sub> Monograin Powders with Different Compositions, *Energy. Procedia.* 10 (2011) 203-207. <https://doi.org/10.1016/j.egypro.2011.10.178>.
60. E. A. Pogue, A. A. Rockett, Phase Stability of Cu<sub>2</sub>ZnSnS<sub>4</sub>-SnS<sub>2</sub> Interfaces: Cu<sub>2</sub>ZnSn<sub>3</sub>S<sub>8</sub>, IEEE 43rd Photovoltaic Specialists Conference (PVSC), Portland, OR, USA, (2016) 0471-0475. <https://doi.org/10.1109/PVSC.2016.7749638>.



- 
61. J. Paier, R. Asahi, A. Nagoya, G. Kresse,  $\text{Cu}_2\text{ZnSnS}_4$  As A Potential Photovoltaic Material: A Hybrid Hartree-fock Density Functional Theory Study, *Phys. Rev. B.* 79 (2009) 115126. <https://doi.org/10.1103/PhysRevB.79.115126>.
62. A. Nagoya, R. Asahi, R. Wahl, G. Kresse, Defect Formation and Phase Stability of  $\text{Cu}_2\text{ZnSnS}_4$  Photovoltaic Material, *Phys. Rev. B.* 81 (2010) 113202. <https://doi.org/10.1103/PhysRevB.81.113202>.
63. S. H. Chaki, J. P. Taylor, M. P. Deshpande, Covellite CuS–Single Crystal Growth by Chemical Vapour Transport (CVT) Technique and Characterization, *Mater. Sci. Semicond. Processing.* 27 (2014) 577-585. <https://doi.org/10.1016/j.mssp.2014.07.038>.
64. H. Strater, R. Bruggemann, S. Siol, A. Klein, W. Jaegermann, G. H. Bauer, Detailed Photoluminescence Studies of Thin Film  $\text{Cu}_2\text{S}$  for Determination of Quasi-Fermi Level Splitting and Defect Levels, *J. Appl. Phys.* 114 (2013) 233506. <https://doi.org/10.1063/1.4850955>.
65. Y. C. Cheng, C. Q. Jin, F. Gao, X. L. Wu, W. Zhong, S. H. Li, P. K. Chu, Raman Scattering Study of Zinc Blende and Wurtzite ZnS, *J. Appl. Phys.* 106 (2009) 123505. <https://doi.org/10.1063/1.3270401>.
66. T. Sorgenfrei, F. Hofherr, T. Jaub, A. Croll, Synthesis and Single Crystal Growth of SnS by the Bridgman-Stockbarger Technique, *Cryst. Res. Technol.* 48 (2013) 193-199. <https://doi.org/10.1002/crat.201200484>.
67. N. G. Deshpande, A. A. Sagade, Y. G. Gudage, C. D. Lokhande, R. Sharma, Growth and Characterization of Tin Disulfide ( $\text{SnS}_2$ ) Thin Film Deposited by Successive Ionic Layer Adsorption and Reaction (SILAR) Technique, *J. Alloys. Comp.* 436 (2007) 421-426. <https://doi.org/10.1016/j.jallcom.2006.12.108>.
68. J. David, Optical and Electronic Properties of Semiconducting  $\text{Sn}_2\text{S}_3$ , *Appl. Phys. Lett.* 109 (2016) 032102. <https://doi.org/10.1063/1.4959104>.
69. D. M. Berg, R. Djemour, L. Gutay, G. Zoppi, S. Siebentritt, P. J. Dale, Thin Film Solar Cells Based on the Ternary Compound  $\text{Cu}_2\text{SnS}_3$ , *Thin. Solid. Films.* 520 (2012) 6291-6294. <https://doi.org/10.1016/j.tsf.2012.05.085>.
70. H. Guan, H. Shen, C. Gao, X. He, Structural and Optical Properties of  $\text{Cu}_2\text{SnS}_3$  and  $\text{Cu}_3\text{SnS}_4$  Thin Films by Successive Ionic Layer Adsorption and Reaction, *J. Mater. Sci: Mater. Electron.* 24 (2013) 1490–1494. <https://doi.org/10.1007/s10854-012-0960-x>.
71. V. P. Vani, M. Reddy, K. Reddy, Thickness-Dependent Physical Properties of Coevaporated  $\text{Cu}_4\text{SnS}_4$  Films, *Int. Scholarly. Res. Notices.* 2013 (2013) 142029. <https://doi.org/10.1155/2013/142029>.

- 
72. V. Chawla, A Study of CZTS Thin Films for Solar Cell Applications, PhD Thesis. Stanford Uni. (2011).
73. M. Kumar, A. Dubey, N. Adhikari, S. Venkatesan, Q. Qiao, Strategic Review of Secondary Phases, Defects and Defect-complexes in Kesterite CZTS-Se Solar Cells, *Energy. Environ. Sci.* 8 (2015) 3134-3159. <https://doi.org/10.1039/C5EE02153G>.
74. W. Bao, M. Ichimura, Influence of Secondary Phases in Kesterite- $\text{Cu}_2\text{ZnSnS}_4$  Absorber Material Based on the First Principles Calculation, *Int. J. Photoenergy.* 2015 (2015) 592079. <https://doi.org/10.1155/2015/592079>.
75. P. Sarker, M. M. Aljassim, M. N. Huda, Theoretical Limits on the Stability of Single-phase Kesterite- $\text{Cu}_2\text{ZnSnS}_4$ , *J. Appl. Phys.* 117 (2015) 035702. <https://doi.org/10.1063/1.4906065>.
76. P. A. Fernandes, P. M. P. Salome, A. F. da Cunha, Precursors Order Effect on the Properties of Sulfurized  $\text{Cu}_2\text{ZnSnS}_4$  Thin Films, *Semicond. Sci. Technol.* 24 (2009) 105013. <https://doi.org/10.1088/0268-1242/24/10/105013>.
77. P. Kalinauskas, E. Norkus, Z. Mockus, R. Giraitis, G. Stalnionis, V. Jasulaitiene, R. Juskenas, The Influence of Removal of Secondary Phases and Dissolution By-Product from the Surface of  $\text{Cu}_2\text{ZnSnS}_4$  Film on the Photoelectrochemical Response of This Film, *J. Electrochem. Soc.* 167 (2020) 026513. <https://doi.org/10.1149/1945-7111/ab6cef>.
78. A. Fairbrother, E. Garcia-Hemme, V. Izquierdo-Roca, X. Fontane, A. Fabian, O. Vigil, A. Perez-Rodriguez, E. Saucedo, Development of a Selective Chemical Etch to Improve the Conversion Efficiency of Zn-Rich  $\text{Cu}_2\text{ZnSnS}_4$  Solar Cells, *J. Am. Chem. Soc.* 134 (2012) 8018-8021. <https://doi.org/10.1021/ja301373e>.
79. P. Paranthaman, W. Wong-Ng, R. N. Bhattacharya, *Semiconductor Materials for Solar Photovoltaic Cells*, Springer. (2015). <https://doi.org/10.1007/978-3-319-20331-7>.
80. C. Bosson, Understanding  $\text{Cu}_2\text{ZnSnS}_4$  as A Photovoltaic Absorber for The Future of Solar Electricity, PhD Thesis. Durham Uni. (2018).
81. S. Chen, J. Yang, X. Gong, A. Walsh, S. Wei, Intrinsic Point Defects and Complexes in the Quaternary Kesterite Semiconductor  $\text{Cu}_2\text{ZnSnS}_4$ , *Phys. Rev. B.* 81 (2010) 245204. <https://doi.org/10.1103/PhysRevB.81.245204>.
82. A. Crovetto,  $\text{Cu}_2\text{ZnSnS}_4$  Solar Cells: Physics and Technology by Alternative Tracks, PhD Thesis. DTU Nanotech. (2016).
83. S. L. J. Engberg,  $\text{Cu}_2\text{ZnSnS}_4$  Nanoparticle Absorber Layers for Thin Film Solar Cells, PhD Thesis. Technical University of Denmark. (2016).
84. C. Frisk, T. Ericson, S. Li, P. Szaniawski, J. Olsson, C. Platzer-Bjorkman, Combining Strong Interface Recombination with Bandgap Narrowing and Short Diffusion Length in  $\text{Cu}_2\text{ZnSnS}_4$

- 
- Device Modeling, Sol. Energy. Mater. Sol. Cells. 144 (2016) 364-370. <https://doi.org/10.1016/j.solmat.2015.09.019>.
85. C. Persson, Electrical and Optical Properties of Cu<sub>2</sub>ZnSnS<sub>4</sub> and Cu<sub>2</sub>ZnSnSe<sub>4</sub>, J. Appl. Phys. 107 (2010) 053710. <https://doi.org/10.1063/1.3318468>.
86. G. Rey, A. Redinger, J. S. Ler, T. P. Weiss, M. Thevenin, M. Guennou, B. El Adib and S. Siebentritt, The Band Gap of Cu<sub>2</sub>ZnSnSe<sub>4</sub>: Effect of Order-disorder, Appl. Phys. Lett. 105 (2014) 112106. <http://doi.org/10.1063/1.4896315>.
87. C. J. Bosson, M. T. Birch, D. P. Halliday, K. S. Knight, A. S. Gibbs, P. D. Hatton, Cation Disorder and Phase Transitions in the Structurally Complex Solar Cell Material Cu<sub>2</sub>ZnSnS<sub>4</sub>, J. Mater. Chem. A. 2017. 5 (2017) 16672-16680. <http://doi.org/10.1039/c7ta03603e>.
88. C. J. Bosson, M. T. Birch, D. P. Halliday, C. C. Tang, A. K. Kleppe, P. D. Hatton, Polymorphism in Cu<sub>2</sub>ZnSnS<sub>4</sub> and New Off-Stoichiometric Crystal Structure Types, Chem. Mater. 29 (2017) 9829-9839. <http://doi.org/10.1021/acs.chemmater.7b04010>.
89. J. P. Leitão, N. M. Santos, P. A. Fernandes, P. M. Salome, A. F. da Cunha, J. C. Gonzalez, G. M. Ribeiro, F. M. Matinaga, Photoluminescence and Electrical Study of Fluctuating Potentials in Cu<sub>2</sub>ZnSnS<sub>4</sub>-based Thin Films, Phys. Rev. B. 84 (2011) 024120. <http://dx.doi.org/10.1103/PhysRevB.84.024120>.
90. D. P. Halliday, R. Claridge, M. C. J. Goodman, B. G. Mendis, K. Durose, J. D. Major, Luminescence of Cu<sub>2</sub>ZnSnS<sub>4</sub> Polycrystals Described by the Fluctuating Potential Model. J. Appl. Phys. 113 (2013) 223503. <http://dx.doi.org/10.1063/1.4810846>.
91. X. L. Liu, Y. Feng, H. T. Cui, F. Y. Liu, X. J. Hao, G. Conibeer, D. B. Mitzi, M. Green, The Current Status and Future Prospects of Kesterite Solar Cells: A Brief Review, Prog. Photovolt. 24 (2016) 879-898. <http://dx.doi.org/10.1002/pip.2741>.
92. T. Gokmen, O. Gunawan, T. K. Todorov, D. B. Mitzi, Band Tailing and Efficiency Limitation in Kesterite Solar Cells. Appl. Phys. Lett. 103 (2013) 103506. <http://dx.doi.org/10.1063/1.4820250>.
93. T. J. Huang, X. S. Yin, G. J. Qi, H. Gong, CZTS-based Materials and Interfaces and their Effects on the Performance of Thin Film Solar Cells, Physica. Status. Solidi-Rapid. Res. Lett. 8 (2014) 735-762. <http://dx.doi.org/10.1002/pssr.201409219>.
94. G. Rey, G. Larramona, S. Bourdais, C. Chone, B. Delatouche, A. Jacob, G. Dennler, S. Siebentritt, On the Origin of Band-tails in Kesterite, Sol. Energy. Mater. Sol. Cells. 179 (2018) 142-151. <https://doi.org/10.1016/j.solmat.2017.11.005>.
95. M. Lang, T. Renz, A. Opolka, C. Zimmermann, C. Krammer, M. Neuwirth, H. Kalt, M. Hetterich, Impact of the Degree of Cu-Zn Order in Cu<sub>2</sub>ZnSn(S,Se)<sub>4</sub> Solar Cell Absorbers on

- Defect States and Band Tails, *Appl. Phys. Lett.* 113 (2018) 0339901. <http://doi.org/10.1063/1.5036622>.
96. B. G. Mendis, M. D. Shannon, M. C. Goodman, J. D. Major, R. Claridge, D. P. Halliday, K. Durose, Direct Observation of Cu, Zn Cation Disorder in  $\text{Cu}_2\text{ZnSnS}_4$  Solar Cell Absorber Material Using Aberration Corrected Scanning Transmission Electron Microscopy, *Prog. Photovolt.* 22 (2014) 24-34. <http://dx.doi.org/10.1002/pip.2279>.
97. F. Urbach, The Long-wavelength Edge of Photographic Sensitivity and of the Electronic Absorption of Solids, *Phys. Rev.* 92 (1953) 1324-1324. <https://doi.org/10.1103/PhysRev.92.1324>.
98. J. I. Pankove, *Optical Processes in Semiconductors*, Dover Publications. Inc. New York. (1975).
99. P. Aabel, A. Anupama, C. S. Kumar, Preparation and Characterization of CZTS Thin Films by Vacuum-assisted Spray Pyrolysis and Fabrication of Cd-free Heterojunction Solar Cells, *Semicond. Sci. Technol.* 38 (2023) 045010. <https://doi.org/10.1088/1361-6641/acbcea>.
100. K. Wang, O. Gunawan, T. Todorov, B. Shin, S. J. Chey, N. A. Bojarczuk, D. Mitzi, S. Guha, Thermally Evaporated  $\text{Cu}_2\text{ZnSnS}_4$  Solar Cells, *Appl. Phys. Lett.* 97 (2010) 143508. <https://doi.org/10.1063/1.3499284>.
101. A. V. Moholkar, S. S. Shinde, A. R. Babar, K. Sim, H. Lee, K. Y. Rajpure, P. S. Patil, C. H. Bhosale, J. H. Kim, Synthesis and Characterization of  $\text{Cu}_2\text{ZnSnS}_4$  Thin Films Grown by PLD: Solar Cells, *J. Alloys. Comp.* 509 (2011) 7439-7446. <https://doi.org/10.1016/j.jallcom.2011.04.074>.
102. M. Mokhtarimehr, I. Forbes, N. Pearsall, Environmental Assessment of Vacuum and Non-vacuum Techniques for the Fabrication of  $\text{Cu}_2\text{ZnSnS}_4$  Thin Film Photovoltaic Cells, *Jpn. J. Appl. Phys.* 57 (2018) 8S3. <https://doi.org/10.7567/JJAP.57.08RC14>.
103. N. Kamoun, H. Bouzouita, B. Rezig, Fabrication and Characterization of  $\text{Cu}_2\text{ZnSnS}_4$  Thin Films Deposited by Spray Pyrolysis Technique, *Thin. Solid. Films.* 515 (2007) 5949-5952. <https://doi.org/10.1016/j.tsf.2006.12.144>.
104. T. K. Todorov, K. B. Reuter, D. B. Mitzi, High-Efficiency Solar Cell with Earth-Abundant Liquid-Processed Absorber, *Adv. Energy. Mater.* 22 (2010) 156-159. <https://doi.org/10.1002/adma.200904155>.
105. Z. Zhou, Y. Wang, D. Xu, Y. Zhang, Fabrication of  $\text{Cu}_2\text{ZnSnS}_4$  Screen Printed Layers for Solar Cells, *Sol. Energy. Mater. Sol. Cells.* 94 (2010) 2042-2045. <https://doi.org/10.1016/j.solmat.2010.06.010>.

- 
106. S. Ahmed, K. B. Reuter, O. Gunawan, L. Guo, L. T. Romankiw, H. Deligianni, A High Efficiency Electrodeposited Cu<sub>2</sub>ZnSnS<sub>4</sub> Solar Cell, *Adv. Energy. Mater.* 2 (2012) 253-259. <https://doi.org/10.1002/aenm.201100526>.
107. Y. Yin, A. P. Alivisatos, Colloidal Nanocrystal Synthesis and the Organic-inorganic Interface, *Nature*. 437 (2005) 664-670. <https://doi.org/10.1038/nature04165>.
108. Z. A. Peng, X. Peng, Nearly Monodisperse and Shape-Controlled CdSe Nanocrystals via Alternative Routes: Nucleation and Growth, *J. Am. Chem. Soc.* 124 (2002) 3343-3353. <https://doi.org/10.1021/ja0173167>.
109. S. C. Riha, B.A. Parkinson, A.L. Prieto, Solution-based Synthesis and Characterization of Cu<sub>2</sub>ZnSnS<sub>4</sub> Nanocrystals, *J. Am. Chem. Soc.* 131 (2009) 12054-12055. <https://doi.org/10.1021/ja9044168>.
110. Q. Guo, W. Hugh, W. Hillhouse, R. Agrawal, Synthesis of Cu<sub>2</sub>ZnSnS<sub>4</sub> Nanocrystal Ink and Its Use for Solar Cells, *J. Am. Chem. Soc.* 131 (2009) 11672-11673. <https://doi.org/10.1021/ja904981r>.
111. N. J. Carter, W. C. Yang, C. K. Miskin, C. J. Hages, E. A. Stach, R. Agrawal, Cu<sub>2</sub>ZnSn(S,Se)<sub>4</sub> Solar Cells From Inks of Heterogeneous Cu-Zn-Sn-S Nanocrystals, *Sol. Energy. Mater. Sol. Cells*. 123 (2014) 189-196. <http://doi.org/10.1016/j.solmat.2014.01.016>.
112. L. S. Khanzada, I. Levchuk, Y. Hou, H. Azimi, A. Osvet, R. Ahmad, M. Brandl, P. Herre, M. Distaso, R. Hock, W. Peukert, M. Batentschuk, C. J. Brabec, Effective Ligand Engineering of the Cu<sub>2</sub>ZnSnS<sub>4</sub> Nanocrystal Surface for Increasing Hole Transport Efficiency in Perovskite Solar Cells, *Adv. Functional. Mater.* 26 (2016) 8300-8306. <http://dx.doi.org/10.1002/adfm.201603441>.
113. H. W. Hillhouse, M. C. Beard, Solar Cells from Colloidal Nanocrystals: Fundamentals, Materials, Devices, and Economics, *Current Opinion in Colloid. Interface. Sci.* 14 (2009) 245-259. <https://doi.org/10.1016/j.cocis.2009.05.002>.
114. B. D. Chernomordik, A. E. Beland, D. D. Deng, L. F. Francis, E. S. Aydil, Microstructure Evolution and Crystal Growth in Cu<sub>2</sub>ZnSnS<sub>4</sub> Thin Films Formed by Annealing Colloidal Nanocrystal Coatings, *Chem. Mater.* 26 (2014) 3191-3201. <http://doi.org/10.1021/cm500791a>.
115. S. Engberg, K. Agersted, A. Crovetto, O. Hansen, Y. M. Lam, J. Schou, Investigation of Cu<sub>2</sub>ZnSnS<sub>4</sub> Nanoparticles for Thin film Solar Cell Applications, *Thin. Solid. Films.* 628 (2017) 163-169. <http://doi.org/10.1016/j.tsf.2017.03.003>.
116. B. A. Williams, M. A. Smeaton, N. D. Trejo, L. F. Francis, E. S. Aydil, Effect of Nanocrystal Size and Carbon on Grain Growth During Annealing of Copper Zinc Tin Sulfide Nanocrystal Coatings, *Chem. Mater.* 29 (2017) 1676-1683. <http://doi.org/10.1021/acs.chemmater.6b05058>.

- 
117. C. J. Stolle, T. B. Harvey, B. A. Korgel, Nanocrystal Photovoltaics: A Review of Recent Progress, *Current Opinion in Chem. Engineering.* 2 (2013) 160-167 <https://doi.org/10.1016/j.coche.2013.03.001>.
118. A. Khare, A. W. Wills, L. M. Ammerman, D. J. Norris, E. S. Aydil, Size Control and Quantum Confinement in Cu<sub>2</sub>ZnSnS<sub>4</sub> Nanocrystals, *Chem. Communica.* 47 (2011) 11721-11723 <http://doi.org/10.1039/c1cc14687d>.
119. J. Griffin, E. Spooner, H. Hassan, Spin Coating: Complete Guide to Theory and Techniques (2024). [Online]. Available: <https://www.ossila.com/pages/spin-coating#choosing-a-spin-coating-method>.

# Chapter 4:

## Experimental methodology and characterisation techniques

### 4.1. Experimental methodology

#### 4.1.1. CZTS nanocrystal preparation

The CZTS nanocrystal inks are fabricated by the spin coating of hot injection synthesised CZTS nanoparticle solutions. The composition condition of CZTS can be a stoichiometric composition  $\text{Cu}_2\text{ZnSnS}_4$ , (2:1:1:4) or non-stoichiometric such as Cu-poor, Zn-rich compositions. The CZTS nanoparticle solutions preparation are done by following the procedures described by Guo et al. in 2009 [1]. In this method, a three neck-flask (can be 100 or 250 ml volume) is used in order to react the metal salts. Two necks are connected to a Schlenk line for the reason of either purging the reaction with argon gas (Ar) or evacuating the vessel. The third neck is used to locate a thermocouple to monitor the temperature of the reaction and for injecting the cold sulphur solution. The stoichiometric composition nanoparticles are synthesised with the following reagents: 1.5 mmol (0.3924 g) of copper (II) acetylacetonate, 0.75 mmol (0.1970 g) of zinc (II) acetylacetonate, 0.75 mmol (0.3572 g) of tin (IV) bis(acetylacetonate) dibromide and 10 ml of oleylamine (OLA). The reagents are weighed to a precision of 0.1 mg. The reagents are added into the three-neck flask with stirring. Using a heating mantle, the mixture is heated to around 140 °C under vacuum and degassed for 30 minutes, then purged with Ar three times. The temperature is then increased to the required reaction temperature where a solution of 4 mmol (0.1280 g) of sulphur in 4 ml of OLA is injected into the mixture holding the reaction temperature for 30 minutes. Then the mixture is left to cool down to 50 °C by removing the heating mantle for around 20 minutes. Finally, 5 ml of toluene and 40 ml of isopropanol are added into the solution to collect

clean crystals of the synthesised nanoparticles which are collected using a centrifuge at 10,000 rpm for 10 minutes. The supernatant is decanted. Then, 20 ml of toluene and 10 ml of isopropanol are added to the mixture and centrifuged again at 8,000 rpm for 10 minutes and the supernatant is decanted for the second time (this process is repeated twice). The collected CZTS powder is then dried under vacuum and prepared to form the ink solution by adding hexanethiol as a solvent with 250 mg of CZTS in 1 ml of hexanethiol.

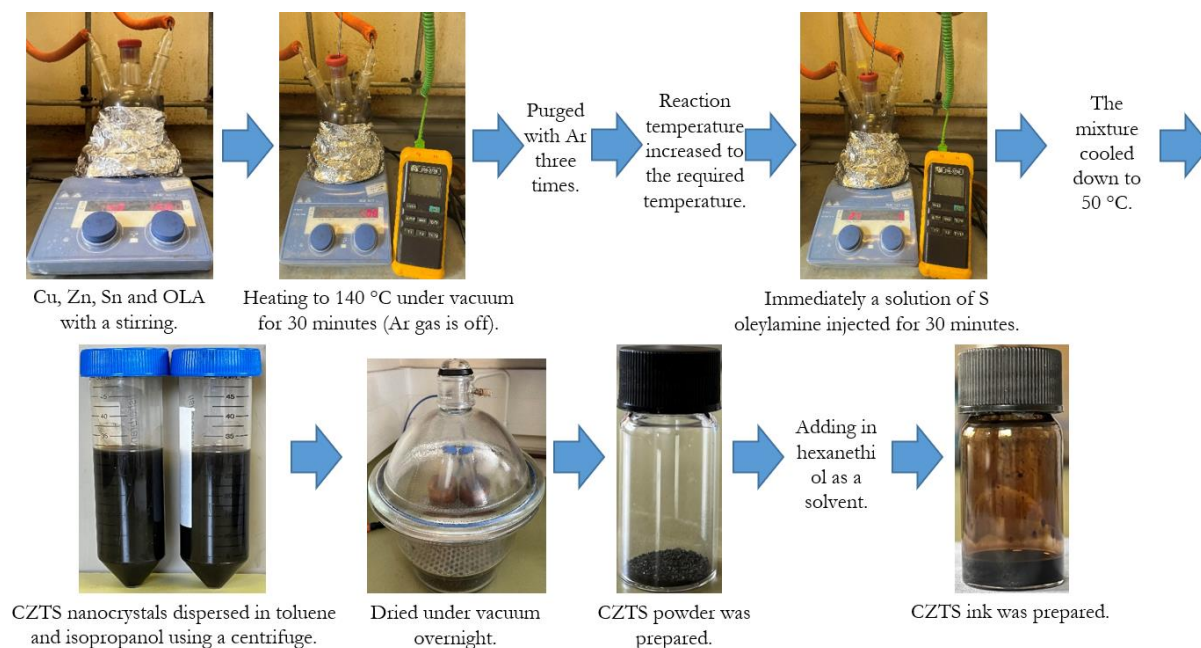


Figure 4.1 CZTS nanocrystal fabrication process.



### 4.1.2. Ink deposition

The CZTS nanoparticle inks are deposited on glass substrates via spin coating technique. The glass was first cleaned and washed by using acetone, methanol and distilled water sequentially for ten minutes, each in an ultrasonic bath. Then, a nitrogen gun is used to dry the glass substrate. After that, the spin coater is set up for the suitable parameters: 2,500 rpm for the spinning speed for 15 seconds. The dried glass is put into the spin coater and 40  $\mu\text{l}$  drops of the ink are dropped into the centre of the glass with the rotated speed mentioned above making sure of achieving uniform thin films. The glass is then heated to 300  $^{\circ}\text{C}$  by a heating mantle in air for 30 seconds for removing any residual solvent after each drop is added for producing stable uniform thin films. These steps can be repeated 10 times to obtain a suitable thickness of CZTS layer of around 1  $\mu\text{m}$ . figure 4.2 shows a deposited CZTS ink on SLG substrate with dimensions of 2.5 x 2.5 cm.



Figure 4.2 CZTS ink deposited on SLG substrate, 2.5 x 2.5 cm, via spin coating technique.

### 4.1.3. Annealing treatment

The prepared CZTS thin films on glass substrates undergo sulphurisation annealing in a suitable atmosphere, nitrogen  $\text{N}_2$  and hydrogenated chalcogen  $\text{H}_2\text{S}$  atmosphere 80:20, to improve the crystallinity which will eventually enhance the potential of producing a high efficiency CZTS solar cell device [2-6]. The sample is loaded in the middle of the furnace tube manually. The two ends of the furnace's tube caps are connected to different valves: a vacuum pump, exhaustion line, nitrogen and  $\text{H}_2\text{S}$  supplies. The annealing process is applied under the conditions of: a desired annealing temperature, a desired annealing time and a ramping rate of 10 degrees per minute. After that the furnace was left to cool naturally overnight and the annealing treatment was finished under a 20% of  $\text{H}_2\text{S}$  and 80% of  $\text{N}_2$  atmosphere. The furnace tube finally was flushed three times with nitrogen gas and vented before retrieving the sample.



Figure 4.3 The furnace used for sulphurisation (annealing system) showing the arrangement of the horizontal tube furnace and the gas flow control system.

## 4.2. Characterisation techniques

Several techniques will be used to study and analyse the characteristics of the absorber materials (CZTS) in the form of solution inks. The optical, structural properties are investigated using several instruments including: X-ray diffraction spectroscopy (XRD), Focused ion beam microscopy (FIB), Energy dispersive spectroscopy (EDS), Raman spectroscopy and Ultraviolet-visible spectroscopy (UV-vis) spectrophotometer.

### 4.2.1. X-ray diffraction spectroscopy (XRD)

This technique is used to identify the crystal structure properties of the materials including associated parameters such as lattice constant and determining the approximate scattering domain size [7,8]. It is based on the concept illustrated by Bragg's law of diffraction who studied a relation between the wavelength, the angle of the incident X-ray and the internal spacing in the crystal where this relationship can be illustrated in figure 4.4 and presented as [9,10]:

$$n\lambda = 2d_{hkl} \sin \theta . \quad (4.1)$$

Where  $n$  is a positive integer (assumed to be 1),  $\lambda$  is the wavelength of the incoming X-rays,  $d_{hkl}$  is the distance between two diffracting planes ( $d$ -spacing) of the (hkl) planes where (hkl) are the Miller indices of the plane and  $\theta$  is the angle between incident rays and the crystal plane [11].

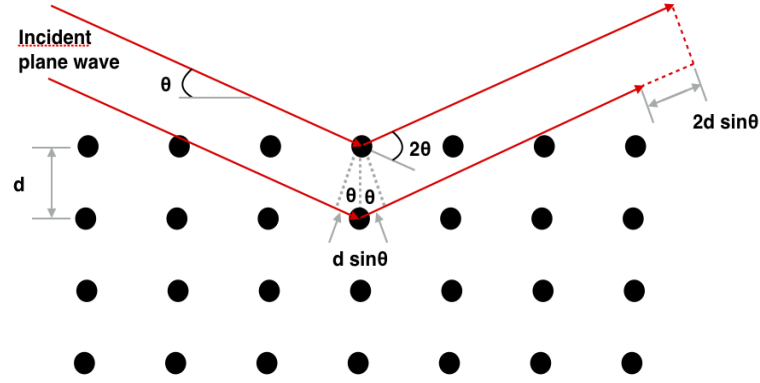


Figure 4.4 Illustration of Bragg's law (from [12]).

The  $d$ -spacing values can be determined using Bragg's law by rearranging equation (4.1) to be:

$$d_{hkl} = \frac{\lambda}{2 \sin \theta} . \quad (4.2)$$

The lattice parameters ( $a$ ,  $b$  and  $c$ ) for the tetragonal structure as CZTS are calculated as:

$$\frac{1}{d^2_{hkl}} = \frac{h^2 + k^2}{a^2} + \frac{l^2}{c^2} , \quad (4.3)$$

where  $a = b \neq c$  and the angles between them  $\alpha = \beta = \gamma = 90^\circ$ .

The size of scattering domain ( $L$ ) is given by Scherrer's equation:

$$L = \frac{K\lambda}{D \cos \theta} . \quad (4.4)$$

Where  $K$  is a dimensionless factor, close to 1, which depends on the shape of the crystallites. For CZTS nanoparticles,  $K = 0.9$  based on the assumption of approximately spherical particles as used by others investigating CZTS [13],  $\lambda$  is the X-ray wavelength (for Cu  $K\alpha$  this is 0.15406 nm),  $D$  is the full width at half maximum in radians (FWHM) and  $\theta$  is the Bragg angle of diffraction peak position.

X-ray spectra can be analysed to determine the approximate size of the scattering domain. This corresponds to the size of a region of single crystal, or crystallite. In general, this will be equal to, or smaller than the CZTS particle size. The size of the scattering domain is inversely proportional to the X-ray peak width. This is because the sharpest X-ray peaks are only found in fully ordered single crystals. In regions of finite crystallites, such as CZTS nanoparticles, incident X-ray radiation

with an angle other than at the Bragg angle will not produce total destructive interference due to the smaller number of scattering centres. This absence of long-range order in regions of multiple crystallites stops the interference from different lattice planes. As a result, the X-ray peaks are broadened over a wider range of  $2\theta$  angles. The smaller the crystallites, the larger the X-ray peak broadening [14]. Nanoparticle size and scattering domain are connected. Generally the scattering domain will always be smaller than the size of nanoparticles as there may be several crystallite regions in each nanoparticle. If the nanoparticle size and scattering domain are very similar, this may imply the nanoparticles are single crystals. Determination of scattering domain size by the Scherrer method is limited as this does not take account of inhomogeneous strain which will also broaden X-ray peaks. Nevertheless, the scattering domain provides a useful means of comparing different nanoparticle films and identifying how different film fabrication conditions impact CZTS film properties.

In this work, XRD measurements were performed using Cu-K $\alpha$  X-rays in Bruker d7 diffractometers. The parameters used in XRD were: 60 minutes for the integration time, 20-70 degrees range, no knife edges and a step size of 0.02°.

#### **4.2.2. Focused ion beam microscopy (FIB)**

FIB has been widely used for topographical or morphological information including surface imaging, cross-sections and estimating thicknesses of layers. The FIB instrument consists of six main parts including: a vacuum system with chamber, a source of a liquid metal ion which gallium (Ga) is commonly used as the ion beam source, an ion column consists of two lenses to define and focus the beam on the sample, a stage for a sample to be measured, detectors and gas delivery system [15]. These parts are connected to a computer to record the images and results.

If an ion beam strikes atoms in material's surface, an interaction between the ion and solid materials are created where the ion loses kinetic energy. As a result of the transformation of energy from the ion to the solid materials, several different processes might occur, including ion reflection and backscattering, electron emission, electromagnetic radiation, atomic sputtering and ion emission, sample damage and sample heating.

The Ga beam source is ionized in a high electric field, creating Ga<sup>+</sup> ions. After the Ga<sup>+</sup> ion beam hits the sample surface and sputters a small amount of the material, secondary ions can be detected to generate images at low beam currents with the ion beam being rastered over the sample surface.

At high beam currents the sputtered materials from the sample can be used to mill a trench into the sample in a process called ion milling for preparing the cross-section of a thin film material for imaging which the images in this work in chapter 8 are recorded by Scanning Electron Microscope (SEM).

SEM imaging uses the same manner that images are produced in a FIB system with the exception of the electron beam that used in this case rather than the ion beam in FIB.

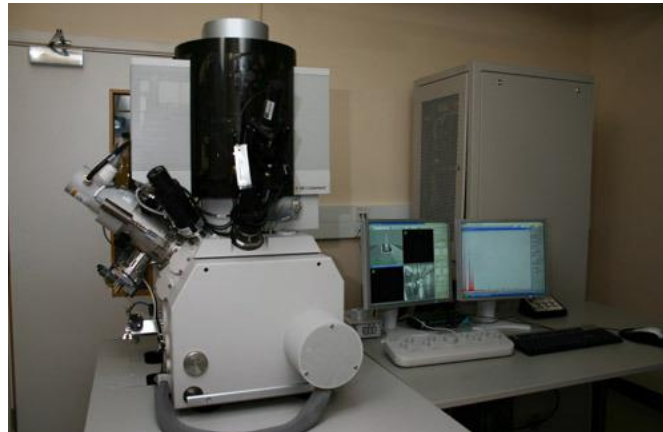


Figure 4.5 The FIB instrument was used in this work where imaging was collected in a FEI Helios Nano Lab 600 Dual Beam microscope which can operate with ion beams or electron beams.

### 4.2.3. Energy dispersive spectroscopy (EDS)

EDS which is usually equipped in a FIB or SEM system, is an analytical technique used for qualitative chemical analysis of the elements in the observed materials. The interaction between the energetic particles beam (e.g. electrons) and the atoms in the samples can excite electrons to be displaced from a lower energy levels of atoms in the sample, leaving a vacancy. An electron from a higher energy level can fill this vacancy state releasing the excess energy as a form of X-ray. The spectrum of this excess energy is used by the X-ray detector coupled with the instrument to determine the elemental composition of the sample as the characteristic decay of each element is different.

EDS analysis for this work was performed with a FEI Helios Nano Lab 600 Dual Beam microscope and the analysis software Aztec 6.0 from Oxford Instruments.

It is known that, when performing EDS measurements, local topography can have a potentially significant impact on EDS results [16]. In particular, surface roughness can distort EDS measurement where X-ray path lengths can vary leading to large changes in EDS signal because

photoelectric X-ray absorption follows the usual exponential law. Low energy photons, below 4 keV, are particularly impacted by path length changes. Samples with rough surfaces are prone to variations in electron scattering, and X-ray generation and propagation leading to systematic errors in EDS data interpretation. Care must be taken to minimise variations due to local surface roughness effects. In this work, EDS data is recorded from around seven selected sites on each sample to minimise these effects. Using the error procedure described in section 5.4.4 gives further confidence in EDS results. Surface roughness of CZTS is also known to be increased by annealing [17]. In CZTS sputtered samples, which are known to be less rough than nanoparticle ink films, the RMS surface roughness increases from 20 nm to 80 nm when annealing at 560 °C. The samples investigated in chapter 7 are likely to experience a similar increase in roughness.

#### **4.2.4. Raman spectroscopy**

Raman spectroscopy measures vibrational modes of the materials which gives information about structure and the potential presence of secondary phases [18, 19]. This technique is based on inelastic scattering (Raman scattering) of monochromatic light such as a laser [20]. This inelastic scattering is the reason behind the shifts in wavelength, which can then be used in order to deduce information about the energy of characteristic vibrational modes to identify the material. In Rayleigh scattering, which is an elastic scattering, when the incident light (photon) interacts with a substance, the electron does not obtain or lose energy during the effect. Thus, the starting and final energy state is the same which means the light stays at the same wavelength where the amount of scattering is strongly dependent on the wavelength [21]. However, Raman scattering is different, when the incident photon interacts with the substance, the electron obtains or loses energy during the scattering process [22]. Therefore, the final energy state is a slightly different than the starting one; either higher, meaning the scattered light has less energy than the incident photon (longer wavelength), which is called Stokes Raman scattering, or lower, meaning the scattered light has gained more energy than the incident photon (shorter wavelength), which is called Anti-Stokes Raman scattering [23].

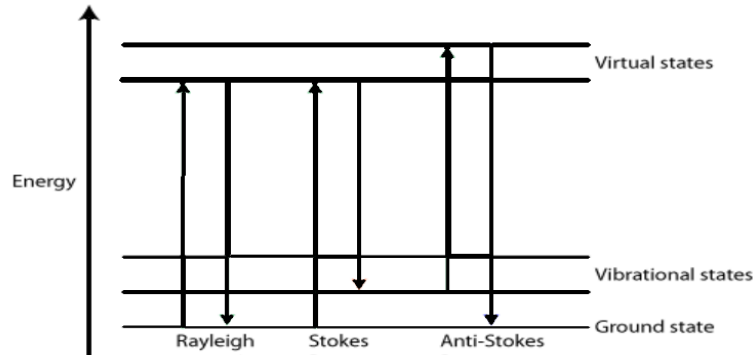


Figure 4.6 Rayleigh scattering, Stokes Raman scattering and Anti-Stokes Raman scattering.

The expected secondary phases of CZTS and their principal Raman peaks are shown in table 4.1.

Secondary phase	Principal Raman peaks ( $\text{cm}^{-1}$ )	References
CuS	137, 265, 472	[24, 25]
Cu <sub>2</sub> S	475	[26]
ZnS	273, 276, 290, 352, 386, 422	[27, 28]
SnS	96, 160, 190, 219, 288	[26, 29]
SnS <sub>2</sub>	215, 314	[29]
Sn <sub>2</sub> S <sub>3</sub>	52, 60, 71, 87, 183, 234, 251, 306	[29]
Cu <sub>2</sub> SnS <sub>3</sub>	290, 352	[30]
Cu <sub>3</sub> SnS <sub>4</sub>	318	[26]
Cu <sub>4</sub> SnS <sub>4</sub>	317	[31]
Cu <sub>4</sub> Sn <sub>7</sub> S <sub>16</sub>	78, 94, 182, 192, 274, 305, 311, 350, 365, 466	[32]
MoS <sub>2</sub>	288, 384, 410	[26, 33]

**Table 4.1:** The expected secondary phases in CZTS and their principal Raman peaks.

The Raman spectra carried out in this work were collected in a Horiba JY lab RAM-HR microscope using 532 nm excitation at room temperature.

### 4.2.5. Ultraviolet-visible (UV-vis) spectroscopy

This technique is very important to investigate the optical properties of the materials which uses the interaction of light with matter based on the absorption of light by the sample [34, 35]. In UV-vis spectroscopy, the absorption of a material will be normally investigated via illuminating the sample with various photon energies under the ultraviolet (around 190-400 nm) and visible (around 400-780 nm) regions [36-38]. The basic concept of the instrument can be explained as follows: when light travels through or is reflected from a sample, the amount of light absorbed is then determined as the difference between the incident radiation intensity  $I_0$  and the transmitted radiation  $I$  [39]. The absorbed amount of light is represented as either transmittance  $T$  or absorbance  $A$  where transmittance normally is given in terms of a fraction of 1 or alternatively as a percentage. The Beer-Lambert law is considered to give the basic principle of the absorbance analysis [40, 41]. This law can be defined as follows:

$$T = \frac{I}{I_0} \text{ or } T\% = \frac{I}{I_0} \times 100, \quad (4.1)$$

$$A = \log \frac{1}{T} = \log \frac{I_0}{I} = -a x, \quad (4.2)$$

where  $\alpha$  is the absorption coefficient. If  $\alpha$  is known, then the thickness  $x$  of the film can be determined using Beer-Lambert law [42]. This method is used to determine the energy bandgap  $E_g$  of the materials CZTS by the Tauc plot as explained in section (3.4) in chapter 3 [43].

The optical spectroscopy was performed in a Shimadzu UV-3600 UV-vis spectrometer for all samples examined in this work.



### 4.3. References

1. Q. Guo, W. Hugh, W. Hillhouse, R. Agrawal, Synthesis of  $\text{Cu}_2\text{ZnSnS}_4$  Nanocrystal Ink and Its Use for Solar Cells, *J. Am. Chem. Soc.* 131 (2009) 11672-11673. <https://doi.org/10.1021/ja904981r>.
2. J. J. Scragg, T. Ericson, T. Kubart, M. Edoff, C. Platzer-Björkman, Chemical Insights into the Instability of  $\text{Cu}_2\text{ZnSnS}_4$  Films During Annealing, *Chem. Mater.* 23 (2011) 4625-4633. <https://doi.org/10.1021/cm202379s>.
3. J. J. Scragg, T. Ericson, X. Fontané, V. Izquierdo-Roca, A. Pérez-Rodríguez, T. Kubart, M. Edoff, C. Platzer-Björkman, Rapid Annealing of Reactively Sputtered Precursors for  $\text{Cu}_2\text{ZnSnS}_4$  Solar Cells, *Prog. Photovolt. Res. Appl.* 22 (2014) 10-17. <https://doi.org/10.1002/pip.2265>.
4. L. Grenet, S. Bernardi, D. Kohen, C. Lepoittevin, S. Noel, N. Karst, A. Brioude, S. Perraud, H. Mariette,  $\text{Cu}_2\text{ZnSn}(\text{S}_{1-x}\text{Se}_x)_4$  Based Solar Cell Produced by Selenization of Vacuum Deposited Precursors, *Sol. Energy. Mater. Sol. Cells.* 101 (2012) 11-14. <https://doi.org/10.1016/j.solmat.2012.02.016>.
5. G. Brammertz, M. Buffiere, Y. Mevel, Y. Ren, A. E. Zaghi, N. Lenaers, Y. Mols, C. Koeble, J. Vleugels, M. Meuris, J. Poortmans, Correlation Between Physical, Electrical, and Optical Properties of  $\text{Cu}_2\text{ZnSnSe}_4$  Based Solar Cells, *Appl. Phys. Lett.* 102 (2013) 013902. <https://doi.org/10.1063/1.4775366>.
6. H. Katagiri, N. Sasaguchi, S. Hando, S. Hoshino, J. Ohashi, T. Yokota, Preparation and Evaluation of  $\text{Cu}_2\text{ZnSnS}_4$  Thin Films by Sulfurization of E-B Evaporated Precursors, *Sol. Energy. Mater. Sol. Cells.* 49 (1997) 407-414. [https://doi.org/10.1016/S0927-0248\(97\)00119-0](https://doi.org/10.1016/S0927-0248(97)00119-0).
7. K. Kalantar-zadeh, B. Fry, *Nanotechnology-Enabled Sensors*, Springer. (2008).
8. E. J. Mittemeijer, U. Welzel, *Modern Diffraction Methods*, Wiley. (2013).
9. Y. Waseda, E. Matsubara, K. Shinoda, *X-Ray Diffraction Crystallography; Introduction, Examples and Solved Problems*. Springer (2011).
10. B. D. Cullity, *Elements of X Ray Diffraction*, Creative Media Partners. LLC. (2018).
11. N. A. Dyson, *X-rays in Atomic and Nuclear Physics*, Cambridge University Press. (1990).
12. J. Fast, *Investigation of Bismuth Iodine as Light Absorbing Materials for Solar Cell Applications: From Synthesis to XPS Characterisation*, Uppsala University. (2017).
13. A. D. Collord, H. W. Hillhouse, The Effect of Nanocrystal Reaction Time on  $\text{Cu}_2\text{ZnSn}(\text{S},\text{Se})_4$  Solar Cells from Nanocrystal Inks, *Sol. Energy Mater. Sol. Cells.* 141 (2015) 383-390. <https://doi.org/10.1016/j.solmat.2015.05.010>.
14. R. E. Dinnebier, S. J. L. Billinge, *Powder Diffraction: Theory and Practice*, RSC Publishing. Cambridge, UK, (2008).

- 
15. L. A. Giannuzzi, F. A. Stevie, *Introduction to Focused Ion Beams: Instrumentation, Theory, Techniques and Practice*, Springer. (2005).
  16. D. E. Newbury, N. W. M. Ritchie, Is Scanning Electron Microscopy/Energy Dispersive X-ray Spectrometry (SEM/EDS) Quantitative? *Scanning*. 35 (2013) 141-168. <https://doi.org/10.1002/sca.21041>.
  17. A. Sharmin, M. S. Bashar, M. Sultana, S. M. M. Al Mamun, Sputtered Single-phase Kesterite  $\text{Cu}_2\text{ZnSnS}_4$  (CZTS) Thin Film for Photovoltaic Applications: Post Annealing Parameter Optimization and Property Analysis. *AIP. Advances*. 10 (2020) 015230 <https://doi.org/10.1063/1.5129202>.
  18. C. K. Miskin, W. Yang, C. J. Hages, N. J. Carter, C. S. Joglekar, E. A. Stach, R. Agrawal, 9.0% Efficient  $\text{Cu}_2\text{ZnSn}(\text{S},\text{Se})_4$  Solar Cells form Selenized Nanoparticle Inks, *Prog. Photovolt: Res. Appl.* 23 (2015) 654-659. <https://doi.org/10.1002/pip.2472>.
  19. X. Fontane, L. Calvo-Barrio, V. Izquierdo-Roca, E. Saucedo, A. Perez-Rodriguez, J. R. Morante, D. M. Berg, P. J. Dale, S. Siebentritt, In-depth Resolved Raman Scattering Analysis for the Identification of Secondary Phases: Characterization of  $\text{Cu}_2\text{ZnSnS}_4$  Layers for Solar Cell Applications, *Appl. Phys. Lett.* 98 (2011) 181905. <https://doi.org/10.1063/1.3587614>.
  20. E. Smith, G. Dent, *Modern Raman Spectroscopy- A Practical Approach*, Wiley. (2019).
  21. D. J. Gardiner, P. R. Graves, *Practical Raman Spectroscopy*, Springer. (2012). <https://doi.org/10.1007/978-3-642-74040-4>.
  22. M. A. Green, *Third Generation Photovoltaics: Advanced Solar Energy Conversion*, Springer. (2003).
  23. W. H. Weber, R. Merlin, *Raman Scattering in Materials Science*, Springer. (2000).
  24. S. H. Chaki, J. P. Taylor, M. P. Deshpande, Covellite  $\text{CuS}$ –Single Crystal Growth by Chemical Vapour Transport (CVT) Technique and Characterization, *Mater. Sci. Semicond. Processing*. 27 (2014) 577-585. <https://doi.org/10.1016/j.mssp.2014.07.038>.
  25. C. G. Munce, G. K. Parker, S. A. Holt, G. A. Hope, A Raman Spectroelectrochemical Investigation of Chemical Bath Deposited  $\text{Cu}_x\text{S}$  Thin Films and their Modification, *Colloids and Surfaces A: Physicochemical. Eng. Aspects*. 295 (2007) 152-158. <https://doi.org/10.1016/j.colsurfa.2006.08.045>.
  26. P. A. Fernandes, P. M P. Salome, A. F. de Cunha, Study of Polycrystalline  $\text{Cu}_2\text{ZnSnS}_4$  Films by Raman Scattering, *J. All. Com.* 509 (2011) 7600-7606. <https://doi.org/10.1016/j.jallcom.2011.04.097>.

- 
27. Y. C. Cheng, C. Q. Jin, F. Gao, X. L. Wu, W. Zhong, S. H. Li, P. K. Chu, Raman Scattering Study of Zinc Blende and Wurtzite ZnS, *J. Appl. Phys.* 106 (2009) 123505. <https://doi.org/10.1063/1.3270401>.
  28. W. G. Nilsen, Raman Spectrum of Cubic ZnS, *Phys. Rev.* 182 (1969) 838. <https://doi.org/10.1103/PhysRev.182.838>.
  29. L. S. Price, I. P. Parkin, A. M. E. Hardy, R. J. H. Clark, G. Thomas, K. C. Molloy, Atmospheric Pressure Chemical Vapor Deposition of Tin Sulfides (SnS, Sn<sub>2</sub>S<sub>3</sub>, and SnS<sub>2</sub>) on Glass, *Chem. Mater.* 11 (1999) 1792-1799. <https://doi.org/10.1021/cm990005z>.
  30. D. M. Berg, R. Djemour, L. Gutay, S. Siebentritt, P. J. Dale, X. Fontane, V. Izquierdo-Roca, A. Perez-Rodriguez, Raman Analysis of Monoclinic Cu<sub>2</sub>SnS<sub>3</sub> Thin Films, *Appl. Phys. Lett.* 100 (2012) 192103. <https://doi.org/10.1063/1.4712623>.
  31. V. P. Vani, M. Reddy, K. Reddy, Thickness-Dependent Physical Properties of Coevaporated Cu<sub>4</sub>SnS<sub>4</sub> Films, *Int. Scholarly. Res. Notices.* 2013 (2013) 142029. <https://doi.org/10.1155/2013/142029>.
  32. T. He, N. Lin, Z. Du, Y. Chao, J. Cui, The Role of Excess Sn in Cu<sub>4</sub>Sn<sub>7</sub>S<sub>16</sub> for Modification of The Band Structure and A Reduction in Lattice Thermal Conductivity, *J. Mater. Chem. C.* 5 (2017) 4206-4213. <https://doi.org/10.1039/c7tc00420f>.
  33. S. J. Sandoval, D. Yang, R. F. Frindt, J. C. Irwin, Raman Study and Lattice Dynamics of Single Molecular Layers of MoS<sub>2</sub>, *Phys. Rev. B.* 44 (1991) 3955. <https://doi.org/10.1103/PhysRevB.44.3955>.
  34. P. Sanghera, *Gateway to Nanotechnology: An Introduction to Nanotechnology for Beginner Students and Professionals*. Amazon Group of Companies. (2009).
  35. C. A. Caro, C. Haller, *UV/VIS Spectrophotometry-fundamentals and Applications*, Mettler-Toledo Int. (2015).
  36. G. Ma, H. C. Allen, *Handbook of Spectroscopy*, Guunter Gauglitz and Tuan Vo-Dinh. (2003).
  37. S. Kumar, *Organic Chemistry: Spectroscopy of Organic Compounds*, Guru Nanak Dev Uni Amritsar. (2006).
  38. E. M. Prabhakar, M. A. Dubinskii, *Ultraviolet Spectroscopy and UV Lasers*, CRC Press. (2002).
  39. T. Owen, *Fundamentals of UV-visible Spectroscopy*, Agilent Technol. (2000).
  40. L. H. Lajunen, P. Peramaki, *Spectrochemical Analysis by Atomic Absorption and Emission*, Royal Society of Chemistry. (2004).
  41. A. Jha, *Inorganic Glasses for Photonics: Fundamentals, Engineering, and Applications*, John Wiley & Sons. (2016).
  42. B. Wardle, *Principles and Applications of Photochemistry*, John Wiley & Sons. (2009).

- 
43. A. Tumbul, A. Goktas, M. Z. Zarbali, F. Aslan, Structural, Morphological and Optical Properties of the Vacuum-free Processed CZTS Thin Film Absorbers, Mater. Res. Express. 5 (2018) 066408. <https://doi.org/10.1088/2053-1591/aac80e>.

## **Chapter 5:**

# **Investigations of CZTS nanocrystal ink synthesis temperatures, times and tin content**

### **5.1. Introduction**

CZTS has four constituents of chemical elements, hence it is a complex material in the matter of formation, as discussed in section 3.7. To achieve the goal of increasing the CZTS solar cell device efficiency, identification of the optimum conditions for the synthesis of absorber layer CZTS nanocrystal inks is a good start. One effective method in doing this is to start with a systematic study of the structural and optical properties of the CZTS nanocrystals where several variables of the reaction conditions during the fabrication of the nanocrystal inks are examined. This systematic study will help understand mechanisms impacting the absorber formation. These variables, explored in this chapter, are the reaction temperature, reaction times and tin content. In this chapter, this study will be done without any post-synthesis annealing treatment to prevent any further fabrication steps for the full CZTS solar cell device until optimum conditions of the CZTS nanocrystal inks are studied and identified.

## 5.2. Reaction temperatures

Four samples were created with different reaction temperatures during the synthesis of CZTS nanocrystal inks. The hot injection method was used for the fabrication of these samples which was successfully used by other groups [1-5]. The spin coating technique was used for the deposition of CZTS nanocrystal inks onto glass substrates [6-8]. Several published papers studied a range of different CZTS reaction temperatures [9,10]. However, in this chapter, a new synthesis temperature range was used 225 °C, 250 °C, 275 °C and 300 °C.

## 5.3. Experimental methodology

### 5.3.1. The fabrication of CZTS nanoparticles

CZTS nanoparticles were fabricated via the procedure explained in chapter 4 section 4.1.1 with Cu-poor, Zn-rich compositions in the as synthesised particles. Several modifications to the reaction conditions are reported in this chapter. These changes are as follows:

- The precursor molar ratios were  $\text{Cu}/(\text{Zn} + \text{Sn}) = 0.85$ ,  $\text{Zn}/\text{Sn} = 1.25$  and  $\text{S}/(\text{Cu}+\text{Zn}+\text{Sn}) = 1.28$ . These ratios are chosen to obtain a high PV device efficiency as discussed in chapter 3.
- These ratios are achieved by using reagents: 1.44 mmol (0.3769 g) of copper (II) acetylacetonate, 0.94 mmol (0.2478 g) of zinc (II) acetylacetonate, 0.75 mmol (0.2909 g) of tin (IV) bis(acetylacetonate) dichloride and 10 ml of OLA.
- The setting of the reaction temperature is set at 225 °C, 250 °C, 275 °C and 300 °C for four different batches of ink.
- The time of the reaction is fixed for all samples, 30 minutes.

### 5.3.2. Ink deposition

The CZTS nanoparticle inks are spin coated on SLG substrates using the same methodology as described in chapter 4 section 4.1.2. Between 2-10 drops of a volume of 40  $\mu\text{l}$  of ink are dropped into the centre of the glass by micro pipette with the rotation speed set as 2500 rpm for 15 seconds to achieve uniform thin films. Two different film thicknesses were used: 2 drops for thin 0.2  $\mu\text{m}$  films for SEM, EDS and UV-vis measurements, and 10 drops for thick 1.0  $\mu\text{m}$  films prepared for XRD and Raman measurements.

## 5.4. Results and discussion

### 5.4.1. Crystal structure - XRD

For structural measurements, XRD was used to determine the crystal structure and lattice constants of CZTS nanoparticle thin films as well as the size of the scattering domain. Individual X-ray peaks were fitted with Lorentzian curves using the MagicPlot software. Lorentzian curves provided the closest fit to the X-ray data as shown in figure 5.1 which includes a fitted baseline.

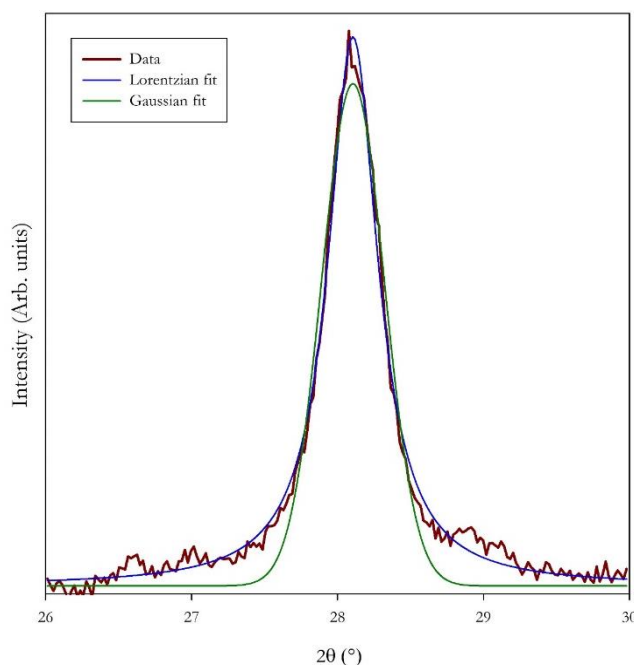


Figure 5.1 An example of XRD peak fitting using Lorentzian fit and Gaussian fit for (112) X-ray peak for CZTS sample of 250 °C reaction temperature for 30 minutes.

Values for FWHM and peak position were taken from the individual Lorentzian curves. For the example shown in figure 5.1, the Coefficient of Determination  $R^2 = 0.992$ , demonstrating an effective fit using Lorentzian curves.

The XRD patterns of the fabricated CZTS nanoparticles at different reaction temperatures 225-300 °C are shown in figure 5.2.

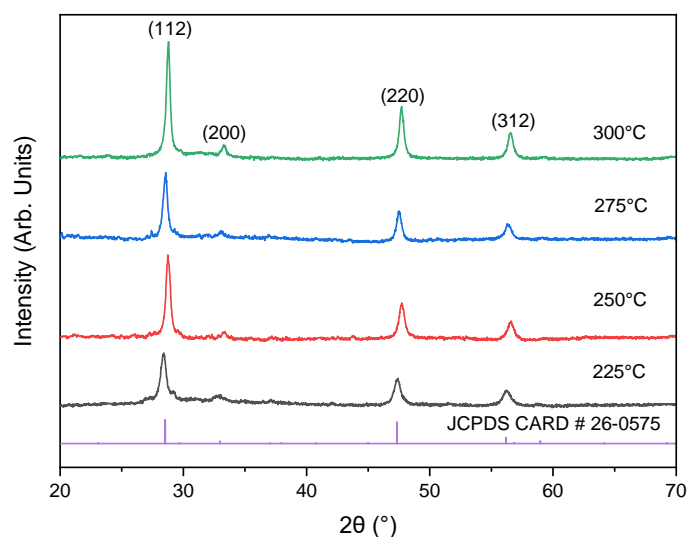


Figure 5.2 XRD for samples of CZTS with different reaction temperatures, including the CZTS PDF reference.

The major XRD diffraction peaks for all samples appeared at locations matching well with the kesterite phase shown in reference PDF card 026-0575 as in table 5.1. However, it should be noted that X-rays cannot distinguish clearly between the kesterite and stannite phases of CZTS. X-ray diffraction confirms the presence of crystalline CZTS. It is known that kesterite has a lower energy configuration than stannite, thus is more likely to be the CZTS structure. Because of the similarity of the major XRD diffraction peaks locations with the secondary phases of ZnS (PDF card 65-1691) and  $\text{Cu}_2\text{SnS}_3$  (PDF card 27-0198), it is difficult to distinguish between them and the presence of CZTS [11]. Therefore, Raman spectroscopy is used to identify any secondary phases present as shown in figure 5.5 [12].



Temperature (°C)	2 $\theta$ (°) for structure planes (112)	2 $\theta$ (°) for structure planes (200)	2 $\theta$ (°) for structure planes (220)	2 $\theta$ (°) for structure planes (312)
225	28.41	32.14	46.65	55.56
250	28.55	32.60	47.10	55.88
275	28.68	32.40	46.78	55.72
300	28.82	32.67	47.02	55.77

**Table 5.1:** Values of 2  $\theta$  for principal CZTS Peaks with different reaction temperatures.

In figure 5.2, X-ray diffraction demonstrates improvement in crystallinity through the increase of the scattering domain with increasing reaction temperatures, as shown in table 5.2. It is also noted that there was an increase in intensity of the (112) peak at 300 °C. This trend has been reported in other work [9], [13].

Table 5.2 below presents the values of  $d$ -spacing, size of scattering domain and lattice parameters  $a$  and  $c$ . The value for the  $d$ -spacing is obtained from the X-ray data using equation (4.2). It should be noted that the (112) CZTS peak overlaps with the (111) ZnS peak leading to the possibility of errors if ZnS is present as a secondary phase. To obtain a more precise value for the  $a$  and  $c$  lattice constants of CZTS, the values of  $d$ -spacing obtained for the four most intense X-ray peaks were used – (112), (200), (220) and (312). A least squares fitting algorithm was used to adjust the values of  $a$  and  $c$  to minimise the total  $\delta^2$  value for the difference between calculated and observed values of  $2\theta$  for all four X-ray peaks, based on equation 4.3. This compensates in part for the possibility of the main (112) CZTS peak being shifted by the presence of ZnS. The scattering domain size  $L$  was calculated from equation (4.4) [14].

Error propagation can be used on equation (4.4) to determine the error in  $L$  which gives:

$$\frac{\Delta L}{L} = \sqrt{\left(\left(\frac{\Delta D}{D}\right)^2 + (\Delta\theta \tan \theta)^2\right)} \quad (5.1)$$

For a more detailed discussion of errors in calculating particle sizes see [15]. Equation 5.1 is used to determine the uncertainty in the scattering domain size.

Temperature (°C)	<i>d</i> -spacing (nm)	<i>a</i> (nm)	<i>c</i> (nm)	Scattering domain (nm)
225	0.3192	0.5506	1.115	13 ± 2
250	0.3169	0.5455	1.112	15 ± 6
275	0.3183	0.5481	1.116	16 ± 5
300	0.3172	0.5461	1.112	39 ± 7

**Table 5.2:** Values of *d*-spacing, size of scattering domain and lattice parameters *a* and *c* with different reaction temperatures.

Tables 5.1 and 5.2 show similar *d*-spacing, *a* and *c* lattice numbers and diffraction peak location values of (112) crystal plane to the literature paper for 250 °C and 300 °C reaction temperatures [16].

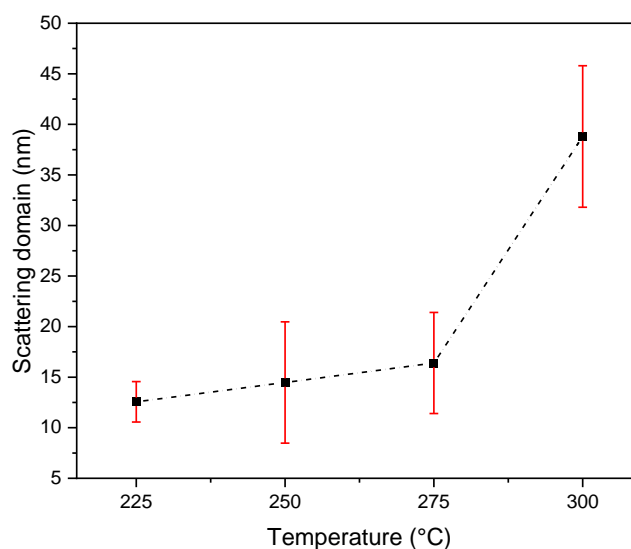


Figure 5.3 The trend of scattering domain size of CZTS with different reaction temperatures.

In figure 5.3, the trend of the scattering domain size is in good agreement with the SEM measurements shown in figure 5.6. This behaviour is reported in other published literature papers [17-21].

#### 5.4.2. Raman spectroscopy

Individual Raman peaks were fitted with Lorentzian curves using the MagicPlot software with an example fit shown in figure 5.4.

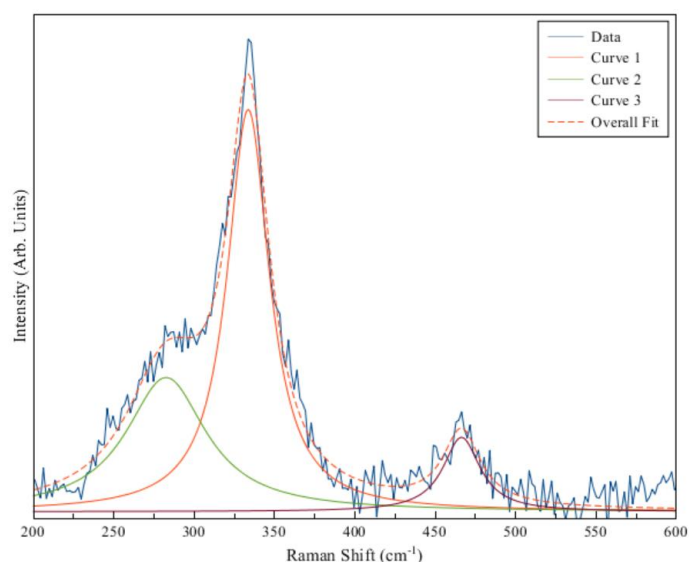


Figure 5.4 An example of Raman peak fitting using Lorentzian curves for CZTS sample of 275 °C reaction temperature for 30 minutes.

Figure 5.5 shows Raman spectroscopy measurements which confirms the crystal structure of the nanoparticles. Raman main and strong peaks of CZTS are located at 334  $\text{cm}^{-1}$  for 225 °C, 337  $\text{cm}^{-1}$  for 250 °C, 336  $\text{cm}^{-1}$  for 275 °C and 335  $\text{cm}^{-1}$  for 300 °C as shown in figure 5.5 below. These peak locations are in good agreement with the literature [22] for the expected characteristic CZTS peak 332-339  $\text{cm}^{-1}$  [23-28]. Another peak appears at 472  $\text{cm}^{-1}$  for 225 °C which seems to be a secondary phase of CuS [29,30]. For 250 °C, two peaks appear at 288 and 317  $\text{cm}^{-1}$  which may be secondary phases of SnS and  $\text{Cu}_4\text{SnS}_4$  [30]. Two peaks appear at 265 and 466  $\text{cm}^{-1}$  for 275 °C which might be a secondary phase of CuS and  $\text{Cu}_4\text{Sn}_7\text{S}_{16}$  [31]. However, these secondary phases did not appear at 300 °C. The formation of a specific secondary phase will depend on a series of factors including vapour pressure, element diffusivity, formation energy and kinetics, and temperature.

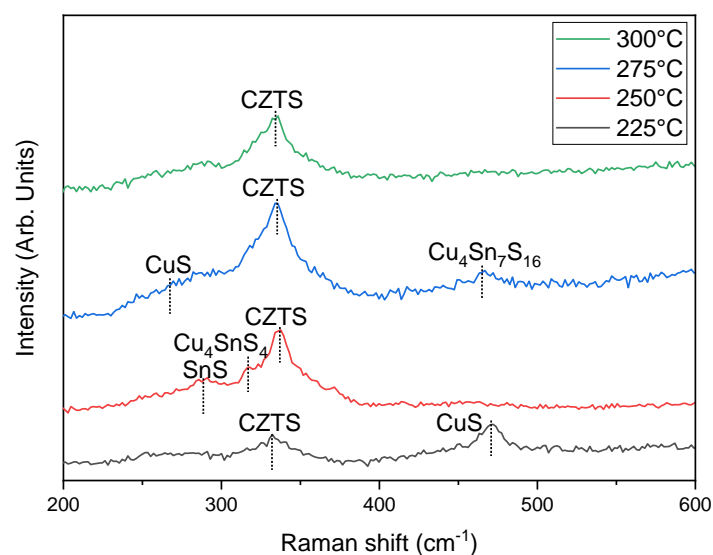


Figure 5.5 Raman spectra of CZTS samples with different reaction temperatures. CZTS and secondary phases are identified from their principal Raman peaks.

### 5.4.3. Morphology

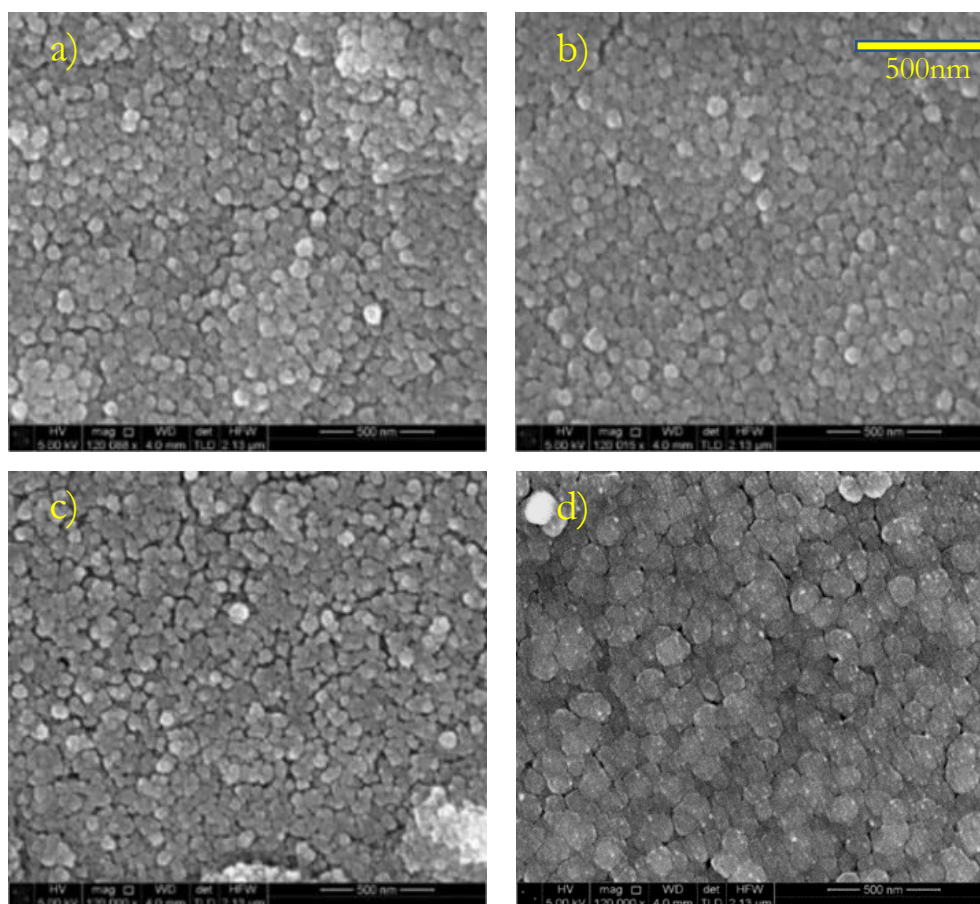


Figure. 5.6 SEM images at scale of 500 nm for CZTS nanoparticles with different reaction temperatures as a) 225 °C b) 250 °C c) 275 °C and d) 300 °C.

From figure 5.6, the nanoparticles are approximately spherical and uniformly shaped for all samples. The size of the particles was determined by measuring the diameter of 5-6 individual particles directly from SEM images and found to be similar, around 13 nm, for the three reaction temperatures 225 °C, 250 °C and 275 °C with little increase in size with each increase of the reaction temperature. However, at the highest reaction temperature, 300 °C, the size of the particles increased noticeably from around 13 nm for image 5.4 a) to 43 nm for image 5.4 d). This agrees with data from scattering domain size, in table 5.2, which suggests that some nanoparticles may be composed of a single scattering domain. In the matter of uniformity, there was not a significant difference in the particle distribution in these images, but 250 °C and 300 °C appear to be more coherent films with fewer gaps in comparison with the other reaction temperatures.

#### 5.4.4. Chemical composition

The elemental analysis of the CZTS synthesised samples at different reaction temperatures were performed by EDS where the results are summarised in table 5.3 below. An example EDS spectra is shown in figure 5.7.

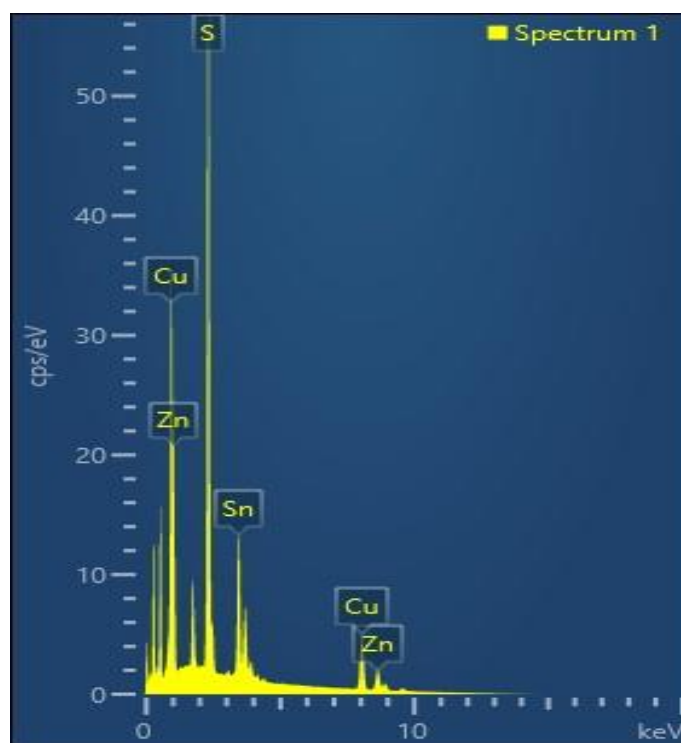


Figure. 5.7 An example of an EDS spectra for CZTS nanoparticles for the sample of 250 °C as reaction temperature for 30 minutes.

The EDS was taken from the film's surface by analysing 7 spectra which were acquired from different regions of the samples and the results averaged. Each of the 7 regions were selected to be representative of the sample, and therefore more likely to be CZTS rather than another phase. As noted in section 4.2.3, care must be taken to minimise the impact of surface roughness on EDS measurements. Taking the average values from seven different spots will minimise errors. It is however possible that regions of secondary phases underneath the surface may be probed by the electron beam. The lateral spread of the beam as it propagates through the sample also means that secondary phases at grain boundaries may also be included. This means that EDS measurements may include an average over all phases present and not just CZTS. This procedure is done also for EDS measurements in chapters 6 and 7. The electron beam energy used for EDS was 5 keV in chapters 5 and 6. Figure 5.8 shows a Monte-Carlo simulation of the primary electron beam interaction volume for a 1  $\mu\text{m}$  CZTS layer on a SLG substrate at energies of 12 keV and 15 keV.

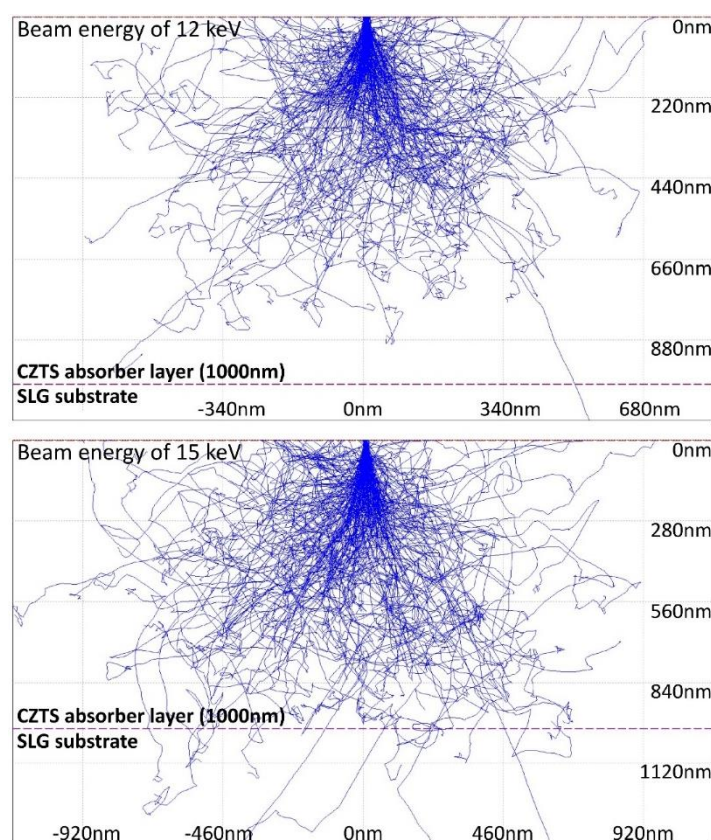


Figure 5.8 The interaction volume of the primary electron beam (in blue) for a one micron thick CZTS layer on a SLG substrate is simulated for a beam energy of 12 keV (top) and 15 keV (bottom). The dashed line indicates the border between absorber layer and substrate. The software used, CASINO (version 2.51), has been developed as a tool for 'Monte Carlo simulations of electron trajectories in solids' by D. Drouin et al. (Université de Sherbrooke, Sherbrooke, Quebec, Canada). Figure from [32].

On the basis of figure 5.8, it is reasonable to infer that, for lower electron beam energies of 5 keV, the electron interactions will be confined to the CZTS layers which have a nominal thickness of 1  $\mu\text{m}$ , with limited electron interactions in the substrate. No EDS peaks associated with the SLG substrate were observed in EDS measurements. For analysis of chemical compositions from EDS, the software Aztec 6.0 from Oxford Instruments was used as mentioned in section 4.2.3. The standard deviation ( $SD$ ) of Cu, Zn, Sn and S concentrations are given by the software. Therefore, equation (5.2) can be used to calculate the standard error ( $SE$ ), where  $n$  here refers to the number of spectra measured of a single sample.

$$SE = \frac{SD}{\sqrt{n}} \quad (5.2)$$

Also, the average value for each element can be determined from the software. Then, the equation (5.3) can be used to obtain the error.

$$Error = \frac{SE}{\text{The average value for each element}} \quad (5.3)$$

Temperature ( $^{\circ}\text{C}$ )	Cu/(Zn+Sn)	Sn/Cu	Zn/Sn	S/(Cu+Zn+Sn)
225	$0.66 \pm 0.03$	$0.46 \pm 0.03$	$1.07 \pm 0.01$	$1.32 \pm 0.01$
250	$0.82 \pm 0.01$	$0.77 \pm 0.04$	$1.19 \pm 0.02$	$1.25 \pm 0.04$
275	$0.88 \pm 0.04$	$0.76 \pm 0.04$	$1.28 \pm 0.02$	$1.37 \pm 0.01$
300	$0.94 \pm 0.06$	$0.60 \pm 0.03$	$1.32 \pm 0.02$	$1.35 \pm 0.04$

**Table 5.3:** Composition ratios of CZTS nanoparticles with different reaction temperatures.

From table 5.3, all samples showed a Cu-poor, Zn-rich composition, consistent with the ratio of precursors. The rate of ion incorporation during growth depends on the reaction temperature, hence the changing ratios. However, the 250  $^{\circ}\text{C}$  sample has the closest Cu-poor, Zn-rich ratio value to the desired ratio for the highly efficient solar cell device (12.6%) compared to the rest of the reaction temperatures [33].

### 5.4.5. Optical properties

A series of fabricated CZTS films from inks at different reaction temperatures 225 °C, 250 °C, 275 °C and 300 °C was created to investigate optical properties without annealing. The energy bandgap of the thin films is determined by UV-vis spectroscopy from the absorption spectrum using the Tauc plot method.

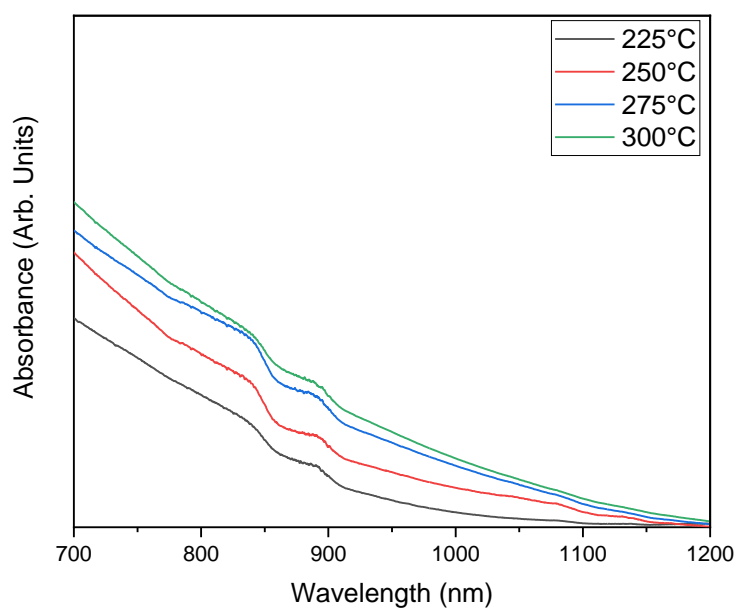


Figure 5.9 Absorbance spectrum of CZTS samples with different reaction temperatures.

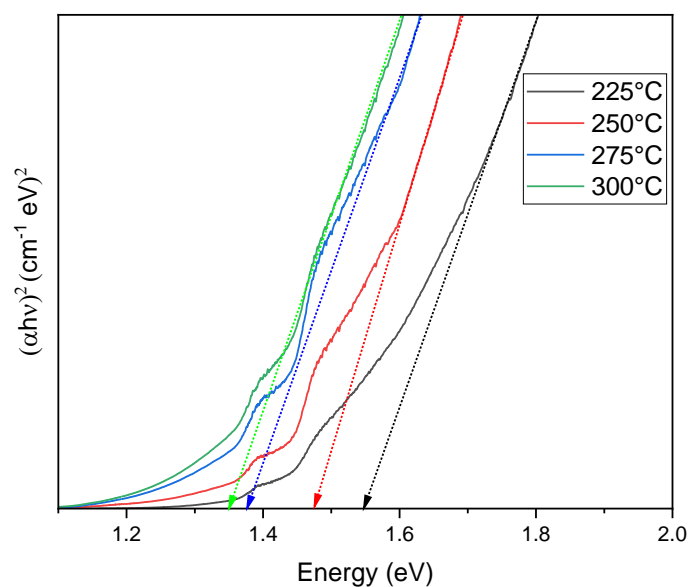


Figure 5.10 Tauc plot to show the bandgap of CZTS versus different reaction temperatures.



The absorbance spectra were recorded in the range of 700-1200 nm as shown in figure 5.9. The energy bandgap was determined by the Tauc plot as shown in figure 5.10 where a straight line can be drawn to extrapolate the plot of  $(\alpha h \nu)^2$  in the y axis versus the energy ( $E_g$ ) on the x axis using the following equation:

$$(\alpha h \nu) = A \sqrt{(h \nu - E_g)}. \quad (5.4)$$

Where  $A$  is a constant determined by the electronic band structure,  $h$  is the Planck constant,  $\nu$  is the frequency of the light, and  $E_g$  is the bandgap of the material [34]. Error bars for the band gap were calculated from the least squares linear fitting of equation 5.4 to the data.

Temperature (°C)	$E_g$ (eV)
225	$1.55 \pm 0.02$
250	$1.48 \pm 0.03$
275	$1.38 \pm 0.06$
300	$1.34 \pm 0.02$

**Table 5.4:** The different reaction temperatures of CZTS versus the energy bandgap.

Table 5.4 shows that when the reaction temperatures were increased, the energy bandgap of the as deposited CZTS film decreases. The decreasing bandgap arises from changes in the CZTS composition as shown in table 5.3. There may also be some change due to the increasing size of nanoparticles as shown in figure 5.6, although, as discussed in section 3.10, quantum confinement effects are not likely to be observed in these samples. The observed bandgap of temperatures 225 °C and 250 °C ( $1.55 \pm 0.02$  eV and  $1.48 \pm 0.03$  eV) respectively correspond well with that reported in the literature of (1.40–1.60 eV) [35-37].

Malerba et al [38] identified a clear relationship between the composition ratio Sn/Cu and the energy bandgap as discussed in section 3.7. An increase in Sn/Cu is related to an increase in the energy bandgap. Such a clear relationship is not observed here. The samples used by Malerba et al consisted of sulphurised metal precursors, likely to have less disorder than these nanoparticle samples.

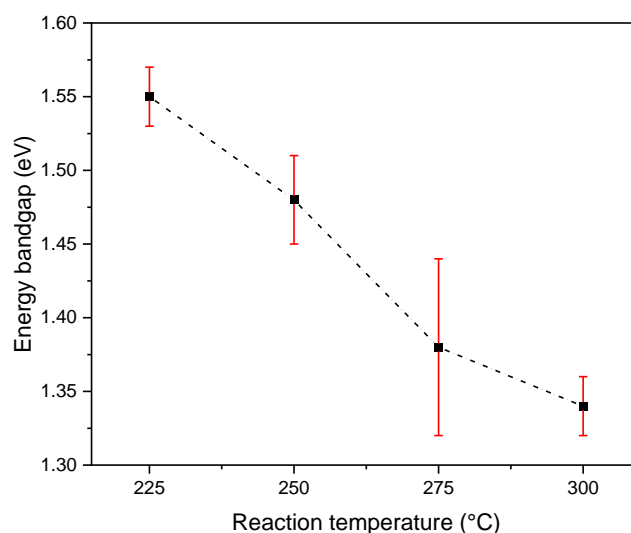


Figure. 5.11 The trend of the bandgap of as synthesised CZTS thin films with different reaction temperatures.

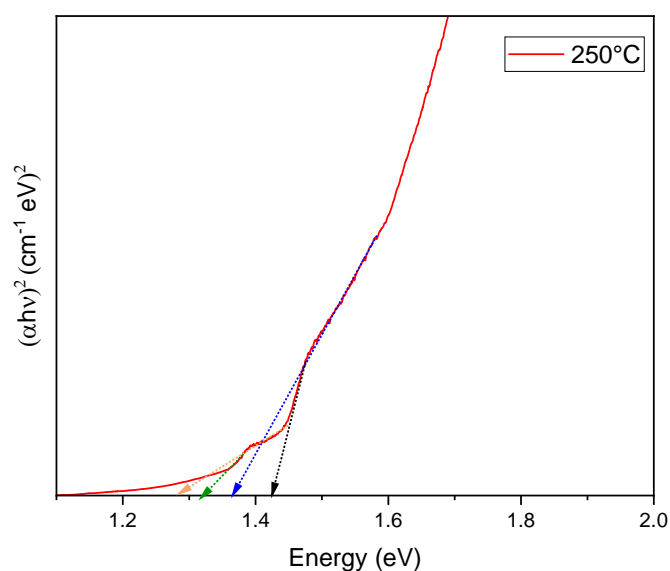


Figure. 5.12 An example Tauc plot fit showing the different bandgaps obtained when fitting linear regression curves to different sections of the Tauc plot not related to the CZTS energy bandgap. The bandgaps obtained can be used to correlate the presence of possible secondary phases. This is for the sample of 250 °C for 30 minutes.

The Tauc plot in figure 5.10 shows different inflection points in the region 1.2-1.5 eV. This is possibly due to the presence of secondary phases with bandgaps different from those of CZTS. By performing a Tauc plot to different regions of the curve in figure 5.12 it is possible to identify other energy bandgaps. There is also a long tail of weak absorption into the energy bandgap in the 1.1-1.3 eV, this is the Urbach tail as described by equation 3.5 in section 3.7. The different energy bandgaps extracted using the method shown in figure 5.12 are given in table 5.5. The possible secondary phases related to these energy bandgaps are also listed.

Temperature (°C)	Energy bandgaps from Tauc plot (eV)	Possible secondary phases related to bandgaps
225	1.30, 1.42, 1.43	SnS, Cu <sub>2</sub> SnS <sub>3</sub>
250	1.28, 1.32, 1.36, 1.43	SnS, ?, Cu <sub>2</sub> SnS <sub>3</sub>
275	1.20, 1.32	Cu <sub>2</sub> S/Cu <sub>3</sub> SnS <sub>4</sub> /Cu <sub>4</sub> SnS <sub>4</sub> , SnS
300	1.20, 1.32	Cu <sub>2</sub> S/Cu <sub>3</sub> SnS <sub>4</sub> /Cu <sub>4</sub> SnS <sub>4</sub> , SnS

**Table 5.5:** Possible secondary phases and their bandgaps with different reaction temperatures.

As table 5.5 shows, there is evidence of possible secondary phases in each of these samples from the Tauc plot analysis.

Table 5.6 gives a comparison of possible secondary phases identified from both Raman spectroscopy and UV-vis spectroscopy measurements.

Temperature (°C)	Secondary phases from Raman spectroscopy	Secondary phases from Tauc plot analysis (eV)
225	CuS	SnS, Cu <sub>2</sub> SnS <sub>3</sub>
250	<b>SnS</b> , Cu <sub>4</sub> SnS <sub>4</sub>	<b>SnS</b> , ?, Cu <sub>2</sub> SnS <sub>3</sub>
275	CuS, Cu <sub>4</sub> Sn <sub>7</sub> S <sub>16</sub>	Cu <sub>2</sub> S, Cu <sub>3</sub> SnS <sub>4</sub> , Cu <sub>4</sub> SnS <sub>4</sub> , SnS
300	-	Cu <sub>2</sub> S, Cu <sub>3</sub> SnS <sub>4</sub> , Cu <sub>4</sub> SnS <sub>4</sub> , SnS

**Table 5.6:** Comparison of possible secondary phases identified from Raman and UV-vis spectroscopy measurements.

Possible secondary phases identified in table 5.6 include: CuS, SnS, Cu<sub>2</sub>SnS<sub>3</sub>, Cu<sub>3</sub>SnS<sub>4</sub>, Cu<sub>4</sub>SnS<sub>4</sub>, and Cu<sub>4</sub>Sn<sub>7</sub>S<sub>16</sub>. Only one sample, synthesised at 250 °C, shows the same secondary phases identified by both techniques making indicating their presence is more likely in this sample.

From all the five different sets of characterisation results above, 225 °C, 250 °C and 275 °C reaction temperatures, the findings show that they are suitable reaction temperatures for the synthesis of CZTS nanocrystal inks. Hence, this reaction temperature range is appropriate for continuing the systematic study which will be on the reaction times. The exclusion of the higher 300 °C reaction temperature was decided based on the Tauc plot analysis that did not show a value of bandgap,  $1.34 \pm 0.02$  eV, sufficiently close to the theoretical CZTS bandgap (1.40-1.60 eV) when compared with other samples. The investigation of the impact of different reaction times uses the three reactions temperatures investigated in section 5.4: 225 °C, 250 °C and 275 °C.

## 5.5. Reaction times

Twelve different samples were prepared with different reaction temperatures and times during the synthesis of CZTS nanocrystal inks. The hot injection method was used for the fabrication of these samples and the spin coating technique was used for the deposition of CZTS nanocrystal inks onto glass substrate. In this section, reaction times from 15-60 minutes were applied during the synthesis of the CZTS thin films with reaction temperature range of 225 °C, 250 °C and 275 °C.

## 5.6. Experimental methodology

### 5.6.1. The fabrication of CZTS nanoparticles

CZTS nanoparticle preparation was successfully done with the same method as in the previous section using Cu-poor, Zn-rich compositions in the as synthesised particles, using the same precursor molar ratios. The procedures are as follows:

- The setting of the reaction temperatures is varied as 225 °C, 250 °C, and 275 °C for 4 different reaction times each.
- The time of the reaction is varied as 15, 30, 45 and 60 minutes.

### 5.6.2. Ink deposition

The CZTS thin films were spin coated on cleaned SLG substrates using the same method as described in previous section for the ink deposition. Spin coating speed was 2500 rpm for 15 seconds.

## 5.7. Results and discussion

### 5.7.1. Reaction temperature of 225 °C

### 5.7.2. Crystal structure – XRD

The XRD patterns of the fabricated CZTS nanoparticles at 225 °C for the reaction temperature with different reaction times 15-60 minutes are shown in figure 5.13.

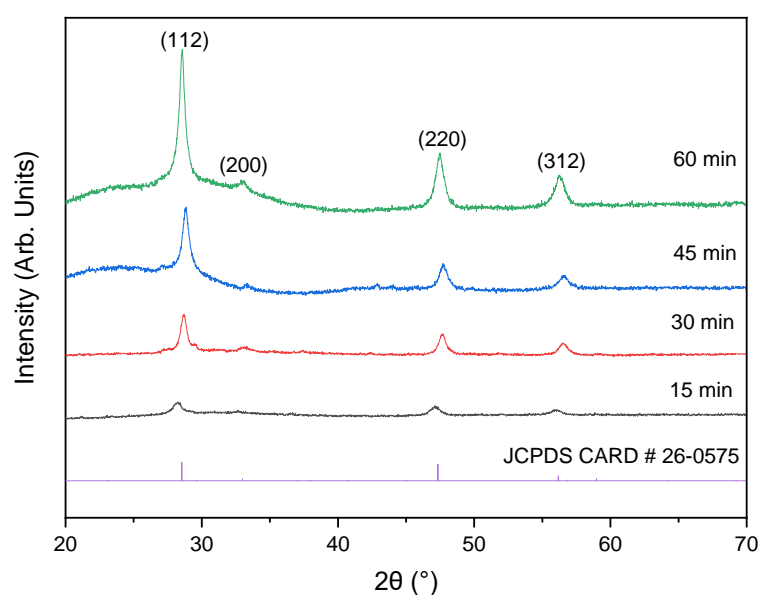


Figure 5.13 XRD for CZTS (225 °C) with different reaction times, including the CZTS PDF reference (# 26-0575).

The major XRD diffraction peaks for 30 to 60 minute samples appeared at locations matching well with the kesterite phase shown in reference PDF card 026-0575 in comparison to the sample of 15 minutes as shown in figure 5.13.

Time (min)	2 $\theta$ (°) for structure planes (112)
15	28.41
30	28.55
45	28.68
60	28.82

**Table 5.7:** Values for  $2\theta$  of (112) crystal plane for CZTS (225 °C) samples with different reaction times.

Table 5.8 below presents the values of  $d$ -spacing, size of scattering domain and lattice parameters  $a$  and  $c$ .

Time (min)	$d$ -spacing (nm)	$a$ (nm)	$c$ (nm)	Scattering domain (nm)
15	0.3129	0.5425	1.171	$3 \pm 1$
30	0.3185	0.5499	1.111	$4 \pm 3$
45	0.3123	0.5414	1.080	$7 \pm 4$
60	0.3218	0.5521	1.136	$20 \pm 6$

**Table 5.8:** Values  $d$ -spacing, size of scattering domain and lattice parameters  $a$  and  $c$  with different reaction times at (225 °C).

Tables 5.7 and 5.8 show similar  $d$ -spacing,  $a$  and  $c$  lattice numbers and X-ray peak location values of (112) crystal plane to the literature paper for 30 minutes of the reaction time [9]. As this table shows, the scattering domain size increases with the increasing reaction time from small  $3 \pm 1$  nm to a larger domain size of  $20 \pm 6$  nm matching other published results with these increases [18].

### 5.7.3. Raman spectroscopy

The crystal structure of the nanoparticles was confirmed by Raman spectroscopy measurements shown in figure 5.14 as the peak locations were in good agreement with the characteristic CZTS peak  $332\text{--}339\text{ cm}^{-1}$  [23–28]. The strong Raman peaks of CZTS (225 °C) are located at  $334\text{ cm}^{-1}$  for 15 min,  $337\text{ cm}^{-1}$  for 30 min,  $339\text{ cm}^{-1}$  for 45 min and  $337\text{ cm}^{-1}$  for 60 min. Another peak appears at  $472\text{ cm}^{-1}$  for 15 and 45 min which seems to be a secondary phase of CuS [29]. One more peak appears at  $475\text{ cm}^{-1}$  for 30 min which seem to be a secondary phase of Cu<sub>2</sub>S [30]. A very broad band in the range  $270\text{--}280\text{ cm}^{-1}$  appears for the samples annealed at 30–60 minutes. It was not possible to identify the origin of this feature.

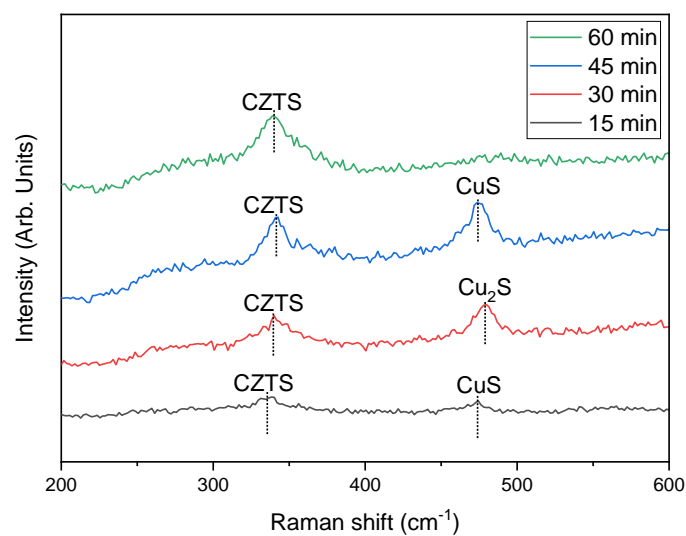


Figure 5.14 Raman spectra of CZTS (225 °C) samples with different reaction times.

#### 5.7.4. Morphology

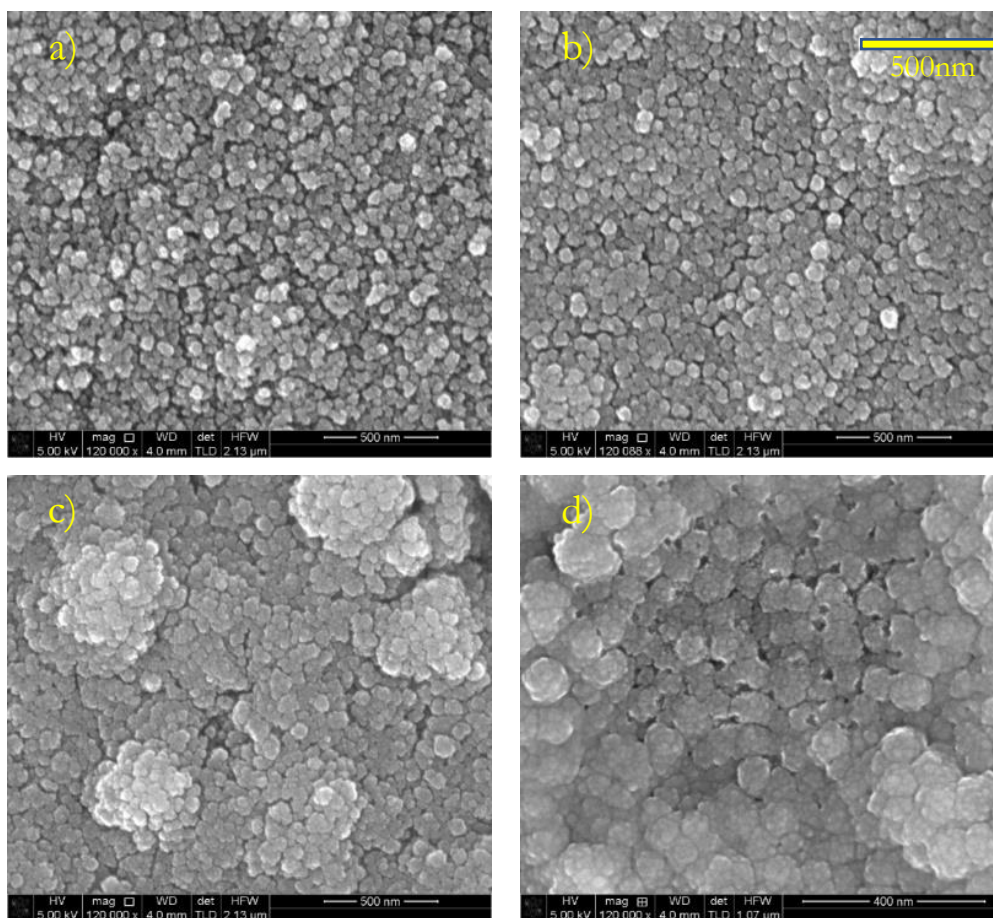


Figure. 5.15 SEM images at scale of 500 nm for CZTS 225 °C nanoparticles with different reaction times as a) 15 min b) 30 min c) 45 min and d) 60 min.

In figure 5.15, the shape of nanoparticles appears uniform and roughly spherical for all samples. The size of the particles was found to increase with the increase of reaction time where this trend is in good agreement with the XRD measurements shown in figure 5.13. In the matter of uniformity, the 30 minute sample appeared to be more uniform with less gaps, and more uniform size distribution than the other reaction times. At longer times, particles appeared to group together to form larger scale structures at 45 and 60 minutes reaction time. However, in all images individual nanoparticles remain visible, even at higher synthesis temperatures where agglomeration into larger structures is visible. Within these larger structures, it is expected that individual grains will remain separated by grain boundaries. These samples have not been annealed in a high temperature sulphur environment, typically in the range 400-600 °C, which is normally required to promote nanoparticle aggregation and grain growth. The behaviour of charge carriers is therefore unlikely to change significantly with agglomeration until group of particles merge to form single, larger grains which is not seen in these images. It is also expected that measurement of the scattering domain will not be influenced by the larger agglomerations, as these are not larger grains but will consist of crystallite regions representative of fabricated nanoparticles. The scattering domain will reflect the size of crystallites within individual grains as seen in the SEM images in figure 5.15.

### 5.7.5. Chemical composition

Table 5.9 below summarises the EDS result of the 225 °C CZTS synthesised samples at different reaction times (15, 30, 45 and 60 minutes) using the EDS procedure described in section 5.4.4.

Time (min)	Cu/(Zn+Sn)	Sn/Cu	Zn/Sn	S/(Cu+Zn+Sn)
15	$0.49 \pm 0.20$	$0.41 \pm 0.04$	$2.38 \pm 0.10$	$0.56 \pm 0.08$
30	$0.71 \pm 0.06$	$0.46 \pm 0.03$	$1.13 \pm 0.03$	$0.96 \pm 0.04$
45	$0.25 \pm 0.07$	$0.53 \pm 0.02$	$2.68 \pm 0.10$	$0.98 \pm 0.06$
60	$0.92 \pm 0.04$	$0.58 \pm 0.01$	$0.82 \pm 0.03$	$1.08 \pm 0.01$

**Table 5.9:** Composition ratios of 225 °C CZTS nanoparticles with different reaction times.



In table 5.9, it is clear that the 30 minutes sample has the improved Cu-poor, Zn-rich ratio in comparison with the rest of the reaction times. The ratio of  $S/(Cu+Zn+Sn)$  showed a trend of increasing value with increasing reaction time, demonstrating greater sulphur ion incorporation into the CZTS with longer reaction times. The general trend in table 5.9 suggests that the sample produced at 45 minutes may be impacted by other factors, although this does not appear in the energy bandgap data presented below.

### 5.7.6. Optical properties

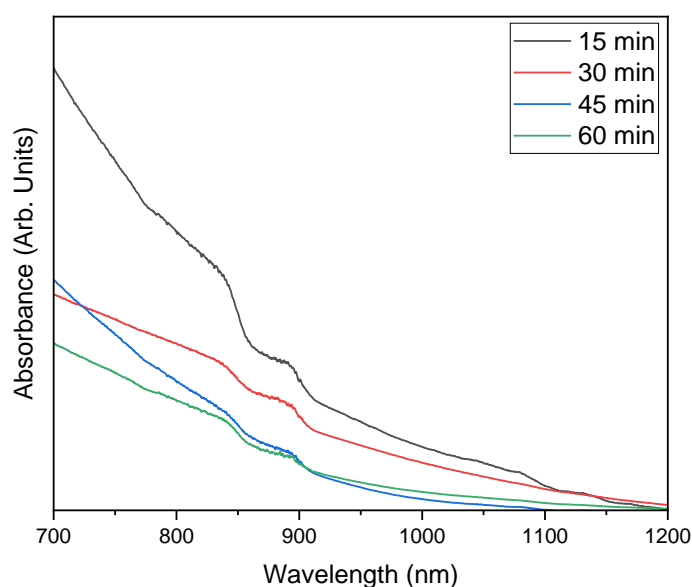


Figure 5.16 Absorbance spectrum of CZTS (225 °C) samples with different reaction times.

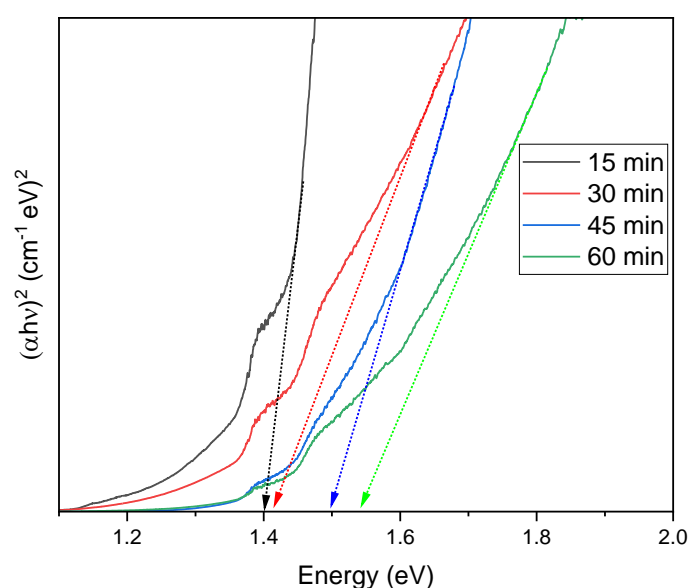


Figure 5.17 Tauc plot to show the bandgap of CZTS (225 °C) versus different reaction times.

The absorbance spectra in the range 700-1200 nm are shown in figure 5.16. The corresponding Tauc plots to determine the CZTS bandgaps are shown in figure 5.17.

Time (min)	$E_g$ (eV)
15	$1.40 \pm 0.02$
30	$1.41 \pm 0.03$
45	$1.50 \pm 0.04$
60	$1.54 \pm 0.02$

**Table 5.10:** The different reaction times of CZTS at 225 °C versus the CZTS energy bandgap.

Table 5.10 shows a clear relationship between the reaction time and the energy bandgap with a clear systematic trend. This trend also was confirmed in other published work [9]. The observed bandgap of all reaction times in table 5.10 corresponded well with that reported in the literature 1.40-1.60 eV [35-37].

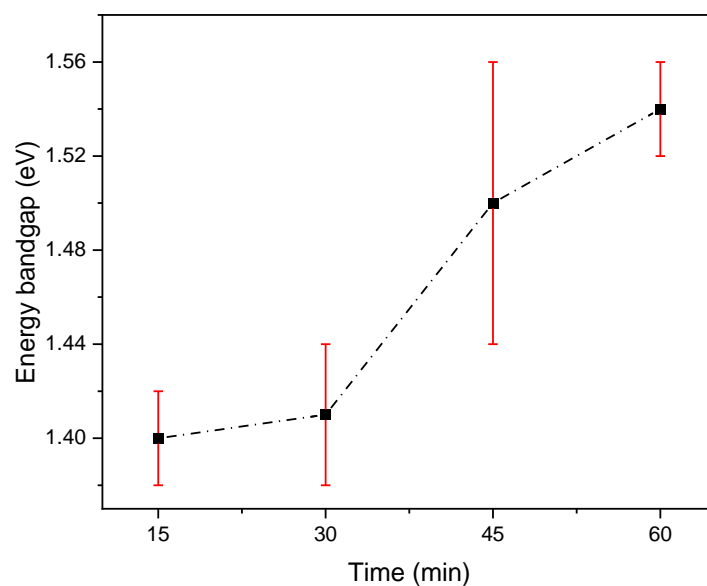


Figure. 5.18 The trend of the bandgap of as synthesised CZTS (225 °C) thin films with different reaction times.

Figure 5.17 shows different linear regions indicating the possible existence of secondary phases with energy bandgaps different from CZTS. Using the procedure described in section 5.4.5 and illustrated in figure 5.12, values of additional bandgaps linked to possible secondary phases can be extracted. The different energy bandgaps extracted using this method are given in table 5.11. The possible secondary phases related to these energy bandgaps are also listed.

Time (min)	Energy bandgaps from Tauc plot (eV)	Possible secondary phases related to bandgaps
15	1.20, 1.22, 1.32	Cu <sub>2</sub> S/Cu <sub>3</sub> SnS <sub>4</sub> /Cu <sub>4</sub> SnS <sub>4</sub> , SnS
30	1.21, 1.30, 1.35, 1.38	Cu <sub>2</sub> S/Cu <sub>3</sub> SnS <sub>4</sub> /Cu <sub>4</sub> SnS <sub>4</sub> , SnS, ?
45	1.30, 1.37, 1.40	SnS, ?, Cu <sub>2</sub> SnS <sub>3</sub>
60	1.37, 1.40, 1.42	?, Cu <sub>2</sub> SnS <sub>3</sub> ,

**Table 5.11:** Possible secondary phases and their bandgaps with different reaction times of 225 °C.

As discussed in section 5.4.5, a correlation between the energy bandgap and CZTS composition was not observed when increasing reaction temperatures. This was based on the trend identified by Malerba et al [38] where an increase in the Sn/Cu ratio was correlated to an increase in the energy bandgap. By comparing table 5.9 with table 5.10, a trend relating increasing Sn/Cu ratio to increasing energy bandgap is observed.

### 5.7.7. Reaction temperature of 250 °C

### 5.7.8. Crystal structure – XRD

The XRD patterns of the fabricated CZTS nanoparticles at 250 °C with different reaction times 15-60 minutes are shown in figure 5.19.

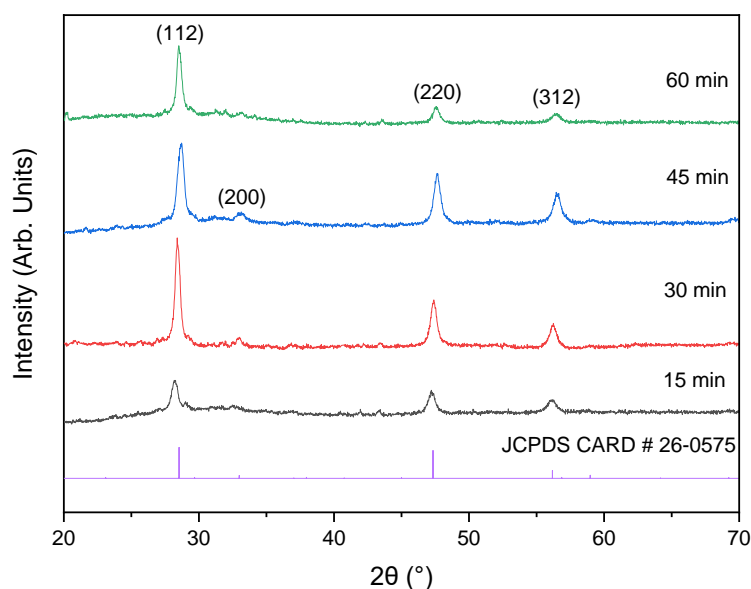


Figure 5.19 XRD for CZTS (250 °C) with different reaction times, including the CZTS PDF reference (# 26-0575).

The major XRD diffraction peaks for 30 minute samples appeared at locations in good agreement with the kesterite phase shown in reference PDF card 026-0575 in figure 5.19.

Time (min)	2 $\theta$ (°) for structure planes (112)
15	28.20
30	28.45
45	28.70
60	28.55

**Table 5.12:** Values for 2  $\theta$  of (112) crystal plane for CZTS (250 °C) samples with different reaction times.

Table 5.13 below presents the values of  $d$ -spacing, size of scattering domain and lattice parameters  $a$  and  $c$ .

Time (min)	$d$ -spacing (nm)	$a$ (nm)	$c$ (nm)	Scattering domain (nm)
15	0.3175	0.5484	1.106	$7 \pm 2$
30	0.3134	0.5413	1.092	$5 \pm 5$
45	0.3167	0.5680	1.104	$20 \pm 6$
60	0.3251	0.5438	1.103	$37 \pm 7$

**Table 5.13:** Values  $d$ -spacing, size of scattering domain and lattice parameters  $a$  and  $c$  with different reaction times at 250 °C.

Tables 5.12 and 5.13 show similar  $d$ -spacing,  $a$  and  $c$  lattice numbers and x-ray peak location values of (112) crystal plane to the literature paper for 30 minute reaction time [9]. The scattering domain size increases with the increasing reaction time again from  $7 \pm 2$  nm to a larger domain size of  $37 \pm 7$  nm.

### 5.7.9. Raman spectroscopy

The crystal structure of the nanoparticles was confirmed by Raman spectroscopy measurements shown in figure 5.20 as the peak locations were in good agreement with the expected characteristic CZTS peak 332-339  $\text{cm}^{-1}$  [23-28]. The strong Raman peaks of CZTS 250  $^{\circ}\text{C}$  are located at 339  $\text{cm}^{-1}$  for 15 min, 337  $\text{cm}^{-1}$  for 30 min, 336  $\text{cm}^{-1}$  for 45 min and 337  $\text{cm}^{-1}$  for 60 min. A weak peak appears at 475  $\text{cm}^{-1}$  for 15 min which seemed to be a secondary phase of  $\text{Cu}_2\text{S}$  [30]. Two peaks appear at 288 and 317  $\text{cm}^{-1}$  for 30 min which might be secondary phases of  $\text{SnS}$  and  $\text{Cu}_4\text{SnS}_4$  [29]. In the sample of 45 min, a weak peak appears at 317  $\text{cm}^{-1}$  which might be a secondary phase of  $\text{Cu}_4\text{SnS}_4$  [30]. No other common secondary phases like  $\text{CuS}$  and  $\text{Cu}_4\text{Sn}_7\text{S}_{16}$  were observed in the Raman spectra.

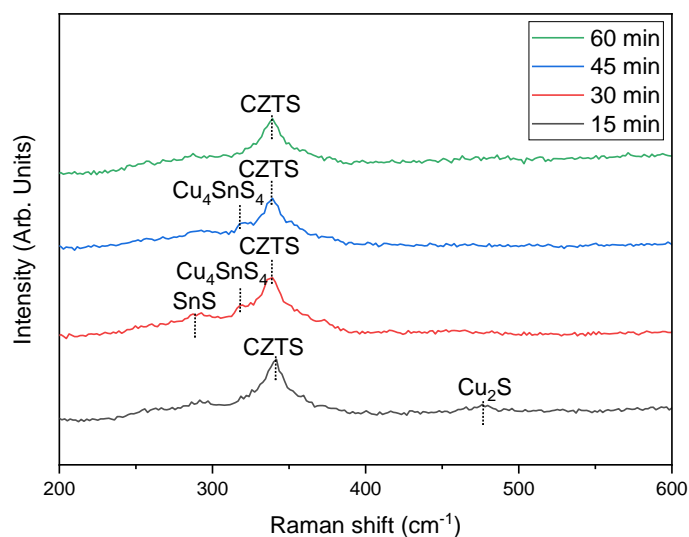


Figure 5.20 Raman spectra of CZTS 250  $^{\circ}\text{C}$  samples with different reaction times.

### 5.7.10. Morphology

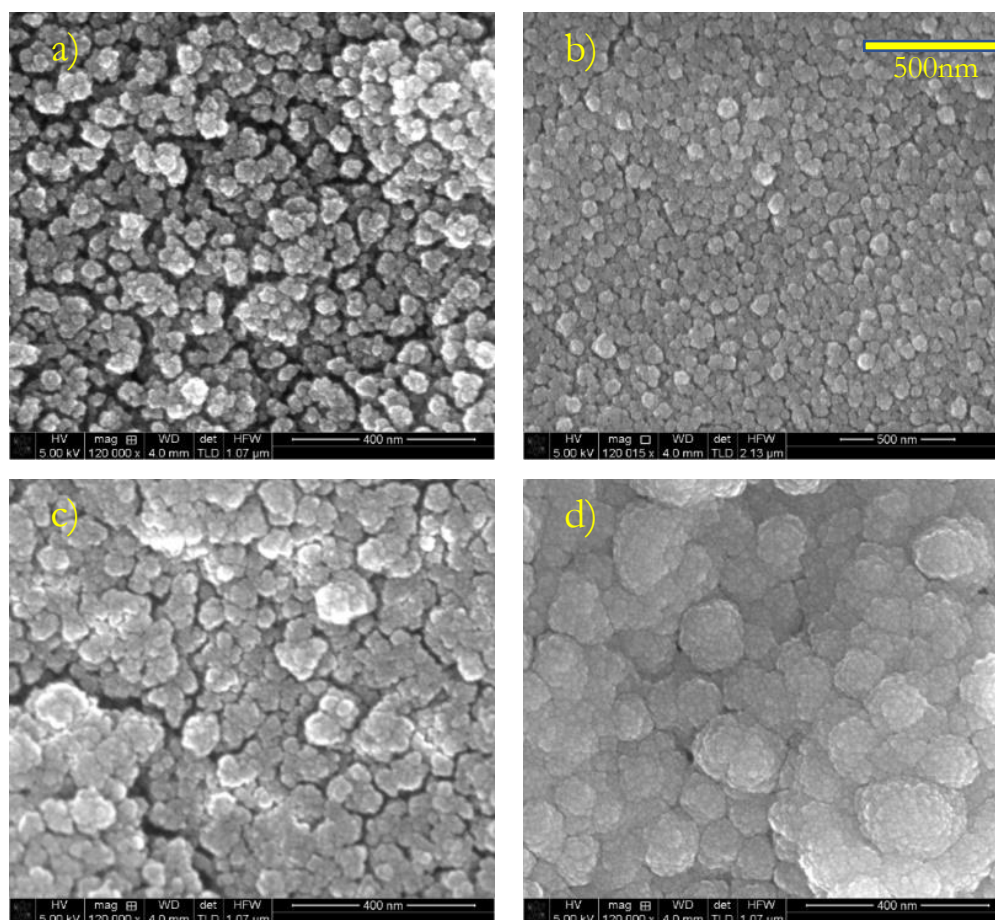


Figure. 5.21 SEM images at scale of between 400 to 500 nm for CZTS (250 °C) nanoparticles with different reaction times as a) 15 min b) 30 min c) 45 min and d) 60 min.

The SEM microscope images, presented in figure 5.21, showed that the shape of the nanoparticles was approximately spherical for all samples. The size of the particles also increased here with the increase of reaction time. This increase is consistent with the XRD measurements shown in table 5.13. The sample of 30 minutes demonstrated uniform particles with less gaps and a more continuous film. Particles are seen to agglomerate to form larger scale structures at longer reaction times of 60 minutes, as previously discussed in section 5.7.4.

### 5.7.11. Chemical composition

The EDS results in table 5.14 for CZTS synthesised samples 250 °C at different reaction times were taken from the film's surface using the procedure described in section 5.4.4.

Time (min)	Cu/(Zn+Sn)	Sn/Cu	Zn/Sn	S/(Cu+Zn+Sn)
15	$0.64 \pm 0.20$	$1.12 \pm 0.02$	$0.78 \pm 0.50$	$0.85 \pm 0.20$
30	$0.82 \pm 0.06$	$0.77 \pm 0.04$	$1.21 \pm 0.80$	$1.17 \pm 0.20$
45	$0.88 \pm 0.08$	$0.76 \pm 0.01$	$1.03 \pm 0.10$	$1.33 \pm 0.04$
60	$0.93 \pm 0.20$	$0.58 \pm 0.01$	$1.11 \pm 0.10$	$1.96 \pm 0.07$

**Table 5.14:** Composition ratios of CZTS 250 °C nanoparticles with different reaction times.

In table 5.14, the results are similar to those in table 5.9 since again the 30 minutes sample also has the improved Cu-poor, Zn-rich ratio in comparison with the rest of the reaction times for CZTS 250 °C nanoparticles. The ratio of S/(Cu+Zn+Sn) showed a similar trend to that seen in table 5.9 as when the reaction time increases, the ratio value increased indicating increased incorporation of S into the films at longer reaction times.

### 5.7.12. Optical properties

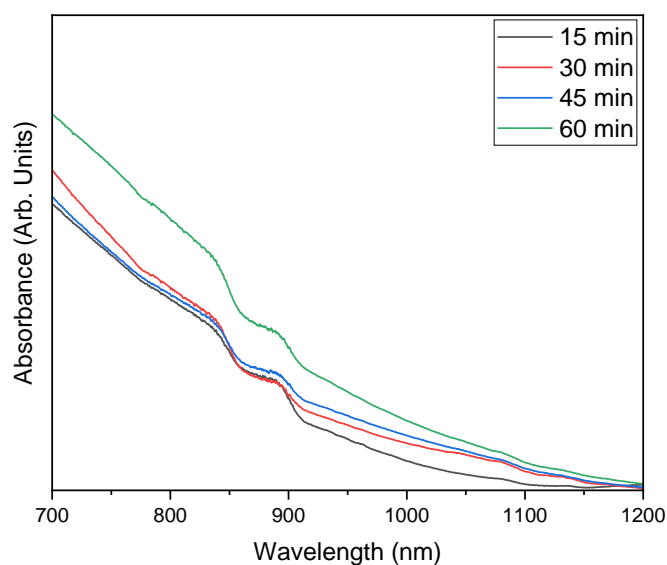


Figure 5.22 Absorbance spectrum (between 700-1200 nm) of CZTS (250 °C) samples with different reaction times.

The absorbance spectra in the range 700-1200 nm are shown in figure 5.22. The corresponding Tauc plots to determine the CZTS bandgap are shown in figure 5.23.

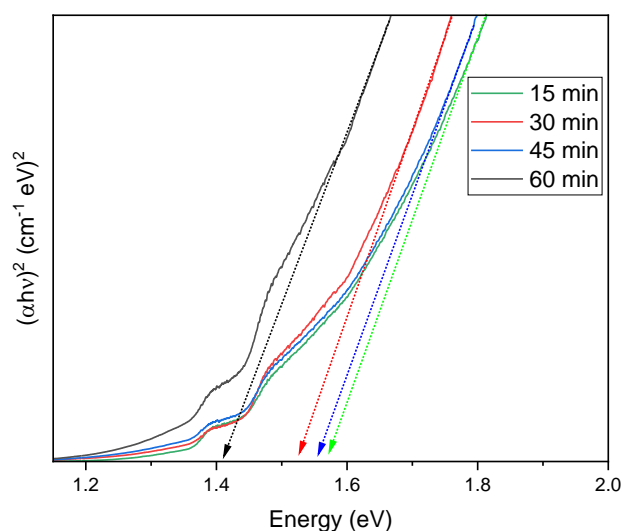


Figure 5.23 Tauc plot to show the bandgap of CZTS (250 °C) versus different reaction times.

Time (min)	$E_g$ (eV)
15	$1.41 \pm 0.01$
30	$1.52 \pm 0.04$
45	$1.55 \pm 0.02$
60	$1.56 \pm 0.03$

**Table 5.15:** The different reaction times of CZTS 250 °C versus the energy bandgap.

An observation of an increasing energy bandgap with the increase of reaction times is shown in table 5.15 above. This observed bandgap of all reaction times here also matches well with published papers reporting values in the range 1.40–1.60 eV [39]. The trend is shown in figure 5.24 below and is similar to the trend as discussed in section 5.7.6 for the 225 °C reaction temperature.

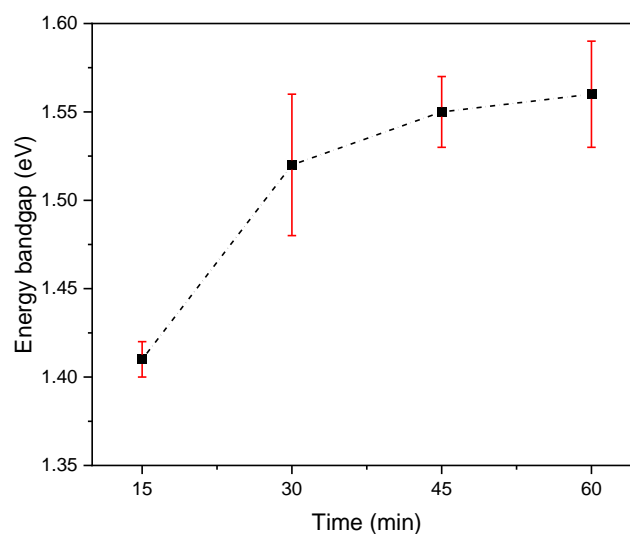


Figure. 5.24 The trend of the bandgap of as synthesised CZTS 250 °C thin films with different reaction times.



Figure 5.23 shows different linear regions indicating the possible existence of secondary phases with energy bandgaps different from CZTS. Using the procedure described in section 5.4.5 and illustrated in figure 5.12, values of additional bandgaps linked to possible secondary phases can be extracted. The different energy bandgaps extracted using this method are given in table 5.16. The possible secondary phases related to these energy bandgaps are also listed.

Time (min)	Energy bandgaps from Tauc plot (eV)	Possible secondary phases related to bandgaps
15	1.20, 1.30, 1.40	Cu <sub>2</sub> S/Cu <sub>3</sub> SnS <sub>4</sub> /Cu <sub>4</sub> SnS <sub>4</sub> , SnS, Cu <sub>2</sub> SnS <sub>3</sub>
30	1.20, 1.30, 1.40	Cu <sub>2</sub> S/Cu <sub>3</sub> SnS <sub>4</sub> /Cu <sub>4</sub> SnS <sub>4</sub> , SnS, Cu <sub>2</sub> SnS <sub>3</sub>
45	1.20, 1.30, 1.40	Cu <sub>2</sub> S/Cu <sub>3</sub> SnS <sub>4</sub> /Cu <sub>4</sub> SnS <sub>4</sub> , SnS, Cu <sub>2</sub> SnS <sub>3</sub>
60	1.20, 1.30, 1.40	Cu <sub>2</sub> S/Cu <sub>3</sub> SnS <sub>4</sub> /Cu <sub>4</sub> SnS <sub>4</sub> , SnS, Cu <sub>2</sub> SnS <sub>3</sub>

**Table 5.16:** Possible secondary phases and their bandgaps with different reaction times of 250 °C.

In section 5.7.6 a trend relating an increase in the ratio Sn/Cu to an increase in energy bandgap was identified, in agreement with the observations of Malerba et al [38]. However, with the set of samples synthesised at 250 °C, no such trend appears. In fact, the Sn/Cu ratio decreases with increasing reaction time implying a more complex relationship in these samples between bandgap and composition.

### 5.7.13. Reaction temperature of 275 °C

### 5.7.14. Crystal structure – XRD

The XRD patterns of the fabricated CZTS nanoparticles at 275 °C with different reaction times 15-60 minutes are shown in figure 5.25.

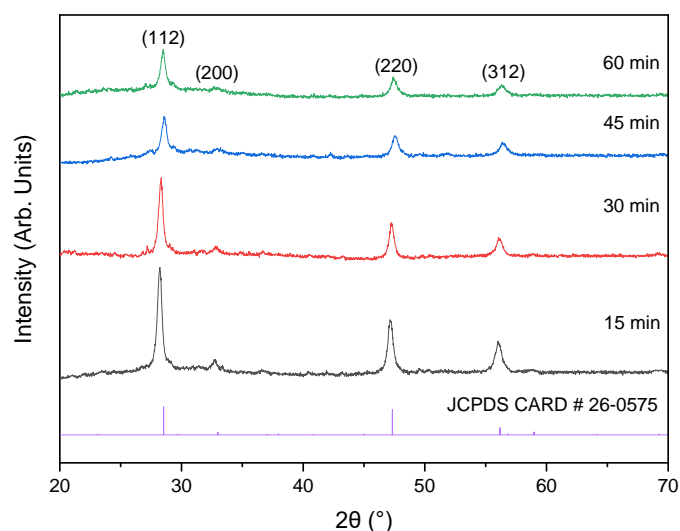


Figure 5.25 XRD for CZTS 275 °C with different reaction times, including the CZTS PDF reference (# 26-0575).

The major XRD diffraction peaks for 30, 45 and 60 minute samples appeared at locations in good agreement with the kesterite phase shown in reference PDF card 026-0575, while this is not the case for the 15 minutes sample as in figure 5.25 above.

Time (min)	2 $\theta$ (°) for structure planes (112)
15	28.34
30	28.54
45	28.74
60	28.50

**Table 5.17:** Values for 2  $\theta$  of (112) crystal plane for CZTS (275 °C) samples with different reaction times.

Table 5.18 below presents the values of  $d$ -spacing, size of scattering domain and lattice parameters  $a$  and  $c$ .

Time (min)	$d$ -spacing (nm)	$a$ (nm)	$c$ (nm)	Scattering domain (nm)
15	0.3143	0.5422	1.097	$20 \pm 5$
30	0.3123	0.5413	1.081	$8 \pm 4$
45	0.3148	0.5448	1.093	$22 \pm 5$
60	0.3128	0.5429	1.079	$11 \pm 1$

**Table 5.18:** Values  $d$ -spacing, size of scattering domain and lattice parameters  $a$  and  $c$  with different reaction times at (275 °C).

Tables 5.17 and 5.18 show similar  $d$ -spacing,  $a$  and  $c$  lattice numbers and X-ray peak location values of (112) crystal plane to the literature paper for the sample of 30 minutes at the reaction temperature of 275 °C [9]. However, the scattering domain size here did not show a systematic increase with the increasing reaction time as 30 and 60 minutes as compared with the trend seen in tables 5.8 and 5.13.

### 5.7.15. Raman spectroscopy

The crystal structure of the nanoparticles was confirmed by Raman spectroscopy measurements as shown in figure 5.26 as the peak locations were in good agreement with the expected characteristic CZTS peak 332-339  $\text{cm}^{-1}$  [23-28]. The strong Raman peaks of CZTS 275 °C are located at 339  $\text{cm}^{-1}$  for 15 min, 336  $\text{cm}^{-1}$  for 30 min, 332  $\text{cm}^{-1}$  for 45 min and 338  $\text{cm}^{-1}$  for 60 min. A weak peak appears at 472  $\text{cm}^{-1}$  for 30 min attributed to the secondary phase of CuS [29]. No other common secondary phases like  $\text{Cu}_2\text{S}$  and  $\text{Cu}_4\text{Sn}_7\text{S}_{16}$  were observed in the Raman spectra. As discussed in section 5.7.3 for the 225 °C samples, a very broad band in the range 270-280  $\text{cm}^{-1}$  appears for the samples annealed at 30-45 minutes. It was not possible to identify the origin of this feature.

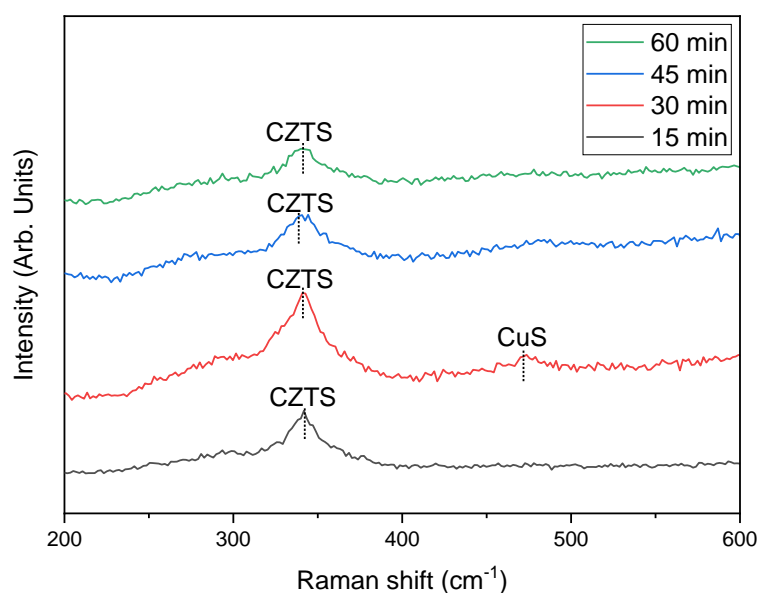


Figure 5.26 Raman spectra of CZTS (275 °C) samples with different reaction times.

### 5.7.16. Morphology

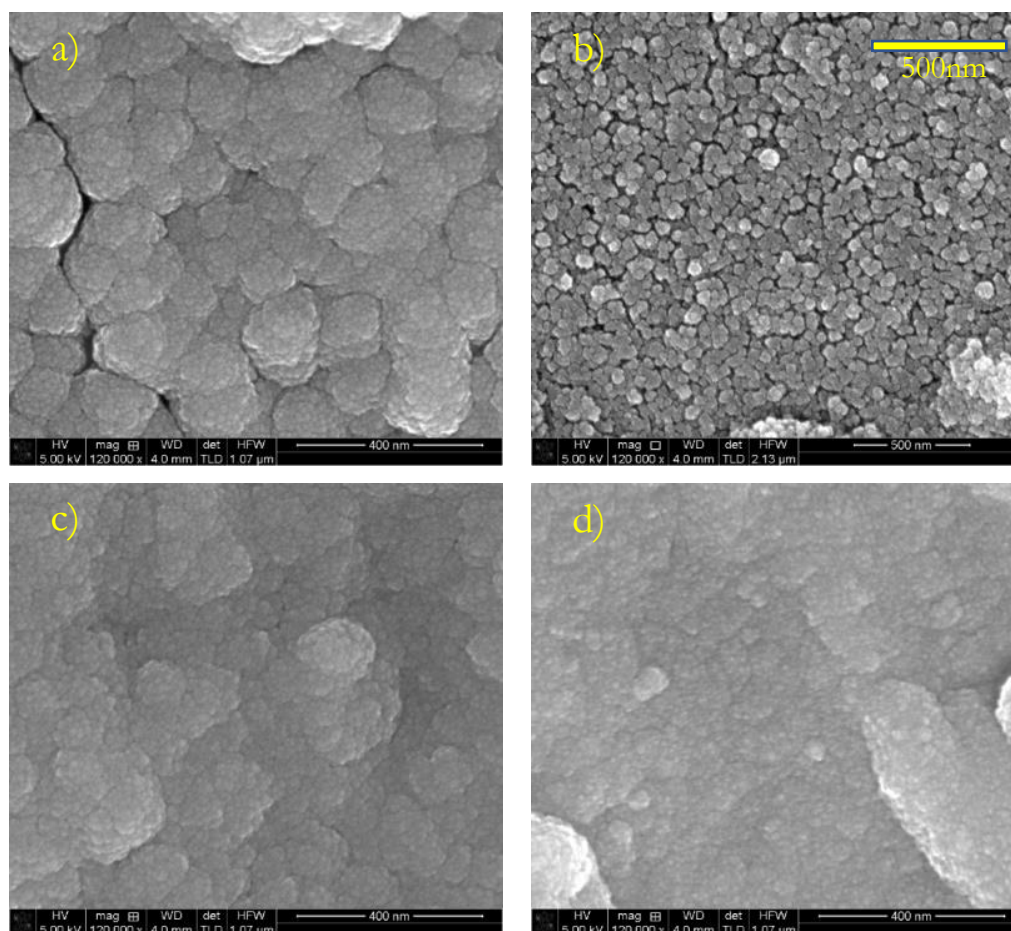


Figure. 5.27 SEM images at scale of between 400 to 500 nm for CZTS 275 °C nanoparticles with different reaction times as a) 15 min b) 30 min c) 45 min and d) 60 min.

The SEM microscope images, in figure 5.27, showed again the spherical shape of the nanoparticles for the three samples excluding the sample of 60 minutes where the shape was not very clear. The overall behaviour at 275 °C is different from the other temperatures as there is more evidence of agglomeration of particles over a wider range of reaction times. The possible impact of agglomeration is discussed in section 5.7.4.

### 5.7.17. Chemical composition

The EDS results in table 5.19 for CZTS 275 °C synthesised samples at different reaction times were taken from the film's surface using the procedure described in section 5.4.4.

Time (min)	Cu/(Zn+Sn)	Sn/Cu	Zn/Sn	S/(Cu+Zn+Sn)
15	$0.85 \pm 0.30$	$0.64 \pm 0.02$	$0.81 \pm 0.60$	$1.07 \pm 0.20$
30	$0.83 \pm 0.70$	$0.76 \pm 0.04$	$0.71 \pm 0.10$	$1.02 \pm 0.20$
45	$0.98 \pm 0.20$	$0.71 \pm 0.05$	$0.80 \pm 0.10$	$0.80 \pm 0.40$
60	$0.53 \pm 0.30$	$0.83 \pm 0.04$	$1.38 \pm 0.20$	$0.51 \pm 0.30$

**Table 5.19:** Composition ratios of CZTS (275 °C) nanoparticles with different reaction times.

In table 5.19, the 30 minutes sample has the better Cu-poor, Zn-rich ratio in comparison with the rest of the reaction times for CZTS 275 °C nanoparticles. The sample of 45 and 60 minutes showed a lack of S in the ratio of S/(Cu+Zn+Sn) as  $0.80 \pm 0.40$  and  $0.51 \pm 0.30$  respectively which might be a tendency of CZTS to have with longer reaction times and higher reaction temperatures.

### 5.7.18. Optical properties

The absorbance spectra in the range 700-1200 nm are shown in figure 5.28. The corresponding Tauc plots to determine the CZTS bandgap are shown in figure 5.29.

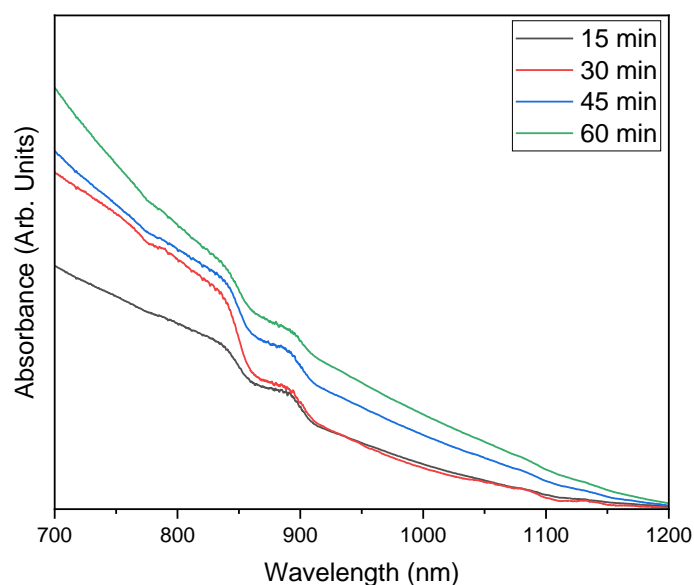


Figure 5.28 Absorbance spectrum between 700-1200 nm of CZTS 275 °C samples with different reaction times.

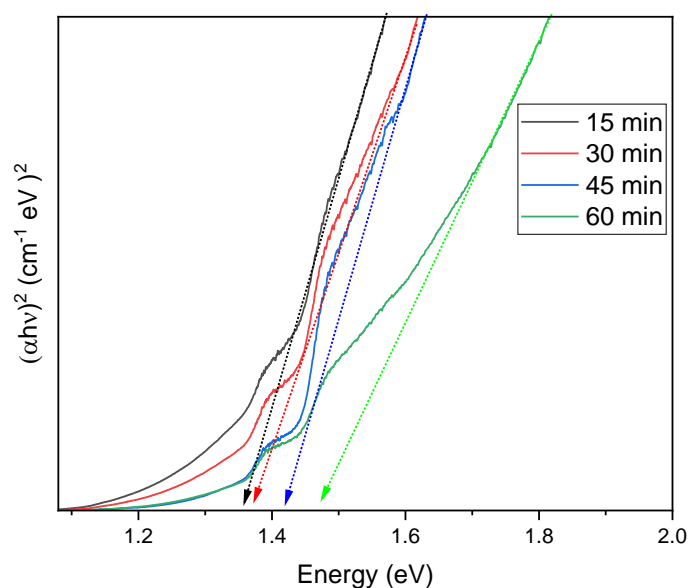


Figure 5.29 Tauc plot to show the bandgap of CZTS 275 °C versus different reaction times.

Time (min)	$E_g$ (eV)
15	$1.35 \pm 0.03$
30	$1.36 \pm 0.04$
45	$1.42 \pm 0.01$
60	$1.46 \pm 0.01$

**Table 5.20:** The different reaction times of CZTS 275 °C versus the energy bandgap.

An observation of the same trend here also occurs for the increasing energy bandgap with the increase of reaction times at 275 °C. The observed bandgap of 45 and 60 minutes of reaction times in table 5.20 above corresponded well with other papers reporting values in the range 1.40–1.60 eV [40, 41]. However, samples of 15 and 30 minutes ( $1.35 \pm 0.03$  and  $1.36 \pm 0.04$  eV) did not show matching bandgap values close to the expected CZTS bandgap value of between 1.40–1.60 eV. The figure of 5.30 below shows the trend demonstrating an increase in the CZTS bandgap with increasing reaction time.

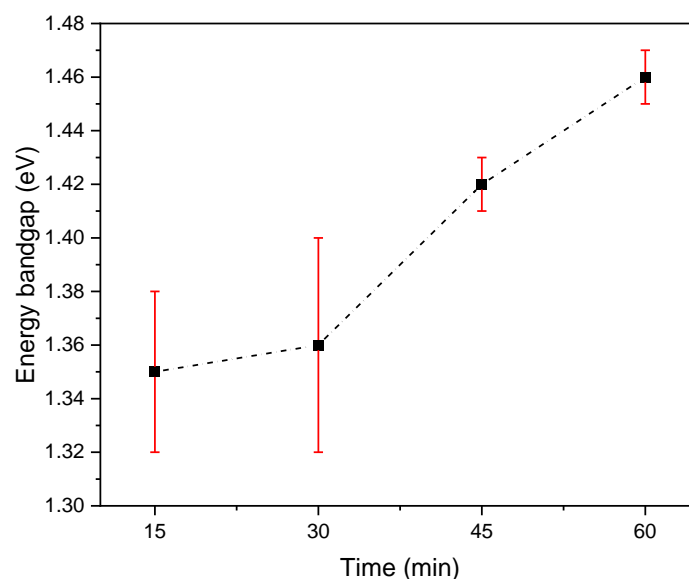


Figure. 5.30 The trend of the bandgap of as synthesised CZTS (275 °C) thin films with different reaction times.

Figure 5.29 shows different linear regions indicating the possible existence of secondary phases with energy bandgaps different from CZTS. Using the procedure described in section 5.4.5 and illustrated in figure 5.12, values of additional bandgaps linked to possible secondary phases can be extracted. The different energy bandgaps extracted using this method are given in table 5.21. The possible secondary phases related to these energy bandgaps are also listed.

Time (min)	Energy bandgaps from Tauc plot (eV)	Possible secondary phases related to bandgaps
15	1.15, 1.30	CuS, SnS
30	1.15, 1.30	CuS, SnS
45	1.20, 1.38, 1.42	Cu <sub>2</sub> S/Cu <sub>3</sub> SnS <sub>4</sub> /Cu <sub>4</sub> SnS <sub>4</sub> , ?, Cu <sub>2</sub> SnS <sub>3</sub>
60	1.20, 1.38, 1.42	Cu <sub>2</sub> S/Cu <sub>3</sub> SnS <sub>4</sub> /Cu <sub>4</sub> SnS <sub>4</sub> , ?, Cu <sub>2</sub> SnS <sub>3</sub>

**Table 5.21:** Possible secondary phases and their bandgaps with different reaction times of 275 °C.

Comparing table 5.19 and 5.20 shows that there might be a relationship between the Sn/Cu ratio and energy bandgap, as previously discussed in sections 5.7.6 and 5.7.12. However, in comparison with the work of Malerba et al [38], there is no clear trend in these samples. The samples synthesised at 225 °C and 275 °C show a similar trend, namely that the increase in CZTS energy bandgap does relate to an increase in the Sn/Cu ratio. However, this correlation is not observed in the time series of samples synthesised at 250 °C. However, in all cases, there is a correlation between increasing reaction time and increasing energy bandgap as shown in figures 5.18, 5.24 and 5.30.

### 5.7.19. Impact of reaction temperature and time on CZTS properties

To conclude the results of the reaction time of the synthesised CZTS nanoparticles, the bandgap energy in all samples confirmed a systematic trend with the reaction times investigated, i.e. 15, 30, 45 and 60 minutes. The sample fabricated at 250 °C with 30 minutes reaction time demonstrated the closest values of X-ray peaks locations, *d*-spacing and *a*, *c* lattice constants to the reference PDF card 026-0575 of CZTS. The CZTS Raman peak positions showed good agreement to other literature papers especially with reaction temperature of 250 °C for 30 minutes with two secondary phases of SnS and Cu<sub>4</sub>SnS<sub>4</sub> at 288 and 317 cm<sup>-1</sup>. In addition, the SEM microscopy image for 250 °C for 30 minutes sample is the most uniform nanoparticle film with less cracks and gaps compared to the other samples and displaying a uniform size distribution. The EDS values shows an excellent ratio for Cu-poor, Zn-rich in 250 °C closest to the composition known to give higher efficiency PV devices. From the characterisation results, 250 °C for 30 minutes might be the most suitable reaction temperature and time compared with the investigated temperature and time ranges for CZTS as an initial step for PV devices. Therefore, these reaction conditions: 250 °C as the reaction temperature and 30 minutes as the reaction time will be used for the next investigation to continue the systematic study which will be on the tin content.

Optical spectroscopy measurements, Raman and UV-vis, show the presence of possible secondary phases in the CZTS layers. As discussed in section 3.5, most secondary phases have a negative impact on CZTS device performance and should thus be reduced or eliminated. As shown above, there is not complete agreement between the two techniques on the presence of secondary phases. In one sample, as shown in table 5.6, both Raman and UV-vis show the presence of SnS. Further work is required to confirm with certainty the exact range of secondary phases present. There is no such correlation between secondary phases identified from Raman and UV-vis in other samples. The presence of secondary phases will impact on the overall chemical composition of the CZTS



layer. In this work EDS is used to identify the chemical composition and establish the important ratios of CZTS elements. As described in section 5.4.4, the EDS values are an average from a number of carefully selected points on the sample surface. These are identified, as much as possible, to be representative of the CZTS layer as a whole. This process will likely minimize the incorporation of secondary phases in the EDS measurements, although it will not eliminate them. If the overall composition shown by EDS is Cu-poor, Zn-rich, then the presence of Cu-rich phases would not be expected. However, the proportion of secondary phases is low in this material. As discussed in section 3.7, many CZTS structural and compositional factors can change the bandgap and other optoelectronic properties, impacting on PV device performance. Previous work by Malerba et al [38] has identified a relationship between increasing Sn/Cu ratio and increasing bandgap. This is thought to be due to a defect induced reduction in the bandgap arising from an increase in the Sn related defects:  $V_{Sn}$ ,  $Cu_{Sn}$  and  $Zn_{Sn}$  antisites. In this work we have observed a similar relationship in some, but not all, samples. It is not possible to confirm a distinct relationship between CZTS composition and bandgap based on these samples. The study by Malerba et al [38] used films synthesised by sulphurisation of multilayer metal precursors, likely to have less disorder than these nanoparticle films. The energy bandgap will be related to composition and the extent of disorder. It is therefore necessary in such a complex system to have a compositional metric which allows direct comparison with other work, as well as being one where a known range of values results in higher device efficiency.

The principal compositional indicator used here to compare and identify the optimum CZTS composition for maximum PV device performance is the cation ratios. These were chosen because there is a significant amount of information in the literature on CZTS devices based on these ratios [33]. Many factors impact the bandgap of CZTS including stoichiometric composition, point defects, and Cu-Zn disorder as discussed in section 3.7. It is not possible to directly measure all these properties of CZTS within the scope of this work. EDS and optical spectroscopy provide important insights into many of these.

Another important indicator of disorder in CZTS is the presence of tail states into the bandgap as discussed in section 3.7. This can be quantified by estimating the Urbach energy, as described in section 3.7 using figure 3.7 and equation 3.5. However, the presence of secondary phases adds further complexity to the interpretation of UV-vis data as shown in figure 5.12. A comparison of figure 5.12 and figure 3.7 suggests that the Urbach energy  $E_U$  is in the range 30-60 meV. Work by Chantana et al [42] has identified that  $E_U$  values greater than 20 meV lead to a larger open circuit voltage deficit and lower device performance. Future strategies to enhance CZTS device

performance should include a consideration of how to reduce disorder by monitoring the Urbach energy to reduce it to less than 20 meV.

## 5.8. Tin content

In this part of the work, seven different samples were synthesised with different tin content during the fabrication of CZTS nanocrystal inks. The CZTS thin films were successfully formed via spin coating after the CZTS nanoparticles were prepared by the hot injection technique. Different tin contents were studied in the range 0.60-0.90 mmol during synthesis by means of characterisation methods XRD, Raman, SEM, EDS and UV-vis. This work is part of the road map to improve CZTS solar photovoltaic device performance by means of continuing the systematic study of the hot injection synthesis conditions, tin contents in this case. In this study the CZTS nanoparticles were prepared without any annealing treatment which is different from the study published by Ali et al [43].

## 5.9. Experimental methodology

### 5.9.1. The fabrication of CZTS nanoparticles

CZTS nanoparticles were prepared following the same procedure discussed in chapter 4 section 4.1.1 with Cu-poor, Zn-rich compositions in the as synthesised particles. However, several changes were applied as follows:

- The precursor molar ratios are shown in table 5.22.
- These ratios are variable for Sn and constant for Cu, Zn and S achieved by using reagents: 1.44 mmol (0.3769 g) of copper (II) acetylacetonate, 0.94 mmol (0.2478 g) of zinc (II) acetylacetonate, variable ratio of tin (IV) bis(acetylacetonate) dichloride and 4 mmol (0.1283 g) of S with 10 ml of OLA.
- The setting of the reaction temperatures is fixed as 250 °C.
- The time of the reaction is fixed at 30 minutes.

Sample	Sn Content (mmol)	Cu/(Zn+Sn)	Sn/Cu	Zn/Sn	S/(Cu+Zn+Sn)
Sn0	0.60	0.94	0.42	1.57	1.34
Sn1	0.65	0.91	0.45	1.45	1.32
Sn2	0.70	0.88	0.49	1.34	1.30
Sn3	0.75	0.85	0.52	1.25	1.28
Sn4	0.80	0.83	0.56	1.18	1.26
Sn5	0.85	0.80	0.59	1.11	1.24
Sn6	0.90	0.78	0.63	1.04	1.22

**Table 5.22:** The initial compositions used for the synthesis of CZTS nanoparticles.

### 5.9.2. Ink deposition

The CZTS nanoparticle inks were synthesised in the same method as explained in section 4.1.2 where 2-10 drops (of a volume of 40  $\mu$ l of ink) are dropped into the centre of the glass by micro pipette. The spin coating setting are: the rotation speed set as 2500 rpm for 15 seconds to achieve uniform thin films. Two different film thicknesses were used: 2 drops for thin 0.2  $\mu$ m films for SEM, EDS and UV-vis measurements, and 10 drops for thick 1.0  $\mu$ m films prepared for XRD and Raman measurements.

## 5.10. Results and discussion

### 5.10.1. Crystal structure – XRD

The XRD patterns of the prepared CZTS nanoparticles at different tin contents (0.60-0.90 mmol) are shown in figure 5.31.

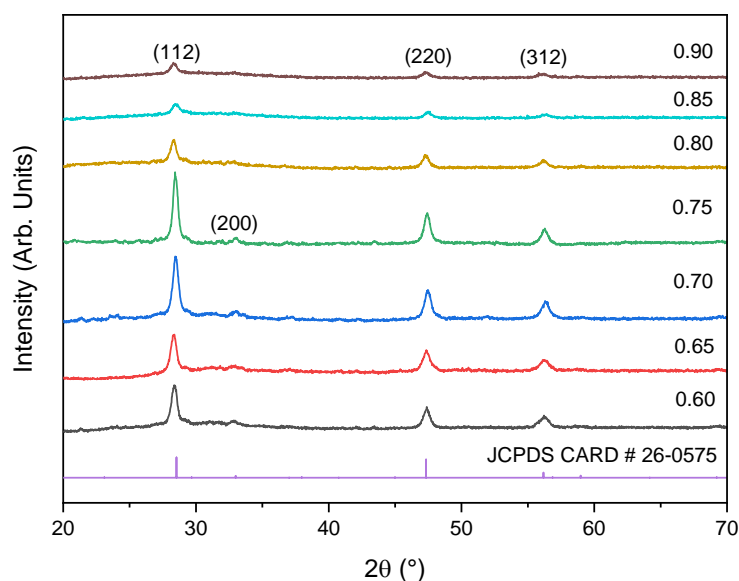


Figure 5.31 XRD for samples of CZTS with different tin contents (0.60-0.90 mmol), including the CZTS PDF reference (# 26-0575).

The major XRD diffraction peaks for samples Sn0-Sn3 (0.60-0.75 mmol Sn) appeared at locations in a good agreement with the kesterite phase shown in reference PDF card 026-0575 as in table 5.23. However, the structural crystal plane of (200) was absent in the other three samples (Sn4-Sn6) where the tin content was higher than 0.75 mmol.

Sample	$2\theta$ (°) for structure planes (112)
Sn0	28.44
Sn1	28.30
Sn2	28.51
Sn3	28.53
Sn4	28.31
Sn5	28.40
Sn6	28.17

**Table 5.23:** Values for  $2\theta$  of (112) crystal plane for CZTS samples with different tin content.

Table 5.24 below presents the values of  $d$ -spacing, size of scattering domain and lattice parameters  $a$  and  $c$ , using the methodology described in section 5.7.

Sample	<i>d</i> -spacing (nm)	<i>a</i> (nm)	<i>c</i> (nm)	Scattering domain (nm)
Sn0	0.3133	0.5428	1.0853	68 ± 2
Sn1	0.3146	0.5430	1.0988	51 ± 2
Sn2	0.3126	0.5416	1.0821	43 ± 5
Sn3	0.3128	0.5417	1.0844	34 ± 5
Sn4	0.3145	0.5443	1.0917	33 ± 5
Sn5	0.3140	0.5418	1.0967	25 ± 3
Sn6	0.3163	0.5442	1.1108	9 ± 7

**Table 5.24:** Values of *d*-spacing, size of scattering domain and lattice parameters *a* and *c* with different tin contents.

Tables 5.23 and 5.24 show similar *d*-spacing, *a* and *c* lattice constants and peak location values of (112) crystal plane to the literature paper for samples Sn2-Sn5 [44]. The scattering domain size shows a general trend of decreasing with the increase of the tin contents, except for sample Sn4, indicating a possible direct relationship between the tin content and the size of the scattering domain. Increasing Sn content reduces the size of crystallites in CZTS.

### 5.10.2. Raman spectroscopy

Raman main and strong peaks of CZTS are located at 334 cm<sup>-1</sup>, 341 cm<sup>-1</sup>, 338 cm<sup>-1</sup>, 337 cm<sup>-1</sup>, 342 cm<sup>-1</sup>, 343 cm<sup>-1</sup> and 340 cm<sup>-1</sup> for Sn0, Sn1, Sn2, Sn3, Sn4, Sn5 and Sn6 respectively as figure 5.32 demonstrates. These peak locations for Sn0, Sn2, and Sn3 are in good agreement with the literature [22] for the expected characteristic CZTS peak 332-339 cm<sup>-1</sup> [23-28]. A small peak appears at 472 cm<sup>-1</sup> for Sn2 which seem to be a secondary phase of CuS [29]. Also, a weak peak appears at 317 cm<sup>-1</sup> for Sn2 and Sn3 which may be secondary phase of Cu<sub>4</sub>SnS<sub>4</sub> [30]. It seems that there are no other expected major secondary phases appearing here like ZnS, SnS, Cu<sub>2</sub>S and Cu<sub>2</sub>SnS<sub>3</sub> [45].

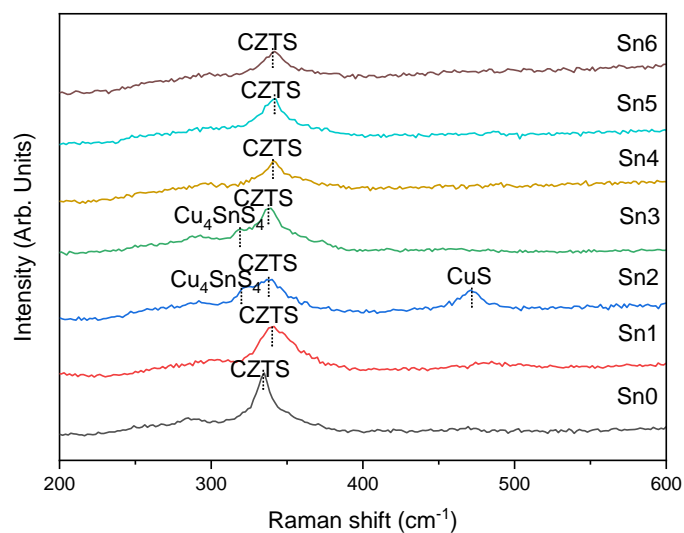


Figure 5.32 Raman spectra of CZTS samples with different tin contents 0.60-0.90 mmol.

### 5.10.3. Morphology

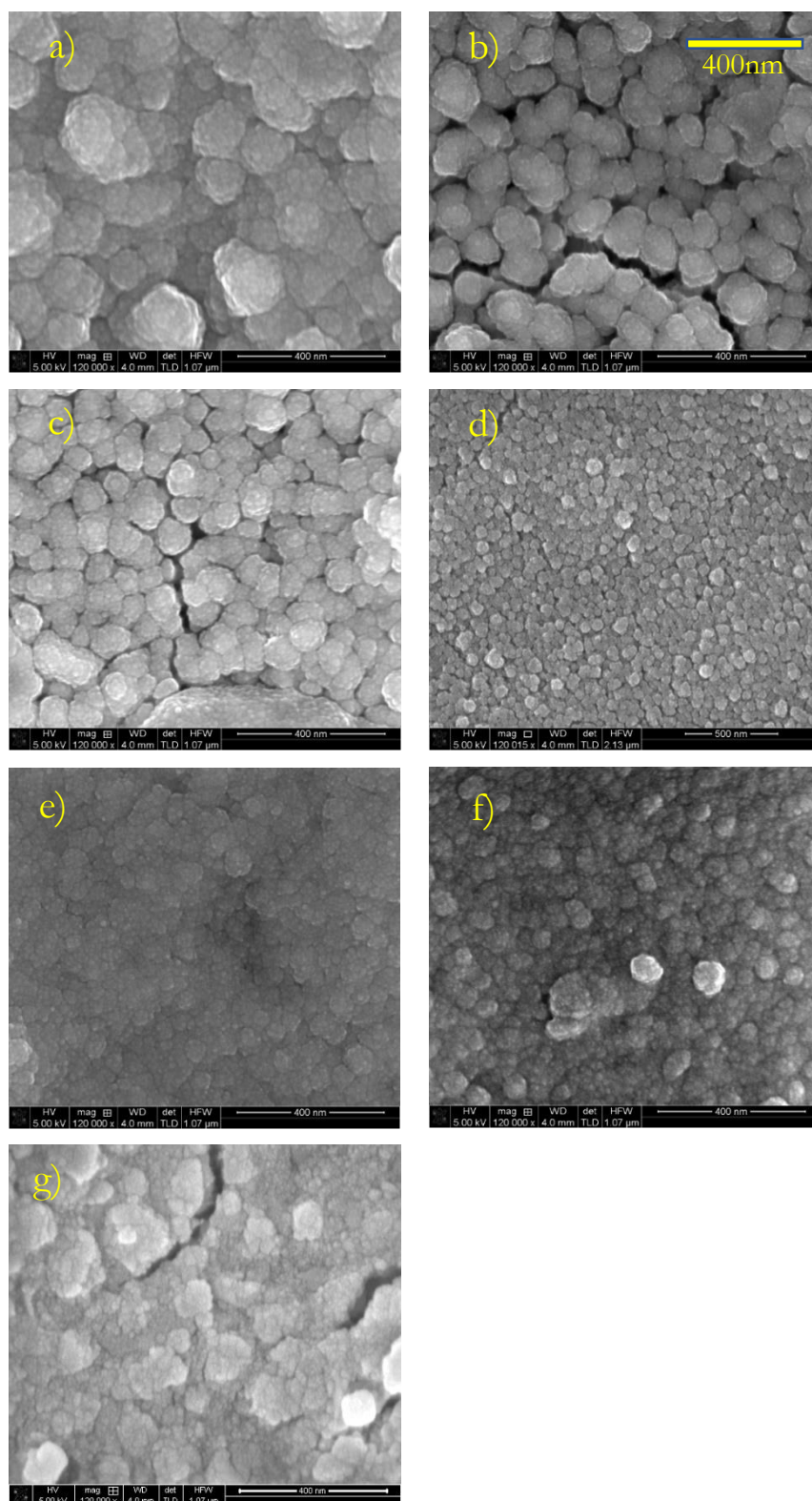


Figure. 5.33 SEM images at scale of 400 nm for CZTS nanoparticles with different tin contents as a) Sn0, b) Sn1, c) Sn2, d) Sn3, e) Sn4, f) Sn5 and g) Sn6.

From the SEM images in figure 5.33, the nanoparticles shape varied non uniformly for all samples except Sn3 where the uniformity is much better. The size of the particles determined using the process described in section 5.4.3 was found to agree with the data from XRD scattering domain size as the decrease is observed in the SEM images from around 62 nm for image a) to 7 nm for image g) in figure 5.33. The images in b, c and g have small gaps in some areas whereas the gaps almost disappear in the rest of the samples, important for ensuring continuous dense CZTS films required for efficient PV devices.

#### 5.10.4. Chemical composition

The elemental analysis of the CZTS synthesised samples at different tin contents was taken from the film's surface by EDS using the procedure described in section 5.4.4.

Sample	Cu/(Zn+Sn)	Sn/Cu	Zn/Sn	S/(Cu+Zn+Sn)
Sn0	$0.92 \pm 0.40$	$0.58 \pm 0.04$	$1.84 \pm 0.10$	$0.62 \pm 0.70$
Sn1	$0.88 \pm 0.30$	$0.56 \pm 0.05$	$1.20 \pm 0.10$	$1.08 \pm 0.30$
Sn2	$0.86 \pm 0.10$	$0.55 \pm 0.05$	$1.06 \pm 0.30$	$0.96 \pm 0.50$
Sn3	$0.83 \pm 0.40$	$0.54 \pm 0.03$	$1.09 \pm 0.30$	$1.12 \pm 0.20$
Sn4	$0.67 \pm 0.30$	$0.73 \pm 0.02$	$1.01 \pm 0.20$	$0.81 \pm 0.40$
Sn5	$0.56 \pm 0.20$	$1.02 \pm 0.03$	$2.20 \pm 0.10$	$1.19 \pm 0.30$
Sn6	$0.53 \pm 0.20$	$1.09 \pm 0.05$	$2.40 \pm 0.30$	$0.74 \pm 0.40$

**Table 5.25:** Composition ratios of CZTS nanoparticles with different tin content determined by EDS.

From table 5.25, Sn3 has the closest Cu-poor, Zn-rich ratio value to the desired ratio for highly efficient solar cell devices which was reported in another published paper [46]. It is also observed that the ratio Cu/(Zn+Sn) decreases with an increase of the ratio of Zn/Sn with increasing Sn content.



### 5.10.5. Optical properties

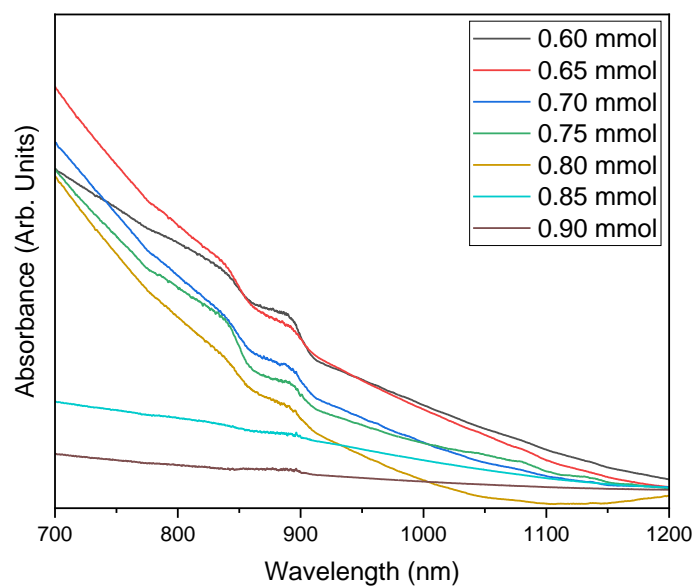


Figure 5.34 Absorbance spectrum of CZTS samples with different tin contents 0.60-0.90 mmol.

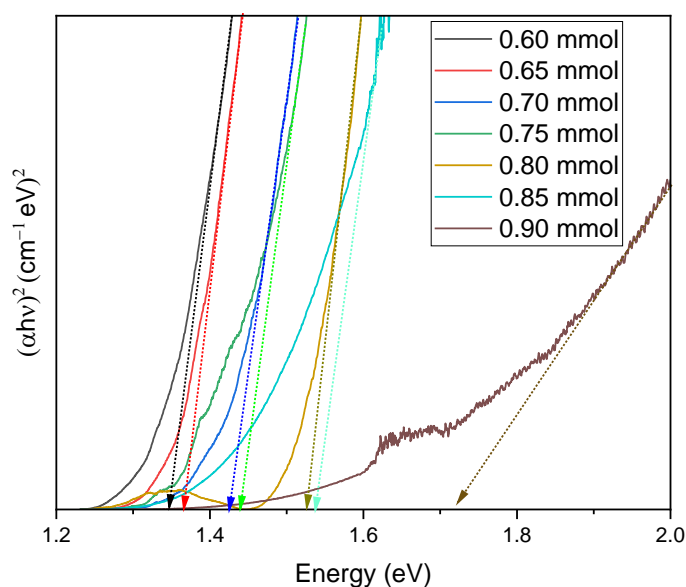


Figure 5.35 Tauc plot to show the bandgap of CZTS versus different tin contents 0.60-0.90 mmol.

The absorbance spectra were recorded in the range of 700-1200 nm as shown in figure 5.34. The corresponding Tauc plots to determine the CZTS bandgap are shown in figure 5.35.

Sample	$E_g$ (eV)
Sn0	$1.34 \pm 0.04$
Sn1	$1.37 \pm 0.03$
Sn2	$1.42 \pm 0.02$
Sn3	$1.44 \pm 0.02$
Sn4	$1.52 \pm 0.04$
Sn5	$1.53 \pm 0.02$
Sn6	$1.71 \pm 0.01$

**Table 5.26:** The different tin contents of CZTS versus the energy bandgap.

Table 5.26 shows that when the tin contents were increased, the energy bandgap of the as deposited CZTS film increases as well. The observed bandgap of samples from Sn2 to Sn5 ( $1.42 \pm 0.02$ ,  $1.44 \pm 0.02$ ,  $1.52 \pm 0.04$ , and  $1.53 \pm 0.02$  eV) respectively correspond well with the theoretical expected bandgap values of CZTS nanoparticles of between 1.40–1.60 eV [34–36].

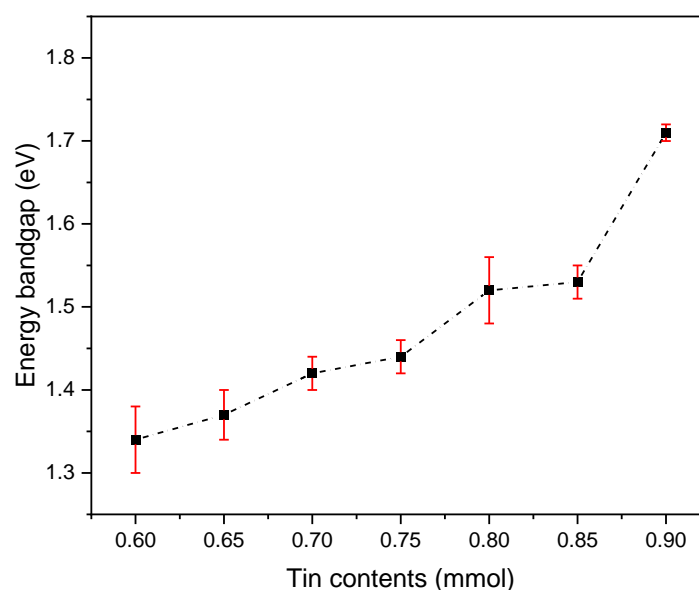


Figure. 5.36 The trend of the bandgap of as synthesised CZTS thin films with different tin contents.

Figure 5.35 shows different linear regions indicating the possible existence of secondary phases with energy bandgaps different from CZTS. Using the procedure described in section 5.4.5 and illustrated in figure 5.12, values of additional bandgaps linked to possible secondary phases can be extracted. The different energy bandgaps extracted using this method are given in table 5.27. The possible secondary phases related to these energy bandgaps are also listed.

Sample	Energy bandgaps from Tauc plot (eV)	Possible secondary phases related to bandgaps
Sn0	1.25, 1.30	Cu <sub>2</sub> S/Cu <sub>3</sub> SnS <sub>4</sub> /Cu <sub>4</sub> SnS <sub>4</sub> , SnS
Sn1	1.25, 1.30	Cu <sub>2</sub> S/Cu <sub>3</sub> SnS <sub>4</sub> /Cu <sub>4</sub> SnS <sub>4</sub> , SnS
Sn2	1.35	SnS
Sn3	1.38	?
Sn4	1.45	Cu <sub>2</sub> SnS <sub>3</sub>
Sn5	1.42	Cu <sub>2</sub> SnS <sub>3</sub>
Sn6	1.40, 1.52	Cu <sub>2</sub> SnS <sub>3</sub> , ?

**Table 5.27:** Possible secondary phases and their bandgaps with different tin contents.

As previously discussed, work by Malerba et al [38] has identified a relationship between increase Sn/Cu ratio and increasing energy bandgap. A comparison of tables 5.25 and 5.26 indicates that such a clear correlation is not established in these samples.

To conclude the results of varying the tin content of the synthesised CZTS nanoparticles, the Raman peak positions and table 5.24 show corresponding values to other literature papers especially with samples Sn2-Sn5. In addition, the SEM image for sample Sn3 has less gaps in the uniformity of nanoparticles compared to the other samples. The EDS values shows a good ratio for Cu-poor, Zn-rich composition where this value is close to the desired ratio for highly efficient solar cell devices. The bandgaps in table 5.26 show that the samples of Sn2-Sn5 are close values to the theoretical expected bandgap values of CZTS. From the characterisation results above, sample of Sn3 (Sn = 0.75 mmol) should be the most suitable tin content from these range studied 0.60-0.90 mmol for CZTS as the initial step for PV devices. Therefore, the reaction conditions: Sn = 0.75 mmol as the tin content will be used for the next investigation to continue the systematic study on deposition conditions discussed in the next chapter.

## 5.11. References

1. H. Wei, W. Guo, Y. Sun, Z. Yang, Y. Zhang, Hot injection Synthesis and Characterization of Quaternary  $\text{Cu}_2\text{ZnSnSe}_4$  Nanocrystals, *Mater. Lett.* 64 (2010) 1424-1426. <https://doi.org/10.1016/j.matlet.2010.03.034>.
2. S. R. Rondiya, Y. A. Jadhav, A. Zivkovic, S. B. Jathar, G. K. Rahane, R. W. Cross, A. V. Rokade, R. S. Devan, S. Kolekar, R. L. Hoye, H. N. Ghosh, Solution-processed Cd-substituted CZTS Nanocrystals for Sensitized Liquid Junction Solar Cells, *J. All. Com.* 890 (2022) 161575. <https://doi.org/10.1016/j.jallcom.2021.161575>.
3. B. R. Bade, S. R. Rondiya, Y. A. Jadhav, M. M. Kamble, S. V. Barma, S. B. Jathar, M. P. Nasane, S. R. Jadhkar, A. M. funde, N. Y. Dzade, Investigations of the Structural, Optoelectronic and Band Alignment Properties of  $\text{Cu}_2\text{ZnSnS}_4$  Prepared by Hot injection Method Towards Low Cost Photovoltaic Applications. *J. All. Com.* 854 (2021) 157093. <https://doi.org/10.1016/j.jallcom.2020.157093>.
4. S.C. Riha, B.A. Parkinson, A.L. Prieto, Solution-based Synthesis and Characterization of  $\text{Cu}_2\text{ZnSnS}_4$  Nanocrystals, *J. Am. Chem. Soc.* 131 (2009) 12054-12055. <https://doi.org/10.1021/ja9044168>.
5. C. Steinhagen, M.G. Panthani, V. Akhavan, B. Goodfellow, B. Koo, B.A. Korgel, Synthesis of  $\text{Cu}_2\text{ZnSnS}_4$  Nanocrystals for Use in Low-cost Photovoltaics, *J. Am. Chem. Soc.* 131 (2009) 12554-12555. <https://doi.org/10.1021/ja905922j>.
6. Q. Guo, G. M. Ford, W. C. Yang, B. C. Walker, E.A. Stach, H. W. Hillhouse, R. Agrawal, Fabrication of 7.2% Efficient CZTSSe Solar Cells Using CZTS Nanocrystals, *J. Am. Chem. Soc.* 132 (2010) 17384-17386. <https://doi.org/10.1021/ja108427b>.
7. K. D. Zhang, Z. R. Tian, J. B. Wang, B. Li, X. L. Zhong, D. Y. Guo, S. M. He, Preparation of  $\text{Cu}_2\text{ZnSnS}_4$  Thin Films Using Spin coating Method with Thermolysis and Annealing, *J. Sol-Gel. Sci. Technol.* 73 (2015) 452-459. <https://doi.org/10.1007/s10971-014-3561-8>.
8. L. Majula, N. R. Mlyuka, M. E. Samiji, R. S. Bryce, D. Y. Kim, S. H. Kim, H. J. Lee, H. J. Choi, Spin coating Kesterite CZTS Thin Films for Photovoltaic Applications, *J. Korean. Phys. Soc.* 67 (2015) 1078-1081. <https://doi.org/10.3938/jkps.67.1078>.
9. Y. Qu, G. Zoppi, R. W. Miles, N. B. Beattie, Influence of Reaction Conditions on the Properties of Solution-processed  $\text{Cu}_2\text{ZnSnS}_4$  Nanocrystals, *Mater. Res. Express.* 1 (2014) 045040. <https://doi.org/10.1088/2053-1591/1/4/045040>.

10. Y. Altowairqi, A. Alsubaie, K. P. Stroh, I. G. Perez-Marin, L. Bowen, M. Szablewski, D. P. Halliday, The Effect of Annealing Conditions: Temperature, Time, Ramping Rate and Atmosphere on Nanocrystal  $\text{Cu}_2\text{ZnSnS}_4$  (CZTS) Thin Film Solar Cell Properties, *Mater. Today: Proceedings*. 18 (2019) 473-486. <https://doi.org/10.1016/j.matpr.2019.06.234>.
11. M. Wei, Q. Du, D. Wang, W. Liu, G. Jiang, C. Zhu, Synthesis of Spindle-like Kesterite  $\text{Cu}_2\text{ZnSnS}_4$  Nanoparticles Using Thiorea as Sulfur Source, *Mater. Lett.* 79 (2012) 177-179. <https://doi.org/10.1016/j.matlet.2012.03.080>.
12. P. A. Fernandes, P. M P. Salome, A. F. de Cunha, Study of Polycrystalline  $\text{Cu}_2\text{ZnSnS}_4$  Films by Ramamn Scattering, *J. All. Com.* 509 (2011) 7600-7606. <https://doi.org/10.1016/j.jallcom.2011.04.097>.
13. M. Li, W. Zhou, J. Guo, Y. Zhou, Z. Hou, J. Jiao, Z. Zhou, Z. Du, S. Wu, Synthesis of Pure Metastable Wurtzite CZTS Nanocrystals by Facile One-Pot Method, *J. Phys. Chem. C*. 116 (2012) 26507-26516. <https://doi.org/10.1021/jp307346k>.
14. S. Mustapha, M. M. Ndamitso, A. S. Abdulkareem, J. O. Tijani, D. T. Shuaib, A. K. Mohammed, A. Sumaila, Comparative Study of Crystallite Size Using Williamson-Hall and debye-Scherrer Plots for ZnO Nanoparticles, *Adv. Nat. Sci: Nanosci. Nanotechnol.* 10 (2019) 045013. <https://doi.org/10.1088/2043-6254/ab52f7>.
15. A. S. Vorokh, Scherrer Formula: Estimation of Error in Determining Small Nanoparticle Size, *Nanosystems: Phys. Chem. Mathematics*. 9 (2018) 364-369. <https://doi.org/10.17586/2220-8054-2018-9-3-364-369>.
16. X. Lin, J. Kavalakkatt, K. Kornhuber, S. Levchenko, M. Lux-Steiner, A. Ennaoui, Structural and Optical Properties of  $\text{Cu}_2\text{ZnSnS}_4$  Thin Film Absorbers from ZnS and  $\text{Cu}_3\text{SnS}_4$  Nanoparticle Precursors, *Thin. Solid. Films*. 535 (2013) 10-13. <https://doi.org/10.1016/j.tsf.2012.10.034>.
17. X. Lu, Z. Zhuang, Q. Peng, Y. Li, Wurtzite  $\text{Cu}_2\text{ZnSnS}_4$  Nanocrystals: A Novel Quaternary Semiconductor, *Chem. Commun.* 47 (2011) 3141-3143. <https://doi.org/10.1039/c0cc05064d>.
18. X. Wang, Z. Sun, C. shao, D. M. Boye, J. Zhao, A Facile and General Approach to Polynary Semiconductor Nanocrystals Via a Modified Two-phase Method, *Nanotechnol.* 22 (2011) 245605. <https://doi.org/10.1088/0957-4484/22/24/245605>.
19. C. Zou, L. Zhang, D. Lin, Y. Yang, Q. Li, X. Xu, X. Chen, S. Huang, Facile Synthesis of  $\text{Cu}_2\text{ZnSnS}_4$  Nanocrystals, *Cryst. Eng. Comm.* 13 (2011) 3310-3313. <https://doi.org/10.1039/C0CE00631A>.
20. U. V. Ghorpade, M. P. Suryawanshi, S. W. Shin, C. W. Hong, I. Kim, J. H. Moon, J. H. Yun, J. H. Kim, S. S. Kolekar, Wurtzite CZTS Nanocrystals and Phase Evolution to Kesterite Thin Film

for Solar Energy Harvesting, *Phys. Chem. Chem. Phys.* 17 (2015) 19777-19788. <https://doi.org/10.1039/C5CP02007G>.

21. M. Suryawanshi, S. W. Shin, U. Ghorpade, D. Song, C. W. Hong, S. Han, J. Heo, S. H. Kang, J. H. Kim, A Facile and Green Synthesis of Colloidal  $\text{Cu}_2\text{ZnSnS}_4$  Nanocrystals and their Application in Highly efficient Solar Water Splitting, *J. Mater. Chem. A* 5 (2017) 4695-4709. <https://doi.org/10.1039/C7TA00257B>.

22. G. S. Babu, Y. B. K. Kumar, P. U. Bhaskar, V. S. Raja, Effect of Post-deposition Annealing on the growth of  $\text{Cu}_2\text{ZnSnSe}_4$  Thin Films for a Solar Cell Absorber Layer, *Semicond. Sci. Technol.* 23 (2008) 085023. <https://doi.org/10.1088/0268-1242/23/8/085023>.

23. J.M.R. Tan, Y.H. Lee, S. Pedireddy, T. Baikie, X.Y. Ling, L.H. Wong, Understanding the Synthetic Pathway of a Single-phase Quarternary Semiconductor Using Surface-enhanced Raman Scattering: A Case of Wurtzite  $\text{Cu}_2\text{ZnSnS}_4$  Nanoparticles, *J. Am. Chem. Soc.* 136 (2014) 6684-6692. <https://doi.org/10.1021/ja501786s>.

24. J. Xu, X. Yang, Q.D. Yang, T.L. Wong, C.S. Lee,  $\text{Cu}_2\text{ZnSnS}_4$  Hierarchical Microspheres as an Effective Counter Electrode Material for Quantum Dot Sensitized Solar Cells. *J. Phys. Chem C* 116 (2012) 19718-19723. <https://doi.org/10.1021/jp306628m>.

25. A. Carrete, A. Shavel, X. Fontané, J. Montserrat, J. Fan, M. Ibáñez, E. Saucedo, A. Pérez-Rodríguez, A. Cabot, Antimony-based Ligand Exchange to Promote Crystallization in Spray-deposited  $\text{Cu}_2\text{ZnSnSe}_4$  Solar Cells, *J. Am. Chem. Soc.* 135 (2013) 15982-15985. <https://doi.org/10.1021/ja4068639>.

26. Y.L. Zhou, W.H. Zhou, M. Li, Y.F. Du, S.X. Wu, Hierarchical  $\text{Cu}_2\text{ZnSnS}_4$  Particles for A Low-cost Solar Cell: Morphology Control and Growth Mechanism, *J. Phys. Chem. C* 115 (2011) 19632-19639. <https://doi.org/10.1021/jp206728b>.

27. Y. Zou, X. Su, J. Jiang, Phase-controlled Synthesis of  $\text{Cu}_2\text{ZnSnS}_4$  Nanocrystals: The Role of Reactivity Between Zn and S, *J. Am. Chem. Soc.* 135 (2013) 18377-18384. <https://doi.org/10.1021/ja405962k>.

28. S. Suehiro, K. Horita, K. Kumamoto, M. Yuasa, T. Tanaka, K. Fujita, K. Shimanoe, T. Kida, Solution-processed  $\text{Cu}_2\text{ZnSnS}_4$  Nanocrystal Solar Cells: Efficient Stripping of Surface Insulating Layers Using Alkylating Agents, *J. Phys. Chem. C* 118 (2013) 804-810. <https://doi.org/10.1021/jp408360j>.

29. S. H. Chaki, J. P. Tailor, M. P. Deshpande, Covellite CuS–Single Crystal Growth by Chemical Vapour Transport (CVT) Technique and Characterization, *Mater. Sci. Semicond. processing* 27 (2014) 577-585. <https://doi.org/10.1016/j.mssp.2014.07.038>.

- 
30. C. G. Munce, G. K. Parker, S. A. Holt, G. A. Hope, A Raman Spectroelectrochemical Investigation of Chemical Bath Deposited  $\text{Cu}_x\text{S}$  Thin Films and their Modification, *Colloids and Surfaces A: Physicochemical. Eng. Aspects.* 295 (2007) 152-158. <https://doi.org/10.1016/j.colsurfa.2006.08.045>.
31. T. He, N. Lin, Z. Du, Y. Chao, J. Cui, The Role of Excess Sn in  $\text{Cu}_4\text{Sn}_7\text{S}_{16}$  for Modification of The Band Structure and A Reduction in Lattice Thermal Conductivity, *J. Mater. Chem. C* 5 (2017) 4206-4213. <https://doi.org/10.1039/c7tc00420f>.
32. K. Stroh,  $\text{Cu}_2\text{ZnSnS}_4$  Nanocrystal Ink Absorber Layers for Thin Film Solar Cells, MSc Thesis. Durham. Uni. (2019).
33. V. V. Satale, S. V. Bhat, Superstrate Type CZTS Solar Cell with All Solution Processed Functional Layers at Low Temperature, *Sol. Energy.* 208 (2020) 220-226. <https://doi.org/10.1016/j.solener.2020.07.055>.
34. P. Makula, M. Pacia, and W. Macyk, How to Correctly Determine the Bandgap Energy of Modified Semiconductor Photocatalysts Based on UV–Vis Spectra, *J. Phys. Chem. Lett.* 9 (2018) 6814-6817. <https://doi.org/10.1021/acs.jpcclett.8b02892>.
35. C. S. Raj, S Sebastian, S. Rajendran, A Review on Spray Pyrolysis Deposited CZTS Thin Films for Solar Cell Applications, *J. Univ. Shanghai. Sci. Technol.* 23 (2021) 1196-1206.
36. M. A. Olgar, Enhancement in Photovoltaic Performance of CZTS Thin Film Solar Cells Through Varying Stacking Order and Sulfurization Time, *J. Mater. Sci: Mater. Electron.* 33, (2022) 20121-20133. <https://doi.org/10.1007/s10854-022-08829-y>.
37. S. Thiruvankadam, S. Prabhakaran, S. Chakravarty, V. Ganesan, V. Sathe, M. S. Kumar, A. L. Rajesh, Effect of Zn/Sn Molar Ratio on the Microstructural and Optical Properties of  $\text{Cu}_2\text{Zn}_{1-x}\text{Sn}_x\text{S}_4$  Thin Films Prepared by Spray Pyrolysis Technique, *Physica. B: Condens. Matter.* 533, (2018) 22-27. <https://doi.org/10.1016/j.physb.2017.12.065>.
38. C. Malerba, F. Biccari, C. Ricardo, M. Valentini, R. Chierchia, M. Muller, A. Santoni, E. Esposito, P. Mangiapane, P. Scardi, A. Mittiga, CZTS Stoichiometry Effects on the Bandgap Energy, *J. Alloys. Comp.* 582 (2014) 528-534. <https://doi.org/10.1016/j.jallcom.2013.07.199>.
39. R. A. Wibowo, E. S. Lee, B. Munir, K. H. Kim, Pulsed Laser Deposition of Quaternary  $\text{Cu}_2\text{ZnSnSe}_4$  Thin Films, *Physica. Status. Solidi (a).* 204 (2007) 3373-3379. <https://doi.org/10.1002/pssa.200723144>.
40. G. Zoppi, I. Forbes, R. W. Miles, P. J. Dale, J. J. Scragg, L. M. Peter,  $\text{Cu}_2\text{ZnSnSe}_4$  Thin Film Solar Cells Produced by Selenisation of Magnetron Sputtered Precursors, *Prog. Photovolt: Res. Appl.* 17 (2009) 315-319. <https://doi.org/10.1002/pip.886>.

- 
41. G. S. Babu, Y. B. K. Kumar, P. U. Bhaskar, V. S. Raja, Growth and Characterization of Co-evaporated  $\text{Cu}_2\text{ZnSnSe}_4$  Thin Films for Photovoltaic Applications, *J. Phys. D: Appl. Phys.* 41 (2008) 205305. <https://doi.org/10.1088/0022-3727/41/20/205305>.
  42. J. Chantana, Y. Kawano, T. Nishimura, A. Mavlonov, T. Minemoto, Impact of Urbach Energy on Open-circuit Voltage Deficit of Thin-film Solar Cells, *Sol. Energy. Mater. Sol. Cell.* 210 (2020) 110502. <https://doi.org/10.1016/j.solmat.2020.110502>.
  43. A. Ali, J. Jacob, A. Ashfaq, K. Mahmood, S. Ahmad, U. Rehman, W. Ahmad, N. Amin, S. Ikram, S. Hussain, N. Ali, Effect of Tin Concentration on the Structural, Optical and Thermoelectric Properties of CZTS Thin Films Grown by Chemical Solution Method, *Ceram. Int.* 45 (2019) 22513-22516. <https://doi.org/10.1016/j.ceramint.2019.07.276>.
  44. A. B. Hirpara, S. H. Chaki, R. M. Kannaujiya, A. J. Khimani, Z. R. Parekh, Y. H. Vaidya, R. K. Giri, M. P. Deshpande, Biological Investigation of Sonochemically Synthesized CZTS Nanoparticles, *Appl. Surf. Sci. Adv.* 12 (2022) 100338. <https://doi.org/10.1016/j.apsadv.2022.100338>.
  45. E. Indubala, S. Sarveshvaran, V. Sudha, A.Y. Mamajiwal, S. Harinipriya, Secondary Phases and Temperature Effect on the Synthesis and Sulfurization of CZTS, *Sol. Energy.* 173 (2018) 215-224. <https://doi.org/10.1016/j.solener.2018.07.085>.
  46. W. Wang, M. T. Winkler, O. Gunawan, T. Gokmen, T. K. Todorov, Y. Zhu, D. B. Mitzi, Device Characteristics of CZTSSe Thin-film Solar Cells with 12.6% Efficiency, *Adv. Energy. Mater.* 4 (2014) 1301465. <https://doi.org/10.1002/aenm.201301465>.



# **Chapter 6:**

## **Investigations of spin coating deposition conditions**

### **6.1. Introduction**

In this chapter, another effective factor, the deposition conditions, in the systematic study of the structural and optical properties of the CZTS nanocrystals is reported in which several variables of the deposition conditions during the deposition of the nanocrystal inks are examined. The deposition method is done by the spin coating technique. This study will show the impact of different spin coating speeds and different spin coating acceleration indices on the properties of CZTS nanocrystal thin films. This study will be done without any post-synthesis annealing treatment to limit any further fabrication steps for the full CZTS solar cell device until optimum conditions of the deposited CZTS nanocrystal inks are studied and identified.

### **6.2. Spin coating speeds**

Eight different samples were created with different spin coating speeds during the deposition of the CZTS nanocrystal inks. The hot injection method was used for the fabrication of these samples followed by the spin coating technique for the deposition of CZTS nanocrystal inks onto glass substrate. Different spin coating speeds were examined, ranging between (1300-9700 rpm).

## 6.3. Experimental methodology

### 6.3.1. The fabrication of CZTS nanoparticles

CZTS nanoparticles were fabricated by the same procedure explained in chapter 5 section 5.9.1 with Cu-poor, Zn-rich compositions in the as synthesised particles. However, several modifications to the reaction conditions were made in this chapter. These use the conditions identified as optimal for the synthesis of CZTS inks and are:

- 0.75 mmol (0.2909 g) of tin (IV) bis(acetylacetonate) used.
- Reaction temperatures fixed as 250 °C for all samples.
- The time of the reaction fixed for all samples (30 minutes).

### 6.3.2. Ink deposition

The CZTS nanoparticle inks are spin coated on SLG substrates using the same methodology as described in chapter 4, section 4.1.2. However, different spin coating speeds were used: 1300, 2500, 3700, 4900, 6100, 7300, 8500 and 9700 rpm.

The spin coating in this chapter was performed for a fixed time (15 seconds) with CZTS ink dropped at 6 seconds using the dynamic dispense spin coating technique, as discussed in section 3.1.1.

## 6.4. Results and discussion

### 6.4.1. Crystal structure - XRD

XRD was used for structural measurements to determine the crystal structure of CZTS nanoparticle thin films, lattice constants and the size of the scattering domain. The XRD patterns of the fabricated CZTS nanoparticles at different spin coating speeds 1300-9700 rpm are shown in figure 6.1.

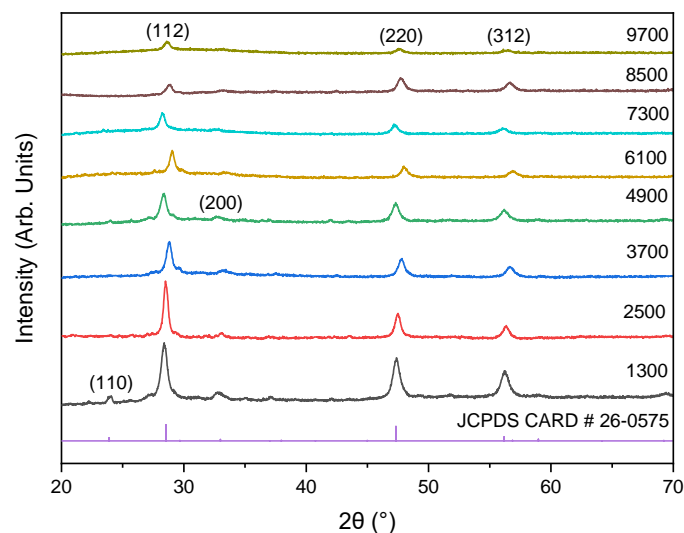


Figure 6.1 XRD for samples of CZTS with different spin coating speeds (1300-9700 rpm), including the CZTS PDF reference (# 26-0575).

The XRD data confirmed the formation of CZTS nanocrystal thin films for all samples as the three main diffraction peaks (112), (220) and (312) appeared at locations matching well with the kesterite phase shown in reference PDF card 026-0575. However, the structure plane of (200) disappeared in samples with high spin coating speeds ranging between 6100-9700 rpm. It is noted in the figure 6.1 above, that the diffraction peak of (110) appeared in the lower spin coating speeds of 1300 rpm which also correspond to JCPDS card number 26-0575. The XRD peak intensities reduced as the spin coating speed increased as shown in figure 6.1, which might be due films being thinner for higher spin speeds and so less diffraction of incident X-rays. This provides evidence of the higher spin speeds leading to reduced film thickness.

Spin coating speed (rpm)	2 $\theta$ (°) for structure planes (112)	$d$ -spacing (nm)	$a$ (nm)	$c$ (nm)
1300	28.35	0.3138	0.5429	1.090
2500	28.48	0.3128	0.5410	1.087
3700	28.80	0.3099	0.5388	1.065
4900	28.21	0.3150	0.5443	1.097
6100	29.03	0.3078	0.5364	1.054
7300	28.08	0.3166	0.5428	1.120
8500	28.75	0.3107	0.5394	1.072
9700	28.62	0.3124	0.5410	1.082

**Table 6.1:** Values of  $d$ -spacing and lattice parameters  $a$  and  $c$  with different spin coating speeds.

The values of  $d$ -spacing,  $a$  and  $c$  lattice numbers in table 6.1 above show similar values of (112) crystal plane to the literature paper for the slower spin coating speeds of between 1300-4900 rpm [1].

Table 6.2 below presents the values of the size of scattering domain. It is noted in the table 6.2 that there was a clear trend of the decreasing scattering domain with the increase of the spin coating speeds from thicker films to thinner. This is due to increasing centrifugal forces at high spin speeds forcing larger particles off the substrate during spinning leading to a general thickness reduction as also seen above in figure 6.1. This should be noted when considering the need for larger particles for device layers to reduce grain boundary recombination losses.

Spin coating speeds (rpm)	Scattering domain (nm)
1300	$17 \pm 2$
2500	$16 \pm 3$
3700	$14 \pm 2$
4900	$12 \pm 3$
6100	$10 \pm 4$
7300	$9 \pm 3$
8500	$8 \pm 2$
9700	$7 \pm 3$

**Table 6.2:** Values of the size of scattering domain with regards to different spin coating speeds.

#### 6.4.2. Raman spectroscopy

Raman spectroscopy was used to identify the presence of secondary phases [2]. Figure 6.2 of Raman spectroscopy measurements also confirms the crystal structure of the nanoparticles. Raman main and strong peaks of CZTS are located at  $340 \text{ cm}^{-1}$ ,  $338 \text{ cm}^{-1}$ ,  $339 \text{ cm}^{-1}$ ,  $337 \text{ cm}^{-1}$ ,  $334 \text{ cm}^{-1}$ ,  $338 \text{ cm}^{-1}$ ,  $343 \text{ cm}^{-1}$ , and  $341 \text{ cm}^{-1}$  for 1300, 2500, 3700, 4900, 6100, 7300, 8500 and 9700 rpm respectively as shown in figure 6.2. below. The Raman peak's location of samples 2500-4900 rpm is in good agreement with the literature [3] for the expected characteristic CZTS peak ( $332\text{-}339 \text{ cm}^{-1}$ ).

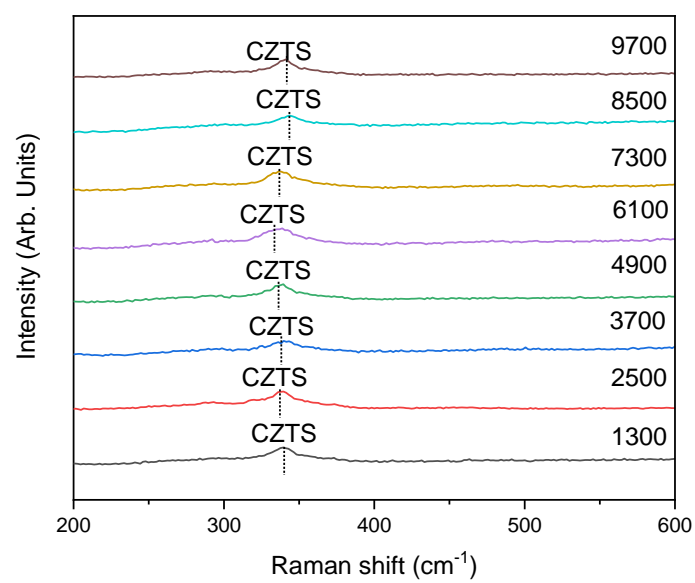


Figure 6.2 Raman spectra of CZTS samples with different spin coating speeds.

### 6.4.3. Morphology

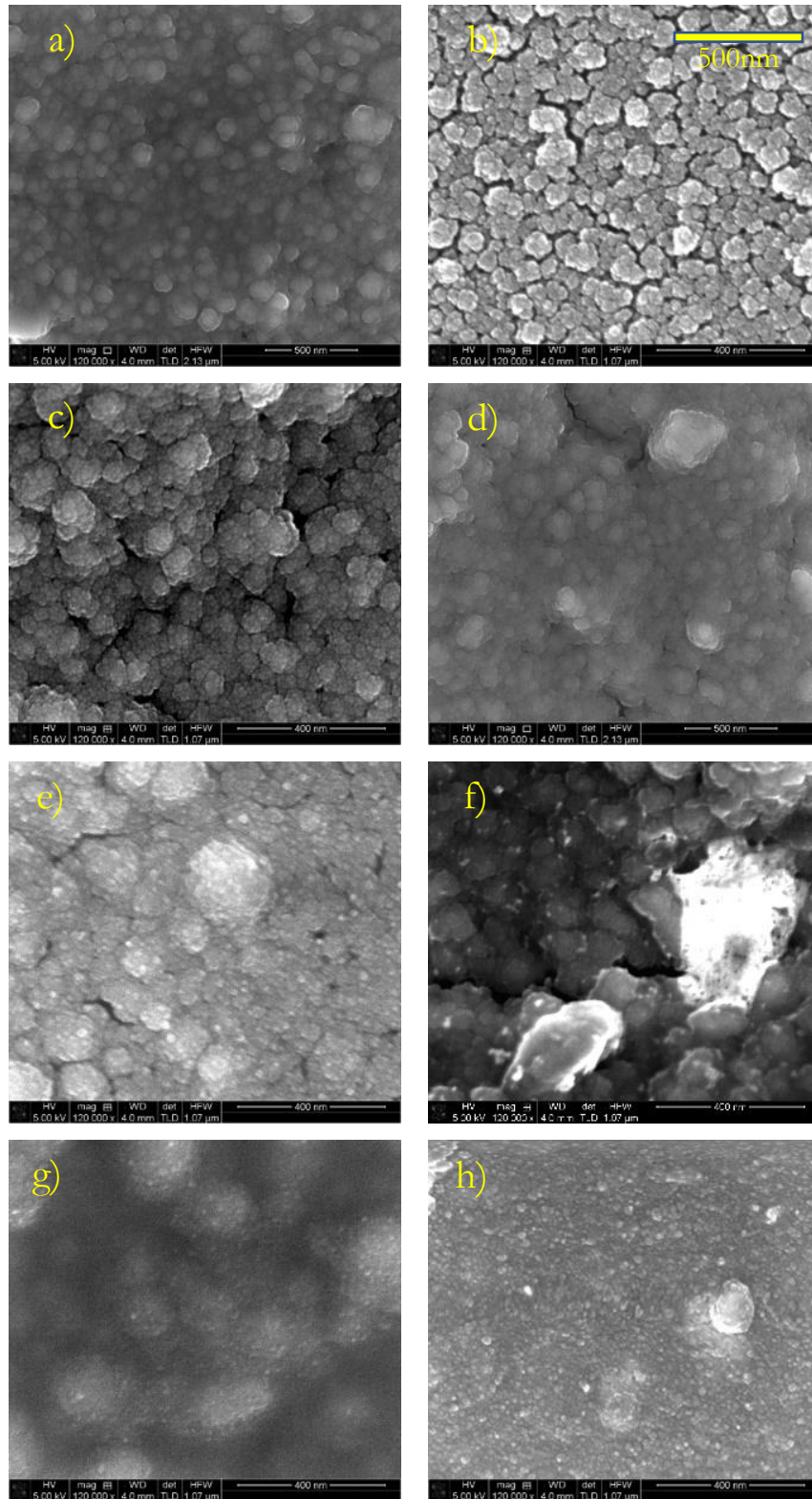


Figure. 6.3 SEM images at scale of between 400 to 500 nm for CZTS nanoparticles with different spin coating speeds as a) 1300 rpm b) 2500 rpm c) 3700 rpm d) 4900 rpm e) 6100 rpm f) 7300 rpm g) 8500 rpm and h) 9700 rpm.

In figure 6.3, it is noted that as the spin coating speed increases, the nanoparticles become more sporadic and combined on top of each other in comparison with the low speed. The uniformity of the nanoparticles looks better in the images of the low speed (1300-4900 rpm). The shape of the nanoparticles was approximately spherical for all samples.

#### 6.4.4. Chemical composition

The results of the EDS are summarised in the table 6.3 below. The EDS was taken from the film's surface using the procedure described in section 5.4.4.

Spin coating speeds (rpm)	Cu/(Zn+Sn)	Sn/Cu	Zn/Sn	S/(Cu+Zn+Sn)
1300	$0.74 \pm 0.20$	$0.85 \pm 0.04$	$0.96 \pm 0.30$	$1.17 \pm 0.20$
2500	$0.82 \pm 0.40$	$0.80 \pm 0.05$	$1.07 \pm 0.01$	$1.12 \pm 0.01$
3700	$0.71 \pm 0.10$	$0.76 \pm 0.01$	$0.87 \pm 0.40$	$1.08 \pm 0.40$
4900	$0.69 \pm 0.20$	$0.72 \pm 0.03$	$0.93 \pm 0.30$	$1.04 \pm 0.01$
6100	$0.62 \pm 0.30$	$0.64 \pm 0.05$	$2.08 \pm 0.40$	$0.67 \pm 0.20$
7300	$0.82 \pm 0.30$	$0.53 \pm 0.02$	$1.15 \pm 0.20$	$0.96 \pm 0.20$
8500	$0.80 \pm 0.20$	$0.50 \pm 0.03$	$1.50 \pm 0.10$	$0.85 \pm 0.30$
9700	$0.72 \pm 0.40$	$0.46 \pm 0.05$	$2.41 \pm 0.20$	$0.23 \pm 0.20$

**Table 6.3:** Composition ratios of CZTS nanoparticles with different spin coating speeds.

From table 6.3, the 2500 rpm sample has the closest Cu-poor, Zn-rich ratio value to the desired ratio for the highly efficient solar cell device (12.6%) compared to the rest of the spin coating speeds. The ratio of S/(Cu+Zn+Sn) showed the trend of decreasing value with the increase of spin coating speeds except with 7300 rpm sample which increased and then again followed the trend with 8500 rpm. As the higher spin coating speed increases the centrifugal force, the larger nanoparticles leave the sample with smaller nanoparticle being remained in the films. Evidence of a correlation between particle size and composition is seen. This is considered further in section 6.7.4.

### 6.4.5. Optical properties

A series of fabricated CZTS films from inks at different spin coating speeds (1300-9700 rpm) was created to investigate electronic properties without annealing. The energy bandgap of the thin film is determined by UV-vis spectroscopy from the absorption spectrum using the Tauc plot method.

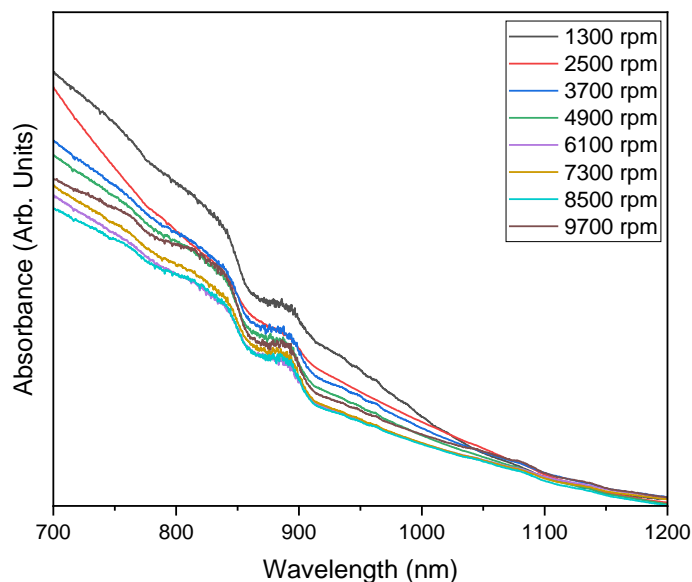


Figure 6.4 Absorbance spectrum of CZTS samples with different spin coating speeds.

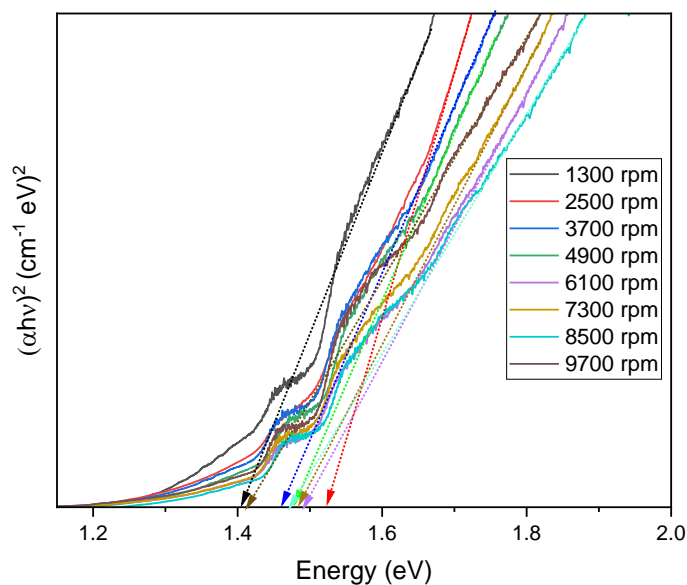


Figure 6.5 Tauc plot to show the bandgap of CZTS versus different spin coating speeds.



The absorbance spectra were recorded in the range of 700-1200 nm as shown in figure 6.4. The energy bandgap was determined by the Tauc plot method.

Spin coating speeds (rpm)	$E_g$ (eV)
1300	$1.40 \pm 0.03$
2500	$1.52 \pm 0.02$
3700	$1.46 \pm 0.02$
4900	$1.47 \pm 0.01$
6100	$1.49 \pm 0.03$
7300	$1.48 \pm 0.02$
8500	$1.47 \pm 0.01$
9700	$1.41 \pm 0.03$

**Table 6.4:** The different spin coating speeds of CZTS versus the energy bandgap.

Table 6.4 shows that the observed bandgap of all samples corresponds well with that reported in the literature of (1.40–1.60 eV) [4-6]. It is noted that there is no obvious trend here as the bandgap slightly fluctuated with the increase of the spin coating speed which might indicate that the spin coating speed play's minor role in affecting the optical properties of CZTS. The bandgap varied from  $1.40 \pm 0.03$  to  $1.52 \pm 0.02$  eV depending on the spin coating speed as stated in table 6.4 above.

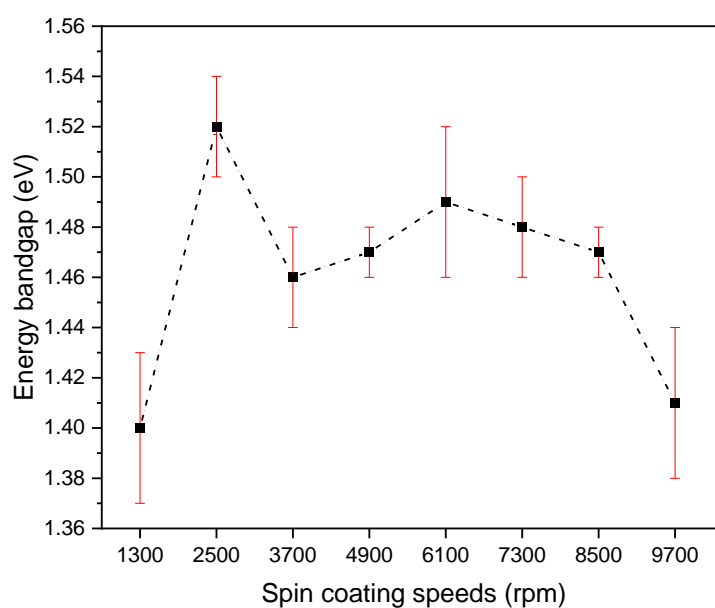


Figure. 6.6 The trend of the bandgap of as synthesised CZTS thin films with different spin coating speeds.

Figure 6.5 shows different linear regions indicating the possible existence of secondary phases with energy bandgaps different from CZTS. Using the procedure described in section 5.4.5 and illustrated in figure 5.12, values of additional bandgaps linked to possible secondary phases can be extracted. The different energy bandgaps extracted using this method are given in table 6.5. The possible secondary phases related to these energy bandgaps are also listed.

Spin coating speeds (rpm)	Energy bandgaps from Tauc plot (eV)	Possible secondary phases related to bandgaps
1300	1.25, 1.50	Cu <sub>2</sub> S/Cu <sub>3</sub> SnS <sub>4</sub> /Cu <sub>4</sub> SnS <sub>4</sub> , ?
2500	1.25, 1.50	Cu <sub>2</sub> S/Cu <sub>3</sub> SnS <sub>4</sub> /Cu <sub>4</sub> SnS <sub>4</sub> , ?
3700	1.25, 1.50	Cu <sub>2</sub> S/Cu <sub>3</sub> SnS <sub>4</sub> /Cu <sub>4</sub> SnS <sub>4</sub> , ?
4900	1.25, 1.50	Cu <sub>2</sub> S/Cu <sub>3</sub> SnS <sub>4</sub> /Cu <sub>4</sub> SnS <sub>4</sub> , ?
6100	1.25, 1.50	Cu <sub>2</sub> S/Cu <sub>3</sub> SnS <sub>4</sub> /Cu <sub>4</sub> SnS <sub>4</sub> , ?
7300	1.25, 1.50	Cu <sub>2</sub> S/Cu <sub>3</sub> SnS <sub>4</sub> /Cu <sub>4</sub> SnS <sub>4</sub> , ?
8500	1.25, 1.50	Cu <sub>2</sub> S/Cu <sub>3</sub> SnS <sub>4</sub> /Cu <sub>4</sub> SnS <sub>4</sub> , ?
9700	1.25, 1.50	Cu <sub>2</sub> S/Cu <sub>3</sub> SnS <sub>4</sub> /Cu <sub>4</sub> SnS <sub>4</sub> , ?

**Table 6.5:** Possible secondary phases and their bandgaps with different spin coating speeds.

The XRD and Raman data showed corresponding values to other literature papers especially with samples of 1300-4900 rpm. The EDS values showed a desired ratio for Cu-poor, Zn-rich in sample 2500 rpm for highly efficient solar cell device. The bandgap, in table 6.4 shows that all samples are in the range of accepted values of the expected theoretical bandgap values of CZTS. However, the small change in the bandgap is a sign of the less significant role playing of spin coating speed on the optical properties of CZTS. The sample of 2500 rpm was considered to be continued used for the next section as it is the most suitable spin coating speeds among other samples due to the composition, crystal structure and size of the scattering domain.

## 6.5. Spin coating acceleration index

The aim of this section work is to study the impact of the spin coating acceleration index on CZTS nanocrystals thin film properties. The acceleration index value is the rate of increase of the spin coating speed per second, and its calculated value constant for each index. For example, the lowest acceleration index 001 is equivalent to a value of 80 rpm s<sup>-2</sup>, meaning it needs 31.25 seconds to

reach to the set spin coating speed of 2500 rpm in this study. The other acceleration indices are equivalent to 400, 800, 1200, 1600, 2000 and 2400 rpm s<sup>-2</sup> for 005, 010, 015, 020, 025 and 030 respectively. The initial acceleration is likely to have an impact on the spin coated thin film as during the initial stage of spinning the film will be spreading out whilst the solvent is evaporating. In this work 15 seconds for the spin coating was determined as enough time to coat the substrate by Laurell technology spin coating instrument. Seven different samples in this section were created with different spin coating acceleration indices during the deposition of the CZTS nanocrystal inks. The hot injection method was used for the fabrication of these samples followed by the spin coating technique for the deposition of CZTS nanocrystal inks onto glass substrates. The range of different spin coating acceleration indices was examined, ranging between 001-030 index.

## **6.6. Experimental methodology**

### **6.6.1. The fabrication of CZTS nanoparticles**

CZTS nanoparticles were fabricated by the same procedure explained in the previous section with Cu-poor, Zn-rich compositions in the as synthesised particles. There were no changes to the reaction conditions in this section.

### **6.6.2. Ink deposition**

The CZTS nanoparticle inks are spin coated on SLG substrates using the same methodology as described in chapter 4 section 4.1.2. However, 2500 rpm as the spin coating speed was used for 15 seconds. The different spin coating acceleration indices were examined: 001, 005, 010, 015, 020, 025 and 030 indices.

## 6.7. Results and discussion

### 6.7.1. Crystal structure - XRD

XRD was used for structural measurements to determine the crystal structure of CZTS nanoparticle thin films, lattice constants and the size of the scattering domain. The XRD patterns of the fabricated CZTS nanoparticles at different spin coating acceleration indices 001-030 are shown in figure 6.7.

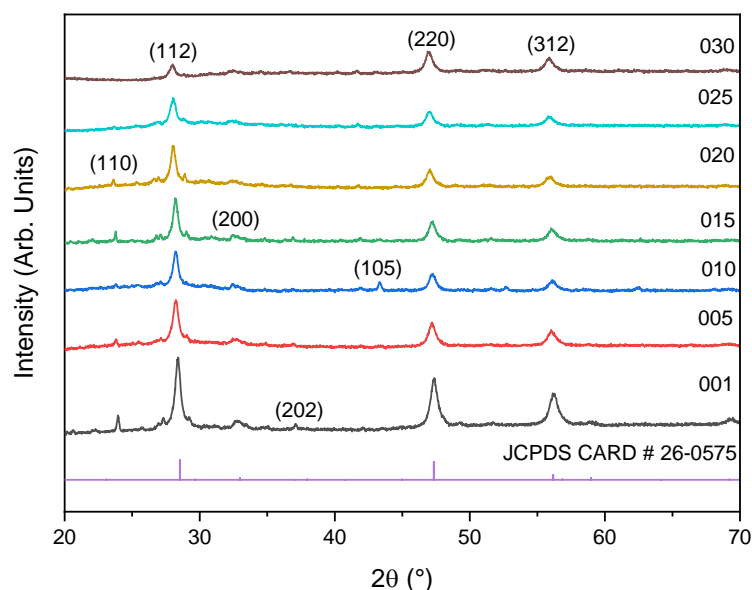


Figure 6.7 XRD for samples of CZTS with different spin coating acceleration indices 001-030, including the CZTS PDF reference (# 26-0575).

The XRD data confirmed the formation of CZTS nanocrystal thin films for all samples as the three main diffraction peaks (112), (220) and (312) appeared at locations matching well with the kesterite phase shown in reference PDF card 026-0575. However, the structure plane of (200) appeared in samples with low spin coating acceleration indices ranging between 001-015. Moreover, (110) diffraction peak appeared in the sample of 001-020 which also correspond to JCPDS card number 26-0575. (110) and (200) diffraction peaks disappeared in the high acceleration indices 0.25-030 and 0.20-0.30 respectively. It is noted that (105) diffraction peak appeared for index 010 only. The XRD peak intensities reduced similarly to figure 6.1 as shown in figure 6.7 with the increase of spin coating acceleration indices impacting the film thickness as it did in the spin coating speeds. The faster the spin coating and acceleration indices, the thinner films can be created.

Spin coating acceleration index	$2\theta$ (°) for structure planes (112)	$d$ -spacing (nm)	$a$ (nm)	$c$ (nm)
001	28.32	0.3139	0.5430	1.091
005	28.18	0.3148	0.5440	1.096
010	28.22	0.3151	0.5447	1.092
015	28.05	0.3166	0.5441	1.114
020	27.91	0.3189	0.5451	1.135
025	28.12	0.3160	0.5457	1.101
030	27.85	0.3190	0.5461	1.131

**Table 6.6:** Values of  $d$ -spacing and lattice parameters  $a$  and  $c$  with different spin coating acceleration indices.

The values of  $d$ -spacing,  $a$  and  $c$  lattice numbers in table 6.6 above show similar values of (112) crystal plane to the literature paper for the lower spin coating acceleration indices of between 001-015 [7].

Table 6.7 below presents the values of the size of scattering domain. It is noted in the table 6.7 that there was a clear trend of the decreasing scattering domain size with the increase of the spin coating acceleration indices. This is similar to the trend observed with increasing spin coating speed and reflects the impact of increased centrifugal forces on the ink particles during the initial deposition stages.

Spin coating acceleration index	Scattering domain (nm)
001	$22 \pm 2$
005	$20 \pm 4$
010	$16 \pm 2$
015	$14 \pm 3$
020	$13 \pm 1$
025	$12 \pm 1$
030	$11 \pm 1$

**Table 6.7:** Values of the size of scattering domain with regards to different spin coating acceleration indices.

### 6.7.2. Raman spectroscopy

Raman spectroscopy measurements confirms the crystal structure of the nanoparticles. Raman main and strong peaks of CZTS are located at  $338\text{ cm}^{-1}$  for 001,  $339\text{ cm}^{-1}$  for 005,  $337\text{ cm}^{-1}$  for 010,  $340\text{ cm}^{-1}$  for 015,  $342\text{ cm}^{-1}$  for 020,  $341\text{ cm}^{-1}$  for 025 and  $334\text{ cm}^{-1}$  for 030. Other than the possible secondary phase of SnS at  $288\text{ cm}^{-1}$  for the sample of 030, figure 6.8 shows no other Raman peaks due to secondary phases detected. As discussed in section 5.7.3 for the  $225\text{ }^{\circ}\text{C}$  samples, a very broad band in the range  $270\text{--}280\text{ cm}^{-1}$  appears here also for all samples. It was not possible to identify the origin of this feature.

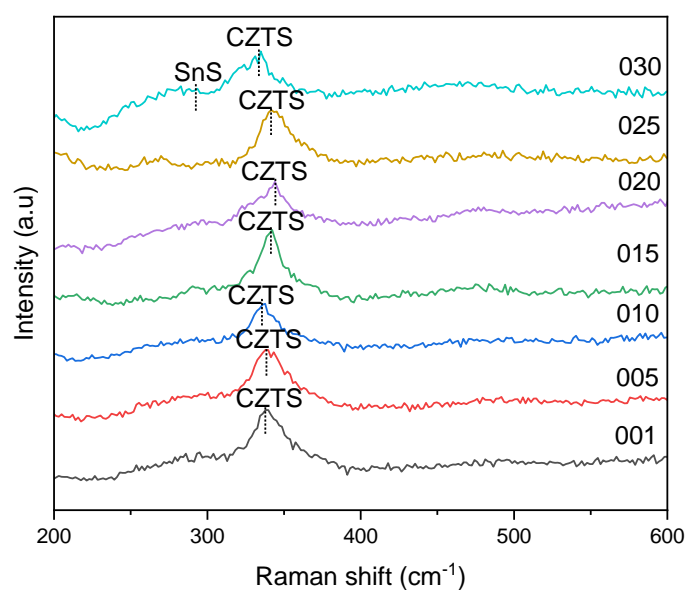


Figure 6.8 Raman spectra of CZTS samples with different spin coating acceleration index.

### 6.7.3. Morphology

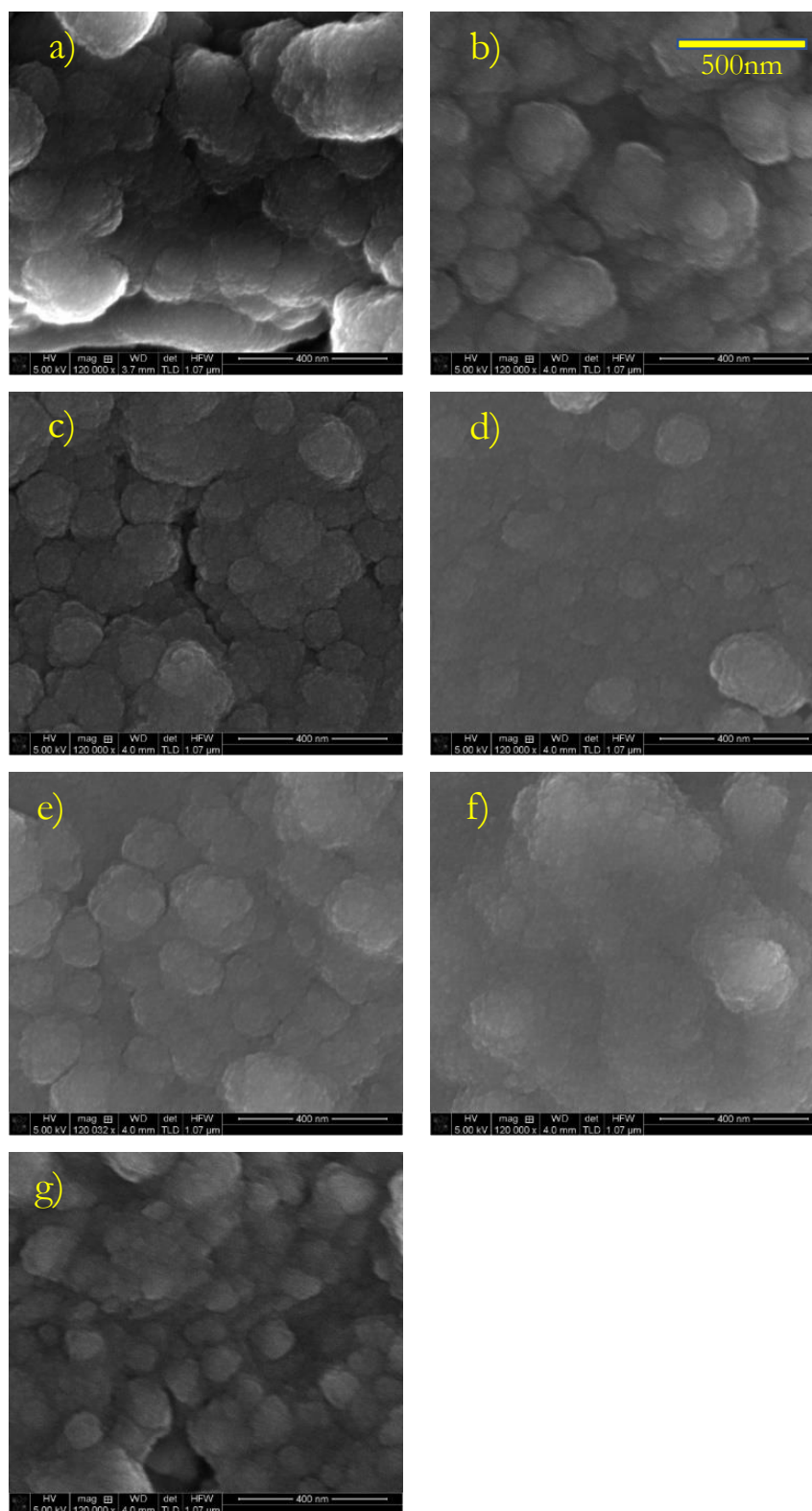


Figure. 6.9 SEM images at scale of 400 nm for CZTS nanoparticles with different spin coating acceleration indices as a) 001 b) 005 c) 010 d) 015 e) 020 f) 025 and g) 030.

In figure 6.9, the nanoparticles combined on top of each other creating layers of nonuniformed nanoparticles except in 015 acceleration index where the grouping of nanoparticles were less. It can also be seen that, at low acceleration indices the films contain larger agglomerations of nanoparticles. The shape of the nanoparticles was approximately spherical for all samples. The size of the particles decreased here from 26 to 14 nm with the increase of spin coating acceleration index which is in good agreement with XRD data shown in table 6.6.

#### 6.7.4. Chemical composition

The results of the EDS are summarised in the table 6.8 below. The EDS was taken from the film's surface using the procedure described in section 5.4.4.

Spin coating acceleration index	Cu/(Zn+Sn)	Sn/Cu	Zn/Sn	S/(Cu+Zn+Sn)
001	$0.76 \pm 0.20$	$0.86 \pm 0.02$	$0.67 \pm 0.40$	$1.27 \pm 0.10$
005	$0.61 \pm 0.10$	$0.85 \pm 0.01$	$0.93 \pm 0.30$	$1.21 \pm 0.20$
010	$0.78 \pm 0.30$	$0.84 \pm 0.03$	$1.02 \pm 0.10$	$1.12 \pm 0.10$
015	$0.81 \pm 0.40$	$0.83 \pm 0.01$	$1.07 \pm 0.40$	$1.27 \pm 0.30$
020	$0.80 \pm 0.10$	$0.74 \pm 0.04$	$1.13 \pm 0.40$	$1.22 \pm 0.10$
025	$0.75 \pm 0.30$	$0.67 \pm 0.01$	$1.75 \pm 0.30$	$1.04 \pm 0.30$
030	$0.24 \pm 0.30$	$0.61 \pm 0.05$	$2.15 \pm 0.10$	$0.50 \pm 0.40$

**Table 6.8:** Composition ratios of CZTS nanoparticles with different spin coating acceleration indices.

EDS data suggests that to get the closest Cu-poor, Zn-rich ratio value for the desired ratio for efficient solar cell device around 12%, a balanced of acceleration indices of between 010-020 should be applied. The data above shows a general trend of increasing Zn and decreasing S concentration with increasing acceleration index.

#### 6.7.5. Optical properties

A series of fabricated CZTS films from inks at different spin coating acceleration indices 001-030 was created to investigate electronic properties without annealing. The energy bandgap of the thin film is determined by UV-vis spectroscopy from the absorption spectrum using the Tauc plot method.



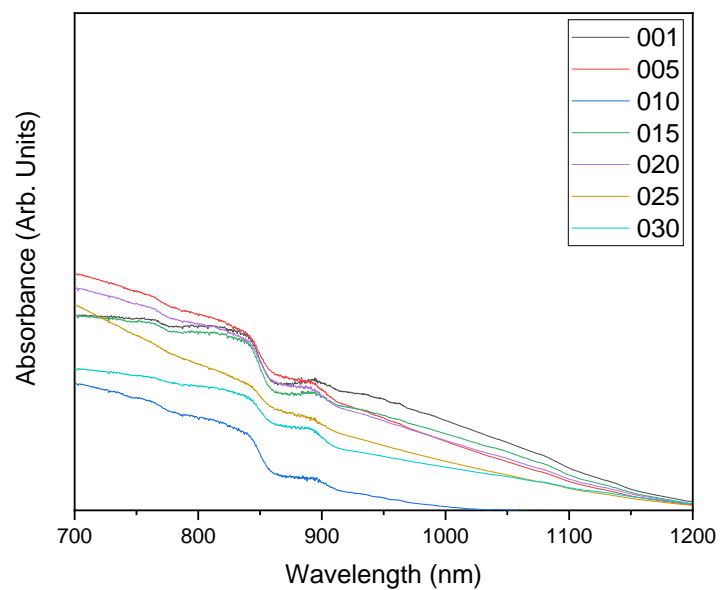


Figure 6.10 Absorbance spectrum of CZTS samples with different spin coating acceleration indices.

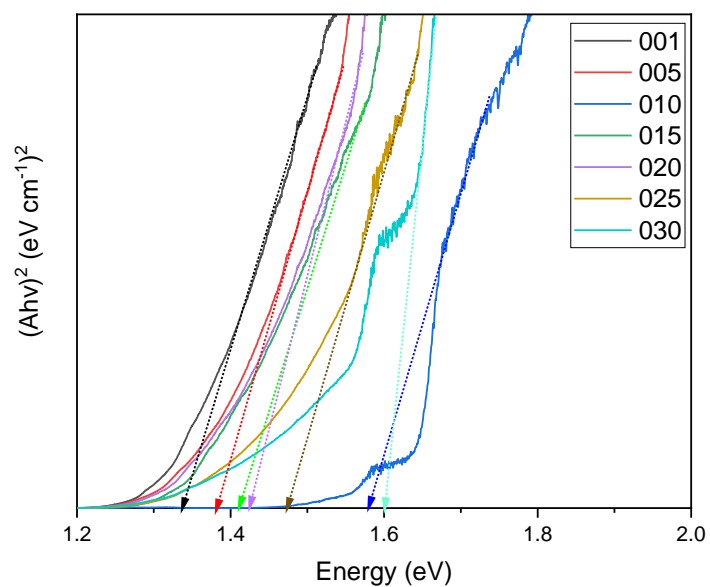


Figure 6.11 Tauc plot to show the bandgap of CZTS versus different spin coating acceleration indices.

The absorbance spectra were recorded in the range of 700-1200 nm in figure 6.10. The energy bandgap was determined by the Tauc plot.

Spin coating acceleration index	$E_g$ (eV)
001	$1.34 \pm 0.02$
005	$1.38 \pm 0.03$
010	$1.57 \pm 0.04$
015	$1.41 \pm 0.03$
020	$1.43 \pm 0.02$
025	$1.47 \pm 0.03$
030	$1.60 \pm 0.04$

**Table 6.9:** The different spin coating speeds of CZTS versus the energy bandgap.

The observed bandgap in table 6.9 of samples 010-030 corresponds well with the theoretical expected bandgap values of CZTS of between 1.40–1.60 eV [8]. The general trend, when increasing the acceleration index is for the bandgap to increase from  $1.34 \pm 0.02$ – $1.60 \pm 0.04$  eV. However, the bandgap for the 010 sample appears to be anomalous and is out of line with overall trend. This could be due to some unexpected properties of this film. Unfortunately, it was not possible to repeat this measurement.

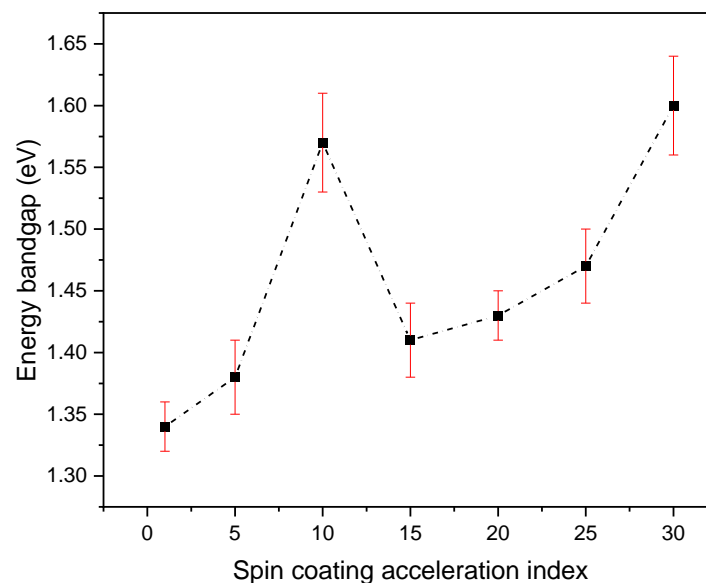


Figure. 6.12 The trend of the bandgap of as synthesised CZTS thin films with different acceleration indices.

Figure 6.11 shows different linear regions indicating the possible existence of secondary phases with energy bandgaps different from CZTS. Using the procedure described in section 5.4.5 and illustrated in figure 5.12, values of additional bandgaps linked to possible secondary phases can be

extracted. The different energy bandgaps extracted using this method are given in table 6.10. The possible secondary phases related to these energy bandgaps are also listed.

Spin coating acceleration index	Energy bandgaps from Tauc plot (eV)	Possible secondary phases related to bandgaps
001	1.30, 1.50	SnS, ?
005	1.30, 1.50	SnS, ?
010	1.30, 1.50	SnS, ?
015	1.30, 1.50	SnS, ?
020	1.35, 1.50	SnS, ?
025	1.35, 1.53	SnS, ?
030	1.50, 1.62	?, ?

**Table 6.10:** Possible secondary phases and their bandgaps with different acceleration indices.

XRD and Raman data confirmed the formation of the CZTS. In addition, the SEM image for 015 seems to produce the most uniform nanoparticles in comparison with the other samples. The EDS values shows an excellent ratio for Cu-poor, Zn-rich in sample 010, 015 and 020. Table 6.9 data for 010-030 indicates that the bandgap was in good agreement with the expected theoretical value. From the characterisation results, 015 index of acceleration spin coating might be the most suitable upon other indices.

The acceleration index has been shown to have a more significant impact on the properties of spin coated CZTS thin films compared to the spin coating speed. This is because the acceleration index has most impact at the start of the deposition process when the ink droplet is spreading out due to centrifugal acceleration and the solvent is evaporating to produce a stable film. It also controls the rotation speed of the substrate when the ink droplet hits the rotating substrate, as described in section 6.3.2. We find that increasing acceleration index results in decreasing scattering domain size, increasing Zn concentration, and decreasing S concentration. Assuming these are correlated, it demonstrates that the energy bandgap can be modified by the smaller particle size, and the change in composition of Zn and S. It implies a correlation between particle size and composition due to the different atomic diffusion coefficients during hot injection synthesis. This correlation provides another mechanism to control the chemical composition of CZTS films during the deposition process.

## 6.8. References

1. S. Engberg, J. Symonowicz, J. Schou, S. Canulescu, K. M. Jensen, Characterization of  $\text{Cu}_2\text{ZnSnS}_4$  Particles Obtained by the Hot Injection Method, *ACS. Omega.* 5 (2020) 10501-10509. <https://doi.org/10.1021/acsomega.0c00657>.
2. Y. Havryliuk, V. Dzhan, A. Karnaukhov, O. Selyshchev, J. Hann, D. R. Zahn, Raman Spectroscopy and Thermoelectric Characterization of Composite Thin Films of  $\text{Cu}_2\text{ZnSnS}_4$  Nanocrystals Embedded in a Conductive Polymer PEDOT:PSS, *Nanomaterials.* 13 (2022) 41. <https://doi.org/10.3390/nano13010041>.
3. O. Selyshchev, Y. Havryliuk, M. Valakh, V. O. Yurkymchuk, O. Raievska, O. L. Stroyuk, V. Dzhan, D. R. Zahn, Raman and X-ray Photoemission Identification of Colloidal Metal Sulfides as Potential Secondary Phases in Nanocrystalline  $\text{Cu}_2\text{ZnSnS}_4$  Photovoltaic Absorbers, *ACS. Appl. Nano. Mater.* 3 (2020) 5706-5717. <https://doi.org/10.1021/acsanm.0c00910>.
4. E. C. Prima, L. H. Wong, A. Ibrahim, B. Yulianto, Solution-processed Pure  $\text{Cu}_2\text{ZnSnS}_4/\text{CdS}$  Thin Film Solar Cell with 7.5% Efficiency. *Optical. Mater.* 114 (2021) 110947. <https://doi.org/10.1016/j.optmat.2021.110947>.
5. T. Özdal, H. Kavak, Single Step Amperometric Growth of CZTS Thin Film: Deposition Current and Stoichiometry Relationship. *Ceram. Int.* 47 (2021) 24841-24851. <https://doi.org/10.1016/j.ceramint.2021.05.210>.
6. M. A. Olgar, A. Altuntepe, S. Erkan, R. Zan, Fabrication of Cu-rich CZTS Thin Films by Two-stage Process: Effect of Gas Flow-rate in Sulfurization Process, *J. Mol. Struct.* 1230 (2021) 129922. <https://doi.org/10.1016/j.molstruc.2021.129922>.
7. P. Semalti, V. Sharma, M. Devi, P. Prathap, N. K. Upadhyay, S. N. Sharma, Surface Engineering of Colloidal Quaternary Chalcogenide  $\text{Cu}_2\text{ZnSnS}_4$  Nanocrystals: A Potential Low-cost Photocatalyst for Water Remediation, *Environ. Sci. Pollution. Res.* 30 (2023) 79774-79788. <https://doi.org/10.1007/s11356-023-26603-3>.
8. P. Semalti, J. Saroha, J. S. Tawale, S. N. Sharma, Visible-light Driven Noble Metal (Au, Ag) Permeated Multicomponent  $\text{Cu}_2\text{ZnSnS}_4$  Nanocrystals: A Potential Low-cost Photocatalyst for Textile Effluents and Heavy Metal removal, *Environ. Res.* 217 (2023) 114875. <https://doi.org/10.1016/j.envres.2022.114875>.

# **Chapter 7:**

## **Investigation of annealing temperatures and times**

### **7.1. Introduction**

In this chapter, the annealing treatment conditions of the CZTS nanocrystal thin films were studied. These conditions were the post deposition annealing temperatures and times. The purpose of this chapter was to follow up the fabrication steps reported in chapters 5 and 6 with the annealing treatment step to find out the optimum annealing conditions of the CZTS nanocrystal inks by studying the structural and optical properties of the annealed CZTS nanocrystals.

### **7.2. Annealing temperatures**

Six different samples were created, one before annealing and the other five with different annealing temperatures after the CZTS nanocrystal thin films were created. The hot injection method was used for the fabrication of these samples followed by the spin coating technique for the deposition of CZTS nanocrystal inks onto glass substrate. Different annealing temperatures were examined ranging between 560-635 °C in a H<sub>2</sub>S:N<sub>2</sub> 20:80 atmosphere, with one sample annealed with N<sub>2</sub> only atmosphere.

## 7.3. Experimental methodology

### 7.3.1. The fabrication of CZTS nanoparticles

CZTS nanoparticles were fabricated by the same procedure explained in chapter 6 section 6.3.1 with Cu-poor, Zn-rich compositions for the as synthesised particles. There were no modifications to the reaction conditions made in this chapter.

### 7.3.2. Ink deposition

The CZTS nanoparticle inks are spin coated on SLG substrates using the same methodology as described in chapter 6 section 6.6.2. 2500 rpm was used for the spin coating speed, 15 seconds for the time and 015 acceleration index.

### 7.3.3. Annealing treatment

The prepared CZTS thin films on substrates undergo sulphurisation annealing at a suitable atmosphere  $N_2:H_2S$  80:20 to improve the crystallinity. The two ends of the furnace tube caps were connected to different valves: a vacuum pump, exhaust line, nitrogen and  $H_2S$  supplies. The annealing process was applied under the conditions of set temperatures at 560 °C, 585 °C, 610 °C, 635 °C in  $N_2:H_2S$ , and 585 °C with  $N_2$  only atmosphere for one hour at ramping rate of 10 °C per minute. After that the furnace was left to cool naturally overnight. When cooled to room temperature, the furnace tube finally was flushed for several times with nitrogen gas and vented.

## 7.4. Results and discussion

### 7.4.1. Crystal structure - XRD

XRD was used for structural measurements to determine the crystal structure of CZTS nanoparticle thin films, lattice constants and the size of the scattering domain. The XRD patterns of the fabricated CZTS nanoparticles at before annealing and different annealing temperatures 560 °C, 585 °C, 610 °C, 635 °C and 585 °C with N<sub>2</sub> only atmosphere is shown in figure 7.1.

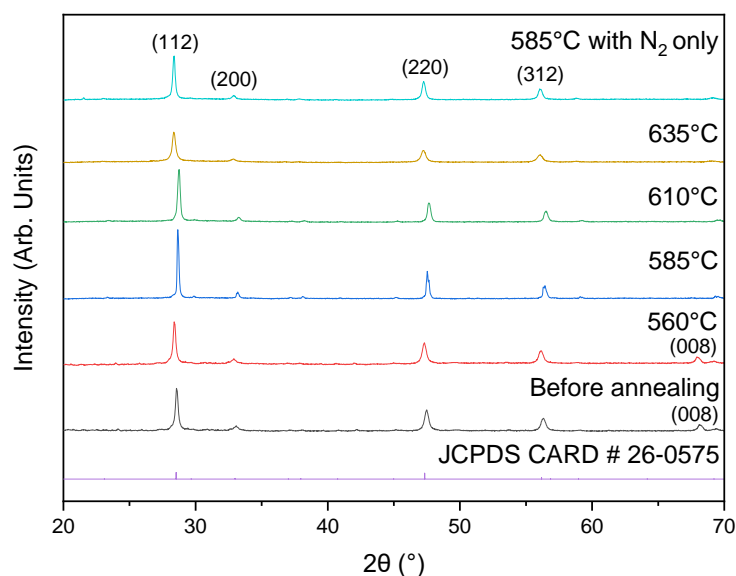


Figure 7.1 XRD for samples of CZTS with different annealing temperatures, including the CZTS PDF reference (# 26-0575).

The XRD data confirmed the formation of CZTS thin films for all annealed and before annealing samples as the four main diffraction peaks (112), (200), (220) and (312) appeared in the locations corresponding to JCPDS card number 026-0575. In addition, the (008) peak is observed in the samples before annealing and annealing at 560°C which also correspond to JCPDS card number 26-0575.

Annealing temperature (°C)	2 $\theta$ (°) for structure planes (112)	$d$ -spacing (nm)	$a$ (nm)	$c$ (nm)
Before annealing	28.47	0.3133	0.5417	1.0895
560	28.34	0.3143	0.5435	1.0929
585	28.66	0.3115	0.5409	1.0738
610	28.74	0.3106	0.5399	1.0690
635	28.35	0.3139	0.5440	1.0868
585 with N <sub>2</sub> only	28.34	0.3147	0.5441	1.0944

**Table 7.1:** Values of  $d$ -spacing and lattice parameters  $a$  and  $c$  with different annealing temperatures.

The  $d$ -spacing,  $a$  and  $c$  values of the 585 °C show similar values with the literature [1]. The possible secondary phases peaks such as SnS<sub>2</sub> at 33.02° (JCPDS card 83-1707), SnS at 45.80° (JCPDS card 83-1758) and Cu<sub>3</sub>SnS<sub>4</sub> at 37.27°, 39.81°, 51.80° (JCPDS card 36-0217) were not observed in figure 7.1 [2, 3].

Table 7.2 below presents the values of the size of scattering domain. The size of scattering domain showed a clear trend which increases with the rise of annealing temperatures except when the H<sub>2</sub>S was absent at 585 °C with a low value of  $14 \pm 2$  nm.

Annealing temperature (°C)	Scattering domain (nm)
Before annealing	$16 \pm 2$
560	$29 \pm 3$
585	$32 \pm 3$
610	$43 \pm 5$
635	$13 \pm 7$
585 with N <sub>2</sub> only	$14 \pm 2$

**Table 7.2:** Values of the size of scattering domain with regards to different annealing temperatures.

#### 7.4.2. Raman spectroscopy

Raman spectroscopy measurements confirm the crystal structure of the nanoparticles. Raman main and strong peaks of CZTS are located at 334 cm<sup>-1</sup> for before annealing and 560 °C, 337 cm<sup>-1</sup> for 585 °C and 635 °C, 335 cm<sup>-1</sup> for 610 °C and 339 cm<sup>-1</sup> for 585 °C with no H<sub>2</sub>S. These locations are in good agreement with the literature papers [4, 5]. Another weak peak appears at 290 cm<sup>-1</sup> for 585 °C with N<sub>2</sub> only which seems to be a secondary phase of ZnS [6, 7].



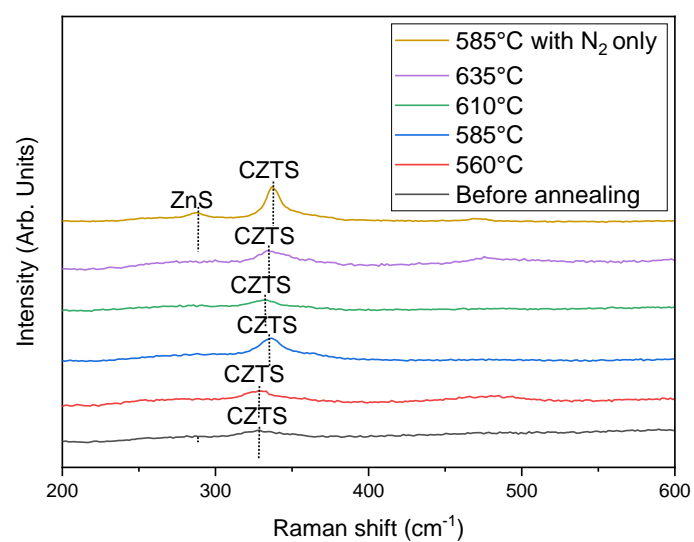


Figure 7.2 Raman spectra of CZTS samples with different annealing temperatures.

### 7.4.3. Morphology

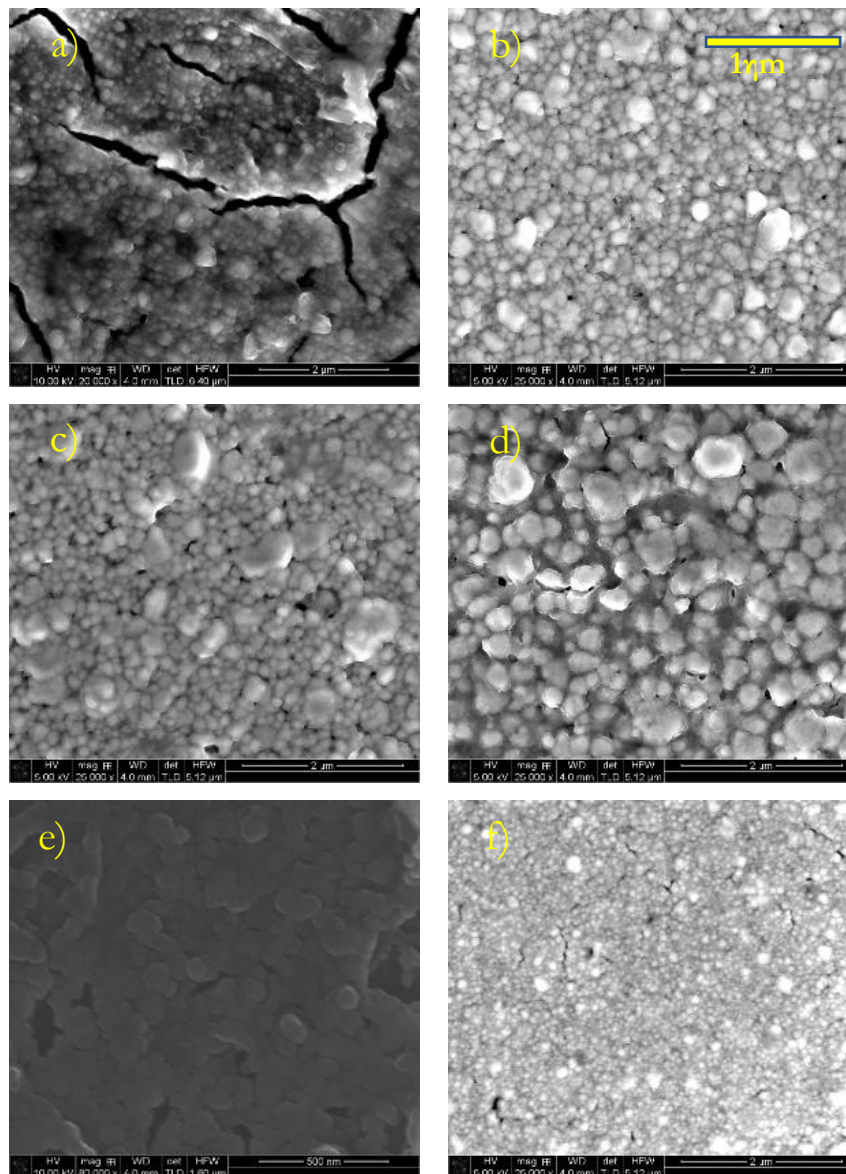


Figure. 7.3 SEM images at scale of 2  $\mu\text{m}$  for CZTS nanoparticles with different annealing temperatures as a) Before annealing b) 560  $^{\circ}\text{C}$  c) 585  $^{\circ}\text{C}$  d) 610  $^{\circ}\text{C}$  e) 635  $^{\circ}\text{C}$  f) 585 with  $\text{N}_2$  only.

As figure 7.3 shows, it is clear that the annealing temperature plays an important role on the uniformity of the CZTS nanoparticles as this improved compared to before annealing. In addition, the gaps and cracks in the film before annealing almost disappeared in all other images which might indicate the development of the crystallinity of the CZTS nanoparticles and the formation of a continuous thin film.

#### 7.4.4. Chemical composition

The results of the EDS are summarised in the table 7.3 below. The EDS was taken from the film's surface.

Annealing temperature (°C)	Cu/(Zn+Sn)	Sn/Cu	Zn/Sn	S/(Cu+Zn+Sn)
Before annealing	$0.65 \pm 0.03$	$0.92 \pm 0.01$	$0.67 \pm 0.04$	$1.17 \pm 0.02$
560	$0.80 \pm 0.03$	$0.80 \pm 0.03$	$1.15 \pm 0.05$	$1.07 \pm 0.05$
585	$0.83 \pm 0.02$	$0.72 \pm 0.03$	$1.17 \pm 0.02$	$1.32 \pm 0.01$
610	$1.05 \pm 0.01$	$0.66 \pm 0.01$	$1.75 \pm 0.01$	$0.85 \pm 0.02$
635	$1.15 \pm 0.04$	$1.12 \pm 0.05$	$2.25 \pm 0.05$	$0.67 \pm 0.03$
585 with only N <sub>2</sub>	$0.41 \pm 0.02$	$0.72 \pm 0.04$	$2.41 \pm 0.05$	$0.80 \pm 0.04$

**Table 7.3:** Composition ratios of CZTS nanoparticles with different annealing temperatures.

From table 7.3, the ratios of 560 °C and 585 °C were similar to the starting composition of Cu-poor, Zn-rich in the experimental details. However, the temperature of 585 °C with only N<sub>2</sub> showed different ratios than the original films due to the absence of the H<sub>2</sub>S atmosphere. The 585 °C (N<sub>2</sub>:H<sub>2</sub>S) sample has the closest Cu-poor, Zn-rich ratio value to the desired ratio for the highly efficient solar cell device (12.6%) compared to the rest of the annealing temperatures samples.

#### 7.4.5. Optical properties

A series of fabricated CZTS films from inks at different annealing temperatures 560 °C, 585 °C, 610 °C, 635 °C and 585 °C with N<sub>2</sub> only atmosphere was created to investigate electronic properties. The energy bandgap of the thin film is determined by UV-vis spectroscopy from the absorption spectrum using the Tauc plot method.

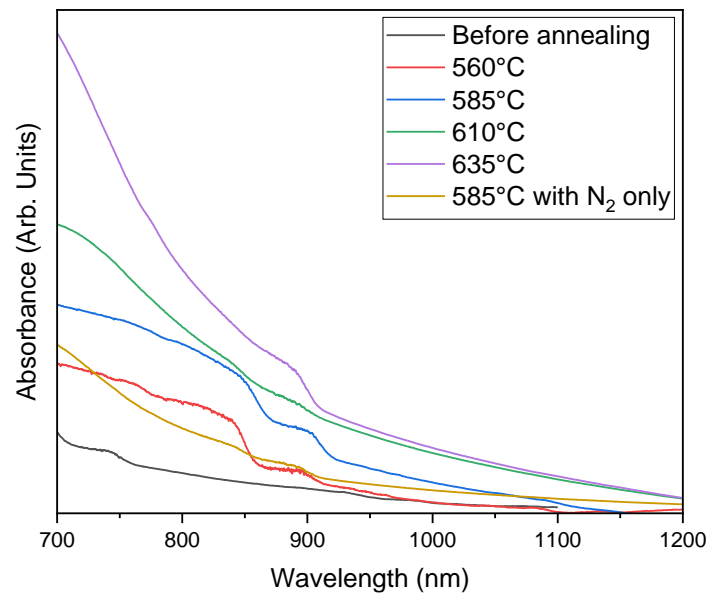


Figure 7.4 Absorbance spectrum of CZTS samples with different annealing temperatures.

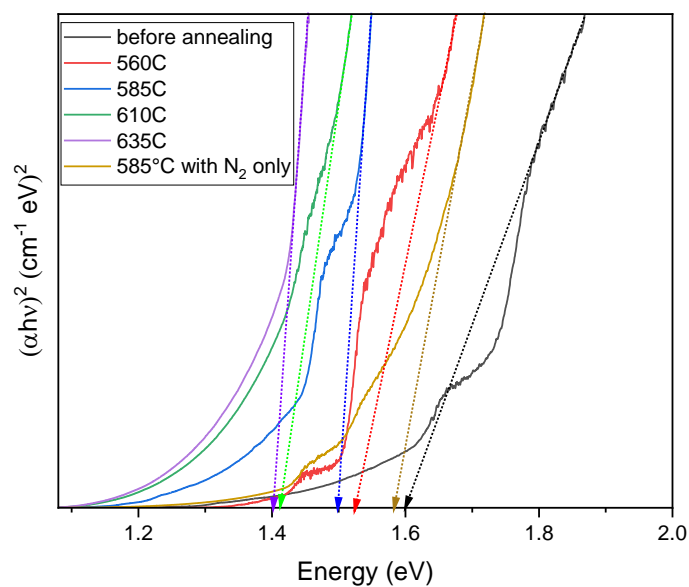


Figure 7.5 Tauc plot to show the bandgap of CZTS versus different annealing temperatures.

The absorbance spectra were recorded in the range of 700-1200 nm in figure 7.4. The energy bandgap was determined by the Tauc plot.

Annealing temperature (°C)	$E_g$ (eV)
Before annealing	$1.60 \pm 0.02$
560	$1.52 \pm 0.01$
585	$1.50 \pm 0.01$
610	$1.41 \pm 0.02$
635	$1.40 \pm 0.02$
585 with N <sub>2</sub> only	$1.58 \pm 0.03$

**Table 7.4:** The different annealing temperatures of CZTS versus the energy bandgap.

All these energy bandgaps in the above table 7.4, correspond well with that reported in literature of between 1.40-1.60 eV [8]. It is observed that there is a direct relationship between the energy bandgap and the annealing temperatures except for the sample annealed at 585°C with N<sub>2</sub> only atmosphere. The sample with the highest relative concentration of Zn+Sn has the largest bandgap.

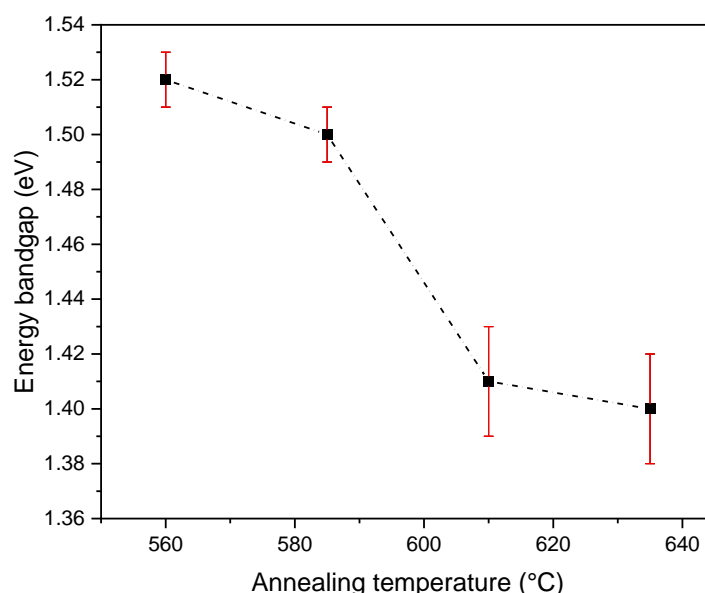


Figure. 7.6 The trend of the bandgap of CZTS samples vs different annealing temperatures.

Figure 7.5 shows different linear regions indicating the possible existence of secondary phases with energy bandgaps different from CZTS. Using the procedure described in section 5.4.5 and illustrated in figure 5.12, values of additional bandgaps linked to possible secondary phases can be extracted. The different energy bandgaps extracted using this method are given in table 7.5. The possible secondary phases related to these energy bandgaps are also listed.

Annealing temperature (°C)	Energy bandgaps from Tauc plot (eV)	Possible secondary phases related to bandgaps
Before annealing	1.40, 1.60, 1.70	$\text{Cu}_2\text{SnS}_3$ , ?, ?
560	1.40, 1.50	$\text{Cu}_2\text{SnS}_3$ , ?
585	1.25, 1.30, 1.40	$\text{Cu}_2\text{S}/\text{Cu}_3\text{SnS}_4/\text{Cu}_4\text{SnS}_4$ , SnS, $\text{Cu}_2\text{SnS}_3$
610	1.30	SnS
635	1.25	$\text{Cu}_2\text{S}/\text{Cu}_3\text{SnS}_4/\text{Cu}_4\text{SnS}_4$
585 with $\text{N}_2$ only	1.40, 1.50	$\text{Cu}_2\text{SnS}_3$ , ?

**Table 7.5:** Possible secondary phases and their bandgaps with different annealing temperatures.

The Raman data showed corresponding values to other literature papers with all samples. The EDS values showed a desired ratio for Cu-poor, Zn-rich in 585 °C sample for highly efficient solar cell device. The bandgap, in table 7.4 shows that all samples are in the range of accepted values of the expected theoretical bandgap values of CZTS. The temperature of 585°C was used to continue the systematic study for the next section as it is the most suitable annealing temperatures among other samples.

## 7.5. Annealing times

Four different samples were prepared, one before annealing and the other three are with different annealing times after the CZTS nanocrystal thin films were created. The same hot injection method was used for the fabrication of these samples followed by the spin coating technique for the deposition of CZTS nanocrystal inks onto glass substrate. Different annealing times were examined ranging between 30-120 min.

## 7.6. Experimental methodology

### 7.6.1. The fabrication of CZTS nanoparticles

CZTS nanoparticles were fabricated by the same procedure explained in chapter 7 section 7.3.1 with Cu-poor, Zn-rich compositions in the as synthesised particles. There were no modifications to the reaction conditions made in this section.

### 7.6.2. Ink deposition

The CZTS nanoparticle inks are spin coated on SLG substrates using the same methodology as described in chapter 7 section 7.3.2. 2500 rpm, 15 seconds and 015 acceleration index were used for the spin coating conditions.

### 7.6.3. Annealing treatment

The prepared CZTS thin films on substrates undergo sulphurisation annealing at the same method and atmosphere  $N_2:H_2S$  80:20 used in section 7.3.3. However, the annealing process was applied under the conditions of fixed temperature at 585 °C, for several different annealing times 30, 60 and 120 minutes at ramping rate of 10 °C per minute.

## 7.7. Results and discussion

### 7.7.1. Crystal structure - XRD

The XRD patterns of the fabricated CZTS nanoparticles before annealing and different annealing times 30, 60 and 120 minutes are shown in figure 7.7.

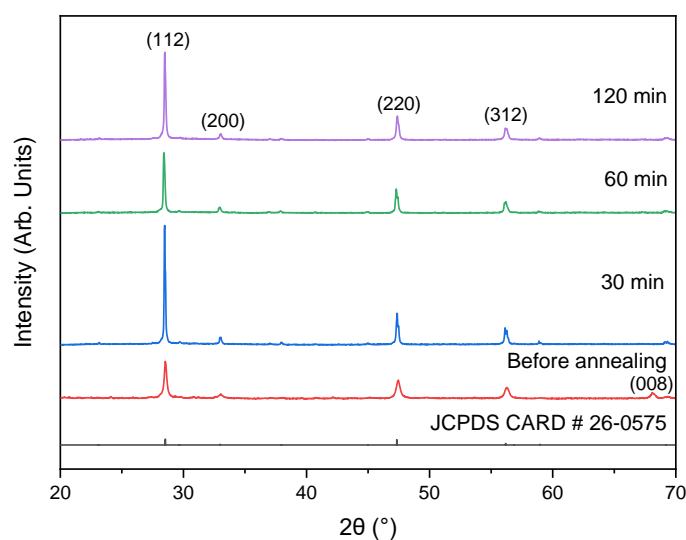


Figure 7.7 XRD for samples of CZTS with different annealing times, including the CZTS PDF reference (# 26-0575).

The XRD data confirmed the formation of CZTS thin films for all annealed and before annealing samples used as the four main diffraction peaks (112), (200), (220) and (312) appeared in the location corresponding to JCPDS card number 026-0575. In addition (008) peak observed in the samples of before annealing.

Annealing time (min)	2 $\theta$ (°) for structure planes (112)	$d$ -spacing (nm)	$a$ (nm)	$c$ (nm)
Before annealing	28.47	0.3133	0.5417	1.0895
30	28.44	0.3136	0.5426	1.0892
60	28.66	0.3115	0.5409	1.0738
120	28.45	0.3134	0.5321	1.0884

**Table 7.6:** Values of  $d$ -spacing and lattice parameters  $a$  and  $c$  with different annealing times.

The  $d$ -spacing,  $a$  and  $c$  values of the 60 min sample show similar values with the literature [1].

Table 7.7 below presents the values of the size of scattering domain. The size of scattering domain showed no trend which the value was fluctuated from  $16 \pm 2$  to  $52 \pm 5$  nm.

Annealing time (min)	Scattering domain (nm)
Before annealing	$16 \pm 2$
30	$67 \pm 7$
60	$32 \pm 3$
120	$52 \pm 5$

**Table 7.7:** Values of the size of scattering domain with regards to different annealing times.

### 7.7.2. Raman spectroscopy

Raman spectroscopy measurements also confirm the crystal structure of the nanoparticles. Raman main and strong peaks of CZTS are located at  $334 \text{ cm}^{-1}$  for before annealing,  $339 \text{ cm}^{-1}$  for 30 min,  $337 \text{ cm}^{-1}$  for 60 min and  $338 \text{ cm}^{-1}$  for 120 min. These locations are in good agreement with the literature papers [4, 5]. Another weak peak appears at  $288 \text{ cm}^{-1}$  for 120 min which seems to be a secondary phase of SnS [9-11].



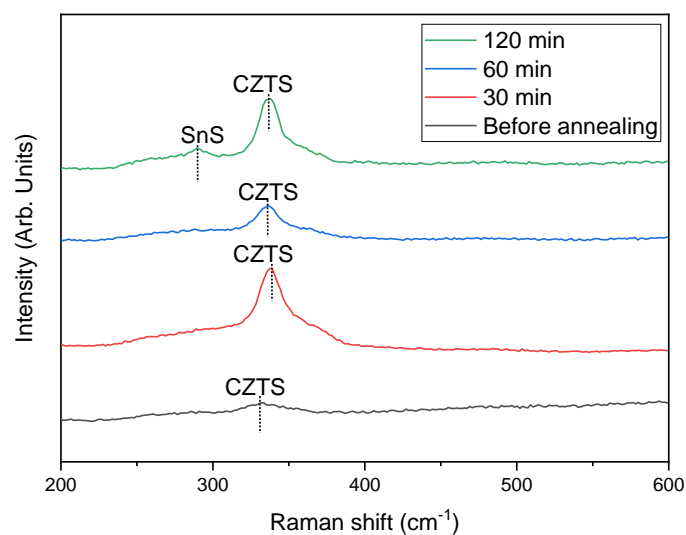


Figure 7.8 Raman spectra of CZTS samples with different annealing times.

### 7.7.3. Morphology

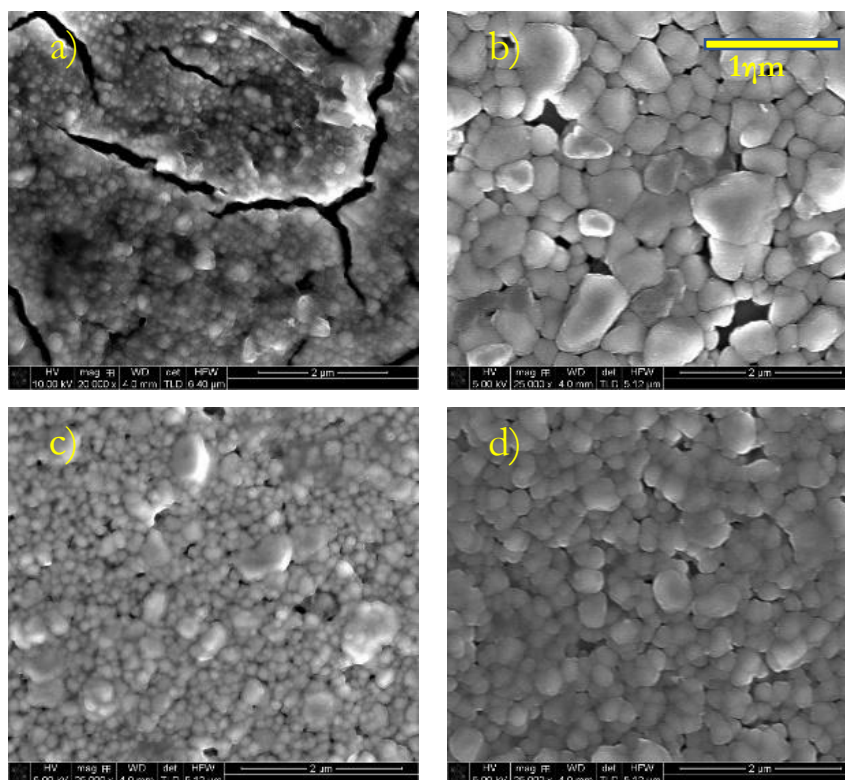


Figure. 7.9 SEM images at scale of 2  $\mu\text{m}$  for CZTS nanoparticles with different annealing times as a) Before annealing b) 30 min c) 60 min and d) 120 min.

The annealing times also played an important role as the annealing temperatures did on the uniformity of the CZTS nanoparticles. In image c, the development of the crystallinity and uniformity of the CZTS nanoparticles was much better than on other samples, displaying a consistently uniform range of particle sizes. In addition, the gaps and cracks in the film before annealing almost disappeared in images c, and d, which might indicate the development of the crystallinity of the CZTS nanoparticles and the formation of a continuous thin film.

#### 7.7.4. Chemical composition

The results of the EDS are summarised in the table 7.7 below. The EDS was taken from the film's surface.

Annealing time (min)	Cu/(Zn+Sn)	Sn/Cu	Zn/Sn	S/(Cu+Zn+Sn)
Before annealing	$0.65 \pm 0.03$	$0.92 \pm 0.01$	$0.67 \pm 0.04$	$1.17 \pm 0.02$
30	$0.76 \pm 0.01$	$0.55 \pm 0.07$	$1.40 \pm 0.02$	$0.93 \pm 0.02$
60	$0.83 \pm 0.02$	$0.72 \pm 0.03$	$1.17 \pm 0.02$	$1.32 \pm 0.01$
120	$0.91 \pm 0.03$	$0.65 \pm 0.05$	$1.57 \pm 0.04$	$1.47 \pm 0.01$

**Table 7.8:** Composition ratios of CZTS nanoparticles with different annealing times.

From table 7.8, The 60 min sample has the closest Cu-poor, Zn-rich ratio value to the desired ratio for the highly efficient solar cell device (12.6%) compared to the rest of the annealing temperatures samples.

#### 7.7.5. Optical properties

A series of fabricated CZTS films from inks at different annealing times 30 min, 60 min and 120 min was created to investigate electronic properties. The energy bandgap of the thin film is determined by UV-vis spectroscopy from the absorption spectrum using the Tauc plot method.

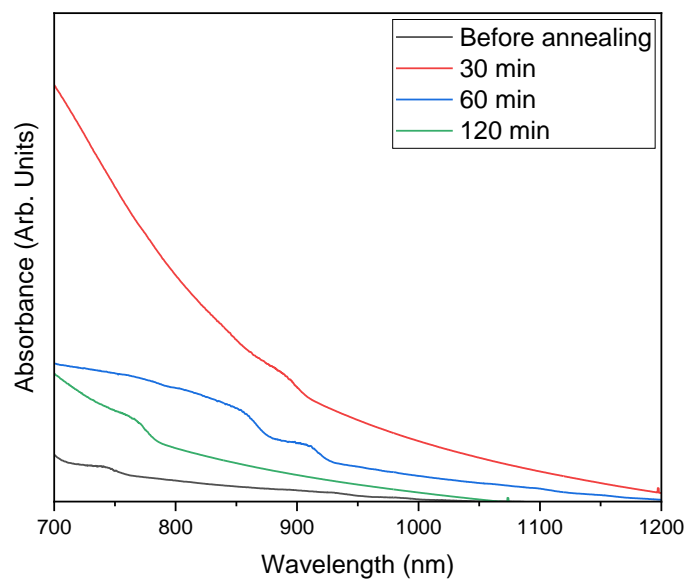


Figure 7.10 Absorbance spectrum of CZTS samples with different annealing times.

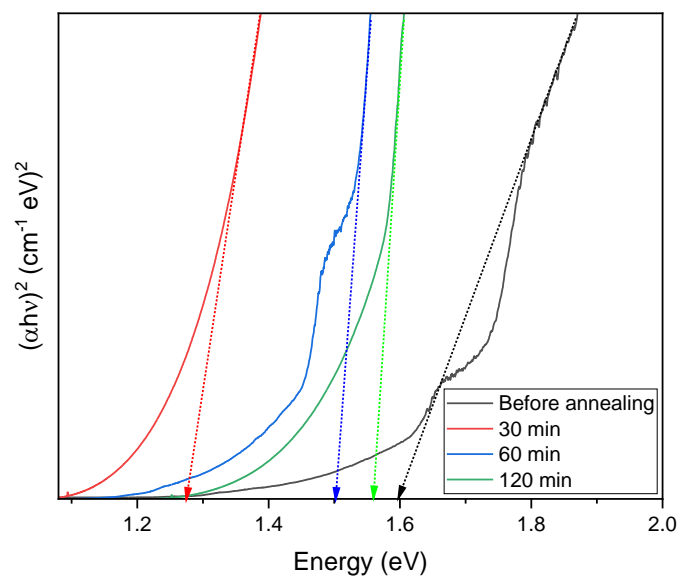


Figure 7.11 Tauc plot to show the bandgap of CZTS versus different annealing times.

The absorbance spectra were recorded in the range of 700-1200 nm in figure 7.10. The energy bandgap was determined by the Tauc plot.

Annealing time (min)	$E_g$ (eV)
Before annealing	$1.60 \pm 0.02$
30	$1.28 \pm 0.03$
60	$1.50 \pm 0.01$
120	$1.56 \pm 0.03$

**Table 7.9:** The different annealing times of CZTS versus the energy bandgap.

The observed energy bandgap of the 60 and 120 min time period  $1.50 \pm 0.01$  and  $1.56 \pm 0.03$  eV, correspond well with that of the expected theoretical value of CZTS nanocrystal thin film of between 1.40-1.60 eV [12, 13]. It seems that too short annealing time was not enough to form crystalline CZTS.

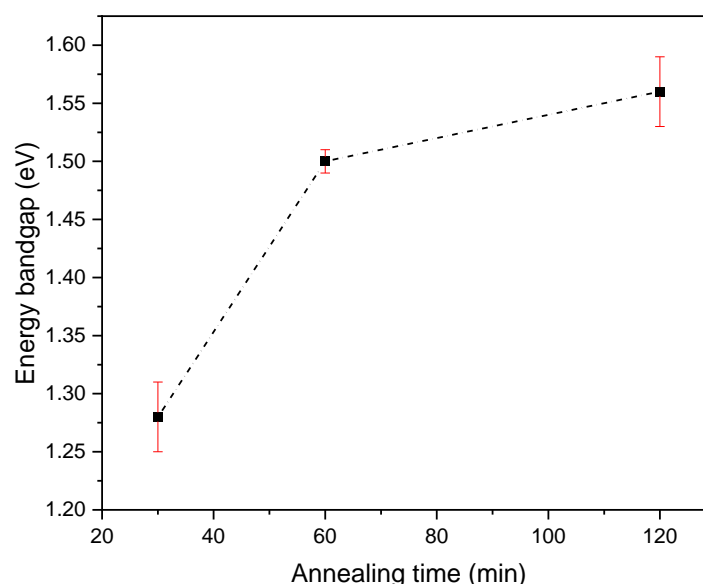


Figure. 7.12 The trend of the bandgap of CZTS samples vs different annealing times.

Figure 7.11 shows different linear regions indicating the possible existence of secondary phases with energy bandgaps different from CZTS. Using the procedure described in section 5.4.5 and illustrated in figure 5.12, values of additional bandgaps linked to possible secondary phases can be extracted. The different energy bandgaps extracted using this method are given in table 7.10. The possible secondary phases related to these energy bandgaps are also listed.

Annealing time (min)	Energy bandgaps from Tauc plot (eV)	Possible secondary phases related to bandgaps
Before annealing	1.40, 1.60, 1.70	$\text{Cu}_2\text{SnS}_3$ , ?, ?
30	1.20	$\text{Cu}_2\text{S}/\text{Cu}_3\text{SnS}_4/\text{Cu}_4\text{SnS}_4$
60	1.25, 1.30, 1.40	$\text{Cu}_2\text{S}/\text{Cu}_3\text{SnS}_4/\text{Cu}_4\text{SnS}_4$ , SnS, $\text{Cu}_2\text{SnS}_3$
120	1.30, 1.40	SnS, $\text{Cu}_2\text{SnS}_3$

**Table 7.10:** Possible secondary phases and their bandgaps with different annealing times.

The XRD and Raman data confirmed the formation of the crystal structure of the nanoparticles showing corresponding values to other literature papers with all samples. The EDS values showed a desired ratio for Cu-poor, Zn-rich in sample 60 min for highly efficient solar cell device. The

---

bandgap, in table 7.9 shows that the 60 and 120 min time period are in the range of accepted values of the expected theoretical bandgap values of CZTS.

The temperature of 585°C for 60 min annealing time was the most suitable annealing temperatures and times among other samples to improve the performance of a CZTS solar cell device, hence these annealing conditions will be used for the next section (testing the performance of the CZTS solar cell device).

## 7.8. References

1. Q. Tian, X. Xu, L. Han, M. Tang, R. Zou, Z. Chen, M. Yu, J. Yang, J. Hu, Hydrophilic  $\text{Cu}_2\text{ZnSnS}_4$  Nanocrystals for Printing Flexible, Low-cost and Environmentally Friendly Solar Cells, *Cryst. Eng. Comm.* 14 (2012) 3847-3850. <https://doi.org/10.1039/C2CE06552E>.
2. J. Raiguru, B.V.R.S. Subramanyam, K. Sa, I. Alam, S. Das, J. Mukherjee, P. C. Mahakul, B. Subudhi, P. Mahanandia, Impact of Annealing Temperature on the Phase of CZTS with the Variation in Surface Morphological Changes and Extraction of Optical Bandgap, *IOP. Conf. Ser.: Mater. Sci. Eng.* 178 (2017) 012017. <https://doi.org/10.1088/1757-899X/178/1/012017>.
3. S. Bahramzadeh, H. Abdizadeh, M. R. Golobostanfard, Controlling the Morphology and Properties of Solvothermal Synthesized  $\text{Cu}_2\text{ZnSnS}_4$  Nanoparticles by Solvent Type, *J. All. Com.* 642 (2015) 124-130. <https://doi.org/10.1016/j.jallcom.2015.04.093>.
4. P. A. Fernandes, P. M. P. Salome, A. F. Cunha, Growth and Raman Scattering Characterization of  $\text{Cu}_2\text{ZnSnS}_4$  Thin Films, *Thin. Solid. Films.* 517 (2009) 2519-2523. <https://doi.org/10.1016/j.tsf.2008.11.031>.
5. M. Altosaar, J. Raudoja, K. Timmo, M. Danilson, M. Grossberg, J. Krustok, E. Mellikov,  $\text{Cu}_2\text{Zn}_{1-x}\text{Cd}_x\text{Sn}(\text{Se}_{1-y}\text{S}_y)_4$  Solid Solutions as Absorber Materials for Solar Cells, *Physica. Status. Solidi (a)*. 205 (2008) 167-170. <https://doi.org/10.1002/pssa.200776839>.
6. Y. C. Cheng, C. Q. Jin, F. Gao, X. L. Wu, W. Zhong, S. H. Li, P. K. Chu, Raman Scattering Study of Zinc Blende and Wurtzite  $\text{ZnS}$ , *J. Appl. Phys.* 106 (2009) 123505. <https://doi.org/10.1063/1.3270401>.
7. W. G. Nilsen, Raman Spectrum of Cubic  $\text{ZnS}$ , *Phys. Rev.* 182 (1969) 838. <https://doi.org/10.1103/PhysRev.182.838>.
8. H. Matsushita, T. Maeda, A. Katsui, T. Takizawa, Thermal Analysis and Synthesis from the Melts of Cu-based Quaternary Compounds  $\text{Cu-III-IV-VI}_4$   $\text{Cu}_2\text{-II-IV-VI}_4$  (II=Zn, Cd; III=Ga, In; IV=Ge, Sn; VI=Se), *J. Cryst. Growth.* 208 (2000) 416-422. [https://doi.org/10.1016/S0022-0248\(99\)00468-6](https://doi.org/10.1016/S0022-0248(99)00468-6).
9. S. J. Sandoval, D. Yang, R. F. Frindt, J. C. Irwin, Raman Study and Lattice Dynamics of Single Molecular Layers of  $\text{MoS}_2$ , *Phys. Rev. B.* 44 (1991) 3955. <https://doi.org/10.1103/PhysRevB.44.3955>.
10. D. Yang, S. J. Sandoval, W. M. R. Divigalpitiya, J. C. Irwin, R. F. Frindt, Structure of Single-molecular-layer  $\text{MoS}_2$ , *Phys. Rev. B.* 43 (1991) 12053. <https://doi.org/10.1103/PhysRevB.43.12053>.

- 
11. L. S. Price, I. P. Parkin, A. M. E. Hardy, R. J. H. Clark, G. Thomas, K. C. Molloy, Atmospheric Pressure Chemical Vapor Deposition of Tin Sulfides ( $\text{SnS}$ ,  $\text{Sn}_2\text{S}_3$ , and  $\text{SnS}_2$ ) on Glass, *Chem. Mater.* 11 (1999) 1792-1799. <https://doi.org/10.1021/cm990005z>.
  12. X. Cui, K. Sun, J. Huang, H. Sun, A. Wang, X. Yuan, M. Green, B. Hoex, X. Hao, Low-temperature Plasma-enhanced Atomic Layer Deposition of  $\text{ZnMgO}$  for Efficient CZTS Solar Cells, *ACS. Mater. Lett.* 5 (2023) 1456-1465. <https://doi.org/10.1021/acsmaterialslett.2c01203>.
  13. H. Li, H. Shen, X. Zhu, J. Zhang, Y. Li, J. Chen, H. Bai, J. Zeng, J. Zheng, Z. Yue, W. Zhang, Enhanced Photoelectric Properties in Flexible CZTS Solar Cells Using O/M/O Structure, *Mater. Sci. Semicond. Processing.* 165 (2023) 107686. <https://doi.org/10.1016/j.mssp.2023.107686>.

# **Chapter 8:**

## **Impact of the reaction conditions of CZTS nanocrystal ink on solar cell device performance**

### **8.1. Introduction**

In this chapter, CZTS solar cells were fabricated using the CZTS inks developed as reported in previous chapters. The performance of CZTS solar cell devices using different CZTS ink fabrication conditions were investigated. The optimum CZTS nanocrystal thin film conditions which were found in chapters 5, 6 and 7 were selected here for building up these CZTS devices in order to identify the optimum conditions for CZTS devices to have a high-performance solar cell. This was done by studying the impact of the properties of different CZTS nanocrystal inks on the completed solar cell devices' performance. Morphological and electrical properties were measured by SEM for the cross-section and  $I$ - $V$  curve measurements of the devices under illumination used to determine overall PV device efficiency.

### **8.2. Device structure**

Six batches of different CZTS devices were prepared using the same procedure explained in chapter 3 section 3.7. A single PV device consists of several layers as follows:

- SLG as the substrate.



- 
- Mo as the back contact deposited on the substrate via the sputtering technique. Mantis Q-prep 500 system was used. It is an ultra-high vacuum system with a typical base pressure better than  $10^{-8}$  Torr. During growth there is a flow of argon gas at 20 sccm flow rate into the chamber, giving a pressure of 1 mTorr. The sputtering power is 50W using a 2 inch diameter target. It took 60 minutes to obtain a 600 nm thick Mo layer.
  - CZTS nanocrystal thin films as the absorber layer synthesised by hot injection method and deposited on Mo via spin coating.
  - CdS as buffer layer deposited via CBD. The solution consisted of  $\text{CdSO}_4$  (2.5 mmol),  $\text{NH}_4\text{OH}$  (15 ml),  $\text{CSN}_2\text{H}_4$  (10 mmol) and distilled water to make a total volume of 150 ml. The solution was heated to  $70^\circ\text{C}$ . The substrate was left in the bath for 20 minutes and resulted in a 60 nm film of CdS.
  - ZnO as window layer was deposited by RF sputtering at a base pressure of  $9 \times 10^{-7}$  Torr for 40 minutes to grow a 100 nm thick layer.
  - ITO as the transparent conductive layer was also deposited by RF sputtering using the same settings for the ZnO layer for 60 minutes to grow a 300 nm thick layer.
  - Au as the front contact layer was deposited by evaporation to give a 300 nm.

This arrangement of layers is shown in figure 3.7 in chapter 3. The focus of this study is only on the impact of one layer on overall device performance which is CZTS. The other layers in the devices were fabricated under identical conditions, the assumption being that differences in device performance would be due to changes in the CZTS layer.

### 8.2.1. The fabrication of CZTS nanoparticles

CZTS nanoparticles were synthesised by the same procedure discussed in chapter 4 section 4.1.1 with Cu-poor, Zn-rich compositions for the as synthesised particles. The main variables for the created CZTS nanocrystals were as follows:

- The precursor molar ratios were  $\text{Cu}/(\text{Zn} + \text{Sn}) = 0.85$ ,  $\text{Zn}/\text{Sn} = 1.25$  and  $\text{S}/(\text{Cu}+\text{Zn}+\text{Sn}) = 1.28$ . These ratios are chosen to obtain a high PV device efficiency as discussed in chapter 3 [1].
- These ratios are achieved by using reagents: 1.44 mmol (0.3769 g) of copper (II) acetylacetonate, 0.94 mmol (0.2478 g) of zinc (II) acetylacetonate, 0.75 mmol (0.2909 g) of tin (IV) bis(acetylacetonate) dichloride and 10 ml of OLA.

- The reaction temperature was set at 225 °C, 250 °C and 275 °C for six different batches of ink.
- The time of the reaction was 30 and 60 minutes at the three different reaction temperatures.

### 8.2.2. Ink deposition

The CZTS nanoparticle inks were deposited by spin coating on the SLG substrates using the same methodology as described in chapter 4 section 4.1.2. 2500 rpm was used for the spin coating speed, 15 seconds for the time and 015 acceleration index.

### 8.2.3. Annealing treatment

The fabricated CZTS thin films on substrates undergo sulphurisation annealing in the same procedure explained in chapter 7 section 7.3.3. The annealing temperature was 585°C for 60 min annealing time in an atmosphere of N<sub>2</sub>:H<sub>2</sub>S 80:20.

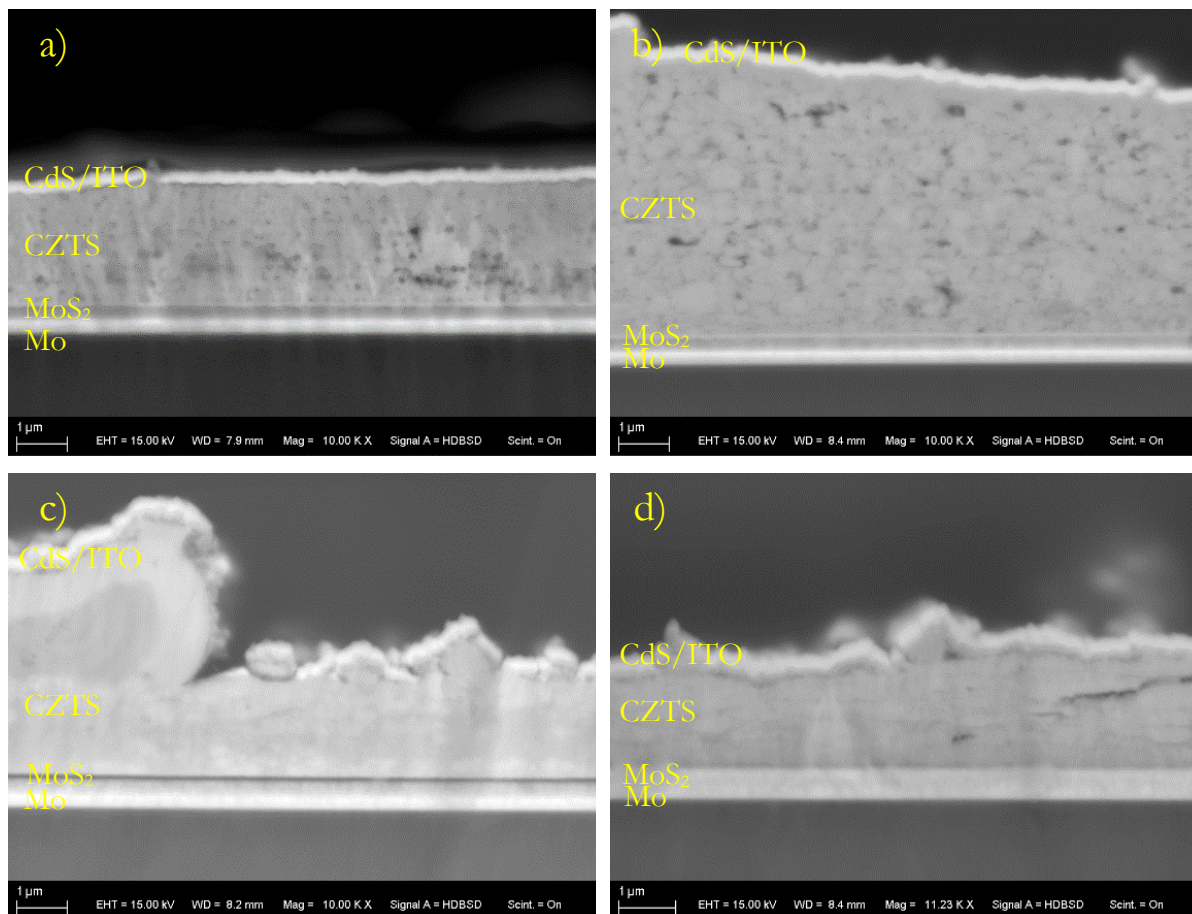
## 8.3. Results and discussion

### 8.3.1. Morphology

SEM was used for the cross-section imaging of the devices to determine the morphology and confirm the device structure. This was done by ZEISS Sigma 300 VP SEM instrument. The cross-section preparation of the devices for imaging was done by the ion milling system.

In figure 8.1 below, the cross-sectional SEM images reveal a six-layer structure. The first layer on bottom was Mo with a thickness of approximately 300 nm. It was uniformly sputtered for all devices. On top of Mo a layer of MoS<sub>2</sub> is often formed by the reaction of Mo with CZTS during annealing, it can be seen in the figure. The formation of p-type MoS<sub>2</sub> is beneficial for the device performance, playing a role in reducing the carrier recombination at the back contact [2]. The CZTS layer is deposited on top of Mo with a thickness of around 1630 to 4680 nm. This layer is meant to be uniform with an intended thickness of 1000 nm for all devices. However, as seen in figure 8.1, it was not uniform for all devices. This might be related to variations occurring during

the spin coating while dropping the ink. This is an important finding which identifies the need to have a consistent approach to spin coating delivering consistent films of the same thickness. Across all devices the thickness of CZTS layers are 2320, 4680, 1910, 1630, 3130 and 1840 nm respectively. The different thickness of CZTS layers will be due to a number of factors including the different concentration of nanoparticles in the different inks, and differences in the spin coating deposition as described above. Images in Figure 8.1 c) and d) show an irregular surface. This appears to be due to an irregular accumulation of particles during the spin coating process where agglomerations of particles lead to irregularities in film thickness. Agglomeration of nanoparticles at different scales has been observed in other work [3]. This may be resolved by ultra-sonic agitation of inks before spin coating.



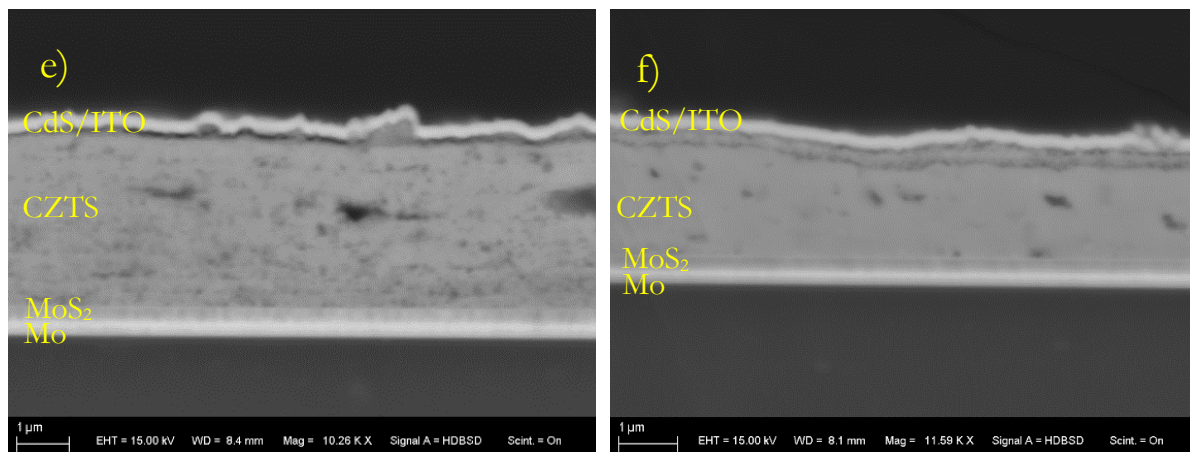


Figure. 8.1 SEM cross-section images at scale of 1  $\mu\text{m}$  for CZTS devices as a) 225  $^{\circ}\text{C}$  for 30 min b) 275  $^{\circ}\text{C}$  for 60 min c) 250  $^{\circ}\text{C}$  for 60 min d) 225  $^{\circ}\text{C}$  for 60 min e) 275  $^{\circ}\text{C}$  for 30 min and f) 250  $^{\circ}\text{C}$  for 30 min.

### 8.3.2. $I$ - $V$ curve measurements

A Keithley 2400 source-measure instrument was used to determine the electrical properties of the prepared CZTS devices by measuring the  $J$ - $V$  curve under illumination in a Lot Oriel solar simulator with AM1.5G irradiation. As explained in chapter 2 section 2.13, the current passing through the solar cell devices by applying an external voltage across the devices will be measured and read by a LabView software package. Figure 8.2 below shows the  $J$ - $V$  curve of the measured devices under dark as black and illuminated as blue. Multiple measurements were taken on the same active area and the best values reported. The active area of devices differs because of different substrate sizes. The active area is determined from the substrate size but excludes the Au contact area. Wire probes were used to connect with the Mo and Au back and front contacts. 6 devices were measured (each device 4 times, choosing the best efficiency). So, calculating the SD for each device, then equations (5.2) and (5.3) can be used.

From figure 8.2, several important parameters can be determined including  $J_{sc}$ ,  $V_{oc}$ , FF and  $\eta$  as explained in Chapter 2.

Power density for all devices under illumination is constant = 100  $\text{mW.cm}^{-2}$ . Table 8.1 presents the important parameters taken from the figure 8.2.

Device	$V_{MP}$ (V)	$J_{MP}$ (mA.cm <sup>-2</sup> )	$I_{MP}$ (mA)	$P_{max}$ (mW)	$V_{OC}$ (V)	$J_{SC}$ (mA.cm <sup>-2</sup> )	$FF$	$Area$ (cm <sup>2</sup> )	$P_{in}$ (mW)	$\eta$ (%)
1	0.300	3.10	4.960	1.48	0.556	4.70	0.35	1.6	160	$0.94 \pm 0.04$
2	0.411	6.30	15.10	6.20	0.693	8.67	0.43	2.4	240	$2.60 \pm 0.05$
3	0.300	0.70	2.100	0.10	0.425	0.96	0.08	3.0	300	$0.03 \pm 0.20$
4	0.132	0.32	0.400	0.10	0.272	0.53	0.63	1.1	110	$0.09 \pm 0.03$
5	0.124	0.31	0.434	0.10	0.262	0.56	0.48	1.4	140	$0.07 \pm 0.06$
6	0.200	0.51	1.100	0.22	0.410	0.90	0.28	2.1	210	$0.11 \pm 0.10$

**Table 8.1:** Important devices parameters for the CZTS solar cells discussed in this work.

In the table 8.1, device 2 has performed  $2.60 \pm 0.05\%$  efficiency with  $J_{SC} = 8.67$  mA.cm<sup>-2</sup> and  $V_{OC} = 0.693$  V. These values are very low in comparison with a CZTS device with recorded efficiency of around 10% with  $J_{SC} = 21$  mA.cm<sup>-2</sup> and  $V_{OC} = 0.736$  V [4].

These low efficiency values indicate that the fabrication of devices has not been fully successful and means that the original purpose of correlating nanoparticle ink fabrication with device efficiency is not possible. The low efficiency values could be due to a number of reasons. The largest value for  $J_{SC}$  is 8.67 mA.cm<sup>-2</sup> which is 41% of the  $J_{SC}$  obtained for the 10% efficiency device. The highest  $V_{OC}$  obtained is 0.693 V which is 94% of the  $V_{OC}$  obtained for the 10% efficiency device. This confirms that the low efficiency is due mainly to recombination losses reducing  $J_{SC}$ . CZTS devices are known to have a low  $V_{OC}$  with this deficit due to point defects and defect complexes altering the energy bandgap where defect states in the bandgap lead to band tailing and bandgap reduction [5]. This is often associated with Cu/Zn antisite defects, although recent work has indicated no correlation between Cu/Zn defects and bandgap [6, 7]. The low values of  $V_{OC}$  may also be related to the excess Sn that remained in the film [8]. The fact that the devices fabricated here have a  $V_{OC}$  which is 94% of the  $V_{OC}$  obtained for the 10% efficiency CZTS devices indicates that the properties of the CZTS film here are likely to be comparable to those of other CZTS devices.

The low efficiency measured here is due mainly to the relatively low value of  $J_{SC}$  which is 41% of the  $J_{SC}$  obtained for the 10% efficiency device. This indicates that attention must be focussed on reducing recombination losses. One of the main reasons for recombination losses in CZTS devices is losses at interfaces and contacts [9]. This confirms the need to optimise the fabrication procedures used here to improve device efficiency.

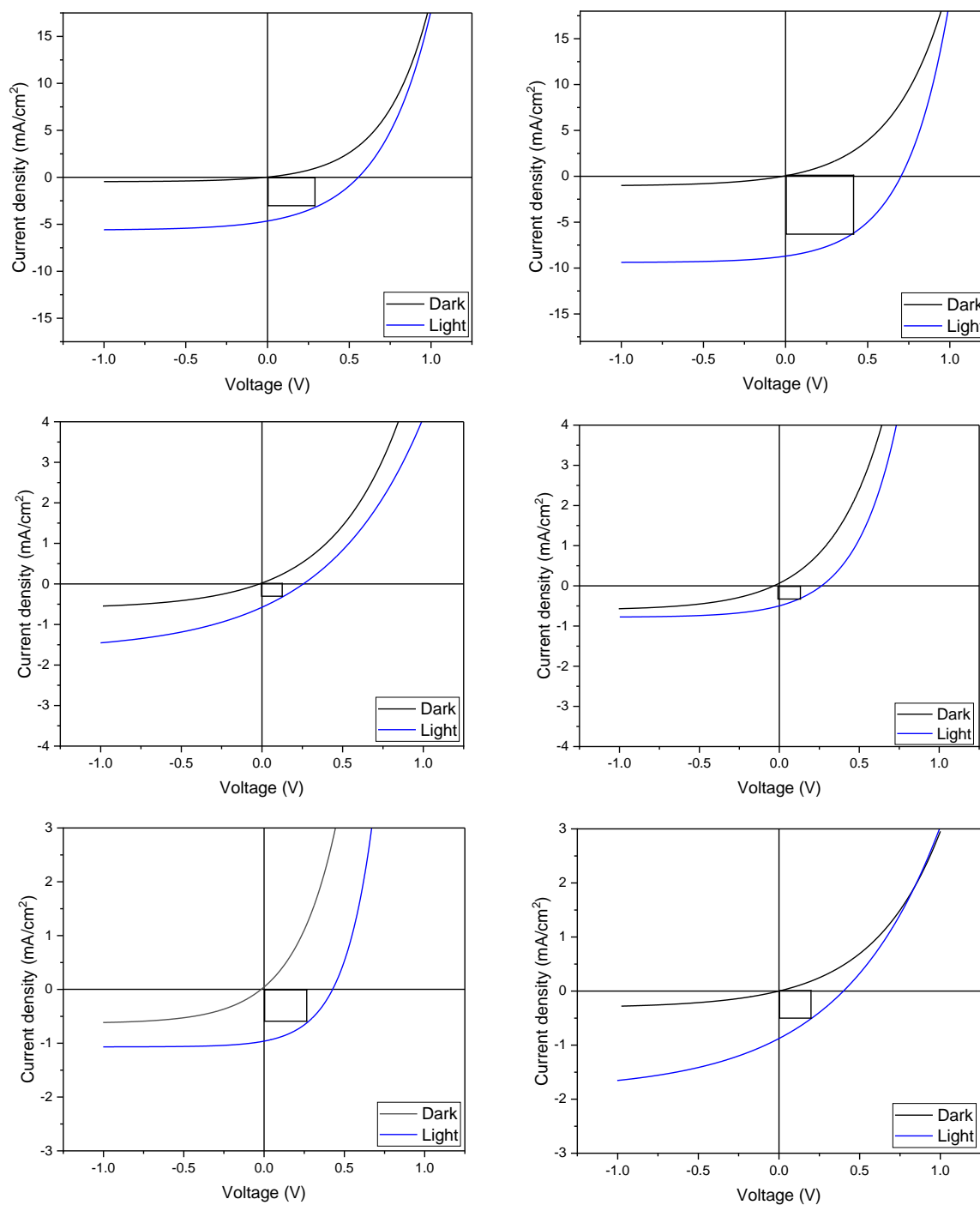


Figure. 8.2 J-V curves for CZTS solar cells devices with different nanoparticle inks.

### 8.3.3. EDS mapping

EDS was used for the cross-sectional images mapping to investigate the elemental distribution of CZTS solar cell devices. As it shows in table 8.1, device 2 has achieved the highest efficiency among the 6 tested devices with 2.6%, thus mapping imaging for this device is shown in figure 8.3 below.

---

The layers of the fabricated CZTS devices were configured as Mo/CZTS/CdS/ZnO/ITO/Au grid. Figure 8.3 shows the distribution of all measured elements throughout the device. The MoS<sub>2</sub> layer is clearly seen on top of Mo formed during the annealing process. This appears to have a higher concentration of S than the CZTS absorber layer. This MoS<sub>2</sub> layer might be considered to be beneficial to the device performance if it enhanced the bandgap alignment between the CZTS and Mo contact layer [10], although as noted above it may also increase recombination losses. The Mo element map shows diffusion of Mo throughout the full device structure. However, this is not due to diffusion of Mo, but appears because of strong overlap of the S K and Mo L EDS peaks. The Mo map shows a higher concentration in the Mo contact layer. It is not possible to say anything about diffusion of Mo into the device because of the overlap with the S EDS signal. The S element map shows a higher concentration of S in MoS<sub>2</sub> compared with CZTS. This requires further investigation to determine the impact on device efficiency. Figure 8.3 confirmed that Cu, Zn, and Sn were distributed approximately evenly and uniformly among the CZTS nanocrystals. This supports the conclusion above that these CZTS layers are comparable to those in higher efficiency devices. The CdS layer is extremely thin at around 50 nm. CdS deposited by chemical bath deposition is conformal following the underlying surface. This conformal behaviour is seen in the maps below. The layer of ITO is observed to have been deposited as expected.



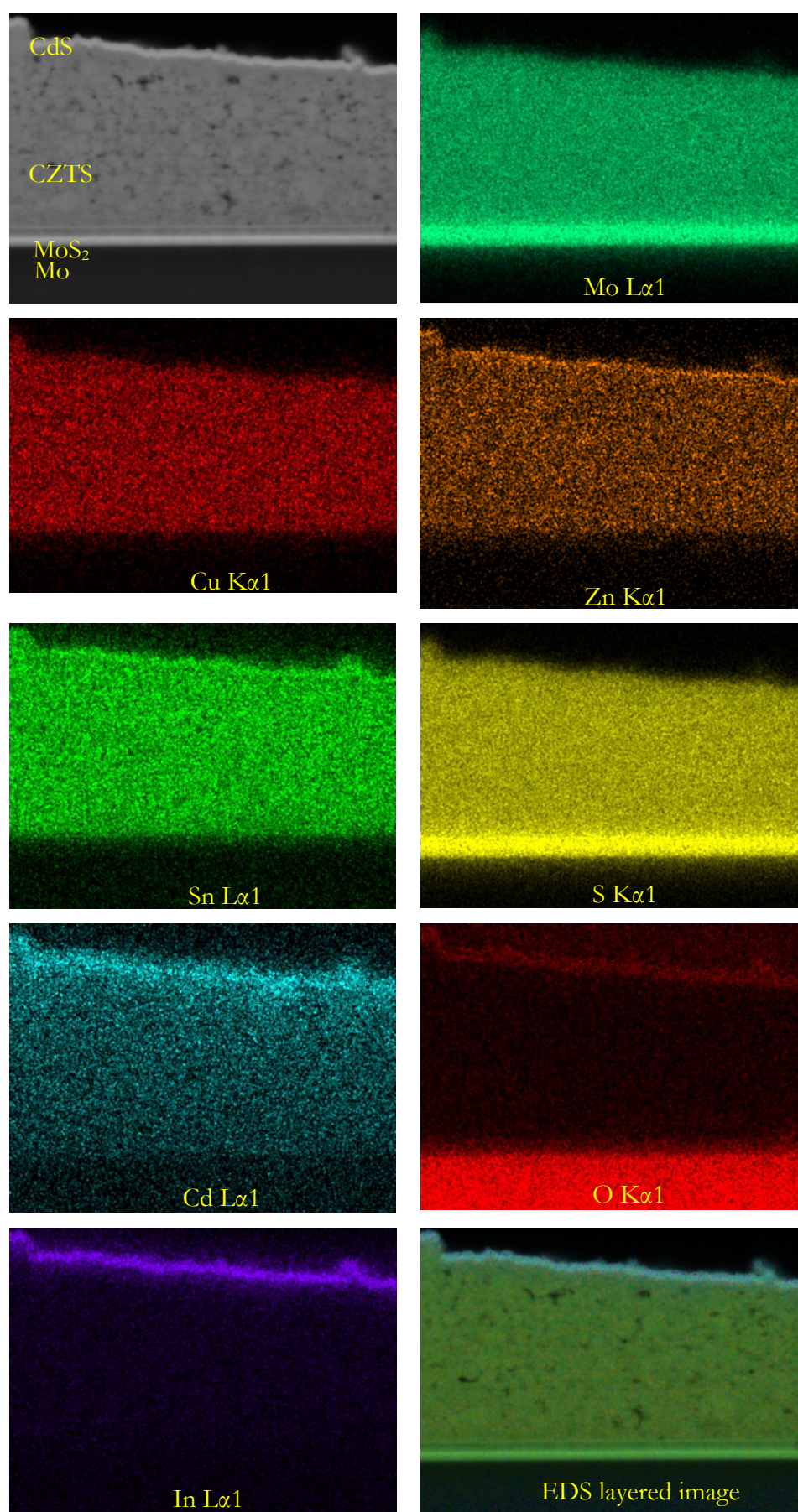


Figure. 8.3 EDS mapping of device 2 of CZTS solar cells at scale of 2.5  $\mu\text{m}$ .



In conclusion, the overall low efficiency indicates the need to optimise the device fabrication process and that because of this, it is not possible to determine the impact of different absorber layers on device efficiency as originally intended at this stage.

## 8.4. References

1. B. Shin, O. Gunawan, Y. Zhu, N. A. Bojarczuk, S. J. Chey, S. Guha, Thin Film Solar Cell with 8.4% Power Conversion Efficiency Using an Earth-abundant  $\text{Cu}_2\text{ZnSnS}_4$  Absorber, *Prog. Photovolt. Res. Appl.* 21 (2011) 72-76. <https://doi.org/10.1002/pip.1174>.
2. M. T. Ferdaous, S. A. Shahahmadi, P. Chelvanathan, Md. Akhtaruzzaman, F. H. Alharbi, K. Sopian, S. K. Tiong, N. Amin, Elucidating the Role of Interfacial  $\text{MoS}_2$  Layer in  $\text{Cu}_2\text{ZnSnS}_4$  Thin Film Solar Cells by Numerical Analysis, *Sol. Energy.* 178 (2019) 162-172. <https://doi.org/10.1016/j.solener.2018.11.055>.
3. C. Mary, S. Ananthakumar, M. Senthilkumar, S. M. Babu, Synthesis and Characterization of Amine Capped  $\text{Cu}_2\text{ZnSnS}_4$  (CZTS) Nanoparticles (NPs) for Solar Cell Application, *Mater. Today. Proceedings.* 4 (2017) 12484-12490. <https://doi.org/10.1016/j.matpr.2017.10.048>.
4. X. Cui, K. Sun, J. Huang, J. S. Yun, C. Lee, C. Yan, H. Sun, Y. Zhang, C. Xue, K. Eder, L. Yang, J. M. Cairney, J. Seidel, N. J. Ekins-Daukes, M. Green, B. Hoex, X. Hao, Cd-Free  $\text{Cu}_2\text{ZnSnS}_4$  Solar Cell with an Efficiency Greater Than 10% Enabled by  $\text{Al}_2\text{O}_3$  Passivation Layers, *Energy. Environ. Sci.* 12 (2019) 2751-2764. <https://doi.org/10.1039/C9EE01726G>.
5. D. Shin, B. Saparov, D. B. Mitzi, Defect Engineering in Multinary Earth-Abundant Chalcogenide Photovoltaic Materials, *Adv. Energy. Mater.* 7 (2017) 1602366. <https://doi.org/10.1002/aenm.201602366>.
6. S. K. Wallace, D. B. Mitzi, A. Walsh, The Steady Rise of Kesterite Solar Cells, *Am. Chem. Soc. Energy. Lett.* 2 (2017) 776-779. <https://doi.org/10.1021/acseenergylett.7b00131>.
7. G. Rey, G. Larramona, S. Bourdais, C. Chone, B. Delatouche, A. Jacob, G. Dennler, S. Siebentritt, On the Origin of Band-tails in Kesterite, *Sol. Energy. Mater. Sol. Cells.* 179 (2018) 142-151. <https://doi.org/10.1016/j.solmat.2017.11.005>.
8. Y. Feng, Y. Fan, Q. Song, Z. Li, W. Li, J. Tong, C. Yang, The Dependence of Open circuit Voltage on the Element Component in  $\text{Cu}_2\text{ZnSnS}_4$  Film Solar Cells, *Surface. Coatings. Technol.* 320 (2017) 65-69. <https://doi.org/10.1016/j.surfcoat.2017.01.117>.
9. T. J. Huang, X. Yin, G. Qi, H. Gong, CZTS-based Materials and Interfaces and their Effects on the Performance of Thin Film Solar Cells, *Physica. Status. Solidi. Rapid. Res. Lett.* 8 (2014) 735-762. <https://doi.org/10.1002/pssr.201409219>.
10. S. Padhy, R. Mannu, U. P. Singh, Graded Bandgap Structure of Kesterite Material Using Bilayer of CZTS and CZTSe for Enhanced Performance: A Numerical Approach, *Sol. Energy.* 216 (2021) 601-609. <https://doi.org/10.1016/j.solener.2021.01.057>.

# Chapter 9:

## Conclusions

### 9.1. Conclusions

In this thesis, CZTS thin film nanoparticle inks as absorber layers for thin film solar cells were studied systematically to find out the optimum synthesis conditions for high-performance thin film PV devices. The detailed study was divided into four experimental chapters. One was an investigation of the CZTS nanocrystal ink fabrication conditions: reaction temperature, time and tin content and their effect on the structural and optoelectronic properties of CZTS thin films. The second investigation was on the CZTS ink deposition conditions: spin coating speed and acceleration index. The third was on the post-deposition thin films annealing treatment conditions: temperature and time. These three chapters were followed by a chapter on applying these findings to build up complete CZTS solar cell devices and test their performance to determine the impacts of the tested variables on the CZTS solar cell device efficiency.

In chapter 5, using the hot injection method, CZTS nanoparticle thin film inks were successfully synthesised. The deposition of the inks was successfully achieved by the spin coating technique. A range of different reaction temperatures (225 °C, 250 °C, 275 °C and 300 °C) were investigated to find out the effect on the properties of CZTS thin films using XRD, SEM microscopy, EDS, Raman and UV-vis spectroscopy. The crystal  $d$ -spacing,  $a$  and  $c$  lattice constants and scattering domain, and the Raman peak positions of samples fabricated at reaction temperatures 250 °C and 300 °C showed values corresponding most closely to other literature reports. Moreover, the SEM image for 250 °C demonstrates the most uniform nanoparticles with small gaps compared to the other reaction temperatures. The EDS values for this sample showed a ratio of  $\text{Cu}/(\text{Zn}+\text{Sn}) = 0.82 \pm 0.01$  and  $\text{Zn}/\text{Sn} = 1.19 \pm 0.02$  demonstrating the formation of Cu-poor, Zn-rich CZTS at 250 °C, the composition at which higher efficiency devices are known to be

achieved. The bandgap, determined from a Tauc plot analysis, shows that the two temperatures (225 °C and 250 °C) result in bandgaps closest to the theoretical bandgap of CZTS at  $1.55 \pm 0.02$  and  $1.48 \pm 0.03$  eV. Both Raman and UV-vis spectroscopy identified the presence of possible secondary phases, although there was no consistent correlation between Raman and UV-vis data. From these characterisation results, the reaction temperatures of 225 °C, 250 °C and 275 °C were used to carry out the later systematic study in the following chapters.

The reaction time of the synthesised CZTS nanoparticles was studied and reported in the same chapter using the same procedure for producing the CZTS thin film inks. The reaction times investigated were 15, 30, 45 and 60 minutes, at the temperatures reported above. The sample of 250 °C with 30 minutes reaction time demonstrated the closest values of X-ray peak locations,  $d$ -spacing and  $a$ ,  $c$  lattice constants to the reference PDF card 026-0575 of CZTS. The Raman peak positions corresponded well with other literature papers especially with reaction temperature of 250 °C for 30 minutes. Two secondary phases of SnS and Cu<sub>4</sub>SnS<sub>4</sub> with a Raman peaks at 288 and 317 cm<sup>-1</sup> were present in the 250 °C for 30 minutes sample. The bandgap energy confirmed a systematic increasing trend with the increase of the reaction times in all samples. In addition, the SEM microscopy image for the 250 °C for 30 minutes sample shows the most uniform nanoparticle film with less cracks and gaps compared to the other samples and displaying a uniform size distribution. The EDS values show an excellent ratio for Cu-poor, Zn-rich in 250 °C for 30 minutes with  $\text{Cu}/(\text{Zn} + \text{Sn}) = 0.82 \pm 0.06$ ,  $\text{Zn}/\text{Sn} = 1.21 \pm 0.80$  and  $\text{S}/(\text{Cu} + \text{Zn} + \text{Sn}) = 1.17 \pm 0.20$ . Analysis of data was not able to identify any clear, consistent correlation between CZTS composition, primarily the Sn/Cu ratio, and the energy bandgap as has been identified in previously published work. From the characterisation results, 250 °C for 30 minutes was used for the following study.

The tin content of the synthesised CZTS nanoparticles was studied using the range of (0.60-0.90 mmol) of Sn using the synthesis conditions reported above. Characterisation of the thin films showed that Raman peak positions (338, 337 and 342 cm<sup>-1</sup>),  $d$ -spacing (0.3126, 0.3128 and 0.3145 nm),  $a$  lattice value (0.5416, 0.5417 and 0.5443 nm) and  $c$  lattice value (1.0821, 1.0844 and 1.0917 nm) had values corresponding to other literature papers for samples having 0.70, 0.75 and 0.85 mmol of Sn. In addition, the SEM image of the 0.75 mmol sample showed uniform nanoparticles compared to the other samples. The EDS values shows an excellent ratio for Cu-poor, Zn-rich in 0.75 mmol of Sn where this ratio is  $\text{Cu}/(\text{Zn} + \text{Sn}) = 0.83 \pm 0.40$ ,  $\text{Zn}/\text{Sn} = 1.09 \pm 0.30$  and  $\text{S}/(\text{Cu} + \text{Zn} + \text{Sn}) = 1.12 \pm 0.20$ . This is close to the composition found

in the most highly efficient CZTS solar cell devices. The Tauc plot showed that the samples of 0.70-0.85 mmol of Sn had energy bandgap values ( $1.42 \pm 0.02$ ,  $1.44 \pm 0.02$ ,  $1.52 \pm 0.04$  and  $1.53 \pm 0.02$  eV) close to the theoretically expected bandgap values of CZTS. From the characterisation results, sample Sn3 with 0.75 mmol of Sn was identified as the optimum tin content for the initial step for PV device fabrication. A clear correlation was found with increasing Sn content leading to increased energy bandgap.

In chapter 6, the hot injection reaction temperature of 250 °C for 30 minutes with 0.75 mmol for Sn are used to fabricate CZTS nanocrystal thin films for assessing the impact of spin coating parameters. The deposition of the inks was successfully done by dynamic spin coating. Different spin coating speeds 1300-9700 rpm were used to study their effect on the properties of the deposited ink films. The sample of 2500 rpm exhibited the desired compositional ratio for Cu-poor, Zn-rich for highly efficient solar cell devices confirmed by EDS with  $\text{Cu}/(\text{Zn} + \text{Sn}) = 0.82 \pm 0.40$ ,  $\text{Zn}/\text{Sn} = 1.07 \pm 0.01$  and  $\text{S}/(\text{Cu}+\text{Zn}+\text{Sn}) = 1.12 \pm 0.01$ . The bandgap shows values close to the expected theoretical bandgap values of CZTS for all samples ranging between  $1.40 \pm 0.03$  to  $1.52 \pm 0.02$  eV. The sample of 2500 rpm was used for later work as it was the most suitable spin coating speed. Increased spin coating speed produced films with smaller scattering domain sizes, but no clear trend in the energy bandgap.

The acceleration indices of 001-030, corresponding to acceleration values of 80-2400 rpm s<sup>-2</sup>, were used to investigate their impact on the properties of CZTS nanoparticle films. Based on the Raman data, there was a possible secondary phase of SnS present at peak location of 288 cm<sup>-1</sup> in the sample of acceleration 2400 rpm s<sup>-2</sup>. In addition, the SEM image for acceleration 2400 rpm s<sup>-2</sup> presents the most uniform nanoparticles in comparison with the other samples with particle size of around  $14 \pm 3$  nm. Importantly, it was found that acceleration index has a more pronounced impact on CZTS films than spin coating speed. Increased acceleration index produced films with smaller scattering domain sizes, more Zn, less S, and a systematically larger energy bandgap.

In chapter 7, the post deposition annealing temperatures and times were studied. A set of annealing temperatures was used at 560 °C, 585 °C, 610 °C, 635 °C in an atmosphere of N<sub>2</sub>:H<sub>2</sub>S 80:20, and 585 °C with N<sub>2</sub> only atmosphere for one hour. Table 7.4 shows that the bandgaps of all samples ( $1.52 \pm 0.01$ ,  $1.50 \pm 0.01$ ,  $1.41 \pm 0.02$ ,  $1.40 \pm 0.02$  and  $1.58 \pm 0.03$  eV respectively) are in the range of accepted values of the expected theoretical bandgap values of CZTS. The temperature of 585 °C was identified as the best temperature and used to continue the systematic study.

The impact of different annealing times of 30, 60 and 120 minutes were studied. The energy bandgap of the 60- and 120-min annealing time periods,  $1.50 \pm 0.01$  and  $1.56 \pm 0.03$  eV, correspond well with that of the expected theoretical value of CZTS nanocrystal thin film. It seems that using too short annealing times was not sufficient to form crystalline CZTS. The EDS values showed a desired ratio for Cu-poor, Zn-rich in sample 60 min with  $\text{Cu}/(\text{Zn} + \text{Sn}) = 0.83 \pm 0.02$ ,  $\text{Zn}/\text{Sn} = 1.17 \pm 0.02$  and  $\text{S}/(\text{Cu} + \text{Zn} + \text{Sn}) = 1.32 \pm 0.01$ . The temperature of  $585^\circ\text{C}$  for 60 min annealing time in  $\text{H}_2\text{S}:\text{N}_2$  was the most suitable annealing temperature and time.

In chapter 8, the CZTS nanocrystal thin film fabrication conditions which were identified in chapters 5, 6 and 7 were used to build up CZTS devices to test PV device performance. These conditions are reaction temperatures ( $225^\circ\text{C}$ ,  $250^\circ\text{C}$  and  $275^\circ\text{C}$ ) for 30 and 60 minutes. Six CZTS solar cell devices were built, testing their  $I$ - $V$  characteristics and PV conversion efficiency performance and cross section imaging the interfaces between the layers by SEM and EDS. The cross-section images of the devices by SEM showed a thick layer of around between 1630 to 4680 nm of CZTS in all devices. Among the devices tested,  $2.6 \pm 0.05\%$  was the highest efficiency performance reported with  $J_{sc} = 8.67 \text{ mA.cm}^{-2}$  and  $V_{oc} = 0.693 \text{ V}$ . The EDS mapping image was presented for the highest PV efficiency device performance. PV device performance results identified the need to reduce recombination losses, potentially due to interface and defect recombination. EDS element maps identified significant interdiffusion of elements throughout the device structure. As a result of high recombination losses, it was not possible to correlate overall device efficiency with CZTS fabrication conditions.

## 9.2. Recommendations for future studies

At the end of this study, several challenges are still not fulfilled to deepen the understanding of the CZTS absorber layer. These challenges include the following:

- The CZTS nanoparticle thin films inks were prepared by the hot injection method which is a chemical one. Stability of the pure phase of CZTS nanoparticle thin films inks for long term usage can be difficult and should be studied in more depth.
- Controlling the Mo/CZTS interface is a crucial challenge.
- Controlling the uniformity of CZTS by more reproducible approaches to spin coating deposition is required.

- 
- Strategies to reduce recombination losses are essential to improve device efficiency and to enable the correlation of CZTS absorber layer properties with overall PV device performance.